

# Double Chooz: A Search for the Neutrino Mixing Angle $\theta_{13}$

F. Ardellier<sup>19</sup> I. Barabanov<sup>10</sup> J. C. Barrière<sup>19</sup> F. Beißel<sup>1</sup>  
S. Berridge<sup>23</sup> L. Bezrukov<sup>10</sup> A. Bernstein<sup>14</sup> T. Bolton<sup>12</sup>  
N.S. Bowden<sup>20</sup> Ch. Buck<sup>16</sup> B. Bugg<sup>23</sup> J. Busenitz<sup>2</sup> A. Cabrera<sup>4</sup>  
E. Caden<sup>6</sup> C. Cattadori<sup>7,17</sup> S. Cazaux<sup>19</sup> M. Cerrada<sup>5</sup> B. Chevis<sup>23</sup>  
H. Cohn<sup>23</sup> J. Coleman<sup>15</sup> S. Cormon<sup>21</sup> B. Courty<sup>4</sup> A. Cucoanes<sup>1</sup>  
M. Cribier<sup>4,19</sup> N. Danilov<sup>11</sup> S. Dazeley<sup>15</sup> A. Di Vacri<sup>7</sup>  
Y. Efremenko<sup>23</sup> A. Etenko<sup>13</sup> M. Fallot<sup>21</sup> C. Fernández-Bedoya<sup>5</sup>  
F. von Feilitzsch<sup>22</sup> Y. Foucher<sup>21</sup> T. Gabriel<sup>23</sup> P. Ghislain<sup>4</sup>  
I. Gil Botella<sup>5</sup> G. Giurgiu<sup>3</sup> M. Goeger-Neff<sup>22</sup> M. Goodman<sup>3\*</sup>  
D. Greiner<sup>24</sup> Ch. Grieb<sup>22</sup> V. Guarino<sup>3</sup> A. Guertin<sup>21</sup> P. Guillouet<sup>4</sup>  
C. Hagner<sup>8</sup> W. Hampel<sup>16</sup> T. Handler<sup>23</sup> F. X. Hartmann<sup>16</sup>  
G. Horton-Smith<sup>12</sup> P. Huber<sup>22†</sup> J. Jochum<sup>24</sup> Y. Kamyshev<sup>23</sup>  
D. M. Kaplan<sup>9</sup> H. de Kerret<sup>4</sup> T. Kirchner<sup>21</sup> V. Kopeikin<sup>13</sup>  
J. Kopp<sup>22</sup> A. Kozlov<sup>23</sup> T. Kutter<sup>15</sup> Yu. S. Krylov<sup>11</sup> D. Kryn<sup>4</sup>  
T. Lachenmaier<sup>24</sup> C. Lane<sup>6</sup> T. Lasserre<sup>4,19\*</sup> C. Lendvai<sup>22</sup> Y. Liu<sup>2</sup>  
A. Letourneau<sup>19</sup> D. Lhuillier<sup>19</sup> M. Lindner<sup>22</sup> J. LoSecco<sup>18</sup>  
I. Machulin<sup>13</sup> F. Marie<sup>19</sup> J. Martino<sup>21</sup> D. McKee<sup>2</sup> R. McNeil<sup>15</sup>  
F. Meigner<sup>19</sup> G. Mention<sup>19</sup> W. Metcalf<sup>15</sup> L. Mikaelyan<sup>13</sup>  
A. Milsztajn<sup>19</sup> J. P. Meyer<sup>19</sup> D. Motta<sup>19</sup> L. Oberauer<sup>22</sup>  
M. Obolensky<sup>4</sup> C. Palomares<sup>5</sup> P. Perrin<sup>19</sup> W. Potzel<sup>22</sup>  
J. Reichenbacher<sup>3</sup> B. Reinhold<sup>1</sup> D. Reyna<sup>3</sup> M. Rolinec<sup>22</sup>  
L. Romero<sup>5</sup> S. Roth<sup>1</sup> S. Schoenert<sup>16</sup> U. Schwan<sup>16</sup> T. Schwetz<sup>22</sup>  
L. Scola<sup>19</sup> V. Sinev<sup>13,19</sup> M. Skorokhvatov<sup>13</sup> A. Stahl<sup>1</sup> I. Stancu<sup>2</sup>  
N. Stanton<sup>12</sup> S. Sukhotin<sup>4,13</sup> R. Svoboda<sup>14,15</sup> A. Tang<sup>12</sup>  
A. Tonazzo<sup>4</sup> D. Underwood<sup>3</sup> F.J. Valdivia<sup>5</sup> D. Vignaud<sup>4</sup>  
D. Vincent<sup>4</sup> W. Winter<sup>22‡</sup> K. Zbiri<sup>21</sup> R. Zimmermann<sup>8</sup>

20 June 2006 (revised 26 October 2006)

1. RWTH **Aachen** University
2. University of **Alabama**
3. **Argonne** National Laboratory
4. **AstroParticule** et Cosmologie Université Paris 7 (APC)
5. **CIEMAT** Centro de Investigaciones Energéticas, Medioambientales y Tecnológicas Madrid
6. **Drexel** University
7. INFN, Laboratori Nazionali del **Gran Sasso**
8. Universität **Hamburg**
9. **Illinois** Institute of Technology
10. **Institute** for Nuclear Research RAS
11. **Institute** for Physical Chemistry and Electrochemistry RAS
12. **Kansas** State University
13. RRC **Kurchatov** Institute
14. Lawrence **Livermore** National Laboratory
15. **Louisiana** State University
16. **Max-Planck-Institut** für Kernphysik (Heidelberg)
17. INFN, Milano
18. University of **Notre Dame**
19. CEA/DSM/DAPNIA **Saclay**
20. **Sandia** National Laboratories
21. **SUBATECH** Nantes (IN2P3 - Université de Nantes - EMN)
22. Technische Universität **München**
23. University of **Tennessee**
24. Eberhard-Karls Universität **Tübingen**

---

\*corresponding authors

†Now at University of Wisconsin

‡now at Institute for Advanced Study, Princeton

# Contents

<b>1</b>	<b>Overview</b>	<b>3</b>
1.1	Physics case and experimental context . . . . .	3
1.2	Experimental site: the Chooz nuclear reactors . . . . .	3
1.3	The new Double Chooz detector concept . . . . .	5
1.4	Time scale . . . . .	8
<b>2</b>	<b>Performance and Physics Reach</b>	<b>10</b>
2.1	Signal . . . . .	10
2.2	Experimental errors . . . . .	13
2.2.1	Reactor induced uncertainties . . . . .	13
2.2.2	Spent Fuel signal at Chooz . . . . .	15
2.2.3	Detector induced uncertainties . . . . .	16
2.2.4	Uncertainties in the efficiency determination . . . . .	18
2.2.5	Summary of the systematic uncertainty cancellations . . . . .	19
2.3	Backgrounds . . . . .	19
2.3.1	Accidental backgrounds . . . . .	20
2.3.2	Simulation of muon background . . . . .	22
2.3.3	Neutron-like background . . . . .	23
2.3.4	Fast neutron background . . . . .	26
2.3.5	Muon capture . . . . .	27
2.3.6	Cosmogenic correlated background: Lithium 9 . . . . .	29
2.3.7	Background subtraction error . . . . .	32
2.4	Sensitivity and discovery potential . . . . .	32
2.5	Complementarity with the Superbeam program . . . . .	34
2.6	Other physics . . . . .	39
2.6.1	Study of the directionality . . . . .	39
2.6.2	Mass-varying neutrinos . . . . .	40
<b>3</b>	<b>Detector Structures, Materials and Radiopurity</b>	<b>43</b>
3.1	Detector dimensions . . . . .	43
3.2	Double acrylic vessel . . . . .	43
3.3	Stainless steel Buffer vessel . . . . .	49
3.4	PMT supporting structure . . . . .	51
3.5	Inner Veto Mechanics . . . . .	51
3.6	Steel Shielding . . . . .	52
3.7	Simulation of the detector geometry . . . . .	54
3.8	Simulation of the detector materials . . . . .	55
3.9	Outer Veto . . . . .	57
3.10	Radiopurity Assessment . . . . .	58
<b>4</b>	<b>Scintillator, Fluid Handling and Purification</b>	<b>63</b>
4.1	Detector liquids and fluid handling . . . . .	63
4.2	Target . . . . .	63
4.3	Gamma-Catcher . . . . .	65

4.4	Buffer . . . . .	66
4.5	Fluid handling and purification . . . . .	67
4.6	Material compatibility . . . . .	67
4.7	Scintillator stability . . . . .	68
4.7.1	Methods . . . . .	68
4.7.2	Results . . . . .	69
4.7.3	Discussion . . . . .	70
4.7.4	Simulation: Optical properties . . . . .	71
<b>5</b>	<b>Photodetection</b>	<b>75</b>
5.1	Target and Gamma-Catcher . . . . .	75
5.1.1	Coverage . . . . .	75
5.1.2	Radiopurity Requirements . . . . .	75
5.1.3	PMT Performance . . . . .	76
5.1.4	Detailed Specifications . . . . .	77
5.1.5	Sensitivity to Magnetic Field . . . . .	81
5.1.6	PMT Purchase and Delivery . . . . .	81
5.1.7	Acceptance and Characterization Tests . . . . .	82
5.1.8	Mechanical Assembly and Cleaning . . . . .	83
5.1.9	Installation in the Detector, testing and commissioning . . . . .	83
5.1.10	Optics of the PMTs . . . . .	84
5.2	Inner Veto . . . . .	86
5.3	Simulations . . . . .	89
5.4	Magnetics . . . . .	96
5.4.1	Sensitivity to Magnetic Fields . . . . .	96
5.4.2	Size of the Effect . . . . .	98
5.4.3	De-perming Experiments . . . . .	99
5.4.4	Compensating Coils and Detectors . . . . .	100
<b>6</b>	<b>Trigger, Electronics, and DAQ</b>	<b>101</b>
6.1	High Voltage System . . . . .	101
6.1.1	System Design . . . . .	101
6.1.2	Requirements and Specifications . . . . .	101
6.1.3	Control and Monitoring Software . . . . .	102
6.1.4	Uninterruptible Power Supply . . . . .	102
6.1.5	Cabling . . . . .	103
6.1.6	Evaluation Phase . . . . .	103
6.2	Electronics . . . . .	103
6.2.1	HV Splitter . . . . .	103
6.2.2	Front-End Electronics . . . . .	106
6.2.3	Inner Veto Electronics . . . . .	107
6.2.4	Outer Veto Electronics . . . . .	107
6.2.5	Toward the Level-1 Trigger . . . . .	108
6.3	Trigger and Timing . . . . .	108
6.3.1	Concepts . . . . .	108
6.3.2	Trigger Outline . . . . .	110

6.3.3	Clock and Timing . . . . .	110
6.4	Data Acquisition System . . . . .	110
6.5	Main Features of The Waveform Digitizer module . . . . .	111
6.5.1	Operation of the Waveform Digitizer . . . . .	112
6.5.2	VME layout of the Read-out . . . . .	113
6.5.3	Second Level Trigger and Data Reduction . . . . .	113
6.5.4	A possible Data Reduction Strategy . . . . .	113
6.5.5	Dead time . . . . .	114
6.6	Slow Monitoring . . . . .	115
6.6.1	Monitoring via 1-Wire interface . . . . .	115
6.6.2	Radon monitoring . . . . .	118
6.6.3	Interface to other subsystems . . . . .	118
<b>7</b>	<b>Calibration</b>	<b>120</b>
7.1	Calibration Goals . . . . .	120
7.2	Calibration Sources and Deployment . . . . .	121
7.2.1	Gamma Sources . . . . .	121
7.2.2	Neutron Sources . . . . .	122
7.2.3	Light Flashers . . . . .	124
7.3	Calibration Deployment . . . . .	125
7.3.1	Introduction . . . . .	125
7.3.2	Deployment Methods . . . . .	125
7.3.3	Detector Interface . . . . .	127
7.3.4	Control Systems . . . . .	128
7.4	Calibration and Monitoring Plan . . . . .	128
<b>8</b>	<b>Simulation and Software</b>	<b>130</b>
8.1	Software and Simulation Goals . . . . .	130
8.2	Software Tools . . . . .	131
8.2.1	Event Generators . . . . .	135
8.2.2	Nuclear Transport Properties . . . . .	136
8.3	Vertex and Energy Reconstruction . . . . .	136
8.4	Calibration . . . . .	138
8.4.1	Light Sources . . . . .	138
8.5	Resources . . . . .	139
8.5.1	On site resources . . . . .	139
8.5.2	Off-site resources . . . . .	141
8.5.3	RoSS . . . . .	141
8.5.4	DOGS . . . . .	142
<b>9</b>	<b>Non proliferation activities</b>	<b>143</b>
9.1	Experimental effort . . . . .	144
9.1.1	Experiments with Lohengrin . . . . .	144
9.2	Simulations . . . . .	146
9.2.1	Simulations of diversion scenarios . . . . .	146
9.3	Experimental effort in the U.S. . . . .	148

9.4	Toward a prototype . . . . .	148
9.4.1	Complementary studies . . . . .	149
9.5	Conclusions . . . . .	149

# Executive Summary

It is widely recognized that the potential of reactor anti-neutrino disappearance experiments has not been fully exploited. High precision neutrino oscillation measurements could be achieved by a multi-detector experiment, whereby the sensitivity of the experiment would be nearly unaffected by the dominant uncertainties related to neutrino production and interaction [1]. This strategy has been adopted by the Double Chooz collaboration in order to search for a non-vanishing  $\theta_{13}$  mixing angle, which might open the way to unveiling CP violation in the leptonic sector. Furthermore, the reactor experiment results are complementary to those from next generation neutrino accelerator experiments, as it has been demonstrated a few years ago [2, 3].

The Double Chooz initiative started in the summer 2003 after reviewing a few possible sites suitable to perform a new reactor neutrino experiment dedicated to  $\theta_{13}$  in France. The Chooz site was selected because of the availability of the underground neutrino laboratory (300 m.w.e) located at 1.05 km from the nuclear cores, funded and constructed by Électricité de France (E.D.F.) [4] for the first experiment done at Chooz, end of the 90's [5]. This site selection was done in parallel with other similar efforts in Brazil, China, Japan, South-Korea, Russia, Taiwan, and the United States. There have been four international workshops mainly dedicated to the feasibility of new reactor neutrino experiments as well as for reviewing the potential of each site. All these initiatives have been described in the White Paper, "A New Nuclear Reactor Neutrino Experiment to Measure  $\theta_{13}$ " [6]. But since its publication the worldwide situation has changed and the projects still being considered are Angra [7] in Brazil, Daya Bay [8] in China, Double Chooz in France (see [9, 10] and this proposal), KASKA [11] in Japan and RENO [12] in South Korea. A recent comparison of the capabilities of these experiments can be found in [13, 14]. Double Chooz is particularly attractive because it could limit  $\sin^2(2\theta_{13})$  to 0.022-030 (for  $\Delta m_{31}^2 = 3.5 - 2.5 \times 10^{-3} eV^2$ ), within an unrivaled time scale and a modest cost. Installation of the experiment will start with the far detector located at the former experimental site of the CHOOZ experiment. This first phase of the experiment will allow us to exceed the CHOOZ sensitivity within a few months, to reach a limit of  $\sin^2(2\theta_{13}) < 0.08$  if no oscillation signal is detected after 1,5 years of data taking. Then the collaboration will install an identical near detector 280 m from the Chooz nuclear cores, in a new neutrino laboratory in a 45 m deep shaft to be excavated. This second phase will considerably reduce the overall systematic uncertainties and allow the final sensitivity of the experiment to be reached within 3 years of data taking.

Double Chooz will also lay the foundation for future experiments through the development of innovative technologies (scintillators, detector inter-calibration, etc). In addition, the International Atomic Energy Agency (IAEA) mandated by the United Nations Organization is interested in the prospect applications of neutrino physics. The detection of the antineutrinos produced by a nuclear power plant would provide a real-time, remote, non-intrusive and impossible-to-fake means to address certain safeguards applications. The near detector of Double Chooz will perform a measurement of the antineutrino flux and energy spectrum with an unprecedented accuracy, which will enable the collaboration to achieve a feasibility study of the detection of antineutrinos for safeguards applications, and test the potential of neutrinos to detect various diversion scenarios.

The Double Chooz collaboration is presently composed of 24 institutions from France, Germany, Italy, Russia, Spain and the United States. In this proposal, and during the funding request phase of the experiment, the detector design has been divided in work packages shared in the collaboration under the assumption that each group is full funded. French groups are responsible for the detector mechanics. They are also in charge of the digitization and the data acquisition systems. German

groups have responsibility for the scintillators, purification, and fluid systems, as well as the inner muon veto, and the level-1 trigger. They are also involved in the calibration. Spanish collaborators are involved in the inner detector photodetection and the related mechanics. United States groups have taken the inner phototubes, the Front-End electronics, the calibration systems, and the slow-control. The Outer Veto is also under the responsibility of the United States groups. Russian groups are involved in simulation, calibration, and scintillator developments. We note as well the participation of the Italian/Russian chemistry group of the INFN–LNGS laboratory to the loaded liquid scintillator effort. Simulation and software developments are distributed throughout the collaboration. Near and Far detector infrastructures, as well as the technical coordination and detector integration are managed by the French institutes. Finally, a few other items are still under discussion.

The Double Chooz experiment has been approved by the French scientific councils of CEA–DSM–DAPNIA and CNRS–IN2P3 since March 2004. Recently it has been reviewed again, leading to the definitive approval and funding from both agencies, starting from 2006. The Double Chooz experiment is supported by the Astroparticle Physics European Coordination (ApPEC) roadmap [15]. In Germany the experiment receives funding through the Max-Planck Society with a substantial increase beginning in 2006. The funding of the university groups is currently in the final approval process at the Deutsche Forschungsgemeinschaft (DFG). In the United States, a new reactor neutrino experiment is one of the high priority recommendations of the APS neutrino study [16]. The Neutrino Scientific Assessment Group (NuSAG) and the High Energy Physics Advisory Panel (HEPAP) both recommended U.S. participation to Double Chooz [17, 18]. However, the High Energy Physics division at DOE turned down the Double Chooz R&D request and has not acted on the construction request. Construction funding is currently being discussed at NSF (National Science Foundation). Russian participation has been funded by Russian Foundation of Basics Research. In Spain funding will be decided in June 2006.

In conclusion, the design and work sharing presented in this proposal may change in the forthcoming months as new collaborators join the experiment. Since the major funding of Double Chooz is secured it is planned to start the far detector integration in 2007 in order to take data in 2008. The near detector will be installed after the completion of the shaft civil engineering construction in 2009.

## Acknowledgments

Upgrade of the far site laboratory is done in cooperation with the CIDEN (Centre d’Ingénierie, Déconstruction et Environnement Nucléaire) division of Électricité de France (E.D.F.) [19]. Study of the near site laboratory civil engineering is done in cooperation with the CNEN (Centre National d’Etudes Nucléaires) division of Électricité de France (E.D.F.). We also thank the staff of E.D.F. CHOOZ nuclear plant [20] for their continuous support. We are very grateful to the Conseil Général des Ardennes for providing us with the facilities for the experiment. We thank also the Mayor of Chooz and the local members of the parliament. Special thanks to the technical staff of our laboratories for their excellent work in designing the detector.



# 1 Overview

## 1.1 Physics case and experimental context

It has recently been widely recognized that a reactor antineutrino disappearance experiment with two or more detectors is one of the most cost-effective ways to extend our reach in sensitivity for the neutrino mixing angle  $\theta_{13}$  without ambiguities from CP violation and matter effects [6]. This is a proposal by an international collaboration of neutrino physicists to modify the existing neutrino physics facility at the Chooz-B nuclear power station in France [9, 10]. The experiment, called Double Chooz, is planned to reach a sensitivity to  $\sin^2 2\theta_{13}$  down to 0.03 over a three year run from early 2009, with two detectors running simultaneously. This will cover roughly 85% of the currently allowed region. The costs and time to first results for this critical parameter can be minimized since our project takes advantage of an existing laboratory.

The Double Chooz reactor neutrino experiment [9] offers the world particle physics community a relatively quick and inexpensive opportunity to measure the mixing angle  $\theta_{13}$  if it is not too small:  $0.19 > \sin^2 2\theta_{13} > 0.03$ . The data taking will be divided in two phases: a first one with the Far detector only, and a second phase with both Near and Far detectors running simultaneously. For  $\Delta m^2 \approx 2.5 \times 10^{-3} \text{eV}^2$ , Double Chooz will be sensitive to 0.05 after 1.5 year of data taking in phase I, and 0.03 or better after 3 years of operation with two detectors. If  $\theta_{13}$  is in this range, long-baseline off-axis neutrino experiments will be able to measure matter effects and search for CP violation [21, 3, 22].

There have been four international workshops and a white paper which have outlined the challenges and benefits of a new reactor experiment to measure  $\theta_{13}$  [6]. Projects currently being considered are ANGRA [7] in Brazil, Daya Bay [8] in China, Double Chooz [23] in France, KASKA [11] in Japan and RENO [12] in South Korea. For a recent comparison of the capabilities of these five experiments, see References [13, 14].

Of these proposed experiments, Double Chooz has the opportunity to obtain results first and quickly explore this important region of neutrino parameter space. The Reactor Neutrino White Paper [6] identified civil construction costs as approximately two-thirds of the cost of a new reactor neutrino experiment. By taking advantage of the Chooz site where a hall near the correct distance already exists, tremendous savings are available, with regard not only to cost and schedule but also in the areas of risk and contingency. Further, a timely measurement of  $\theta_{13}$ , available only from such an experiment, will be of considerable value in planning the more expensive off-axis accelerator projects, which are sensitive to matter effects and CP violation in the neutrino sector, but only if  $\theta_{13}$  is large enough.

## 1.2 Experimental site: the Chooz nuclear reactors

The antineutrinos used in the experiment are those produced by the pair of reactors located at the Chooz-B nuclear power station operated by the French company Electricité de France (EdF) in partnership with the Belgian utilities Electrabel S.A./N.V. and Société Publique d'Electricité. They are located in the Ardennes region, in the northeast of France, very close to the Belgian border, in a meander of the Meuse river (see Figures 1 and 2). At the Chooz site, there are two nuclear reactors. Both are of the most recent “N4” type (4 steam generators), with a thermal power of 4.27 GW<sub>th</sub> each, and were recently upgraded from 1.45 GW<sub>e</sub> to 1.5 GW<sub>e</sub>. Each reactor is off about one month per year. These are pressurized water reactors (PWR) and are fed with UOx type fuel.

They are the most powerful reactor type in operation in the world. One unusual characteristic of the N4 reactors is their ability to vary their output from 30% to 95% of full power in less than 30 minutes, using the so-called gray control rods in the reactor core. These rods are referred to as gray because they absorb fewer free neutrons than conventional (“black”) rods. One advantage is greater thermal homogeneity. A total of 205 fuel assemblies are contained within each reactor core. The entire reactor vessel is a cylinder 4.27 m tall and 3.47 m diameter. The first reactor started full-power operation in May 1997, and the second one in September of the same year.

The Double Chooz experiment will employ two almost identical detectors of medium size, each containing 10.3 cubic meters of liquid scintillator target doped with 0.1% of gadolinium (see Section 4). The neutrino laboratory of the first CHOOZ experiment,<sup>1</sup> located 1.05 km from the two cores of the Chooz nuclear plant, will be used again (see Figure 3). This is the main advantage of this site compared with other locations. We label this site the far detector site or **Double Chooz-**



Figure 1: Overview of the experiment site.

**far.** A sketch of the Double Chooz-far detector is shown in Figure 5. The Double Chooz-far site is shielded by about 300 m.w.e. of  $2.8 \text{ g/cm}^3$  rock. It is intended to start taking data at Double Chooz-far at the beginning of 2008.

<sup>1</sup>For clarity, the first reactor neutrino experiment conducted at the Chooz reactor is herein referred to in uppercase.



Figure 2: Map of the experiment site. The two cores are separated by a distance of 140 meters. The far detector site is located 1.0 and 1.1 km from the two cores.

In order to cancel the systematic errors originating from the nuclear reactors (lack of knowledge of the  $\bar{\nu}_e$  flux and spectrum), as well as to reduce the set of systematic errors related to the detector and to the event selection procedure, a second detector will be installed close to the nuclear cores. We label this detector site the near site or **Double Chooz-near**. An initial study has been completed by the French electric power company EdF to determine the best combination of location and overburden as well as the preliminary cost of the needed civil construction. This study suggested the feasibility of excavating a  $\approx 40$  m deep shaft at a 250–300 m distance from the nuclear reactor cores, see Figure 4. The plan is to start taking data at Double Chooz-near at the end of 2008 or early in 2009.

### 1.3 The new Double Chooz detector concept

The Double Chooz-far detector will consist of a target cylinder of 115 cm radius and 246 cm height, providing a volume of  $10.3 \text{ m}^3$ . The near and far detectors will be identical inside the PMT support structure. This will allow a relative normalization systematic error of 0.6%. However, due to the differing overburdens (70–80 vs. 300 m.w.e.), the outer shielding will not be identical, since the cosmic ray background differs considerably between Double Chooz-near and -far. The overburden of the near detector has been chosen in order to keep a high true-neutrino-signal to background ratio. A review of the backgrounds at both sites is given in Section 2.3.

Starting from the center of the target the detector elements are as follows (see Figure 5):



Figure 3: Picture of the Double Chooz-far detector site taken in September 2003. The original CHOOZ laboratory hall constructed by EdF, located close the old Chooz A underground power plant, is still in perfect condition and could be re-used without additional civil engineering construction.

### Target and $\gamma$ -catcher

Target and  $\gamma$ -catcher vessels will be built from acrylic plastic material, transparent to UV and visible photons with wavelengths above 400 nm. The vessels are designed to contain the target and  $\gamma$ -catcher aromatic liquids with long-term hermeticity (no leak for 10 years) and stability. The strongest constraint is the chemical compatibility between the vessel and the scintillating liquids of the target and  $\gamma$ -catcher (chemical stability for a period of at least 5 years). The  $\gamma$ -catcher vessel must also be chemically compatible with the mineral oil of the buffer region, which is however known to be a weaker constraint. Target and  $\gamma$ -catcher vessels will be made of cast acrylic. The target vessel is a cylinder of 246 cm height, 230 cm diameter, and 8 mm thickness. It contains a target volume of 10.3 m<sup>3</sup>. The  $\gamma$ -catcher is a 55-cm-thick buffer of nonloaded liquid scintillator (22.6 m<sup>3</sup>) with the same light yield as the  $\bar{\nu}_e$  target. This scintillating buffer around the target is necessary for efficiently measuring the gammas from neutron capture on Gd and from positron annihilation, and to reject the background from fast neutrons (see Section 2.3).

### Nonscintillating buffer

A 105-cm-thick region of nonscintillating liquid (114.2 m<sup>3</sup>) serves to decrease the level of accidental background (mainly the contribution from photomultiplier-tube radioactivity). This region is crucial

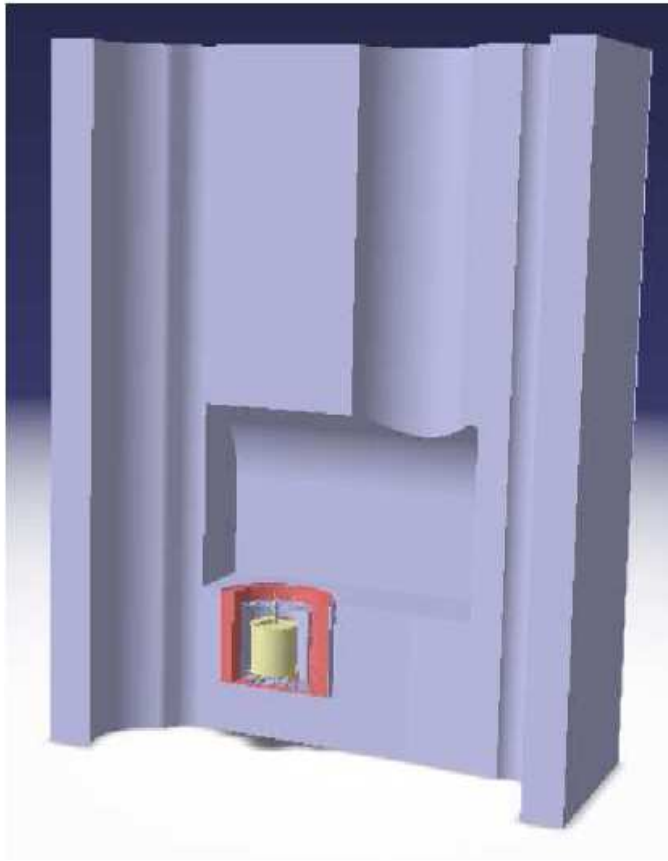


Figure 4: 3D rendering of the Double Chooz-near site. The detector is located in a  $\sim 45$ -meter-deep shaft, about 250–300 meters from the nuclear cores. Several civil engineering options are being studied to provide an overburden of 30 meters of rock ( $2.8 \text{ g/cm}^3$ ). Since more space will be available here than at the far site, we are studying the option of using low-radioactivity sand (70 cm) instead of the steel shielding used at Double Chooz far.

to keeping the singles rate below 10 Hz in the sensitive region (target+ $\gamma$ -catcher).

### **Buffer vessel and PMT support structure**

This vessel is made of 3-mm-thick stainless steel sheets and stiffeners. A total of 534 phototubes (8 inch) in a uniform array are mounted from the interior surface of the buffer vessel.

### **Inner veto system**

A 50-cm-thick veto region filled with liquid scintillator for both the near and far detectors.

### **Outer veto system**

A proportional-tube tracker system will identify and locate “near-miss” muons. This improves the muon rejection by a factor 20 compared to that of the inner veto by itself.

The main uncertainties at CHOOZ came from the uncertainty in the knowledge of the antineutrino flux coming from the reactor. This systematic error is made to vanish by the addition of a near detector. The nonscintillating buffer will reduce the singles rates in each detector by two orders

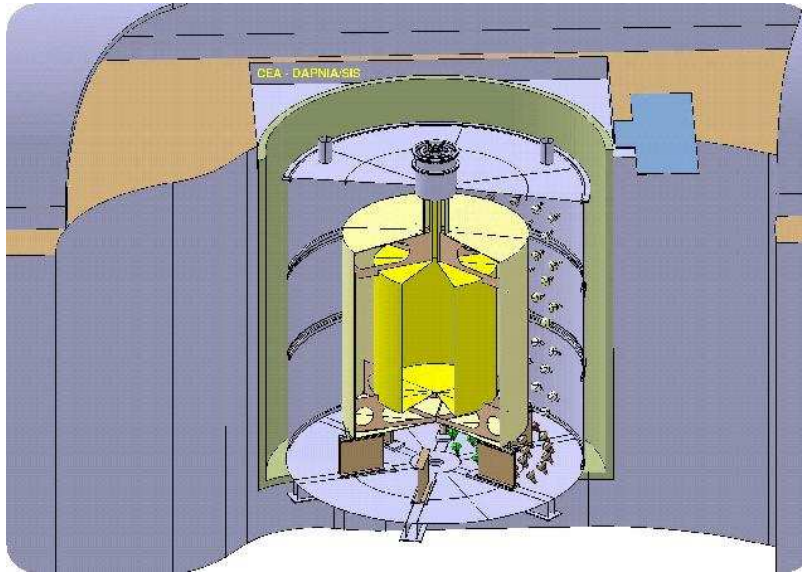


Figure 5: The Double Chooz-far detector, at the Chooz underground site. The detector is located in the tank used for the CHOOZ experiment (7 meters high and 7 meters in diameter) which is still available. A total of  $10.3 \text{ m}^3$  of a dodecane+PXE-based liquid scintillator doped with gadolinium is contained in a transparent acrylic cylinder surrounded by the  $\gamma$ -catcher region ( $22.6 \text{ m}^3$ ) and the buffer ( $114.2 \text{ m}^3$ ). The design goal is to achieve a light yield of about 200 pe/MeV which requires an optical coverage of about 13%, provided by the surrounding PMTs. The PMTs are mounted on the cylindrical steel structure that optically isolates the outer part of the detector, used as a muon veto ( $90 \text{ m}^3$ ), from the inner part.

of magnitude with respect to those in CHOOZ, which had no such buffer. The positron detection threshold will be about 500–700 keV, well below the 1.022 MeV physical threshold of the inverse beta decay reaction. A full review of the detector systematics is given in Section 2.2.

## 1.4 Time scale

A summary of key detector parameters is given in Table 1. At the Chooz site, the laboratory previously used by the CHOOZ experiment is vacant and available for use as a far site with minimal preparation. The ventilation and electrical distribution systems have been upgraded and safety upgrades of the gallery are currently in progress. The relationship between the members of the CHOOZ collaboration and the reactor company, Electricité de France (EdF), has been very cooperative and cordial. For the Double Chooz experiment, EdF has again shown the same level of close cooperation and has signed a letter outlining that cooperation.

The schedule for Double Chooz is aggressive in order to take into account the great worldwide interest in  $\theta_{13}$ . Construction of the far detector will be completed by the end of 2007, and that of the near detector by the end of 2008 (with some uncertainty concerning the schedule of the near laboratory construction). Detector operation will be for 4.5 years, starting with just the far detector, followed by three years of operation with both detectors (2009–2011). Important first results are possible with just the far detector because the luminosity (12 GW-ton-years) of the original CHOOZ experiment will be matched in just a few months. Using both detectors, Double

Table 1: Summary of the some parameters of the proposed Double Chooz experiment.

Thermal power	4.27 GW	each of 2 cores
Electric power	1.5 GWe	each of 2 cores
$\bar{\nu}_e$ target volume	10.3 m <sup>3</sup>	Gd loaded LS (0.1%)
$\gamma$ -catcher thickness	55 cm	Gd-free LS
Buffer thickness	105 cm	non scintillating oil
Total liquid volume	$\sim$ 237 m <sup>3</sup>	
Number of phototubes per detector	534 8"	13% coverage
Far detector distance	1050 m	averaged
Near detector distance	280 m	averaged
Far detector overburden	300 m.w.e.	hill topology
Near detector overburden	70–80 m.w.e.	shaft
$\bar{\nu}_e$ far detector events (5 yr)	75,000	with a 60.5% efficiency
$\bar{\nu}_e$ near detector events (5 yr)	789,000	with a 43.7% efficiency
Relative normalization error	0.5%	
Effective bin-to-bin error	1%	background systematics
Running time with far detector only	1–1.5 year	
Running time with far+near detector	3 years	
$\sin^2(2\theta_{13})$ goal in 3 years with 2 detectors	0.02–0.03	(90% CL)

Chooz will reach a  $\sin^2(2\theta_{13})$  sensitivity of 0.06 in 2009 and 0.03 in 2011. Whether running any longer at that time makes sense will depend on an evaluation of systematic errors and backgrounds achieved, as well as the world situation regarding  $\theta_{13}$ .

## 2 Performance and Physics Reach

### 2.1 Signal

In this section we provide a short summary of the antineutrino energy spectrum as expected in the Double Chooz detectors. We first introduce the energy spectrum parametrization and then include the effect of the oscillations. The goal is to give a good estimation of the sensitivity to small values of  $\sin^2(2\theta_{13})$  in Section 2.4. The antineutrino flux provided by the two nuclear cores of the Chooz power plant results from  $\beta^-$  decay of the fission products of four main isotopes  $^{235}\text{U}$ ,  $^{239}\text{Pu}$ ,  $^{241}\text{Pu}$  and  $^{238}\text{U}$ . The overall  $\bar{\nu}_e$  spectrum is evaluated from measurements of  $^{235}\text{U}$ ,  $^{239}\text{Pu}$ ,  $^{241}\text{Pu}$  and theoretical prediction for  $^{238}\text{U}$  [24]. We take an average burning cycle composition of 55.6% of  $^{235}\text{U}$ , 32.6% of  $^{239}\text{Pu}$ , 7.1% of  $^{238}\text{U}$  and 4.7% of  $^{241}\text{Pu}$ . A ten percent burnup effect is taken into account in detailed simulations however. The  $\bar{\nu}_e$  number produced and the released energy per fission are shown in Table 2. We note the west and east reactor cores as  $R_W$  and  $R_E$ . The

Table 2: Total number of  $\bar{\nu}_e$  produced and energy released by fission above the threshold energy of 1.8 MeV [24].

	Number of $\bar{\nu}_e$ per fission	Energy released per fission (in MeV)
$^{235}\text{U}$	$1.92 \pm 0.036$	$201.7 \pm 0.6$
$^{238}\text{U}$	$2.38 \pm 0.048$	$205.0 \pm 0.9$
$^{239}\text{Pu}$	$1.45 \pm 0.030$	$210.0 \pm 0.9$
$^{241}\text{Pu}$	$1.83 \pm 0.035$	$212.4 \pm 1.0$

maximum operating thermal power of each core amounts to 4.27 GW. The far detector is located at a distance of  $1114.6 \pm 0.1$  m from  $R_E$ , and at  $997.9 \pm 0.1$  m from  $R_W$ , leading to 2.86  $\nu$  events/h. A near detector preferred location has been chosen at 290.7 m from  $R_E$  and 260.3 m from  $R_W$ , leading to 41.2 events/h. At this location, both detectors receive the same neutrino flux ratio coming from both nuclear cores. This cancels systematic uncertainties related to the uncorrelated fluctuations of the thermal power of each reactor (see Section 2.4 for more details).

The Double Chooz Target contains  $10.32 \text{ m}^3$  of liquid scintillator (see Section 4). Before addition of the small amount of fluors as well as the gadolinium compound, the scintillator can be described as 20% of PXE ( $C_{16}H_{18}$ ) and 80% of dodecane ( $C_{12}H_{26}$ ). This leads to  $6.79 \cdot 10^{29}$  free protons available for the detection reaction:

$$\bar{\nu}_e + p \rightarrow e^+ + n . \quad (1)$$

We thus have a direct relation between positron energy and the incoming neutrino energy, taking into account neutron recoil,

$$E_{\bar{\nu}_e} = \frac{1}{2} \frac{2M_p E_{e^+} + M_n^2 - M_p^2 - m_e^2}{M_p - E_{e^+} + \sqrt{E_{e^+}^2 - m_e^2} \cos \theta_{e^+}} . \quad (2)$$

We define the visible energy ( $E_{\text{vis}}$ ) as the kinetic energy from the detected positron plus its annihilation on an electron. Introducing the notation  $\Delta = M_n - M_p = 1.293$  MeV, and assuming  $\langle \cos \theta_{e^+} \rangle = 0$  ( $\theta_{e^+}$  is the angle between the neutrino and positron directions), we have the following expression

$$E_{\text{vis}} = E_{e^+} + m_e \simeq E_{\bar{\nu}_e} - \Delta + m_e . \quad (3)$$



The antineutrino cross-section on proton expressed with the same variables is given by:

$$\sigma(E_{\bar{\nu}_e}) = K \times (E_{\bar{\nu}_e} - \Delta) \sqrt{(E_{\bar{\nu}_e} - \Delta)^2 - m_e^2}, \quad (4)$$

where  $K$  is directly extracted from the neutron lifetime

$$K = (9.559 \pm 0.009) 10^{-44} \text{ cm}^2 \text{ MeV}^{-2}. \quad (5)$$

For  $\sin^2(2\theta_{13})$  above 0.001, oscillation terms with  $\Delta m_{21}^2$  can be ignored, and we can write:

$$P_{ee}(E_{\bar{\nu}_e}, L, \Delta m_{31}^2, \theta_{13}) = 1 - \sin^2(2\theta_{13}) \sin^2 \left( 1.27 \frac{\Delta m_{31}^2 [10^{-3} \text{ eV}^2] L [\text{km}]}{E_{\bar{\nu}_e} [\text{MeV}]} \right). \quad (6)$$

We compute the number of events in detector  $D$  from reactor  $R$  in the  $i^{\text{th}}$  antineutrino energy interval  $[E_i; E_{i+1}]$  as

$$N_i^{R,D} = \mathcal{T}(R) \int_{E_i}^{E_{i+1}} \sigma(E_{\bar{\nu}_e}) \phi_{R,D}(E_{\bar{\nu}_e}) R_i(E_{\bar{\nu}_e}) P_{ee}(E_{\bar{\nu}_e}, L(D, R), \Delta m_{31}^2, \theta_{13}) dE_{\bar{\nu}_e}, \quad (7)$$

where the flux from reactor  $R$  to detector  $D$  has the following expression

$$\phi_{R,D}(E_{\bar{\nu}_e}) = \frac{1}{4\pi L(D, R)^2} \sum_l N_l^{\text{fis},R} \phi_l(E_{\bar{\nu}_e}). \quad (8)$$

We assume a polynomial parametrization of the four isotopes antineutrino energy spectra ( $l = {}^{235}\text{U}$ ,  ${}^{239}\text{Pu}$ ,  ${}^{241}\text{Pu}$  or  ${}^{238}\text{U}$ ):

$$\phi_l(E_{\bar{\nu}_e}) = \exp \left( \sum_{k=0}^6 a_{kl} E_{\bar{\nu}_e}^k \right). \quad (9)$$

The  $a_{kl}$  coefficients may be found in Reference [24], and  $N_l^{\text{fis},R}$  is the number of fissions per second of the isotope  $l$ , which can be extracted from [25].

The generic factor  $\mathcal{T}(R)$  in equation (7) takes into account the experiment life time and the global load factor of reactor  $R$ . The detector ( $D$ ) response is expressed through  $R_i(E_{\bar{\nu}_e})$ , including the number of free protons, a dead time of 30% for the near detector due to its shallow depth, an energy resolution of 7% (at 1 MeV), and a detector efficiency of 80%. The global load factor of the Chooz power plant was 73.3% and 81% for  $R_W$  (Chooz-B1), and 79.7% and 76.2% for  $R_E$  (Chooz-B2), in 2003 and 2004 respectively. In the following we assume the average value of 78%. After 5 years the amount of data available would be 76,000 reactor neutrino events in the far detector (efficiency included) and 800,000 events in the near detector, accounting for the estimated reactor and detector efficiencies (efficiency included). Neutrino rates and associated information are summarized in Table 3. Figure 2.1 shows the positron energy spectrum expected at Chooz-Near and Chooz-Far for 3 years of data taking, assuming a true value of  $\sin^2(2\theta_{13}) = 0.1$  and  $\Delta m_{31}^2 = 2.5 \times 10^{-3} \text{ eV}^2$ .

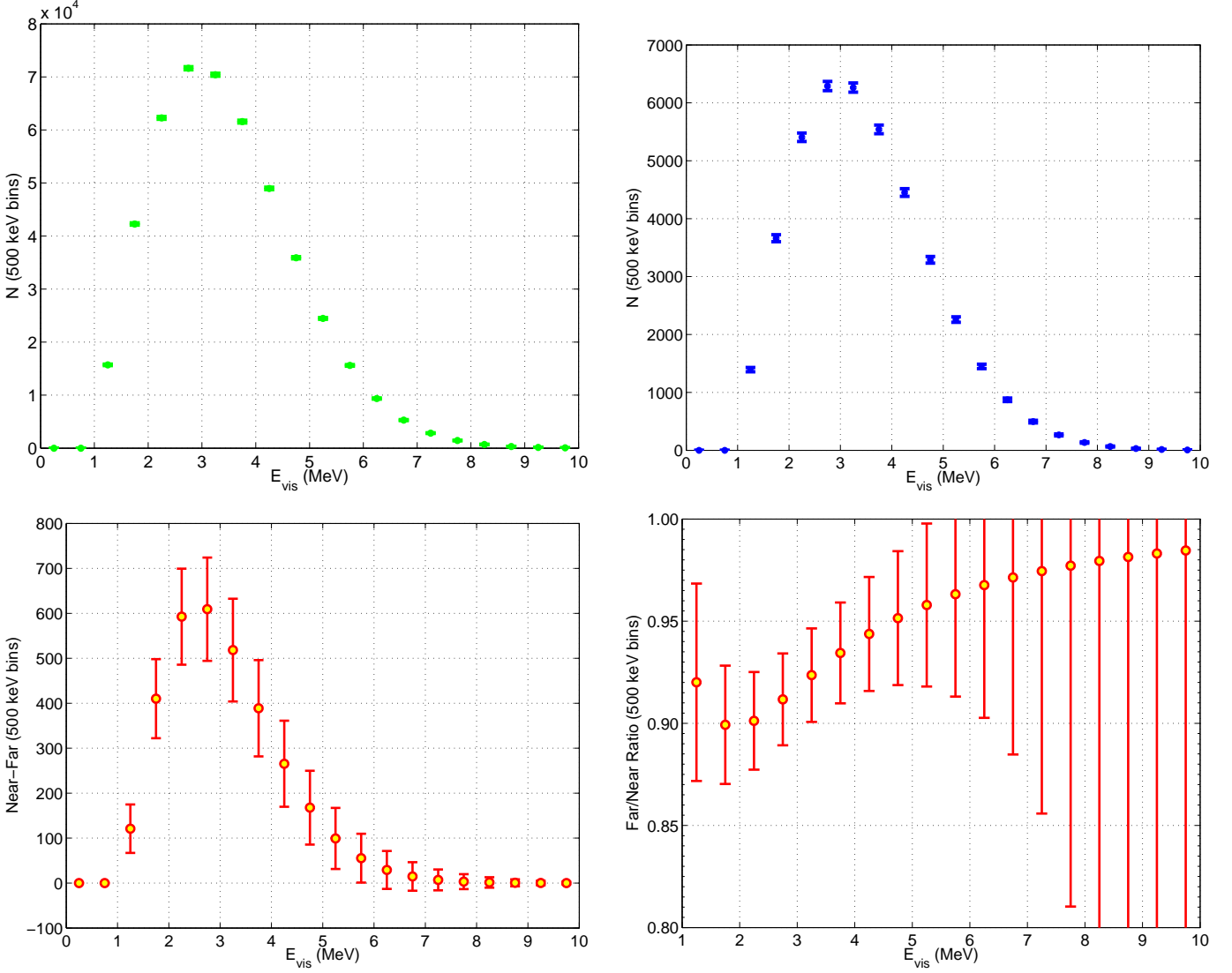


Figure 6: Expected signal assuming a true value of  $\sin^2(2\theta_{13}) = 0.1$  and  $\Delta m_{31}^2 = 2.5 \times 10^{-3} eV^2$ , for 3 years of data taking with both detectors. Top left: positron energy spectrum at the Near detector. Top right: positron energy spectrum at the Far detector. Bottom left: spectrum difference between the Near and Far detector (normalized to the Far detector statistics). Bottom right: Far to Near spectrum ratio. Errors bars quoted are only statistical.

Table 3:  $\nu$  rate expected in the Near and Far detectors, with and without reactor and detector efficiencies. Final distances for the Near detector have not been decided yet, but the values presented are good estimates within 30%. The rate without efficiency is used for signal to background comparison. The integrated rate in the last line includes detector efficiency, dead time, and reactor off periods averaged over a year.

Detector	Near	Far
Distance from West reactor (m)	290.7	$1114.6 \pm 0.1$
Distance from East reactor (m)	260.3	$998.1 \pm 0.1$
Detector Efficiency	80%	80%
Reactor Efficiency	78%	78%
Dead Time	30%	3%
Rate without efficiency ( $d^{-1}$ )	1011.5	68.8
Rate with detector efficiency ( $d^{-1}$ )	566.4	53.4
Integrated rate ( $y^{-1}$ )	161,260	15,200

## 2.2 Experimental errors

Double Chooz will use two  $\bar{\nu}_e$  detectors in order to cancel or decrease significantly the systematic uncertainties that would limit the sensitivity to  $\theta_{13}$ . For the sake of comparison, the total systematic error of the CHOOZ experiment amounted to 2.7% [5]. This error was dominated by the reactor antineutrino flux and spectrum uncertainties, that amounted to 1.9%. At neutrino luminosities addressed by Double Chooz (less than a few hundred thousand events in the far detector) the relative normalization between the two detectors is the most important source of error and must be carefully controlled. The goal of Double Chooz is to reduce this uncertainty to 0.6%. Double Chooz systematic uncertainties were already reviewed in the Double Chooz Letter of Intent (LOI) [9]. We discuss them briefly, focusing on the work done to confirm the LOI [9]. It is worth noting that we do not assume any major innovation to decrease the systematic error below one percent. Considering the CHOOZ results, we identified the uncertainties that cancel (some of them only partially) by using two identical detectors and derived the predicted systematics for Double Chooz. However, two cases are discussed in more detail below because they needed some dedicated R&D in the collaboration: the dead time measurement on page 17, and the Target volume measurement on page 17.

### 2.2.1 Reactor induced uncertainties

Since the neutrino flux is isotropic, all the reactor induced systematic uncertainties cancel but the solid angle. A summary of the reactor induced systematics is given in Table 4.

#### Solid angle

and each core have been measured with a precision of 10 cm. The distances between the center of the detectors and the reactor core center have to be precisely known. The far detector-cores distance have been measured with a precision of 10 cm. Such a precision is achieved using geometric measurements at the near site. Considering a near detector at about 250-300 m, this leads to a systematic error of 0.06%.

Table 4: Reactor induced systematics

Reactor power	CHOOZ	Double Chooz
Reactor power	$\sim 2\%$	negligible
Energy per fission	0.6%	negligible
$\bar{\nu}_e$ /fission	0.2%	negligible
Neutrino cross section	0.1%	negligible

Two other effects at this baseline distance could add up: a statistical fluctuation of the neutrino detected number whose mean may vary; a displacement of the production “barycenter” inside cores.

Concerning the first effect, a simple Monte Carlo simulation shows us the distance traveled by neutrinos between production and detection closely follows a normal distribution, and the most important point is that its skewness is very low. A study using the central limit theorem tells us the mean won’t vary by more than 0.01%.

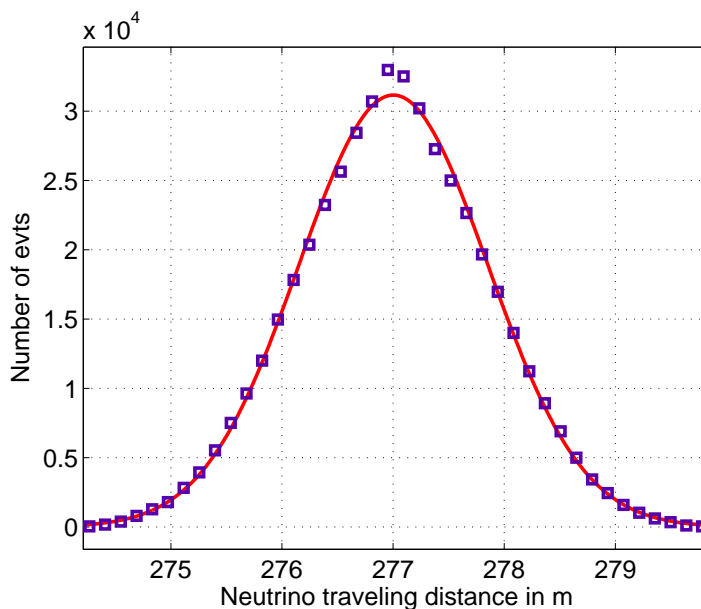


Figure 7: Neutrino traveling distance histogram for near detector (274 m away, 40 m depth). The traveling distance distribution is centered around 277 m, with no bias (skewness around  $10^{-3}$ ). In this Monte Carlo simulation we assumed a uniform neutrino production inside a typical cylindrical reactor core.

Regarding the second effect, the “barycenter” of the neutrino emission in the reactor core have to be monitored with a similar precision (a level of 5 cm was achieved in the Bugey experiment [26]). Such an effect would lead to an uncertainty of 0.03%. Actually it was shown in the Bugey experiment that the barycenter moves by tens of centimeters vertically, but is very stable laterally. A 10 cm vertical displacement would lead to a distance variation of about 1 cm (at 300 m and 40 m depth) which is negligible. In conclusion, determining precisely the barycenter of each reactor core and the center of each detector is sufficient to take into account flux uncertainties from finite size effects.

**Core power uncertainties:** The thermal power of each core may not be known with a precision better than 1 to 3%. Specific reactor core power uncertainties have been included in a  $\chi^2$  statistical study. Results are illustrated on Figure 8. From this study we observe that even a large 3% uncorrelated uncertainty on each core power does not significantly degrade the  $\sin^2(2\theta_{13})$  sensitivity (left figure), the main degrading effect coming from reactor spectrum shape uncertainty (right figure), since installing the near detector farther from cores results in a poorer knowledge of the reactor spectrum shape. In order to eliminate core power uncertainties and other possible core uncertainties, the best choice is to place the near detector on the same flux ratio line as for the far detector. The best near detector location is marked by a red dot (solid circle) on Figure 8 (260.3 m away from the east reactor and 290.7 m away from the west reactor).

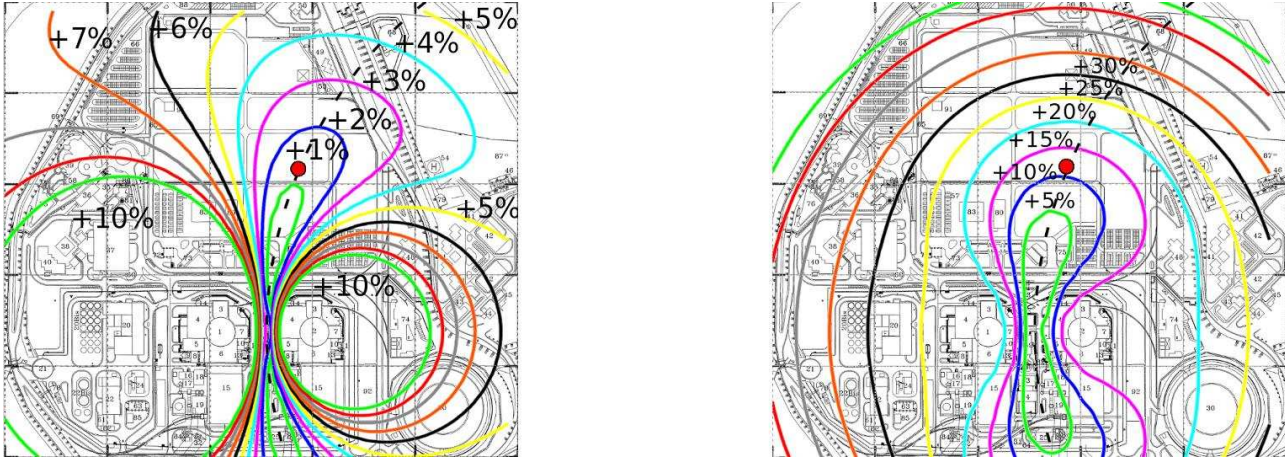


Figure 8: Iso-sensitivity contours as a function of the near detector location superimposed on the power plant viewgraph. Buildings 1 and 2 respectively are the west and east reactor cores. For the left figure, we assumed a 3% uncorrelated uncertainty on the power of both cores and  $\sigma_{\text{abs}} = 2.0\%$ ,  $\sigma_{\text{rel}} = 0.6\%$ ,  $\sigma_{\Delta m^2} = 20\%$ . Each superimposed colored curve indicates a +1% relative degradation on  $\sin^2(2\theta_{13})$  sensitivity with respect to the best sensitivity inside this plane. On the right figure we assumed the same uncertainties plus  $\sigma_{\text{shp}} = 2.0\%$ . Here, each superimposed colored curve indicates a +5% relative degradation on  $\sin^2(2\theta_{13})$  sensitivity with respect to the best sensitivity inside this plane. On both figures, the red circle shows the chosen location of the near detector.

## 2.2.2 Spent Fuel signal at Chooz

About every 8 months the reactor is stopped for unloading of used fuel and reloading with a fresh fuel enriched at 3.45% in  $^{235}\text{U}$ . During this stop only one quarter of the fuel assembly is exchanged, while the others remains in the core although relocated following a precise design. The operation of the N4-reactor is such that the total amount of energy extracted per ton of enriched Uranium is  $45 \text{ GW}\cdot\text{day}/\text{ton} = 3.89 \cdot 10^{15} \text{ J}/\text{ton}$  or around  $1.2 \cdot 10^{26}$  fissions. This operation produced in particular long lived fissions products which can be evaluated by the cumulative fission yields and checked for some of them by analysis of the spent fuel ; nevertheless the uncertainty on the exact amount can be at the level of 20%. Most of these fission products are beta emitters, but if we restrict ourself to those producing neutrinos above the inverse beta decay threshold (1.8 MeV) with an half-life of more than a day, only 4 fissions products remains : All these fissions products are in pairs: the first one is responsible of the long lifetime and the second one produced much more quickly the

Table 5: Radioelements stored in the spent fuel pool on site. BR stands for branching ratio.

Isotope	$T_{1/2}$	Mass (kg)	$\beta$ -End point	BR > 1.8 MeV
Ba <sup>140</sup> /La <sup>140</sup>	12.752 d	6.15	3.762	4.8
Ce <sup>144</sup> /Pr <sup>144</sup>	284.893 d	5.44	2.997	100.
Ru <sup>106</sup> /Rh <sup>106</sup>	373.59 d	3.06	3.678	86.
Sr <sup>90</sup> /Y <sup>90</sup>	28.79 y	3.81	2.280	100.

beta decay with the end point indicated in the table. The amount indicated above corresponds to the total production of a N4-reactor when the 120 tons of enriched UO<sub>2</sub> has produced the required energy ; hence only one quarter is added every 8 months in the pool closed to the reactor core. The pools at Chooz stores all the spent fuel since the start of operation of the reactor. These pools are located in a building closer from the near site by about 30 m compared to the nuclear core. The evaluation of the signal induced by these fission product can be made using the informations in the table and the cross section. The signal due to the Ba<sup>140</sup>/La<sup>140</sup> is weakened by the small branching ratio of energetic antineutrinos and decays quickly. On the longer term Sr<sup>90</sup>/Y<sup>90</sup> produced a more or less constant background less than 0.5 interaction per day for both pools.

The signal due to spent fuel accumulated in the past years averaged over the year compared to the signal directly produced by the two cores is around 0.1%. But it is concentrated in the lower part of the positron spectrum (< 1.7 MeV) where it represents an excess close to 1

### 2.2.3 Detector induced uncertainties

The uncertainty from detector hardware and the selection cuts has to be reduced by a factor of three from the CHOOZ experiment. A new detector design provides us with such an improvement, as well as a reduction of the accidental backgrounds. A steel shield will be used instead of the sand that was used in CHOOZ. A non scintillating region, called the “Buffer”, is created to reduce the single rate in the Target+ $\gamma$ -catcher. An efficient Inner Veto is designed for muon tagging and fast neutron background rejection. An outer muon tracker will allow us to further reduce the cosmogenic backgrounds. Possible detector-related contributions to systematic error are considered in what follows.

### Gadolinium concentration

The concentration of Gd will be identical in both detectors since Target liquids will be produced in a single batch. It can be measured from the neutron capture time at a level of 0.3% [5] or by analyzing the neutron multiplicity from a Californium source (see Section 7.1). The major concern is a non-uniform Gd concentration (e.g., a top/bottom asymmetry). This can be studied with a z-axis Californium calibration. Comparison between the near and far detectors, with the same set of calibration sources, will allow us to detect less than 0.3% time capture differences.

### spill in - spill out

A neutrino event is defined by the neutron capture on Gd after positron annihilation. It is possible to have a neutrino interacting in the Target region but a neutron capture in the  $\gamma$ -catcher region, called “spill out”, and the n capture on Gd for an event interacting in the  $\gamma$ -catcher, called “spill

in". In CHOOZ the spill-in effect accounted for 4% of the events, and the spill-out 2% (the quoted error was about 40%). It led to a  $\sim 1\%$  uncertainty (from Monte-Carlo simulation). However, the effect cancels if the two detectors have a similar Target (a few millimeter geometrical effect has a negligible effect on the results).

## Target proton measurement

The Target liquid will be prepared in a large single batch of about 16 tons. Thus, the uncertainty on the scintillator density ( $\sim 0.01\%$ ) as well as chemical composition ( $\sim 1\%$ ) disappears from the relative normalization error.

The mass of both Targets has to be known with an uncertainty of 0.1%. In 2004-2005, we made investigations on several different methods to ensure accurate volume measurements. Two particular methods have been designed and tested: MPI-Heidelberg suggested to use pH-metry and showed that the volume determination can reach 0.2% of uncertainty (with water). The CEA-DAPNIA proposed a different method: a weight measurement. For the experiment, the idea is to weigh an intermediate vessel before and after the filling of the Target. The difference between the two measurements gives the weight of liquid in the detector. In order to reduce systematics, the same intermediate vessel, equipped with the weight sensors has to be used for both the far and near detectors. We performed tests on the weight sensors. We first checked their repeatability, weighing a 1.5 ton mass 20 times. The standard deviation was 0.15 kg. Then, we made a cross-check between a flow-meter and the weight sensors filling a 2 cubic meter stainless-steel vessel. The flow meter data sheet indicates a global accuracy of 0.5% which can be reduced to 0.3% with local calibration. (This calibration uses a weight measurement). After the calibration of the flow meter and several trials with both sensors, we obtained compatible values of volume with a (one sigma) dispersion of 0.12%. We plan to make an absolute calibration of the weight sensor at Laboratoire National d'Essais in Paris. We are working on a simple method to ensure the local value of gravity is the same at the far and near sites.

To achieve that, we have accurately weighed a 100 g standard at both the near and far sites. Any weight difference below 10 mg means that this gravity variation can be neglected. We have measured differences smaller than 3 mg. (The precision scale we have used was calibrated by measuring the same standard on different sites close to Chooz, at different altitudes and thus different values of g.) As was written before, the result of these measurements is a weight. To compute the volume, we also have to perform a density measurement. For that, we checked the availability of a densitometer which can perform measurements with an accuracy of  $10^{-4}$  g/cm<sup>3</sup>. This device uses a measurement of the sound velocity and it is not affected by variations of gravity. A temperature control and stabilizer at the level of one degree Celsius will be installed in the detector.

## Dead time measurement

As explained in Section 6.5.2, the digitization and acquisition systems do not introduce dead time. The only two sources of dead time are the first level trigger (hardware) and the offline cuts:

1. the first level trigger necessarily introduces dead time: when an event comes very shortly after a first one, it cannot be detected;
2. offline, a short veto will be applied after each event, to reject pile-up, and, more importantly, a 500  $\mu$ s veto after each muon.

Table 6: Systematic uncertainties related to the Target free H measurement. This error will be less than 0.2% since a single batch will be prepared for both detector Target. The “Single Detector” case is important for the non proliferation component of Double Chooz, however. The H/C determination depends on the scintillator solvent composition. Dodecane is favored over mineral oil whose composition is less well defined (1%). In the case of a single detector we estimate a systematic error contribution of <0.55%.

	Single Detector	Double Chooz
Volume	0.2%	0.2%
Ratio H/C	< 0.5%	0
Density	0.01%	0
Gravimetry (g)	0.005%	0.002%
Total	<0.55%	0.2%

The veto times will always be longer than the electronics dead time and care will be taken that they always include it. Therefore, the veto times account for the total detector dead time. This time can be measured with the precision of the main clock.

The main clock is distributed to the Waveform Digitizers by the hardware trigger system. The stability of this clock is still not known but a precision of  $10^{-4}$  (9s/d) is achieved in modest devices. The frequency and instability of the clock will be measured with a GPS clock.

Since the uncertainty on dead time contributes directly to the uncertainty of the neutrino flux measurement and the dead time itself differs strongly between the two detectors, a cross check is performed by the mean of a random fake event generator which produces light pulses in the inner volume of the detectors and records them. It is then possible to count how many have been rejected or missed.

Those methods of dead time measurements will be intensively tested with the Far detector. Simulation of the Near detector higher rate could be tested using the random fake event generator.

#### 2.2.4 Uncertainties in the efficiency determination

$\bar{\nu}_e$  events manifest themselves as two local energy depositions of more than 500 keV in less than 200  $\mu$ s. Delayed energy should be consistent with a neutron capture on Gd. In the CHOOZ experiment, the selection cut uncertainty was 1.5%, coming from a set of 7 analysis cuts to extract the  $\bar{\nu}_e$  candidates [5]. The Double Chooz detector design differs slightly from CHOOZ since a non scintillating Buffer region shields the active region (Target and  $\gamma$ -catcher) from the phototube intrinsic radioactivity. This allows us to reduce the number of selection cuts, while keeping a small accidental background contamination (a few percent of the signal). A summary of the systematic errors associated with  $\bar{\nu}_e$  event selection cuts is given in Table 7.

#### Identification of the prompt positron signal

The positron induced by the antineutrino interaction in the Target has a very short track in the detector. It annihilates and creates two back-to-back 511 keV gammas. One of the gammas may leave the Target, but most of the time it will deposit a large fraction of its energy in the Target+ $\gamma$ -catcher sensitive volume. Thanks to the addition of a Buffer volume between phototubes and the



active detection region, the energy threshold will be between 500 and 700 keV. Using the expected energy resolution of 7% at 1 MeV, the fraction of neutrino events leading to a positron below the threshold will be smaller than 0.03%. Thus almost no  $\bar{\nu}_e$  candidate will be rejected by a prompt event energy cut since the antineutrino induced positron deposits at least 1 MeV. The systematic error associated is negligible.

### Identification of the neutron delayed signal

Neutrons induced by neutrino interactions can travel about 5 cm before being captured. The thermal neutron is captured either on hydrogen or on gadolinium. (We neglect here carbon captures.) The gammas emitted after the capture on Gd can escape in some cases the Target+ $\gamma$ -catcher volume (when a high energy gamma is emitted in the gamma shower). Thanks to the two detector concept, the error on the the absolute knowledge of the gamma spectrum from a Gd neutron capture disappears. The selection cut that identifies the neutron will be set at about 6 MeV (an optimization is in progress). An error of  $\sim 100$  keV in the energy scale leads to a 0.2% effect on the neutron selection.

### Neutron time capture on Gd

The analytical behavior describing the neutron capture time on Gd is not known. The shape is rather exponential, however. Furthermore there is no reason that Gd capture differs significantly from neutron capture on light nuclei which follows a Gamow-like behavior. With a single detector at CHOOZ, the systematics error was 0.4%, but a relative comparison between detectors with identical scintillator relies only on the control of the electronic time cuts. A relative comparison of the electronics of the two detectors will lead to an effect less than 0.1%.

Table 7: Summary of the uncertainties associated with the data reduction (selection cuts). CHOOZ values have been taken from [5].

	CHOOZ	Double Chooz
selection cut	rel. error (%)	
e <sup>+</sup> capture energy containment	0.8	0.1
neutron capture	1.0	0.2
n capture energy containment	0.4	0.2
neutron delay	0.4	0.1
combined	1.4	$\sim 0.3$

### 2.2.5 Summary of the systematic uncertainty cancellations

Table 8 summarizes the identified systematic errors that are currently being considered for the Double Chooz experiment.

## 2.3 Backgrounds

There are backgrounds from primordial and man-made radioactivity, as well as backgrounds induced by cosmic ray interactions. Previous experiments provide quantitative guidance on how to design

Table 8: Total systematic error on the normalization between the detectors

			CHOOZ	Double Chooz
Reactor		Solid Angle	—	0.06%
Detector	H nuclei in Target	Volume	0.3%	0.2%
		Fiducial Volume	0.2%	0
		Density		0.1%
		H/C	0.8%	0
Detector	Electronics	Dead Time	—	0%
Particle Identification	Positron	Escape	0.1%	0
		Capture	0	0
		Energy Cut	0.8%	0.2%
Particle Identification	Neutron	Escape	1.0%	0
		Capture (% Gd)	0.85%	0.3%
		Identification Cut	0.4%	0.1%
Particle Identification	Antineutrino	Time Cut	0.4%	0.1%
		Distance Cut	0.3%	0
		Unicity	0.5%	0
Total			1.5%	0.5%

an experiment which, in principle, allows us to measure  $\bar{\nu}_e$ 's with a high signal to noise ratio.

### 2.3.1 Accidental backgrounds

Naturally occurring radioactivity can create accidental as well as correlated backgrounds. Selection of high purity materials for detector construction and passive shielding provide an efficient handle against this type of background. Gamma, beta and neutron signals in the inner detector or in the rock may generate accidental background events which mimic prompt  $\bar{\nu}_e$  interaction signal (positron-like). The delayed background (neutron-like) comes mainly from neutron capture on Gd. However, part of those neutron-like events could be due to bremsstrahlung photons radiated from cosmic muons which traverse the rock surrounding the detector. The neutron like background rate had been measured at the far site in the CHOOZ detector, at the level of  $45 \pm 2/h$  (after cuts) [5]. Based on that measurement and the new target volume, we assume a neutron rate of 83/h in Double Chooz. However, such a high rate remained unexplained in CHOOZ, and current simulation is not reliable in that it gives a much smaller rate (see Section 2.3.3 for details). The neutron-like rate is taken at  $0.023Hz$  in the Target and can thus be neglected as a relevant contribution for the positron-like events since phototubes contribute at the level of the Hertz.

The accidental background rate  $b_{acc}$  is given by  $b_{acc} = b_p V_p b_d V_d \tau_d$ . Here  $b_p$  and  $b_d$  are the specific background rates (in units of  $Hz m^{-3}$ ) for the prompt and the delayed events, respectively. The time window for the coincidence is given by  $\tau_d \sim 100 \mu s$ ,  $V_p = V_T + V_{GC} = 32.89 m^3$  is the volume considered for the positron-like event (no use of a distance cut),  $V_d = V_T = 10.32 m^3$  is the volume accounted for the neutron-like event. We note  $R_p = b_p V_p$  the total prompt positron-like events, and  $R_d = b_d V_d$  the total delayed neutron-like events. A good estimate of the daily accidental background

without distance cut is given by

$$b_{acc} \sim 0.2 \times \frac{R_p}{1 \text{ s}^{-1}} \times \frac{R_d}{83 \text{ h}^{-1}} \text{ day}^{-1} . \quad (10)$$

If we now require that the accidental background rate from all material but phototubes is less than 1% of the neutrino signal (69/d and 1012/d at the far and near site respectively), we get the constraints  $R_p^{far} < 10 \text{ Hz}$  and  $R_p^{near} < 14 \text{ Hz}$ . As a guideline, we require each detector element contribution to be less than 0.2 Hz (6 detectors components and 3 isotopes).

### Inner detector materials and phototubes

The results presented here have been obtained by using the DCGLG4sim simulation, the adaptation to Double Chooz of the GLG4sim GEANT4-based simulation (see Section 8.2). The inner detector simulated here includes three perfectly cylindrical volumes: the inner Target, the  $\gamma$ -catcher and the Buffer. The three regions are filled with liquids, whose chemical and physical properties are those of the base-case currently considered (for Target and  $\gamma$ -catcher, PXE/Dodecane mixture with 20% and 80% volume ratio, plus addition of fluors and -for the Target only- of a Gd-complex to a Gd concentration of 1 g/l; pure dodecane for the Buffer). However, all optical properties have been switched off for the calculation presented here, since the focus here is on the fraction of energy deposited in the sensitive volumes, rather than on the exact detector response. The Target and  $\gamma$ -catcher vessels are made of acrylics and have a thickness of 8 mm and 12 mm, respectively. The  $^{40}\text{K}$ ,  $^{238}\text{U}$  and  $^{232}\text{Th}$  nuclides have been generated uniformly in several parts of the detector: Target scintillator, acrylics of the Target vessel,  $\gamma$ -catcher scintillator,  $\gamma$ -catcher acrylics, Buffer liquid, stainless steel Buffer tank. Phototubes have been simulated separately. The simulation gives the spectra of the energy deposited in the sensitive volumes. We then extract the fraction of events depositing an energy in the Target plus  $\gamma$ -catcher volumes above a 500 keV threshold and we define the maximum concentration of  $^{40}\text{K}$ ,  $^{238}\text{U}$ ,  $^{232}\text{Th}$  allowed for each detector component. Phototubes

Table 9: Allowed concentration (g/g) of  $^{40}\text{K}$ ,  $^{238}\text{U}$ , and  $^{232}\text{Th}$  for the main components of the Double Chooz detector (with a safety margin). All values above  $\sim 10^{-11}$  g/g can be measured through gamma spectroscopy at underground laboratories. For the case of Target and  $\gamma$ -catcher liquid scintillator, other counting methods will have to be used to reach a sensitivity at the level  $10^{-13}$  g/g.

	$^{40}\text{K}$	$^{238}\text{U}$	$^{232}\text{Th}$	$^{60}\text{Co}$
	g/g	g/g	g/g	mBq/Kg
Target LS	$10^{-10}$	$10^{-13}$	$10^{-13}$	—
Target Acrylics	$10^{-8}$	$10^{-11}$	$10^{-11}$	—
GC LS	$10^{-10}$	$10^{-13}$	$10^{-13}$	—
GC Acrylics	$10^{-8}$	$10^{-11}$	$10^{-11}$	—
Buffer Oil	—	$10^{-12}$	$10^{-12}$	—
Buffer Vessel	—	$10^{-9}$	$10^{-9}$	15
Veto LS	—	$10^{-10}$	$10^{-10}$	—

will be selected according to their radiopurity, and their contribution to the single rate is expected to

dominate, at the level of a few Hertz. Several phototube candidates are being currently investigated, from ETL, Hamamatsu and Photonis. This is discussed in details in Section 5. Estimates can be given taking into account the whole set of measurements for each phototube candidates. In that case the expected single rate (positron-like) above 500 keV is expected to be between 9 and 14 Hz for ETL and Hamamatsu. With extra care, this could be lowered to 4-10 Hz. This translates to 1-1.4 and 0.4-1 accidental events per day respectively.

We remind here that accidental background (rate and spectrum) can be measured *in situ* with a precision better than 10%.

## Steel shielding thickness optimization

The Double Chooz inert steel shield has been designed to minimize the incidence of the gamma-rays from the rock surrounding the detector into the target volumes (referring to the so-called Target and  $\gamma$ -catcher volumes). This element grants Double Chooz with a critical reduction on the uncorrelated background, as compared to the CHOOZ experiment. Simulation studies based on GEANT3 and GEANT4 have been performed to infer the optimal thickness of the shield. The contribution of the K, U and Th were modulated by the available knowledge gathered by the CHOOZ collaboration [5] (and references therein) about the activity of the relevant types of rock found in the detector cavity. The goal of the optimization is to keep the rate of rock gammas with energy deposition above the prompt energy threshold (set at 0.5 MeV) lower than the expected activity from the PMTs, which has been estimated to be  $\mathcal{O}(5 \text{ Hz})$ ; see Section 2.3.1. The studies have shown that a 17 cm shield would suffice. In such a scenario, the overall rate of rock gammas is expected to be  $< 2 \text{ Hz}$ , dominated by 0.98 Hz due to  $^{208}\text{Tl}$  (Th chain) and 0.86 Hz due to  $^{40}\text{K}$ . Figure 34 shows the current baseline engineering model for the Double Chooz shield.

### 2.3.2 Simulation of muon background

To properly simulate the detector response to cosmic muons, it is necessary to use angular resolved muon distributions and energy spectra for both detector locations. The muon propagation tool MUSIC [27] (see Section 8.2) was used for this purpose, in combination with GEANT4 and FLUKA based simulations.

### Far site

A measurement of the angular distribution of muons at the Double Chooz far site was performed prior to the Chooz experiment [28]. No measurement of the energy spectrum, however, is available. A modification of the MUSIC code was used to create an independent spectrum and angular distribution by propagating surface muons through rock [29]. Details on the rock composition, as measured by chemical analysis of several samples in [28], were taken into account. The strong angular dependence of the muon flux is justified by the large variation of the rock overburden with the incoming muon direction: this required the creation of a digitized topographical map of the Chooz hill profile, shown in Figure 9. The simulation predicts a muon flux of  $(6.2) \cdot 10^{-5} \text{ cm}^{-2} \text{ s}^{-1}$ , (about 5 Hz through the target region) slightly higher than the approximate measured value quoted in [5]. The calculated angular distributions of the muons are shown in Figure 10. The simulation agrees well with the measured data, once the acceptance of the experimental apparatus is taken into account. The simulated energy spectrum of the muons is presented in Figure 11. The mean muon energy at the far detector location will be about 61 GeV. With these muon distributions,

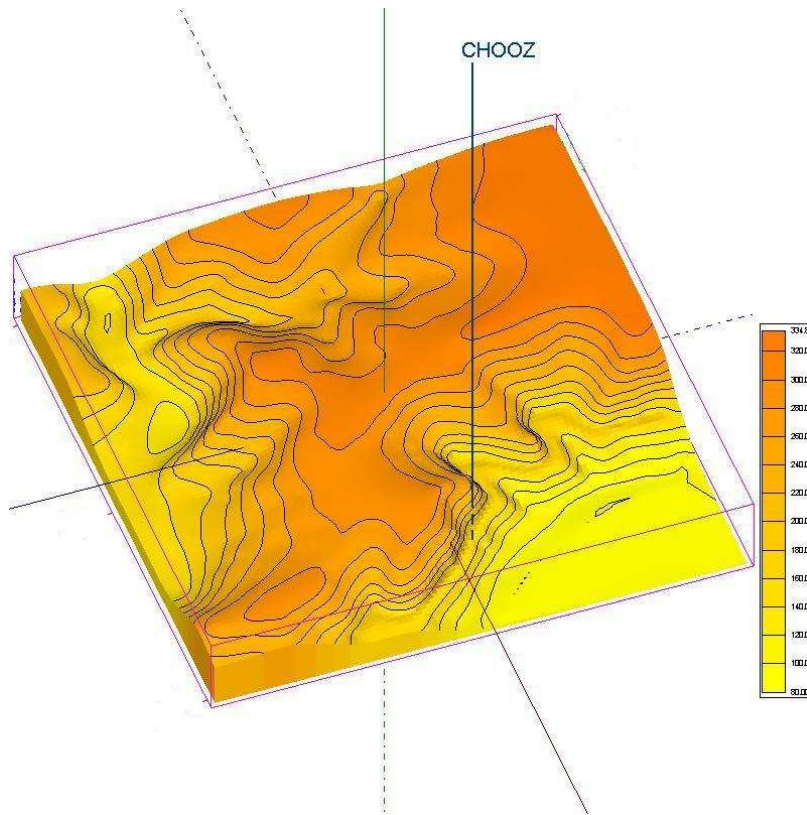


Figure 9: Hills surrounding the Chooz sites.

a secondary neutron spectrum was generated with the DCGLG4sim software, as shown in plot 12. This neutron distribution is used as a starting point for dedicated neutron simulations (as in Section 5).

### Near site

During the design phase, the calculation of muon background at the near detector site will be essential for the definition of the near lab design.

A calculation of the muon energy spectrum, assuming a flat topography of the rock overburden, was performed with the MUSIC code. The calculated energy spectrum is shown in Figure 13: the mean energy is 30 GeV, and the flux  $5.9 \cdot 10^{-4} \text{ cm}^{-2} \text{ s}^{-1}$  (about 55 Hz through the target).

### 2.3.3 Neutron-like background

All energy deposit over 6 MeV isolated in time from other deposits are candidate single neutrons. In the first CHOOZ experiment, events occurred with a rate of about  $10^{-2}$  Hz. The origin of these energy deposits is unknown. The radial distribution of the reconstructed vertices, decreasing by two orders of magnitude from the outer wall to the center, suggests an origin outside the detector.

The hypothesis has been made that neutron-like events could be due to bremsstrahlung photons radiated from cosmic muons which traverse the rock surrounding the detector (“near-miss” muons).

A detailed Monte Carlo study was carried out to test this hypothesis. Cosmic muon samples were generated according to the measured angular distributions [28] at the site and to an energy

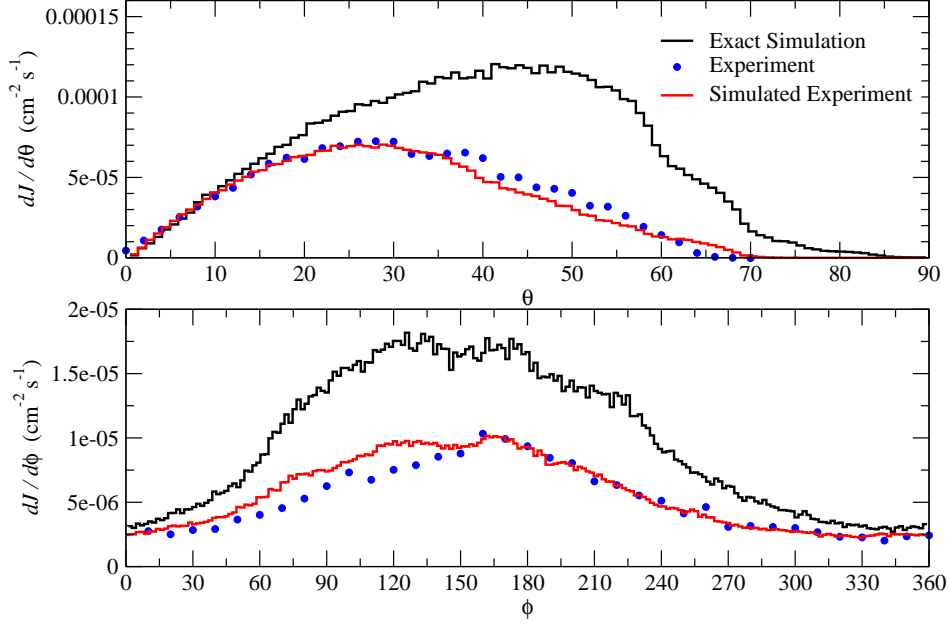


Figure 10: Comparison of angular dependence of muons for the far detector [29]. The experiment refers to data from an RPC setup which was used to characterize the  $\mu$  flux during the original CHOOZ experiment. The exact simulation shows the expected  $\mu$  rates for the CHOOZ site as derived from the new MUSIC propagation simulation. When the results from the exact simulation are combined with the known acceptances of the RPC setup, the resulting simulated experiment is in good agreement with the measured data.

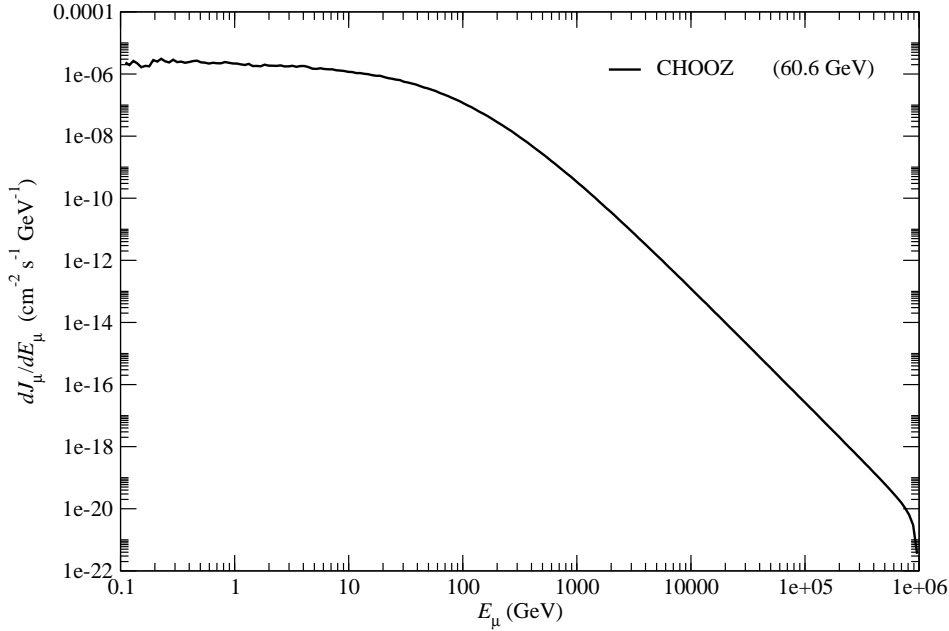


Figure 11: Energy spectrum of cosmic muons at the far detector.

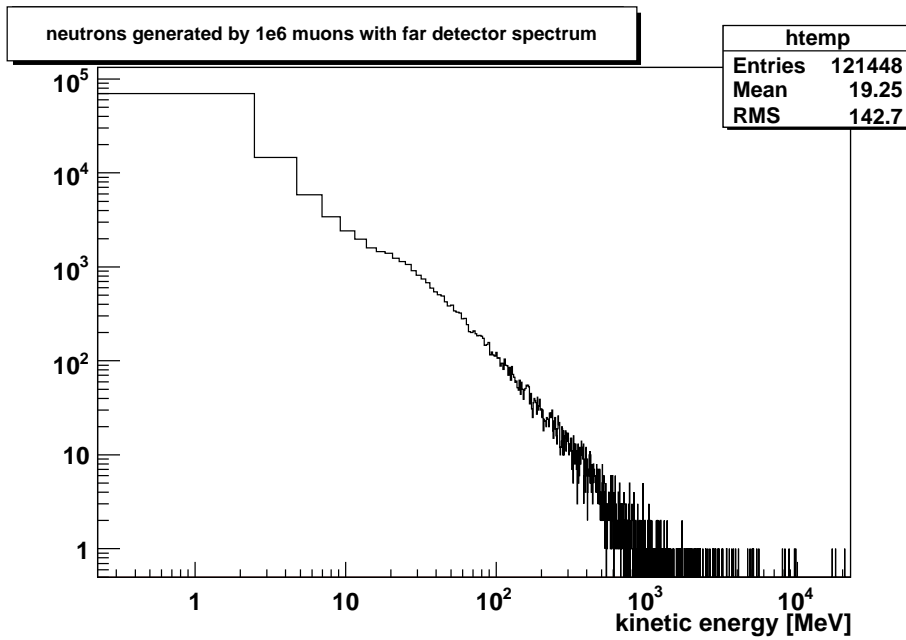


Figure 12: Neutron energy distribution as generated by the far detector muon spectrum in detector and surrounding rock.

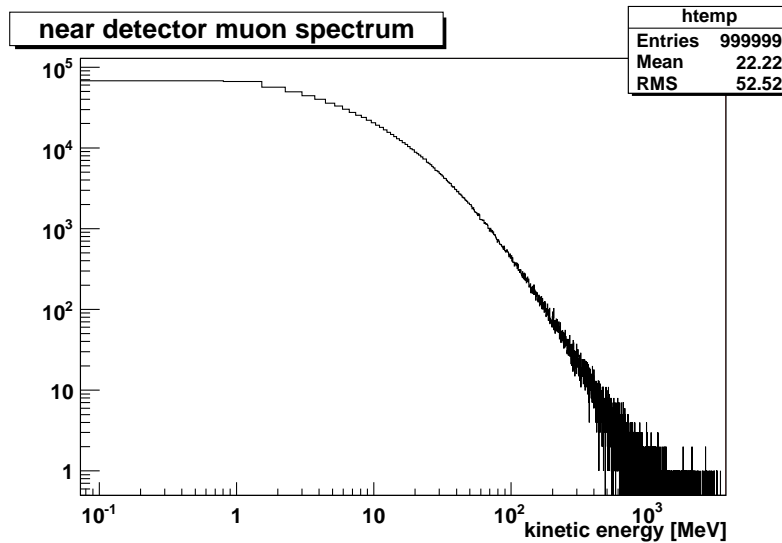


Figure 13: Preliminary energy spectrum of cosmic muons for the near detector, simulated with a flat topography.

spectrum appropriate for an overburden of 300 m.w.e. [31]. The interaction with the rock and in a detector with similar geometry to CHOOZ were simulated with the GEANT4 package.

The bulk of the photons entering the detector were found to have originated from delta and knock-on electrons produced by muons in the rock. The spectrum of energy deposits in the Target due to such photons is shown in Figure 14(left): it reproduces very well the shape observed in Chooz. The probability to have such a signal in the Target is at the level of  $10^{-4}$  per muon; taking into account the measured muon rate at the site,  $0.4 \text{ Hz}/(\text{m}^2)$ , and the surface area relevant for the muon interactions, a rate of events in the Target of about of  $0.006 \text{ Hz}$  is found, which is the same order of magnitude as the measured one.

However, most of these signals in the Target are accompanied by significant energy deposition in the veto, as shown in Figure 14(right), due to the showering of the photons. Using a threshold around  $200 \text{ MeV}$ , only about 10% of the events would not be tagged in the veto, while no signal is present in the neutron-like background.

In conclusion, detailed simulation of photons from “near-miss” muons explains only 1/10 of the neutron-like energy deposits observed in CHOOZ. We don’t know yet the origin of these energy deposits. It will be an item of study in Double Chooz.

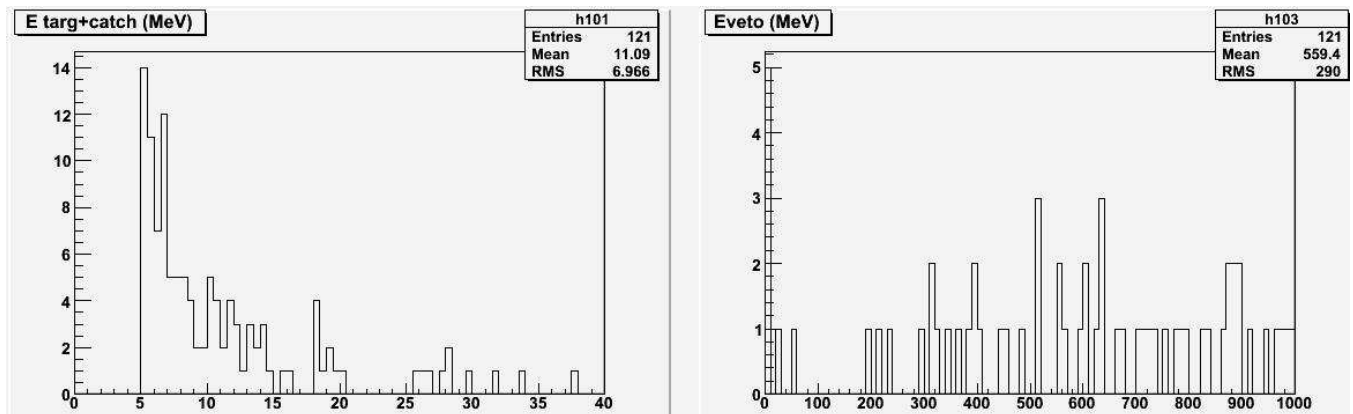


Figure 14: Distribution of the energy deposited by photons originated from near-miss muons in the Target (left) and in the veto (right).

### 2.3.4 Fast neutron background

The fast neutron background was the main single source of background in the CHOOZ experiment [5]. This background was also studied in other neutrino experiments such as Bugey, Karmen and Palo Verde. These fast neutrons are created by near miss muons interacting around the detector. Their large interaction length allows them to cross over the full detector. Some of them happen to be slowed down in the central scintillators, and eventually be captured in the target. The recoil proton can mimic the positron (the deposited energy is higher, but part of it can be unseen), and the neutron capture is obviously correlated as a neutrino event. Some secondary neutrons can also contribute. The energy shape of these events is known from previous experiments to be very smooth. In the CHOOZ paper (Figure 46 of [5]) a rather flat spectrum is shown, with some saturation effect even creating a slow rise. Since there is no reactor neutrino over some  $15 \text{ MeV}$ , this background can be permanently monitored in the  $15 - 50 \text{ MeV}$  range. The total correlated background in the CHOOZ experiment was published at  $1.01 \text{ event/day}$ , and found to be in good



agreement with the extrapolation of the measured rate over 15 MeV. To prepare the new experiment, the Munich group[32] first tried to reproduce these numbers by simulation. 31 hours of data taking in the CHOOZ experiment were simulated, and 1 background event observed. This is 0.8/day, corresponding to an upper limit of 3.0 event/day at 90% confidence level. This is in good agreement with the 1 event/day quoted in Reference [5].

Having validated the Monte Carlo, the Double Chooz detector was simulated. The program was run with an overburden of 100 m.w.e., and then a scaling done to the actual overburden of 300 m.w.e. for the far site and 80 m.w.e. for the near one. 43 hours of data taking were simulated, and 1 event observed. This leads to expect 0.15 event/day at the far site (less than 0.6 event/day at 90% confidence level) and 3.3 event/day at the Near detector. This is significantly less than that in the CHOOZ experiment, as expected due to improvements in the detector design. Using steel instead of sand increases the neutron path toward the target by about one attenuation length, from which a factor 3 decrease can be predicted, leading to 0.3 event/day. This number is in good agreement with the simulation result quoted above. All this work was done without using the muon tracker. An additional background rejection of a factor of 15 is expected, making this fast neutron background very small. Another handle on rejecting fast neutrons is that some would make an energy deposit in the Inner Veto. In the Double Chooz experiment, some Pulse Shape

Table 10: Summary of the fast neutron background prediction in Double Chooz Near and Far detectors. This can be compared with the data of the CHOOZ experiment at the Far site as well as its new simulation.

Event/day	Data	Simulation	
		Mean	90% C.L. Upper Limit
CHOOZ	$1.01 \pm 0.04 \pm 0.1$	0.8	3.0
Double Chooz Far	—	0.2	0.8
Double Chooz Near	—	1.3	5.0

Discrimination (PSD) will be possible, allowing us to separate the recoil proton signal, which is more highly ionizing and slower, from the neutron one. This will be used, not to reject the noise (which would create systematic errors), but to tag and monitor the background, and measure its energy shape. Since it will also be measured above 15 MeV and below 1 MeV (once the accidentals events are subtracted), a three-fold fit will be possible.

### 2.3.5 Muon capture

Muon capture contributes to the background by creating gammas, neutrons, and cosmogenic nuclei. Cosmogenic nuclei are described on page 30 and gamma backgrounds have been discussed previously in this section. We focus here on neutrons from such a capture. Fast neutrons are a potential source of correlated background: they may propagate through the detector and reach the  $\gamma$ -catcher or even the Target, creating recoil protons that can mimic the positron inverse beta decay signal, and later on the capture on Gd. If the recoil protons are not seen, the neutron capture can be randomly associated with a gamma, creating an accidental background event. The rate of this background can be neglected compared to other accidental backgrounds in the detector.

The main issue concerning the capture of muons on nuclei in the detector is the presence of dead materials along the muons track. We review below the potentially critical detector elements. The

corresponding background is summarized in the Table 11, which gives an estimate accurate to an order of magnitude.

### **Target and $\gamma$ -catcher**

Inside the Target and the  $\gamma$ -catcher, muon tracks as well as neutron capture are seen due to the huge amount of energy deposit. However, the acrylic supports linking the Target and the  $\gamma$ -catcher vessels are dead materials. The corresponding muon capture background is estimated to 0.1 event/day, and the rejections are shown in the rightmost column of the table.

### **Buffer**

The volume of the Buffer is large (114 m<sup>3</sup>). Its contribution is dominated by the last layer, near the  $\gamma$ -catcher. Following a standard rule of thumb, 4 tons of mineral oil close to the  $\gamma$ -catcher, corresponding to one attenuation length (15 cm), will dominate. In the scintillator liquid, less than 10% of neutrons are captured on carbon. These neutrons have to cross the  $\gamma$ -catcher to reach the Target and are vetoed (the efficiency is 99.9%)

### **Buffer vessel**

The Buffer and the stainless steel Buffer vessel are not instrumented (or weakly so, since Cerenkov light from muon tracks in the Buffer could be detected). All stopping muons in these volumes are captured by iron nuclei. Neutrons produced in this 3 mm thick stainless steel vessel have to travel through the Buffer and the  $\gamma$ -catcher to reach the Target (a total path of about 150 cm). The total rejection from the propagation is estimated to be as large as 10<sup>5</sup>. The Inner Veto rejection is also applied. The estimated background is 0.03 event/day.

### **Steel shielding**

The detector shielding is a large amount of iron (about 306 tons), which we consider as dominated by the last attenuation length. This shielding will be covered by the Outer Veto detector providing a rejection factor of about 20 (applied in the table). The resulting background is 0.05 event/d. This number scaled to the far detector is 0.002/d (30 times less cosmic ray muons).

The first CHOOZ experiment provides an experimental confirmation to this estimate. The 70 cm sand layer at the outermost part of the detector was producing fast neutrons from muon capture, roughly as much as the iron shielding of the new experiment. Furthermore, in the new detector the distance from the steel shielding to the Target region is enlarged by 15 cm. Thus, according to our estimate, in the first experiment the sand muon capture background was about 0.15 event/d. This is well within the published total correlated background (1 event/day).

### **Chimney**

The detector chimney is also a dead volume, at least above the Buffer vessel. Muons going down through the chimney are not seen by the vetoes if the chimney is not instrumented. Thanks to an effort to minimize the chimney diameter, this solid angle is small. Since the liquid inside the chimney is scintillating, and further since the chimney is made of transparent acrylics up to the Buffer vessel, the muon track and capture in the chimney would be seen by the inner phototubes. We consider

Table 11: Fast neutron background from muon captures in the near detector (overburden 80 m.w.e). Appropriate masses of material within one interaction length of each component were used in the calculation.

	Steel shielding	Buffer structure	Buffer oil	Chimney	Target structure
mass (tons)	14	7	4	0.005	0.1
Capture rate	70/s	40/s	0.5/s	$0.6 \cdot 10^{-3}/s$	0.01/s
neutron rate	80/s	50/s	0.8/s	$10^{-3}/s$	0.015/s
Target rate (no Veto)	1/d	5/d	160/d	0.1/d	100/d
Target rate (Veto)	0.05/d	0.005/d	0.16/d	0.1/d	0.1/d

here that only a neutron capture at the Buffer vessel level can contribute to the background at a level of 0.1 event/day. (This background would disappear if the liquid level is kept below the Buffer vessel).

### Muon capture summary

In this study, neutron propagation was estimated taking into account its energy spectrum and the corresponding attenuation length. The neutron energy from muon capture is peaked toward low energy: 90% of the produced neutrons have an energy lower than 10 MeV and the corresponding attenuation length makes them unable to cross the  $\gamma$ -catcher and reach the Target. In Table 11 higher energy neutrons were propagated using an attenuation length of 15 cm, which corresponds to 20 MeV neutrons. For a reasonable variation of the energy spectrum and attenuation length, it was checked that the result is stable within an order of magnitude.

In conclusion, the muon capture correlated background is well below 1% of the signal at the near and far detectors. The accidental background originating from these neutrons is small. With less than 1 neutron per day together with a few Hertz of gammas within 100  $\mu$ s, the background is less than  $10^{-3}$  events per day, which is negligible.

### 2.3.6 Cosmogenic correlated background: Lithium 9

The cosmogenically-produced isotope  ${}^9\text{Li}$  can be a serious problem for reactor experiments, since the beta decay has a branching ratio of about 50% into states that de-excite via neutron emission. This means that the electron plus neutron combination can mimic a reactor neutrino signal. The 178 ms half life could also make it difficult to veto since it would lead to an unacceptable deadtime. In addition, the best measurements of cosmogenic production come from large depths, where the hard muon flux makes extrapolation to shallow depths uncertain.

Fortunately, Double Chooz has the great advantage of having the data from the original CHOOZ experiment to draw on (especially 138 days of Reactor Off data). This allows us to extract the expected rate of  ${}^9\text{Li}$  at our Far Lab based on using data rather than MC or extrapolation from large depths. The expected rate is 1-2% of the signal (before veto). Thus, this is a background we can handle by veto and measurement, as shown below.

Detecting the initial muon is a necessary part of being able to measure and subtract the background due to  ${}^9\text{Li}$ . Both the Near and Far Detectors will have 50-cm thick,  $4\pi$  scintillating muon

vetoed in order to tag incoming events with high efficiency<sup>2</sup>. In addition, each lab will have a muon tracker on top. Thus entering muons will be efficiently detected. In addition, the current plan for the electronics has included the concept of “muon electronics” specifically designed to measure the muon energy deposit over a much larger dynamic range than that planned for the waveform digitizers being designed for the low-energy events.

In the KamLAND experiment, it was found that a cut of  $10^6$  photoelectrons was effective in tagging muon-initiated showers that were important in  $^9\text{Li}$  production. The  $10^6$  photoelectron cut in KamLAND has been simulated by using the KamLAND detector simulation program, KLG4sim. The simulation predicts that about  $7.7 \pm 0.4\%$  of cosmic ray muons will be cut by a cut at  $10^6$  p.e. (which corresponds to roughly 3.3 GeV of deposited energy). This is to be compared with 6% obtained by an analysis of one day of KamLAND data - a reasonably good agreement. The *same* simulation package adapted for Double Chooz depth (300 m.w.e.) and geometry predicts that a similar cut (slightly above the peak of the energy loss distribution, about 2.8 GeV) would cut only 1.3% in Double Chooz (Far). With a muon rate of 25 Hz, this would correspond to a veto rate of only one every 3 seconds.

### What can we learn from the CHOOZ data

We have extracted the  $^9\text{Li}$  production rate in the CHOOZ experiment in three different ways: (1) total background rate, (2) spectral fit to official CHOOZ data between 2.8 and 10.0 MeV, and (3) a more recent spectral fit to extended CHOOZ data between 2.8 and 30.0 MeV.

CHOOZ had a measured accidental coincidence background of  $0.42 \pm 0.05$  event/day and a background from fast neutrons of  $1.01 \pm 0.11$  event/day during the period when most of their Reactor On data was taken. The corresponding background rate from Reactor Off data in this same period was  $1.4 \pm 0.24$  event/day, which is consistent with the sum of the two individual rates. Based on the 0.11 event/day uncertainty in extrapolating the proton recoil spectrum below 10 MeV, there could be as much as 0.2 event/day of  $^9\text{Li}$  hidden under the reactor signal. This analysis depends critically on systematic uncertainties which are difficult to quantify. A better technique is to fit the shape of the prompt energy spectrum.

A spectral fit to the official CHOOZ Reactor Off data is shown in figure 15. The fit is to a flat proton recoil visible energy spectrum and a  $^9\text{Li}$ -shaped decay spectrum that includes the effect of the broad lines on the endpoint. The fit is only done above 2.8 MeV to avoid the peak due to accidental coincidences below that energy. The best fit for the  $^9\text{Li}$  rate is  $0.6 \pm 0.4$  event/day, although the rates of the two backgrounds are highly correlated.

The degeneracy between the two backgrounds can be broken by fitting the background above 10 MeV, beyond the  $^9\text{Li}$  endpoint. Such data is not (yet) officially available by consensus from the CHOOZ collaboration, but an unofficial spectrum can be fit based on roughly 114 days of reactor off data with energy up to 30 MeV, as shown in their published scatter plot. This is shown in Figure 16. Now the degeneracy is almost completely broken, and the measured rate is  $0.7 \pm 0.2$  event/day.

### Extrapolation from CHOOZ to Double Chooz

The three methods using CHOOZ data imply a  $^9\text{Li}$  rate for Double Chooz in the range 0.5 to 1.5 event/day, or about 1-2% of the expected signal. This is a rate that can be handled either by veto,

---

<sup>2</sup>The Near Detector veto may be thicker than 60 cm

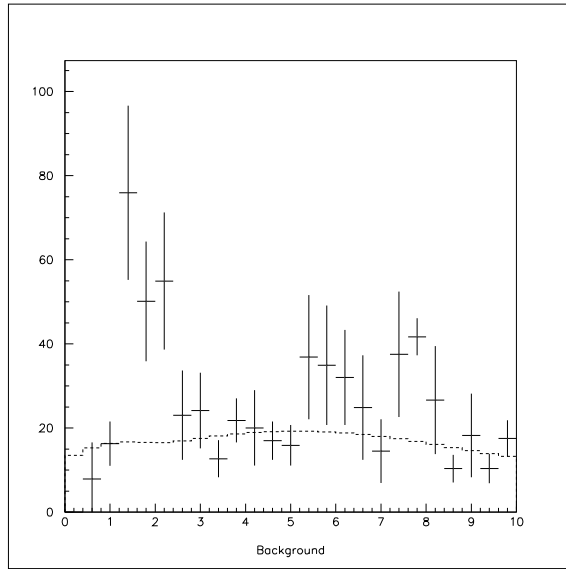


Figure 15: Official CHOOZ scaled Reactor Off visible energy spectrum fit with a combination of flat and  ${}^9\text{Li}$ -shaped background. The fit is only above 2.8 MeV to avoid the accidentals below that energy. The best fit for  ${}^9\text{Li}$  is  $0.6 \pm 0.4$  event/day.

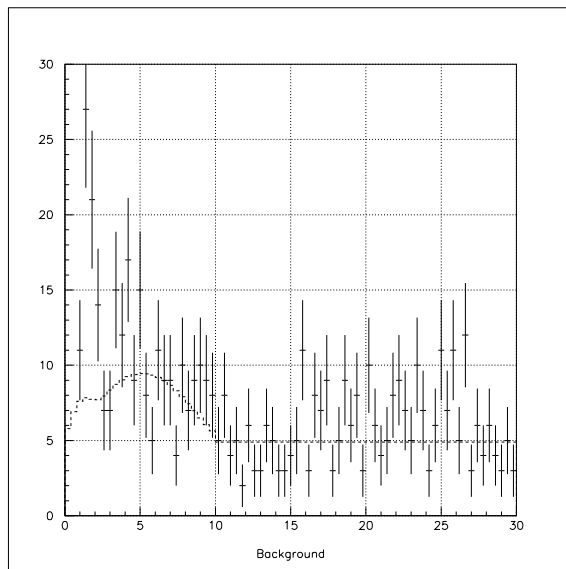


Figure 16: Unofficial CHOOZ Reactor Off visible energy spectrum fit with a combination of flat and  ${}^9\text{Li}$ -shaped background. The fit is only above 2.8 MeV to avoid the accidentals below that energy. The best fit for  ${}^9\text{Li}$  is  $0.7 \pm 0.2$  event/day.

measurement to an accuracy of 10%, or (most likely) both. With the expected muon rate through the Target of 25 Hz, we could afford to veto these muons for up to 400 ms (factor of ten reduction) before incurring substantial dead time. Thus  ${}^9\text{Li}$  in the Far Detector can be dealt with in multiple ways.

In the Near Detector, the extrapolated rate using an  $E^{0.75}$  dependence gives a rate of 0.9% of the expected signal. The muon rates are expected to be too high to effectively veto  ${}^9\text{Li}$ , however, a better than 20% measurement of this rate can be done with the expected One Reactor Off time required for refueling (one month per year per reactor), or with two weeks of Two Reactor Off time. Thus, this background can be subtracted to the required precision.

### 2.3.7 Background subtraction error

In this section we summarize the backgrounds estimated in the Double Chooz detectors. We also refer to the background measured in CHOOZ [5]. The results are presented in Table 12. Accidental backgrounds have been estimated through simulation (see Section 2.3.1). For Double Chooz we separate the contribution of the detector materials from the phototubes. The radiopurity of our PMT candidates have been used for this estimation. We only report the total accidental background measured in CHOOZ. In the case of the correlated background we also split the different contributions: fast neutron (see Section 2.3.4), muon capture (see Section 2.3.5), and  ${}^9\text{Li}$  production (see Section 2.3.6). We report the total correlated background measured in CHOOZ, and we also present an attempt to extract the different contributions of fast neutron and  ${}^9\text{Li}$  from a new analysis of the CHOOZ data ( ${}^9\text{Li}$  induced background had not been measured in CHOOZ).

To estimate the background at the Near detector site different methods are used: a full simulation at 100 m.w.e. for the fast neutron background (see Section 2.3.4), and a rescaling for the accidental backgrounds, the muon capture and the  ${}^9\text{Li}$  backgrounds. We scale the background rate using the ratio of muon flux times the mean muon energy to the power 0.75, between 300 m.w.e. and 80 m.w.e., leading to a factor of 7 to a good approximation. Taking into account all those backgrounds and a 0.6% relative systematics error leads to a sensitivity of  $\sin^2(2\theta_{13}) < 0.027$  (90% C.L.) after 3 years of data taking with two detectors (at  $\Delta m_{31}^2 = 2.5 \times 10^{-3} \text{ eV}^2$ ).

## 2.4 Sensitivity and discovery potential

We used a  $\chi^2$  pull approach in order to compute the  $\sin^2(2\theta_{13})$  sensitivity. This method allows us to introduce and assess the impact of systematic errors with ease and to study the interplay between them by switching them on/off. This type of  $\chi^2$  has a generic structure: a sum over terms like:

$$\left( \frac{\text{Data} - \text{Prediction} - \text{Systematics effects}}{\text{Uncorrelated error}} \right)^2$$

and another sum term which weights the systematic effects by the accuracy with which we know them:

$$\left( \frac{\text{Systematic effect amplitude}}{\text{Systematic effect knowledge}} \right)^2.$$

Table 12: Summary of the background subtraction error at the Far and Near detector (preliminary). Background rate and shape with their corresponding uncertainties are used for the calculation of the sensitivity. The systematics correspond to our best estimate of the error associated with each particular background (this can be used as a “background systematic error”). The uncertainty on the background rate is larger than the systematic error because we haven’t yet chosen certain materials, though when we do, the error will be quite small.

Detector	Site		Background				
			Accidental		Fast n	Correlated	
			Materials	PMTs			$\mu$ -Capture
CHOOZ (24 $\nu$ /d)	Far	Rate ( $d^{-1}$ )	—	—	—	—	$0.6 \pm 0.4$
		Rate ( $d^{-1}$ )	$0.42 \pm 0.05$		$1.01 \pm 0.04(stat) \pm 0.1(sys)$		
		bkg/ $\nu$	1.6%			4%	
		Systematics	0.2%			0.4%	
Double Chooz (69 $\nu$ /d)	Far	Rate ( $d^{-1}$ )	$0.5 \pm 0.3$	$1.5 \pm 0.8$	$0.2 \pm 0.2$	$< 0.1$	$1.4 \pm 0.5$
		bkg/ $\nu$	0.7%	2.2%	0.2%	$< 0.1\%$	1.4%
		Systematics	$< 0.1\%$	$< 0.1\%$	0.2%	$< 0.1\%$	0.7%
Double Chooz (1012 $\nu$ /d)	Near	Rate ( $d^{-1}$ )	$5 \pm 3$	$17 \pm 9$	$1.3 \pm 1.3$	0.4	$9 \pm 5$
		bkg/ $\nu$	0.5%	1.7%	0.13%	$< 0.1\%$	1%
		Systematics	$< 0.1\%$	$< 0.1\%$	0.2%	$< 0.1\%$	0.2%

This overall  $\chi^2$  is minimized with respect to all systematic amplitudes. In the case of Double Chooz, this leads to the following  $\chi^2$  formula [33]:

$$\chi^2 = \min_{\{\alpha_{i,k}^D\}} \left\{ \sum_{D=N,F} \sum_{i=1}^{N_{\text{bins}}} \left[ \left( \frac{O_i^D - T_i^D - \sum_{k=1}^K \alpha_{i,k}^D S_{i,k}^D}{U_i^D} \right)^2 + \sum_{k=1}^K c_{i,k}^D \left( \frac{\alpha_{i,k}^D}{\sigma_k^D} \right)^2 \right] \right\}. \quad (11)$$

where there are  $N_{\text{bins}}$  energy bins. This  $\chi^2$  includes all the spectral shape and normalization from both detectors ( $D = N, F$ ). The ( $K = 5$ ) systematic amplitudes included,  $\alpha_{i,k}^D$ , are gathered in Table 13. The current knowledge of the antineutrino reactor spectrum, although already well

Table 13: Table of systematic parameters used in the  $\chi^2$ .

Error type	$k$	$c_{i,k}^D$	$\alpha_{i,k}^D$	$S_{i,k}^D$	$\sigma_k^D$
Global normalization	1	$1/2N_{\text{bins}}$	$\alpha_{\text{abs}}$	$T_i^D$	$\sigma_{\text{abs}} = 2.0\%$
Relative normalization	2	$1/N_{\text{bins}}$	$\alpha_{\text{rel}}^D$	$T_i^D$	$\sigma_{\text{rel}} = 0.6\%$
Spectrum shape	3	1/2	$\alpha_{i,\text{shp}}$	$T_i^D$	$\sigma_{\text{shp}} = 2.0\%$
Energy scale	4	$1/N_{\text{bins}}$	$\alpha_{i,\text{scl}}^D$	$\left. \frac{dN_i^D}{d\alpha_{i,\text{scl}}} \right _{\alpha_{i,\text{scl}}^D=0}$	$\sigma_{\text{scl}} = 0.5\%$
$\Delta m_{31}^2$ knowledge	5	$1/2N_{\text{bins}}$	$\alpha_{\Delta m_{31}^2}$	—	$\sigma_{\Delta m_{31}^2} = 10 - 20\%$

known is limited, due to production/detection uncertainties, to about 2% of the precision on the rate (the number of  $\bar{\nu}_e$  in the full range between 1.8 and 10 MeV) and the shape (number of  $\bar{\nu}_e$  per

energy interval in the same range). These two limitations are included in the  $\chi^2$  through  $\alpha_{i,1}^D = \alpha_{\text{abs}}$  and  $\alpha_{i,3}^D = \alpha_{i,\text{shp}}$  which do not depend on  $D$ , the detector index, since they have an identical effect in both detectors. We also introduced a relative normalization error between the two detectors through  $\alpha_{i,2}^D = \alpha_{\text{rel}}$ . Moreover we took into account the fact that the  $\Delta m_{31}^2$  is not known at a precision better than 20% as a systematic effect (at the time of this proposal, but it should be known with a better precision of 10% with MINOS data)[37].

We define our  $\sin^2(2\theta_{13})$  sensitivity limit as the lowest value of  $\sin^2(2\theta_{13})$  we can obtain with an experiment at a given confidence level if  $\theta_{13} = 0$ . We compute the expected number of events  $O_i^D$  as  $N_i^D(\Delta m_{31}^2, \theta_{13} = 0) \sum_{R_1, R_2} N_i^{R,D}(\Delta m_{31}^2, 0)$ . (see Equation 7). The theoretical prediction on the number of events,  $T_i^D$ , is computed by the same formula but with a value of  $\theta_{13}$ .  $S_{i,k}^D$  describes the  $1\sigma$  systematic impact on the number of events moderated by the amplitude  $\alpha_{i,k}^D$ .

We also include background rejection uncertainties,  $\sigma_{\text{bkg}}$ , in both detectors through the uncorrelated errors  $U_i^D$ :

$$U_i^D = \sqrt{O_i^D + B_i^D(1 + \sigma_{\text{bkg}}^2 B_i^D)} \quad (12)$$

Table 14 displays the sensitivity for different values of  $\Delta m_{31}^2$ . According to the last MINOS and Super-Kamiokande results [38, 39, 37], the preferred values lie between 2.5 and 3. times  $10^{-3} eV^2$  (the latter value being the best fit value of MINOS). According to those new results, the optimum distance for a new reactor neutrino experiment is around 1.3 km, thus the Double Chooz far detector (1.05 km) is well located to efficiently search for a non vanishing  $\theta_{13}$  mixing angle.

Table 14: Sensitivity and discovery potential dependence on  $\Delta m_{31}^2$ , for 3 years of data taking with both detectors.

$\Delta m_{31}^2$ ( $10^{-3} eV^2$ )	1.8	2.0	2.2	2.4	2.6	2.8	3.0	3.2	3.4
Sensitivity (90% C.L. )	0.043	0.037	0.032	0.030	0.027	0.025	0.024	0.023	0.022
Discovery potential ( $3\sigma$ )	0.078	0.067	0.060	0.054	0.050	0.046	0.044	0.042	0.041

Figure 19 shows the variation of the sensitivity (limit at 90% C.L. if no signal) with respect to the relative normalization error between the Near and Far detectors. Even though we foresee a relative error of 0.5% (see Table 8), we used 0.6% to quote our results.

Figure 20 displays the variation of the sensitivity (limit at 90% C.L. if no signal) with respect to the energy resolution. We plan to use about 500 PMTs that will lead to 200 to 300 photoelectrons for an energy deposition of 1 MeV at the center of the detector (see Section 5). We can see on the figure that the resolution is not a critical parameter (above 100 p.e./MeV); this is because we do look for an oscillation signal whose shape extend on the MeV scale. A good energy resolution is important for the understanding of the tail of the low energy spectrum, however.

## 2.5 Complementarity with the Superbeam program

In order to discuss the role of Double Chooz in the global context, we show in Figure 21 a possible evolution of the  $\sin^2 2\theta_{13}$  discovery potential (left) and  $\sin^2 2\theta_{13}$  sensitivity limit (right) as function of time. In the left panel of Figure 21, we assume that  $\sin^2 2\theta_{13}$  is finite and that a certain unknown value of  $\delta_{\text{CP}}$  exists. The bands in the figure reflect the dependence on the unknown value of  $\delta_{\text{CP}}$ , *i.e.*, the actual discovery reach will lie in between the best case (upper) and worst case (lower) curve,



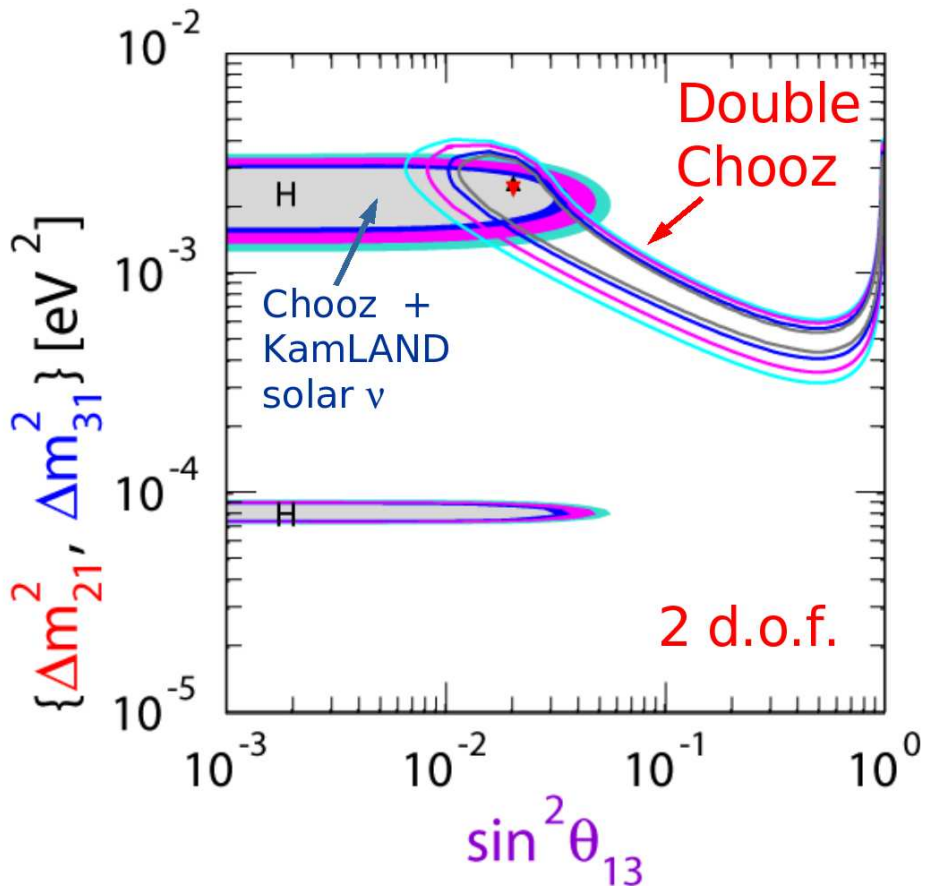


Figure 17: Double Chooz sensitivity contours (gray  $1\sigma$ , blue 90%, magenta  $2\sigma$ , cyan  $3\sigma$  C.L.) in  $(\sin^2\theta_{13}, \Delta m_{31}^2)$  plane generated for  $\sin^2\theta_{13} = 0.02$  and  $\Delta m_{31}^2 = 2.5 \times 10^{-3} \text{ eV}^2$  (which is also the best fit) with 1% background in near and far detectors, systematics included in Table 13 and parametrization described in Section 2, Section 2.1 except that we relaxed the constraint on  $\Delta m_{31}^2$  in this figure and computed contours with 2 degrees of freedom after 3 years of data taking. Also shown here are the current contours from global analysis with the same color convention [36]. Double Chooz is able to provide a 20% precision measurement of  $\theta_{13}$  as long as this parameter is not too low.

depending on the value of  $\delta_{\text{CP}}$  realized in nature. In addition, the curves for the beam experiments shift somewhat to the worse for the inverted mass hierarchy. The right panel of the figure shows the  $\sin^2 2\theta_{13}$  limit which can be obtained for the hypothesis  $\sin^2 2\theta_{13} = 0$ , *i.e.*, no signal. Since particular parameter combinations can easily mimic  $\sin^2 2\theta_{13} = 0$  in the case of the neutrino beams, their final  $\sin^2 2\theta_{13}$  sensitivity limit is spoiled by correlations (especially with  $\delta_{\text{CP}}$ ) compared to Double Chooz<sup>3</sup>. The two panels of Figure 21 very nicely illustrate the complementarity of beam and reactor experiments: Beams are sensitive to  $\delta_{\text{CP}}$  (and the mass hierarchy for long enough baselines), reactor experiments are not. On the other hand, reactor experiments allow for a “clean” measurement of  $\sin^2 2\theta_{13}$  without being affected by correlations.

<sup>3</sup>Note that we define the  $\sin^2 2\theta_{13}$  sensitivity limit as the largest value of  $\sin^2 2\theta_{13}$  which fits (the true)  $\sin^2 2\theta_{13} = 0$  at the given confidence level. Therefore, this definition has no dependence on the true value of  $\delta_{\text{CP}}$ , and the fit  $\delta_{\text{CP}}$  is marginalized over (*cf.*, App. C of Reference [24]).

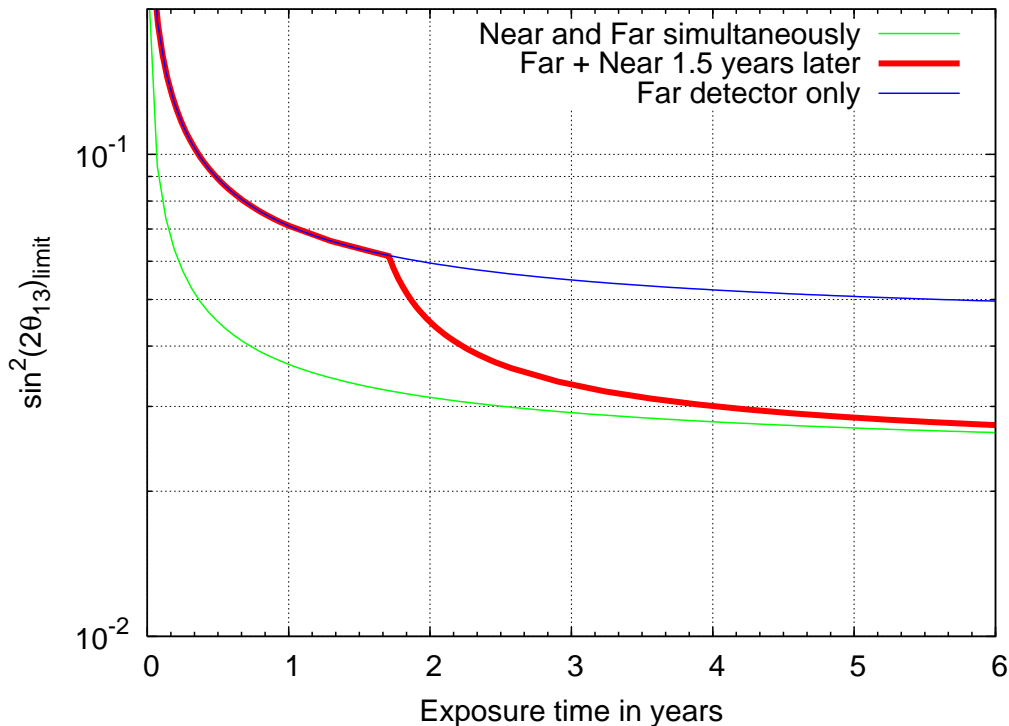


Figure 18:  $\sin^2(2\theta_{13})$  sensitivity limit for the detectors installation scheduled scenario

There are a number of important observations which can be gleaned from Figure 21. First of all, assume that Double Chooz starts as planned (solid Double Chooz curves). Then it will quickly exceed the  $\sin^2 2\theta_{13}$  discovery reach of MINOS and CNGS, especially after the near detector is online (left panel). It will be the most sensitive experiment until at least 2011 and its  $\sin^2 2\theta_{13}$  discovery potential is remarkable. In some scenarios, like inverted mass hierarchy and specific values of  $\delta_{CP}$ , the reactor measurement would have the best discovery potential. Note, that even the far detector of Double Chooz alone would improve the current bounds on  $\sin^2 2\theta_{13}$  considerably down to 0.04 after 4 years and 0.03 after 10 years at the 90% confidence level. The information gained by Double Chooz can also be used for a fine-tuning of the running strategy of second generation superbeams with anti-neutrinos. If a finite value of  $\sin^2 2\theta_{13}$  were established at Double Chooz, the superbeam experiments could possibly avoid the time consuming (due to lower cross sections) anti-neutrino running and gain more statistics with neutrinos. The breaking of parameter correlations and degeneracies could in this case be achieved by the synergy with the Double Chooz experiment.

The Chooz reactor complex even allows for a very interesting upgrade, called Triple Chooz [42]. There exists another underground cavern at roughly the same distance from the reactor cores as the Double Chooz far detector. A 200 t detector could be constructed there without requiring significant civil engineering efforts. This upgrade would in principle be equivalent to the Reactor-II setup described in Reference [3]. Figure 21 shows that it could play a leading role, since its sensitivity is unrivaled by any of the first generation beam experiments for the next decade and even the discovery potential is excellent and covers more than 1/2 of the region superbeams can access. In the case of a value of  $\sin^2 2\theta_{13}$  not too far below the current CHOOZ bound, this might even lead to the possibility to restrict the CP parameter space at superbeams for large enough luminosities. The advantage offered by this staged approach compared to other reactor projects

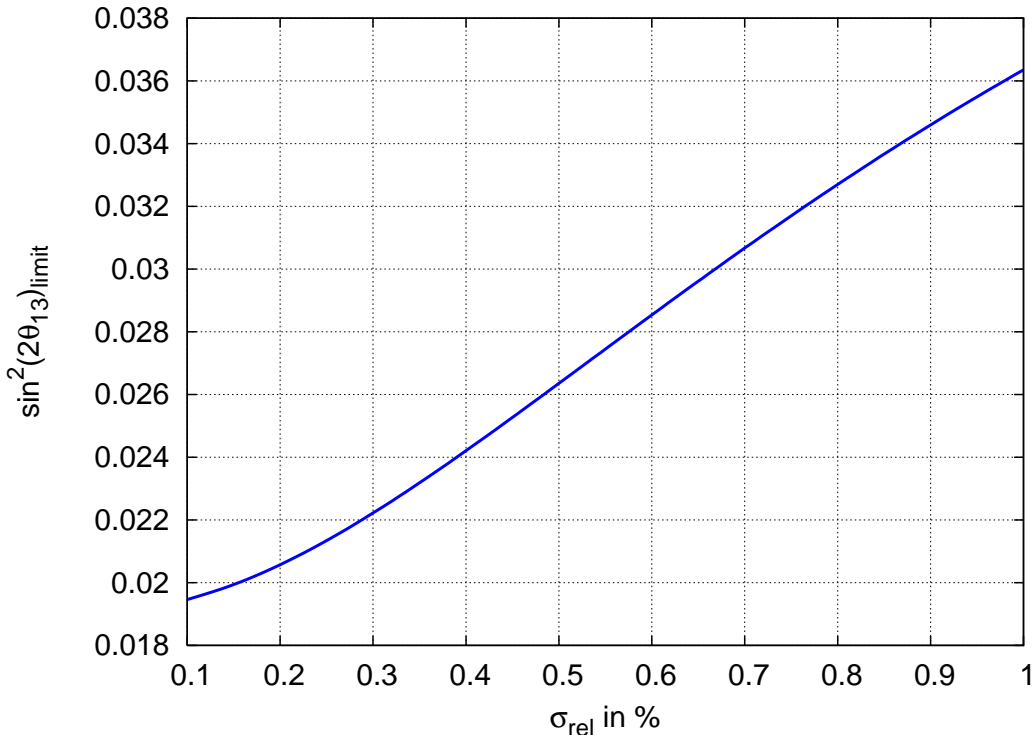


Figure 19:  $\sin^2(2\theta_{13})$  sensitivity (limit at 90% C.L. if no signal) evolution with respect to the relative normalization error, from 0.1% to 1%, between the Near and Far detectors.

which would start right away with a very large detector is that Double Chooz will serve as a testbed for the upgrade. Thus the systematics will be well enough understood to allow a reliable sensitivity prediction for Triple Chooz.

Figure 22 shows the sensitivity to CP violation at  $3\sigma$  C.L. ( $\Delta\chi^2 = 9$ ) for various second generation beam experiments. In this figure two regimes can be clearly distinguished: very large  $\sin^2 2\theta_{13} \geq 0.01$  and very small  $\sin^2 2\theta_{13} \leq 0.01$ . At large  $\theta_{13}$  the sensitivity to CP violation is basically completely determined by factors like systematic errors or matter density uncertainty. Thus the question of the optimal technology cannot be answered with confidence at the moment, since for most of the controlling factors the exact magnitude can only be estimated. The technology decision for large  $\theta_{13}$ , therefore, requires considerable R&D. On the other hand, in the case of small  $\theta_{13}$  the optimal technology seems to be a neutrino factory<sup>4</sup> quite independently from any of the above mentioned factors. The branching point between the two regimes is around  $\sin^2 2\theta_{13} \sim 0.01$  which coincides with the sensitivities obtainable at the Chooz reactor complex. Moreover, the information from Double Chooz would be available around 2010 which is precisely the envisaged time frame for the submission of a proposal for those second generation neutrino beam facilities. Thus the Double Chooz results are of central importance for the long term strategy of beam-based neutrino physics.

Double Chooz is also important for the next generations of searches for neutrino-less double

<sup>4</sup>Not shown in Figure 22 is the  $\gamma = 350$  beta beam [66]. Such a higher gamma beta beam could also play the role of a neutrino factory [46, 49].

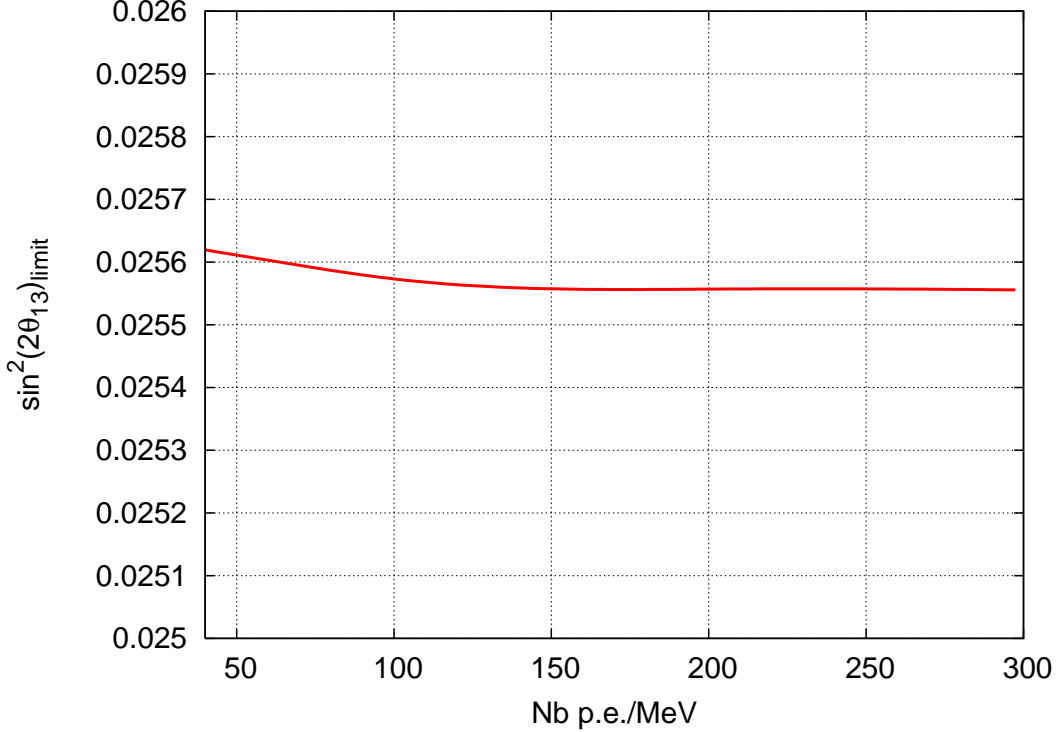


Figure 20:  $\sin^2(2\theta_{13})$  sensitivity (limit at 90% C.L. if no signal) evolution with respect to the energy resolution in photoelectrons (p.e.) per MeV. The Double Chooz predicted value is between 200 and 300 p.e./MeV. The full backgrounds have not been included in this study.

beta decay. The amplitude for this process depends on the so-called effective mass,

$$|m_{ee}| \equiv \left| \sum_i m_i U_{ei}^2 \right| \quad \text{with} \quad m_{ee} = |m_{ee}^{(1)}| + |m_{ee}^{(2)}| e^{2i\alpha} + |m_{ee}^{(3)}| e^{2i\beta} , \quad (13)$$

where  $m_i$  is the mass of the  $i^{\text{th}}$  neutrino state, the sum is over all light neutrino mass states and  $\alpha, \beta$  are the two Majorana phases. For an overview on the current situation of neutrino-less double beta decay, see [50] and references therein.

Assuming a certain value of  $\theta_{13}$  and predicting the effective mass as a function of the smallest neutrino mass [51, 52, 53], one obtains two bands for  $|m_{ee}|$ , corresponding to a positive or negative sign of the atmospheric  $\Delta m^2$  (see Figure 23). This allows one to distinguish the normal from the inverted mass ordering [54, 55, 56]. However, this simplified picture gets changed once the current knowledge on  $\theta_{13}$  is taken into account [57].

As can be seen from Figure 23, the gap between the cases  $\Delta m_{31}^2 > 0$  and  $\Delta m_{31}^2 < 0$  depends on  $\theta_{13}$ . For today's largest possible values of  $\theta_{13}$ , the normal and inverted hierarchy regions overlap, making the distinction of normal and inverted hierarchy impossible. The width of the “chimney” for very small values of  $|m_{ee}|$  also depends strongly on  $\theta_{13}$ , in the sense that it becomes narrower with decreasing  $\theta_{13}$ . For very small  $\theta_{13}$ , a vanishing  $|m_{ee}|$  would correspond to rather specifically chosen parameter values.

All these aspects demonstrate how the outcome of Double Chooz affects the future program for neutrino-less double beta decay.

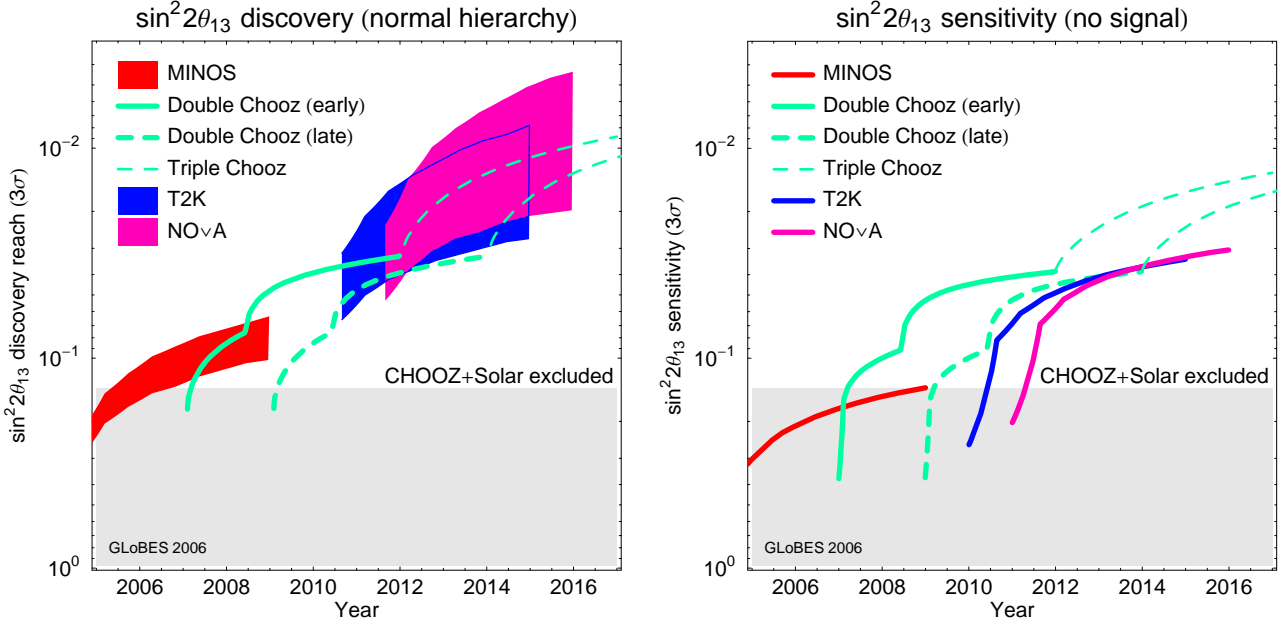


Figure 21: A possible evolution of the  $\sin^2 2\theta_{13}$  discovery potential (left) and  $\sin^2 2\theta_{13}$  sensitivity/exclusion limit (right) at  $3\sigma$  as a function of time including statistics, systematics, and correlations ( $3\sigma$ ). The bands reflect for the neutrino beam experiments the dependence on the unknown value of  $\delta_{CP}$ , *i.e.*, the actual sensitivity evolution will lie in between the best case (upper) and worst (lower) curve depending on the value of  $\delta_{CP}$  chosen by nature. All experiments are assumed to be operated five years and the beam experiments are operated with neutrino running only. The full detector mass is assumed to be available right from the beginning for the beam experiments, *i.e.*, the starting times are chosen accordingly. Double Chooz is assumed to start data taking with the near detector 1.5 years after the far detector, where two possible far detector starting times are shown. In addition, the possible upgrade to Triple Chooz is included after five years of data taking. Though the starting times of the experiments have been chosen as close as possible to those stated in the respective LOIs, they have to be interpreted with care. A normal mass hierarchy is assumed for this plot and for an inverted hierarchy, the accelerator-based sensitivities are expected to be slightly worse. The calculations (including time evolution) are based on simulations with GLoBES [40], which were performed in References [47, 48, 24, 40] for the beams and in ref. [42] for Double Chooz and Triple Chooz. Figure from Reference [42] (similar to the ones in References [43, 44]).

## 2.6 Other physics

### 2.6.1 Study of the directionality

The near detector of Double Chooz will detect on the order of one million events per year, which opens exciting possibilities. One topic is the possibility to determine the direction of the neutrino from the forward scattering of the neutron in the inverse beta decay reaction. Successive scatterings of the neutron leads to a broad distribution of capture locations and it is almost as likely that the neutron is captured in backward direction as in forward direction. This means that the direction of a neutrino source cannot be determined on an event by event basis. However, the neutron has a slightly larger probability to be captured in forward direction, which can be measured with sufficient statistics and resolution. This effect was first seen in the Bugey experiment[26] and even better in

the CHOOZ experiment[5].

The very high statistics of the near detector of Double Chooz will allow a detailed exploration of the directionality effect. The near detector will record events when both reactor cores are on, when one or the other core is off, and it will also have data with both reactors off. A comparison of these data sets, in combination with a modeling of the expected event distributions will allow us to understand and test directionality much better. These studies should ultimately clarify if directionality can be used in future experiments. Possible applications could emerge in astrophysics, reactor physics or in the context of geo-neutrinos.

### 2.6.2 Mass-varying neutrinos

Mass-varying neutrinos are an interesting idea which could be tested by reactor experiments. The concept of mass-varying neutrinos has been introduced by imposing a relation between neutrinos and the dark energy of the Universe [41, 58, 60, 62] through a scalar field, the accelaron. Including the possibility of accelaron couplings to matter fields implies that the neutrino oscillation parameters in vacuum/air and a medium could be very different [61]. Since reactor experiments do have different paths in vacuum and air, or the material along the path may be altered at relatively moderate effort, the direct test of mass-varying neutrinos may be possible using reactor experiments. In Reference [30], a different parameterization of  $\theta_{13}$  and  $\Delta m_{31}^2$  was used for air and matter. This approach allows for arbitrary effects different in air and matter, since any Hermitian addition to the Hamiltonian in matter can be described by a re-diagonalization leading to a different effective mixing angle and mass squared difference in matter. If only one experiment (in air or matter) measures these parameters, no conclusion about mass-varying neutrinos can be drawn. Only by the combination of different experiments in air and vacuum, constraints to mass-varying neutrinos can be obtained. In particular, since the Double Chooz baseline is partly in air (roughly 50%), Double Chooz will be a key component to such measurements to be combined with beam or reactor data in matter. Note that all proposals for other reactor or beam experiments have baselines practically only in matter. Extremely high sensitivities can be finally obtained by physically moving the material between near and far detector, because one does not only have *identical* detectors then, but also *the same* detectors in two consecutive phases of the experiment in order to cancel systematics almost completely. For a more extensive discussion, see Reference [30].

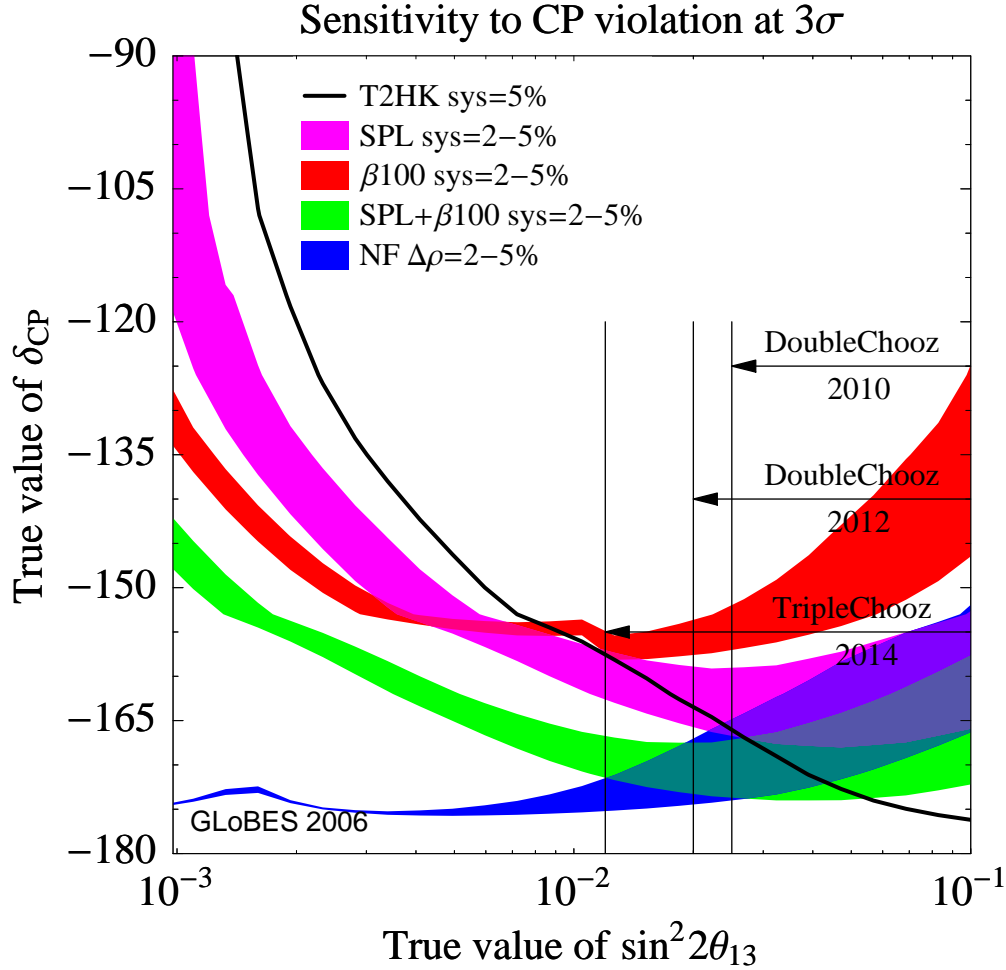


Figure 22:  $\sin^2 2\theta_{13}$  sensitivity limits at 90% C.L. of Double and Triple Chooz in comparison to the  $3\sigma$  discovery reaches for CP violation of various, second generation beam experiments. Sensitivity to CP violation is defined, for a given point in the  $\theta_{13}$ - $\delta$ -plane, by being able to exclude  $\delta = 0$  and  $\delta = \pi$  at the given confidence level. All curves have been prepared with GLoBES [40]. Degeneracies and correlations are fully taken into account. For all setups the appropriate disappearance channels have been included. The beta beam is lacking muon neutrino disappearance, which is replaced by a 10% precision on  $\Delta m_{31}^2$  (corresponding to the T2K disappearance information). In all cases systematics between neutrinos, anti-neutrinos, appearance and disappearance is uncorrelated. For all setups with a water Cerenkov detector the systematics applies both to background and signal, uncorrelated. The neutrino factory assumes  $3.1 \cdot 10^{20} \mu^+$  decays per year for 10 years and  $3.1 \cdot 10^{20} \mu^-$  decays for 10 years. It has one detector with  $m = 100$  kt at 3000 km and another detector with 30 kt at 7000 km. The density errors between the two baselines are uncorrelated. The systematics are 0.1% on the signal and 20% on the background, uncorrelated. The detector threshold and the other parameters are taken from [47] and approximate the results of [45]. The beta beam assumes  $5.8 \cdot 10^{18}$  He decays per year for five years and  $2.2 \cdot 10^{18}$  Ne decays per year for five years. The detector mass is 500 kt. The detector description and the glb-file is from [63]. The SPL setup is taken from [64], and the detector mass is 500 kt. The T2HK setup is taken from [47] and closely follows the LOI [65]. The detector mass is 1000 kt and it runs with 4 MW beam power, 6 years with anti-neutrinos and 2 years with neutrinos. The systematic error on both background and signal is 5%. Figure from Reference [42].

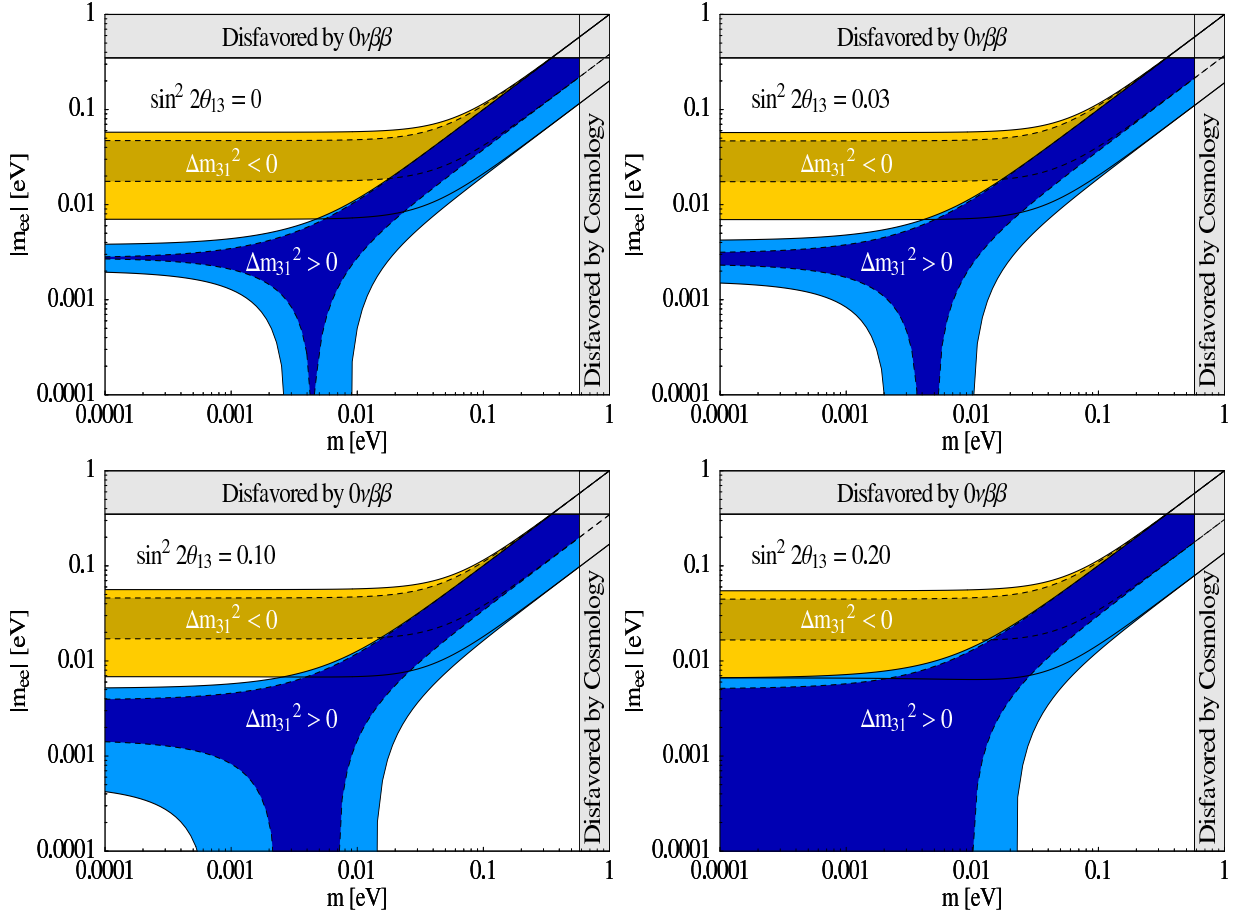


Figure 23: The effective mass (in eV) for the normal and inverted ordering as a function of the smallest neutrino mass (in eV) for different values of  $\sin^2 2\theta_{13}$ . The prediction for the best-fit values of the oscillation parameters and for the  $3\sigma$  ranges is given. A typical bound from cosmology and the current limit on the effective mass are indicated. From [57].



## 3 Detector Structures, Materials and Radiopurity

### 3.1 Detector dimensions

Detector dimensions are summarized in Tables 15, 16, 17. Viewgraph of the Far detector integrated in the the neutrino laboratory are shown in Figures 24, 25, 26.

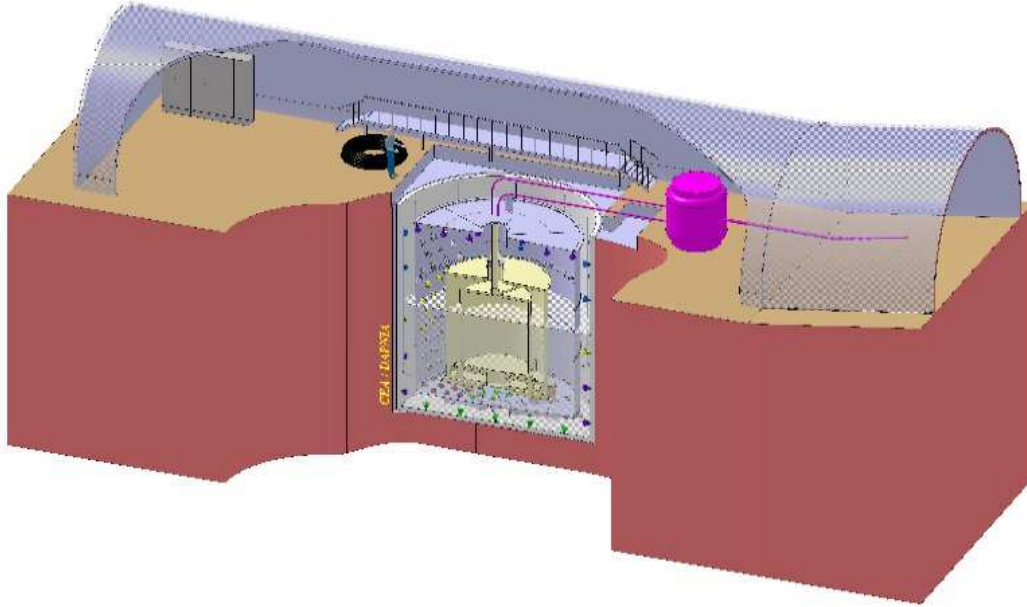


Figure 24: Viewgraph of the Far detector integrated in the the neutrino laboratory located at the end of the "Marinière" gallery, 1 km from the CHOOZ-B nuclear power station cores.

Table 15: Dimensions of the mechanical structure of the detector.

Inner Detector	Inner Diameter (mm)	Inner Height (mm)	Thickness (mm)	Filled with	Volume (m <sup>3</sup> )	Mass (tons)
Target	2300	2458	8	Gd-LS	10.3	0.35
$\gamma$ -catcher PMTs	3392 —	3574 —	12(-15) —	LS —	22.6 —	1.1-1.4 —
Buffer	5516	5674	3	Oil	114.2	7.7
Veto	6590	6640±100	10	Oil	90	20
Shielding	6610	6660±100	170	Steel	—	300
Pit	6950	7000	—	—	—	—

### 3.2 Double acrylic vessel

Target and  $\gamma$ -catcher vessels will be built with acrylic plastic material, transparent to photons with wavelengths above 400 nm. Both vessels are designed to contain the Target and  $\gamma$ -catcher aromatic liquids with a long term tightness (no leak leak for 10 years) and stability. The strongest constraint

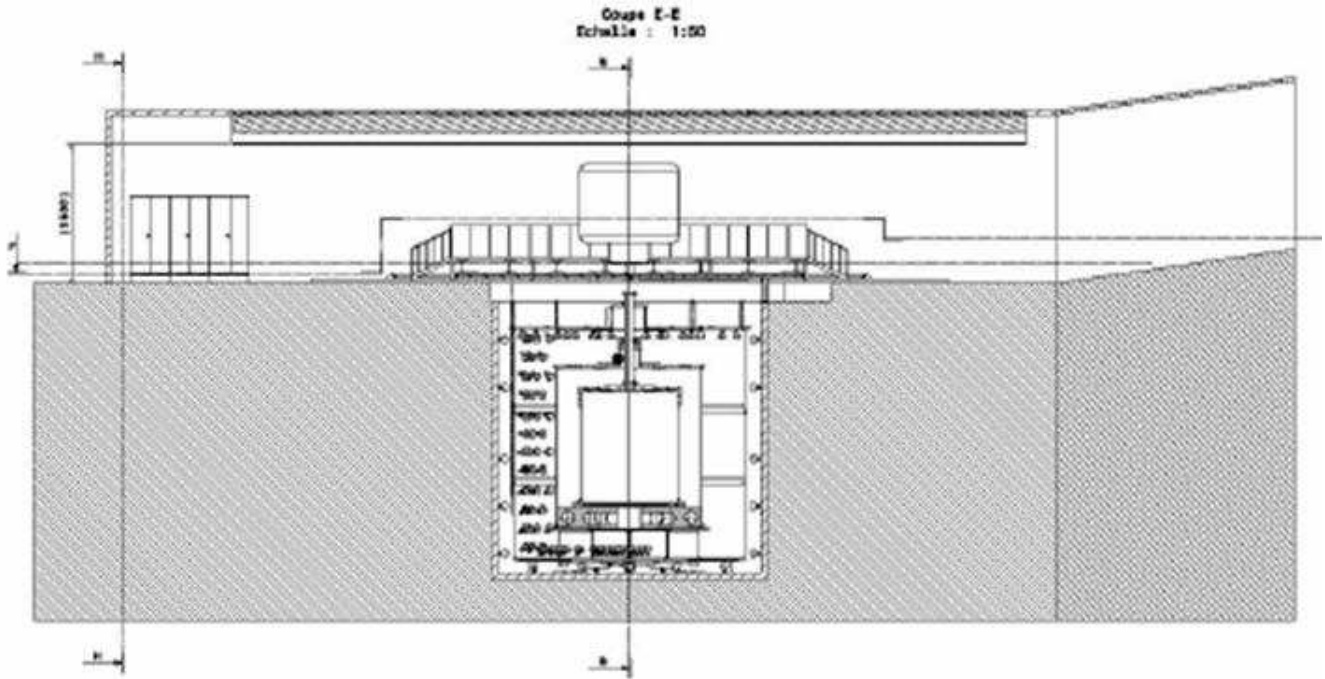


Figure 25: Side view of the Far detector in the neutrino laboratory located at the end of the "Marinière" gallery. The slope at the right side is the entrance of the laboratory.

Table 16: Thickness of the four detector regions filled with liquids

Region	Target	$\gamma$ -catcher	Buffer	Veto
Radial Thickness (mm)	1150	550	1050	500
Vertical Thickness (mm)	2458	550	1050	500 below and 600 above

Table 17: Dimensions of the detector chimneys. The effective radius is defined as the radius available for the calibration systems. It corresponds to the radius of the chimney minus the size taken by the filling tubes.

Chimney	Effective space (mm)	Thickness (mm)	Height (mm)	Filled with
Target	50 (radius)	8		LS+N <sub>2</sub>
$\gamma$ -catcher	40 (gap)	12-15		LS+N <sub>2</sub>

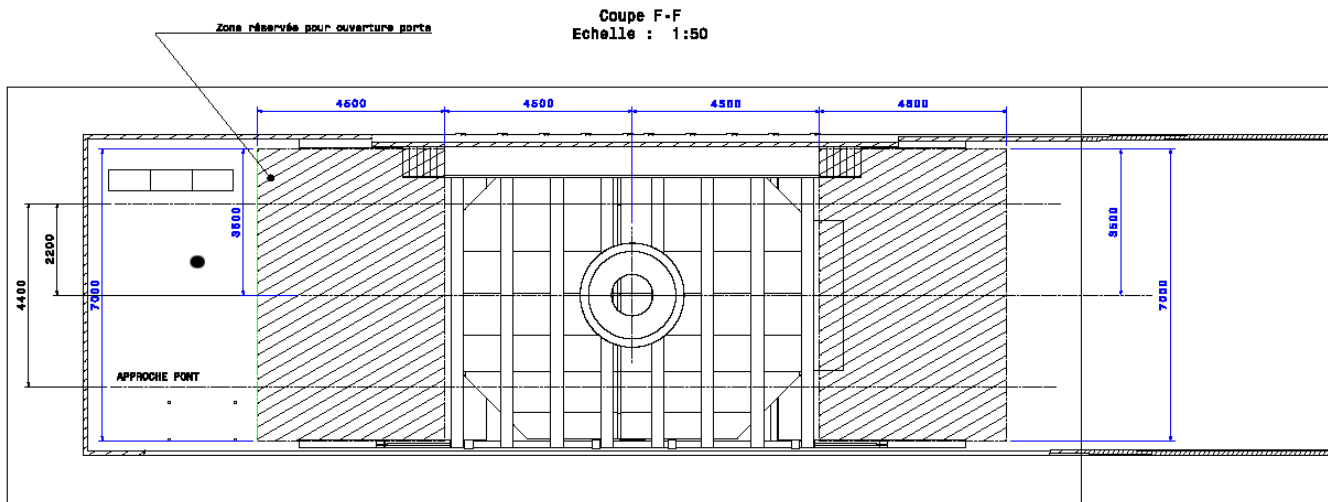


Figure 26: Top view of the the neutrino laboratory located at the end of the "Marinière" gallery. Entrance is at the right side. We can see the bridge crossing the detector that will have to be modified in order to be used as a safety issue in case of incident in the neighboring area (CHOOZ-A).

is the chemical compatibility between the vessel and the scintillating liquids of the Target and  $\gamma$ -catcher, for at least 5 years. We tolerate neither a modification of the liquid properties (scintillation, absorbency) nor a degradation of the acrylic material (breaking or crazing of more than a few percent of the acrylic surface area). The  $\gamma$ -catcher vessel must also be chemically compatible with the mineral oil of the Buffer region, which is known to be a weaker constrain. Material compatibility R&D has been pursued within the collaboration since 2003, based on knowledge obtained from the LENS R&D program [67]. Acrylic materials immersed in liquids of interest have been studied under mechanical stress up to 30 MPa and at different temperature to accelerate the aging processes. According to these studies, partially realized in collaboration with the Roehm acrylic company in Germany [68], the maximum Von Mises stress tolerated in Double Chooz has been set to 5 MPa.

Mechanically, the double vessels have to be strong enough to ensure identical shapes between Near and Far target vessels. No deformations of more than 5 mm are allowed during the running phase. This small geometrical difference between the two target acrylic vessels eliminate any measurable difference of the spill in/out effect between the near and far detectors. We note here that the number of free protons inside the Target vessel has to be measured at better than 0.2%. Thus, according to the 5 mm geometrical tolerance given by the plastic manufacturer, the volume difference between both Target vessel could be as large as 0.6 % (60 liters). In consequence, a weight based measurement method has been developed and tested to control the target content (mass) at the required precision (see page 2.2.3).

The mechanical structures of the double acrylic vessel have been studied with the finite element simulation software CASTEM 2000 [69]. The vessel has been designed to account for the transportation, integration, filling and running phases. The goal of the mechanical simulation was to define the structure of the vessel within the distortion and stress tolerances. During this work a few critical cases have been identified (see below).

In this simulation, some optimizations can be tested to improve the signal to noise ratio. For example, the Target vessel thickness and the acrylic structural materials between the Target and

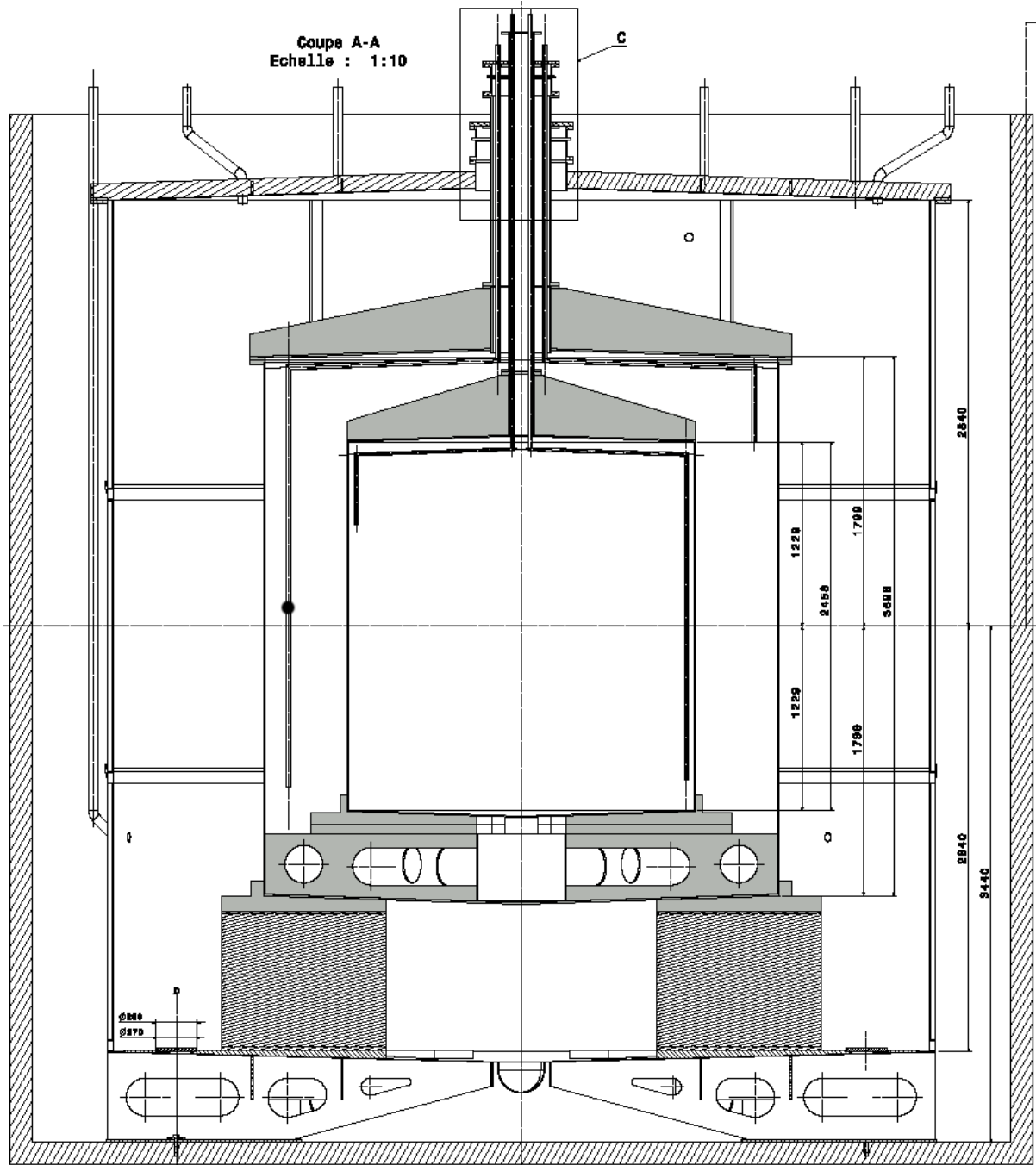


Figure 27: Detail drawing of the Far detector. From the innermost region, one has: the neutrino Target enclosed in a acrylic vessel (8 mm) filled with a Gd-doped liquid scintillator, the  $\gamma$ -catcher region enclosed in another acrylic vessel (12-15 mm) and filled with an undoped liquid scintillator, the Buffer region filled with non scintillating oil enclosed in a stainless steel vessel (3 mm) supporting also the phototubes (534), the Inner Veto enclosed in a steel wall (10 mm) and filled with scintillating oil, and the steel shielding (170 mm). The top of the steel shielding as well as the outer muon veto are not represented.

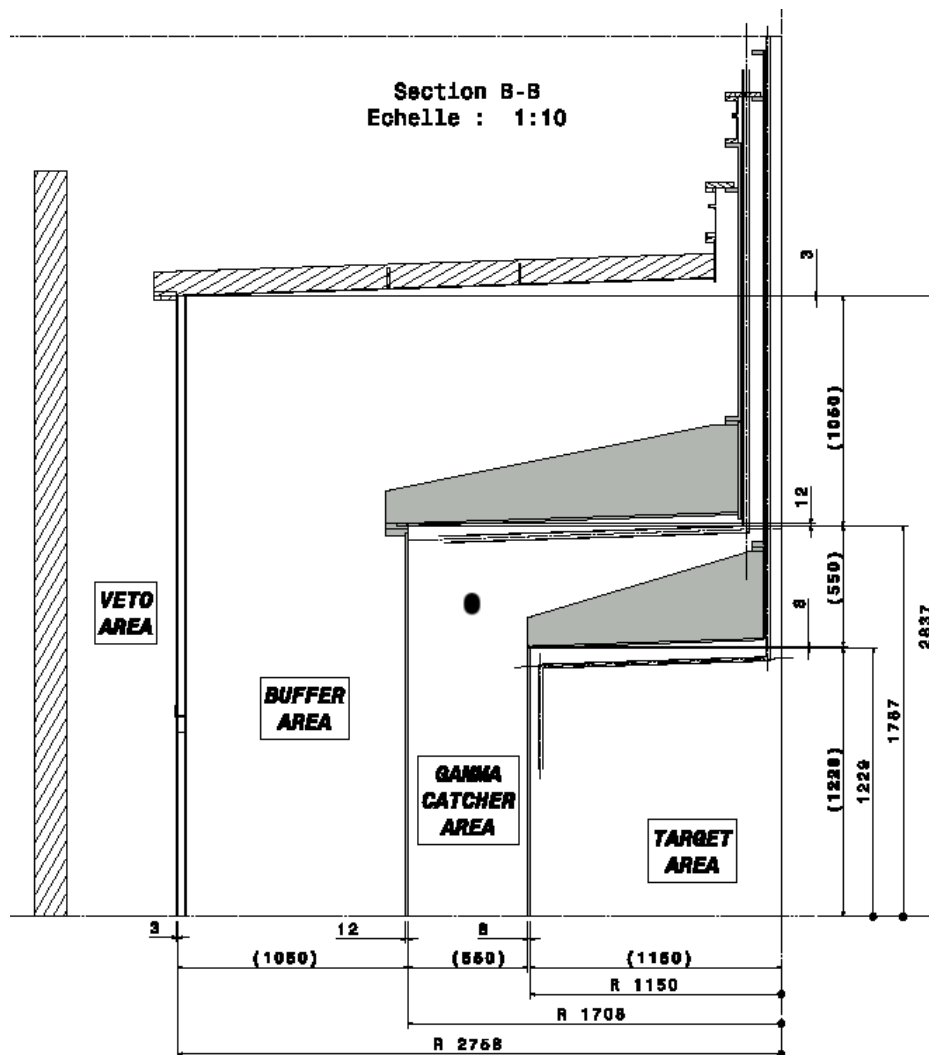


Figure 28: Side view of the detector regions. Effective thickness of the  $\gamma$ -catcher region is 550 mm. Effective thickness of the Buffer region is 1050 mm. Thickness of the Veto region is 500 mm (600 mm on the top part of the Veto).

$\gamma$ -catcher can be minimized to reduce dead materials within the active volume, as well as accidental background originating from radio-impurities. Dead materials can lead to untagged muon capture, see section 2.3.5. The  $\gamma$ -catcher vessel, however, is not considered a dead material, but a part of the non scintillating Buffer. Its thickness is only constrained by its radioimpurities content.

Considering all previous requirements the Target and  $\gamma$ -catcher vessels will be made of cast acrylic from the Roehm Company. The assembly will be done by gluing pieces according to the manufacturer's expertise. The Target vessel is a cylinder of 2474 mm height, 2316 mm diameter (external dimensions), and 8 mm thick. It weights 350 kg, and contains a volume of 10.3 m<sup>3</sup> (without the chimney). The  $\gamma$ -catcher vessel is a cylinder surrounding the Target of 3422 mm height, 3374 mm diameter (external dimensions), and 12 mm thick. It weights 1100 kg, and contains a volume of 22.6 m<sup>3</sup> (without the chimney). The Target chimney diameter will be less than 900 mm. Drawings of the Target and the  $\gamma$ -catcher are shown in Figure 29.

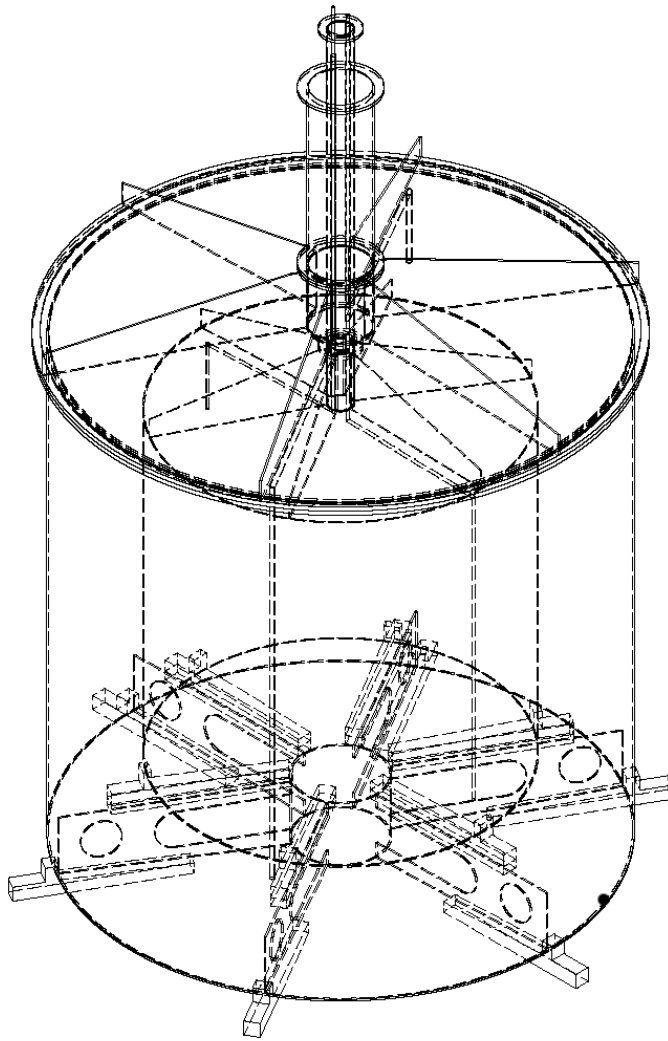


Figure 29: 3D view of the double acrylic vessel. The Target vessel is a cylinder of 2474 mm height, 2316 mm diameter, and 8 mm thick. It weights 350 kg, and contains a volume of  $10.3 \text{ m}^3$ . The  $\gamma$ -catcher vessel is a cylinder surrounding the Target of 3422 mm height, 3374 mm diameter (external dimensions), and 12 mm thick, and contains a volume of  $22.6 \text{ m}^3$

Simulation has shown that the transportation phase is hazardous for a double acrylic vessel which has been completely assembled by glue. Vibrations generated by the suspension system during ground transportation could be significant if the full double vessel construction was completed at the manufacturer's point. Calculation of the structural brittleness of the acrylic gives a maximum acceptable acceleration of  $11 \text{ g}$ . To avoid any resonance problem and completely decouple from the suspension system, the eigen frequency of the structure must be greater than 10 Hz. The computation shows that the first eigen frequencies of our double vessel are close to 8 Hz. A first simple solution would be to add acrylic stiffeners to the structure. Eigen frequencies will then be raised to more than 13 Hz, above the critical region. This problem could also be solve, without changing the baseline design, by transporting the Target and  $\gamma$ -catcher vessels separately, integrate them in the pit, and glue the  $\gamma$ -catcher top lid and the Chimney in the neutrino laboratory. There will be no annealing after the vessels are made, since the oven is far from Chooz and the transportation

would induce intolerable stress.

As a result of these studies, it has been decided that the integration of the double acrylic vessel will be done in several steps: a) the Target vessel will be entirely built, annealed and checked for tightness at the manufacturer; b) The chimney will be glued in the Chooz far site laboratory; c) the  $\gamma$ -catcher vessel will be built without top lid—it will be glued later in the pit of the detector. For the final step, air conditions in the neutrino laboratory (in and just around the pit) have to be well controlled. During the 24 hours of the polymerization of the glue, the temperature has to be kept above 25 degrees centigrade and the relative humidity at 40%, whereas nominal conditions in the tunnel are 14 degrees centigrade and 100% respectively. In both Chooz neutrino laboratories, the assembly in the pit will be handled with the ceiling crane and specifically developed on tools (see Figure 30). The  $\gamma$ -catcher vessel will arrive mounted on a supporting structure used to minimize the

Figure 30: Dedicated tool to handle the acrylics vessel from the construction till the integration in the detector. A full mechanical study has been performed to guarantee a tolerable stress level during all the phases of the life of the acrylic vessels.

deformations, driven in the tunnel, and rotated above the pit prior to its final insertion in the Buffer vessel (phototubes will already be partially mounted). The Target vessel will then be inserted into the  $\gamma$ -catcher. After a first cleaning on site the top lid of the  $\gamma$ -catcher and the chimney will be glued by technicians from the manufacturer.

In Double Chooz all regions within the Buffer vessel have to be filled simultaneously. The filling phase generates constraints related to the differences in height of liquid. According to the mechanical simulation, if we neglect density variations, the difference in height acceptable is 30 cm.

During the running phase static loads induced by slight liquid density differences, put stress in the acrylic vessels. Simulations have been done to assess the stress levels with respect to density differences. The following table is the summary of the slight densities differences acceptable in each zone.

Table 18: Summary of stress and effects induced by density differences between the Target,  $\gamma$ -catcher and buffer liquids.

Density difference	Dead load	0%	1% (T & GC)	1% (GC & Buffer)
Max. distortion in the top lid (mm)	-2	-1	-1	-2
Max. distortion in the bottom (mm)	-1	-0.7	-2.8	2.7
Max. stress (MPa)	1.2	0.9	1.2	1.0

### 3.3 Stainless steel Buffer vessel

The Buffer vessel surrounds the  $\gamma$ -catcher region, 1050 mm away from the double acrylic vessel. It will be built with stainless steel 304L, and has the following requirements: a) to be tight to mineral oil over a long term (10 years); b) to be chemically compatible with the mineral oil of the Buffer region and the scintillating oil of the Inner Veto region; c) to be strong enough to support the five hundred photomultiplier tubes (positioning precision is given at about 1 cm); d) to be as light as possible to reduce backgrounds.

The Buffer vessel is a cylinder of 5680 mm height, 5522 mm diameter (external dimensions), and 3 mm thick. It weights 7.7 tons and contains a volume of 114.2 m<sup>3</sup> (without the chimney). A

drawing of the Buffer is shown in Figure 31. The vessel will be made of a stainless steel structure covered by steel sheets 3 mm thick. The structure has been studied with the finite element method of the CASTEM 2000 software [69]. The thickness constraint has been obtained in the critical case of dead load. Risk of buckling have also been considered.

The density of the Veto oil could be slightly different from the density of the Buffer oil. A

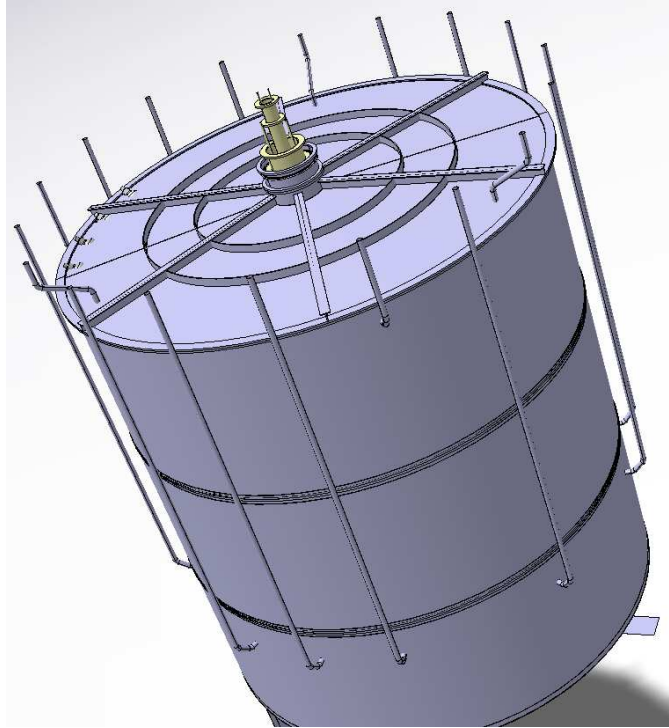


Figure 31: 3D view of the stainless steel Buffer vessel. This is a cylinder of 5680 mm height, 5522 mm diameter, and 3 mm thick (with stiffeners to guarantee the rigidity). It weights 7.7 tons, and contains a volume of 114.2 m<sup>3</sup>. The cable phototubes go out of the detector through stainless steel pipes (welded) that run along the Inner Veto wall.

mechanical simulation of the filling phase leads to an acceptable difference of 3%.

The Buffer vessel will be machined in several pieces by industry and transported to the neutrino laboratories. It consists of six half rings of stainless steel sheet, and two half bottom and top lids. All pieces will be pickled and passivated at the company. Half rings and lids will be initially welded beside the pit. The Buffer vessel structure will be erected by welding 3 rings of stainless steel sheets in the pit. Tubes for the inner photomultipliers cable paths will be welded afterward. Platform and dedicated tools will be developed and realized to facilitate the mounting as well as to guarantee a good cylindricity of the vessel. Special care will be required because part of the welding will be done after the installation of the Tivek sheets (See Section 3.5) and phototubes. Leakage of welds will be systematically checked through the sweating method. The Buffer vessel will then be cleaned with de-ionized water and weak nitric acid. Inside the Buffer we decided to keep the original stainless steel surface , providing a 40% reflectivity, as our baseline solution (see section 5).

At the Far detector site, the integration constraints are given by the size of the access tunnel: about 3.5 meters of diameter (4,3 m width and 4 m high), the height under the crane of 3.5 meters, the crane capacity of 5 tons. In addition, working space available in front and behind the pit is



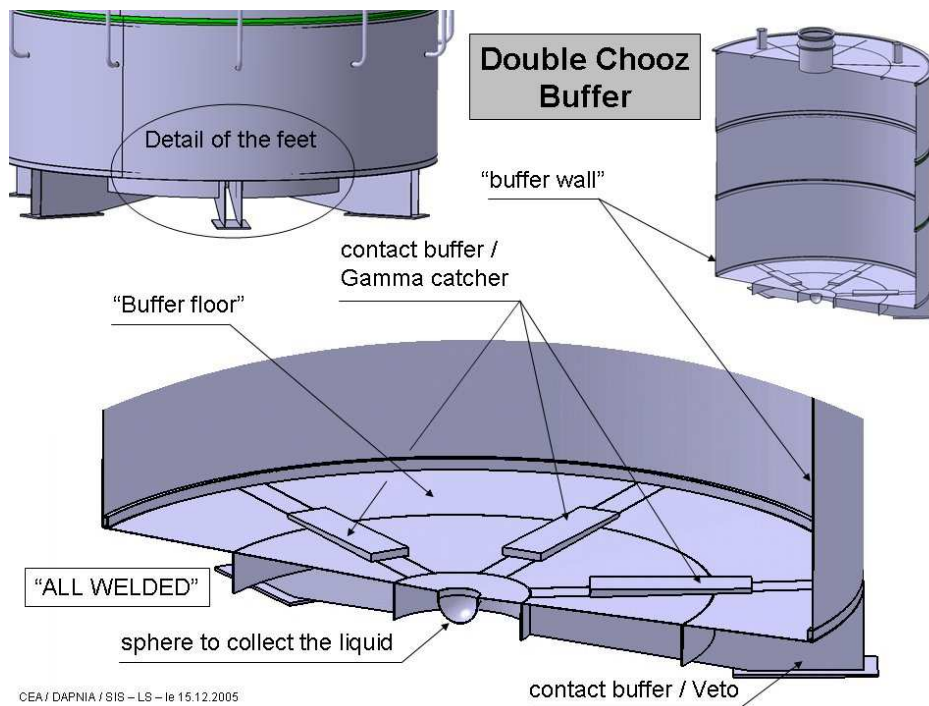


Figure 32: Details of the bottom lid of the Buffer vessel that is supported by six feet.

limited. At the Near detector site, we don't foresee more stringent space constraints.

### 3.4 PMT supporting structure

Each photomultiplier will have an independent mechanical support. As shown later (see section 5.1.4, and Figure 49, we are planning to use light weight mountings similar to the ones developed for the Mini-Boone experiment. Base material of these mechanical supports is stainless steel wire of 2.5 mm diameter (see Figure 33).

The inner face of the stainless steel buffer should be prepared to hold in place, in their assigned locations, the set of photomultipliers. The location will be defined by bar ribs, welded to the buffer vessel inner wall during the assembly process. The photomultiplier mechanical supports will be simply bolted to the ribs, and the photomultiplier location may be surveyed after mounting.

### 3.5 Inner Veto Mechanics

#### Materials and dimensions

The Inner Veto is contained in the cylindrical setup of the detector. In case of the far detector, this means that the dimensions of the Inner Veto have to be chosen to fit in the existing pit in the far laboratory. The veto consists of a steel tank directly inside of the steel shielding, creating a cylindrical shell surrounding the Buffer vessel. The Buffer vessel serves at the same time as support structure for the inner PMTs. Horizontally, the veto region is defined by inner dimensions of the steel cylinder next to the steel shielding and the outer dimensions of the Buffer vessel. The resulting radial veto thickness is 50 cm between Buffer and shielding.

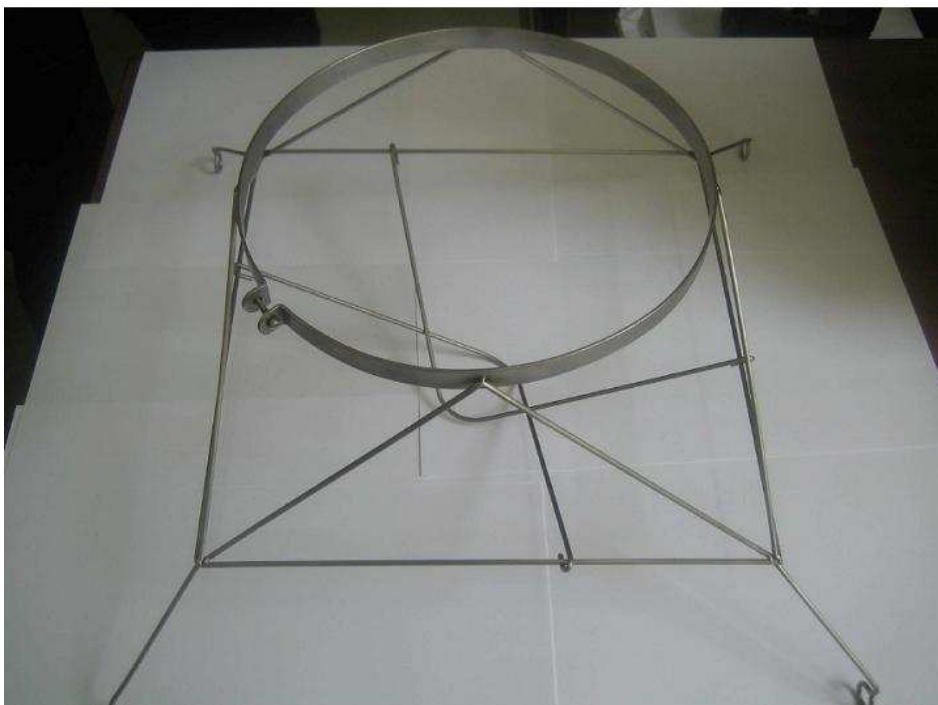


Figure 33: Mockup of the PMT supporting structure done at the CIEMAT.

A stainless steel support for the inner vessels consisting of six girders below the Buffer tank is mounted inside the veto which has an overall height of 50 cm in this region. Above the Buffer vessel, the gap between Buffer and lid is 60 cm. A central chimney with a radius of 15 cm is needed to allow access to the inner vessels at the top. Additionally, several pipes will cross the veto. These pipes are foreseen to feed the cables of the inner PMTs through the veto region up to the top lid of the Buffer. The pipes are attached to the Buffer vessel in the lower third of the vessel. Muons that propagate along one of the pipes are potentially critical, because they might not be detected unless secondary particles enter the scintillator. For this reason, care has to be taken not to allow a path along one of the pipes without at least a part crossing the scintillator liquid.

The remaining space will be filled with a medium light-yield liquid scintillator based on mineral oil. All welds of the steel tank, the Buffer vessel and the pipes for cabling will have to be conducted in an oil-tight manner. A pipe to the bottom of the veto is used for filling. The overall volume to be filled with liquid is approximately  $87 \text{ m}^3$  ( $90.5 \text{ m}^3$  minus PMT volumes).

### 3.6 Steel Shielding

The detector outer vessel will be a steel tank surrounding the Veto region, 500-600 mm away from the Buffer vessel. It is a cylinder of 6966 mm height, 6966 mm diameter (external dimensions), and 10 mm thick, weighing 20 tons. This tank will contain all other liquids in case of any internal mechanical failure. It will be closed by a top lid coupled with a nitrogen blanket system to prevent oxygen contamination of the liquids. Outside this vessel a 170 mm thick low activity steel shielding will protect the detector from the natural radioactivity of the rocks around the pit (see Figure 34). The thickness was determined by a full detector simulation of the accidental backgrounds from the rocks (see section 2.3.1).

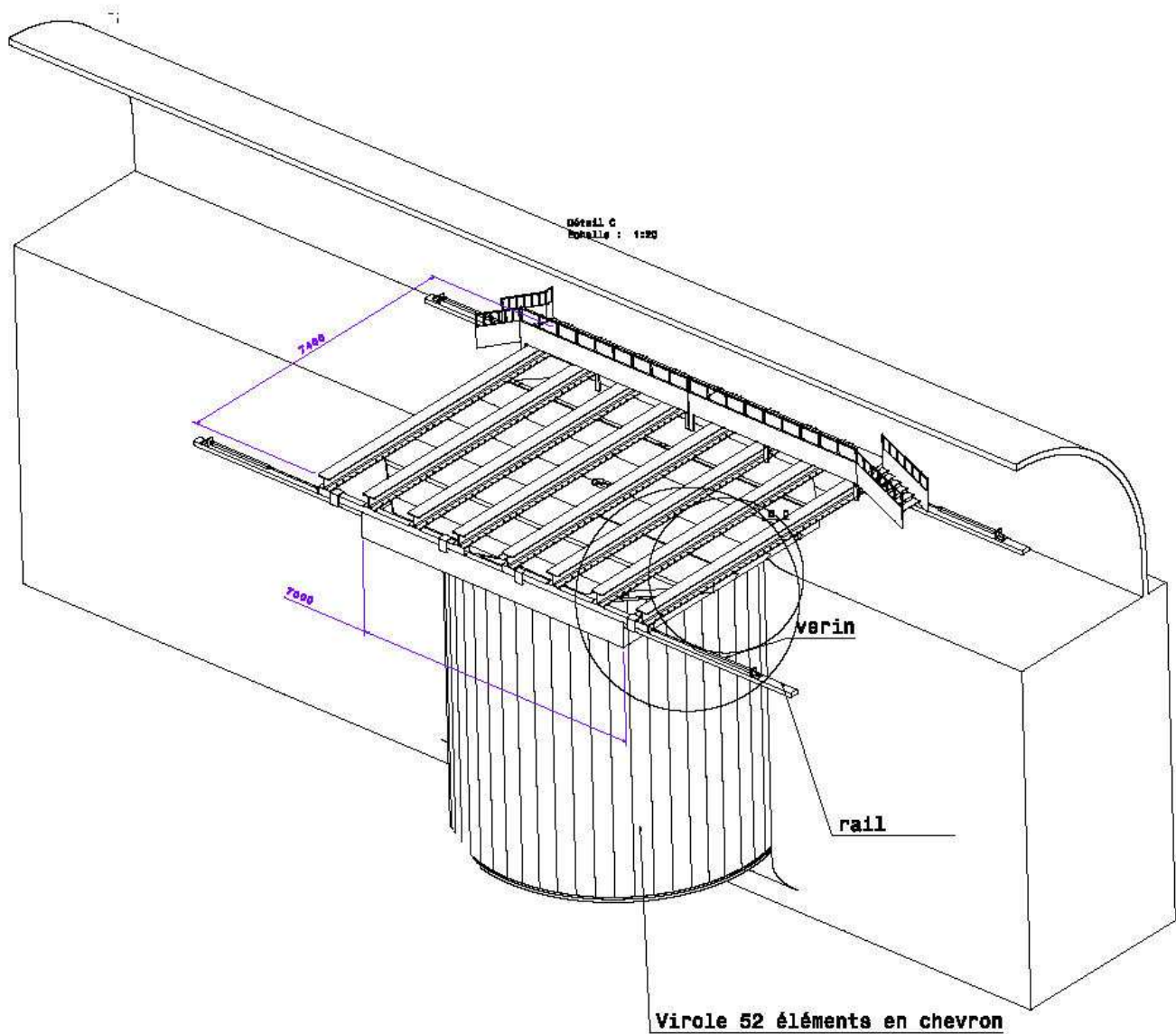


Figure 34: 3D overview of the Steel shielding. The top part of the steel shielding that opens in two halves to access the inner detector.

The shielding will be made of steel S235JRG2 (old French name: E24-2; American name: A283C). Taking into account the limited size of the access tunnel and the limitations of the crane (see Figures 25 and 26), the shielding will be made of 52 identical board-shaped pieces, plus 2 additional pieces to close the system. Each side piece is a bar of 7000 mm long, 400 mm wide and 170.2 mm thick (see Figure 34). The interface between neighboring pieces will be machined with a 60 degrees rafter shape (see Figure 35). This shape is very efficient to avoid gamma ray leaks through the shielding cracks between neighboring pieces. (The thickness "seen" by any gamma ray

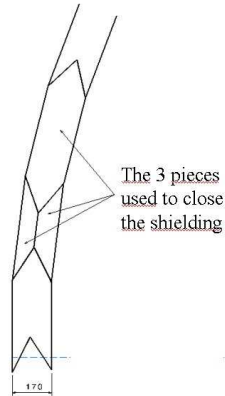


Figure 35: Shape of the shielding bars to prevent gamma ray leaks through air gaps.

is always more than 170 mm independent of the incident angle). The bottom part of the shielding will also be cut into pieces. The top shielding will be assembled in two halves. A rail moving system will allow it to move to the sides of the pit, and thus to access the inner detector (see Figure 34).

The 10 mm thick steel tank integration is also constrained by the limited space in the access tunnel at the far site. The bottom of the tank will be made of 3 parts and the cylindrical side will be cut in 8 to 12 elements. All weldings will be done in the neutrino laboratories. The top part of the side tank will couple to a flange to fit with the lid. The internal surface of the tank will be coated with a highly reflecting white paint (currently being tested in the 1/5 Double Chooz mock-up in Saclay). The cleaning procedure is currently being investigated (under test with the mock-up). A liquid recirculating system in the veto will be needed to have a good temperature homogeneity in the inner detector. The temperature difference between both detectors will be kept within 3 degrees. The top lid will be made of a permanently installed part housing PMTs cables feed through, and a central movable cylindrical part. The lid inner surface will be painted with the same reflecting paint, whereas the external surface will be coated with an epoxy protecting paint. The lid will be fixed on the tank flange, and its tightness provided by a Teflon gasket. It will be equipped of 3 or 5 flanges (1 at the center and one on each side to access  $\gamma$ -catcher and Buffer). These flanges will be located on the closing line between the two shielding halves. The near detector will be very similar to the far one. The differences would be in the shielding (replacing iron by sand is under study) and in the elementary pieces definition (the handling constraints will be different).

### 3.7 Simulation of the detector geometry

At present, the geometry of each detector assembly implemented in DCGLG4sim is a slightly simplified version of the envisaged final detector geometry. Work is underway to further improve

Table 19: Geometrical parameters of the simulated inner detector. All units in mm

Region	Radius (mm)	Height (mm)	Thickness (mm)	Vert. translation (mm)	Comment
Pit	3475	7000	0	0	Already existing
Shielding	3475	7200	0	+ 100	Top 200 mm above pit level
Veto	3265	6780	10	0	200 mm shielding + 10 mm tank
Veto chimney	155	500			Same thickness as Veto
Buffer	2758	5674	3	-50	100 mm thicker veto on top
Buffer chimney	150	1000			Same thickness as Buffer
$\gamma$ -catcher	1720	3574	12	0	Vessel acts as buffer extension
$\gamma$ -catcher chimney	113	1992			Same thickness as $\gamma$ -catcher
Target	1150	2458	8	0	Fiducial volume = 10.0 m <sup>3</sup>
Target chimney	75	2550			Same thickness as target

the realism of the simulation. All sub-volumes of the inner detector are perfect coaxial cylinders located inside a pit, also cylindrical. The latter is the only already existing part of the assembly, hence its dimension are an important constraint. Table 19 summarizes the implemented geometry.

Some detector dimensions have slightly changed in the optimization process, but it does not change the results presented. A total of 534 PMTs are arranged in 12 rings of 30 PMTs on the lateral surface of the buffer tank, and in 5 rings of 30, 24, 18, 12 and 3 on the top and bottom caps. The geometry of each PMT is accurately described within GLG4sim through the *GLG4TorusStack* class, which allows the definition of any generic shape (see Figure 36 for an example).

The PMTs can be tilted at any angle, e.g. pointing toward the center of the target (this configuration is preferred, as it assures the best light output), or normal to the Buffer tank. Number and distribution of the PMTs are not yet locked up for the design of the final detector and the simulation will provide useful comparative data as regards this issue.

The detector layout as implemented in DCGLG4sim is shown in Figure 37. As can be seen from the figure, the Monte Carlo representation of the detector is already quite elaborate and faithful, including up to a simplified schema of the chimney, described as a system of coaxial cylinders -each one associated with each of the detector sub-volumes and laid on top of it- with identical properties to the parent volume.

DCGLG4sim is conceived in such a way to retrieve all input parameters of the geometry from external data-base files. This allows to readily change the dimensions of detector sub-units and test the impact on the performance.

### 3.8 Simulation of the detector materials

The volumes displayed in Figure 37 are filled with materials whose properties are already very close to those of the final detector. The rock around the tunnel is defined as SiO<sub>2</sub>, with density  $\rho = 2.7 \text{ g/cm}^3$ . The shielding material and as well the Buffer tank are implemented as stainless steel, with  $\rho = 7.87 \text{ g/cm}^3$  and elemental composition by mass: 71 % Fe, 19 % Cr, 10 % Ni. The  $\gamma$ -catcher and target vessels are made of acrylics  $\rho = 1.14 \text{ g/l}$ , a polymer whose basic monomer is

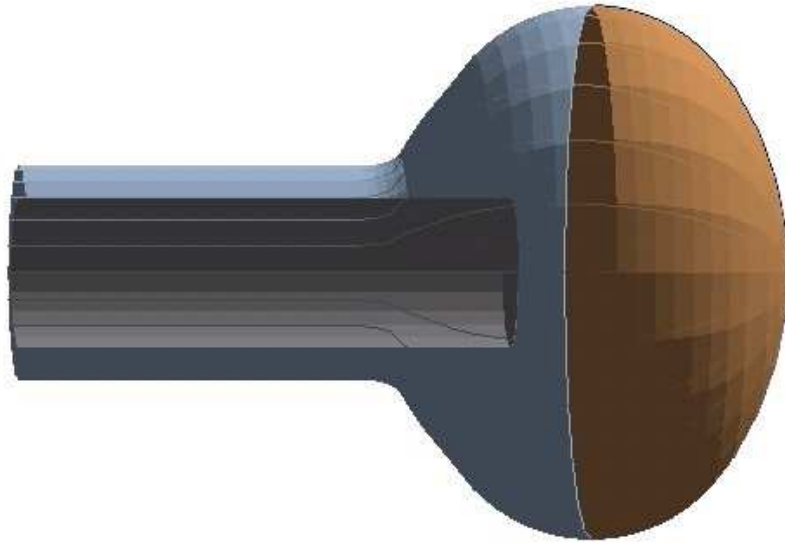


Figure 36: Generic 8" PMT implemented in DCGLG4sim. The shape can be controlled by the user by appropriate choice of the relevant geometrical parameters.

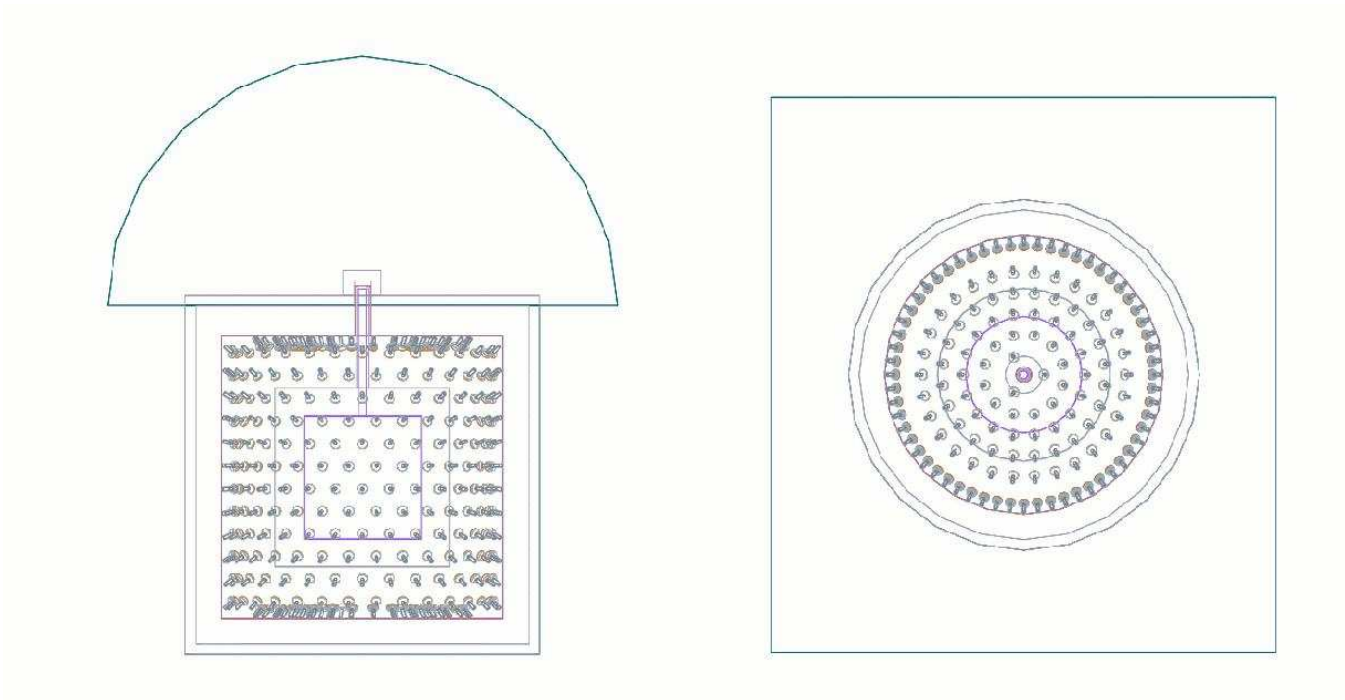


Figure 37: Side and top view of the Double Chooz detector layout as simulated with GEANT4.

Table 20: Typical composition of the Double Chooz liquids implemented in the Monte Carlo.  $C_{12}H_{24}$  stands for Dodecane, and  $C_{16}H_{18}$  stands for PXE.

	Aromatic	Oil	Fluor	WLS	Gd-Compound	Density
Target	$C_{16}H_{18}$ (20 %)	$C_{12}H_{24}$ (80 %)	PPO (6 g/l)	bis-MSB (50 mg/l)	Gd-dpm (1 g/l)	0.800
$\gamma$ -catcher	$C_{16}H_{18}$ (20 %)	$C_{12}H_{24}$ (80 %)	PPO (3 g/l)	bis-MSB (50 mg/l)	/	0.798
Buffer	/	Mineral Oil	/	/	/	0.820
Veto	/	Mineral Oil	PPO (6 g/l)	bis-MSB (10 mg/l)	/	0.821

$[-CH_2 - CH_3 - COOCH_3 - C-]$ .

The four different liquids filling respectively the Target,  $\gamma$ -catcher, Buffer and Veto volumes have been implemented as mixtures of basic components. GEANT4 does not keep track of the molecular composition of materials defined as mixtures, as only the atomic abundances of the final mix are believed to be of relevance. However, since most of the properties of the resulting liquids do depend on the molecular species present in their formulation, and their concentration, we have introduced a sort of chemical approach to their definition, where global variables store the complete information about the liquid composition. This allows at the same time to keep all the detector liquids flexible and user-configured, and to calculate at run-time the optical properties of the detector. A micro-physical approach is implemented, based on the known/measured properties of the basic components and the underlying optical model of the system (see section 4.7.4). A comprehensive set of primary materials has been defined, which are classified as *aromatics* (PXE, PC, ...), *oils* (dodecane, mineral oil, ...), *fluors* (PPO, BPO, ...), *wavelength-shifters* (bis-MSB, ...), and *Gd-Compounds* (Gd-dpm, Gd-acac, Gd-carboxylates). The Monte Carlo user is free to build a detector with any combination of the above ingredients, by specifying content and respective concentrations. The densities are calculated accordingly, as well as the resulting optical properties. In Table 20 the typical liquids simulated are reported. Minor modifications are expected with respect to the final design of Double Chooz.

### 3.9 Outer Veto

Due to the shallow depth at the near detector, a high rate of muons is expected. Since the primary background signal for this measurement will be initiated by cosmic muons, an additional outer veto system is required. This will be used to help identify muons which could cause neutrons or other cosmogenic backgrounds and allow them to be eliminated from the data set. In some sense, the outer veto provides redundancy for the inner veto in tagging background associated coincidences, but such a redundancy is crucial to making a confident measurement of the background. Comparison of a single measurement with a full simulation would not provide such confidence because the cross sections for muon spallation products are not accurately measured. In addition, the outer veto will provide three other benefits: 1) it will achieve a tracking resolution not possible with the inner veto alone, allowing the differentiation between a muon which passed through the target and one which merely passed near the target, 2) it will well measure those muons which only clip the corners of the inner veto. Such muons are especially dangerous because the inner veto efficiency will be low for these. 3) It will provide sufficient granularity to detect high multiplicities that would allow

identification of high-energy showering muons. Evidence from KamLAND suggests that such muons have a high-likelihood of creating the long-lived radioactive isotopes such as  ${}^9\text{Li}$  or  ${}^8\text{He}$ . The overall goal is to provide a system with greater than 99% efficiency that covers sufficient area to reduce the untagged flux of neutrons to less than 0.005 Hz. Reduction to this level should ensure that the correlated background rate is well below 1% of the signal.

## Module Design

The Outer Veto system design is based on the use of individual modules of gas filled long-tube wire proportional chambers. Each chamber will be constructed from 2-inch diameter aluminum tubes with gas tight PVC end plugs which also serve to hold a tensioned gold-tungsten wire which is strung down the length of the tube. The modules will be constructed in a 8 wide by 3 deep close-packed configuration. A gas system will provide a low rate continuous flow of  $\text{Ar}/\text{CO}_2$ . Electronic connection to the module will be made via two threaded brass posts for each individual chamber (tube): one in contact with the crimped wire and the other providing the return current connection to the outer tube.

## Implementation at Near and Far Detectors

The modules mentioned above will be assembled into square, flat panels by placing modules side-by-side and then placing two of these groups together orthogonally. At the near detector laboratory, the limited overburden will require a significant coverage to eliminate all angles of incoming muons. As a result, the intended design will use panels made up of 13 side-by-side 5.3 meter long modules. This will create a panel unit that is a 5.3 m square. The top of the detector will be covered by 4 of the 5.3 m square panels. Six more of these panels will be placed vertically in a hexagon around the side of the detector. The minimum radius of the hexagon will be 4.5 meters. Since the outer wall of the inner veto system will be at 3.4 meters radius, this allows approximately 1 meter of passive neutron absorber (foreseen to be low radioactivity sand) to be inserted between them.

At the far detector, geometric constraints of the already existing laboratory will not allow a similar design for the outer veto to be installed. However, the greater overburden reduces the rate of high angle muons to below our need for identification. As a result, a similar quality of rejection can be achieved by constructing two 6.8m square panels which will cover only the top of the main detector. These panels will be constructed by using 17 side-by-side 6.8 meter long modules.

## 3.10 Radiopurity Assessment

The CHOOZ detector had a background singles rate of around 130 Hz, which became 65 Hz above 1.3 MeV after all data cuts. Coupled with a “neutrino-like” event rate of 45 Hz, this meant that about 30% of their correlated background was due to random coincidences. We wish to improve upon that number for Double Chooz, even though we have a larger detector by a factor of two. To this end, we have designed a shielding plan that improves on the singles rate in the target by more than an order of magnitude while using the same size detector cavity. A calculation of the singles rates in CHOOZ and Double Chooz is shown in Figure 38. This plot is based on a simple analytical model designed to calculate the rate of single gamma hits for detectors with complex multi-layer geometries. Several approximations are made for this estimate:



	Th, ppb	U, ppb	K-40, ppb
Target	0.000001	0.000001	0.000001
Acrylic	0.01	0.01	0.01
PMT	26	28	10
Catcher	0.000001	0.000001	0.000001
Buffer	0.000001	0.000001	0.000001
Veto	0.000001	0.000001	0.000001
Steel	3.3	2.3	0.54
Rock	5000	2000	1638

Table 21: Assumptions for calculation of singles rates.

- To simplify only 1 MeV monoenergetic gammas are simulated. This simple simulation assumed 1 MeV gamma rays since these have the lowest attenuation coefficient. Thus the results represent an upper bound on the number of gamma rays that reach the inner layers of the detector. Furthermore, the mass attenuation coefficients vary slowly in this energy region, meaning that the results will not be much different for higher energy gamma rays of concern, e.g. 2.6 MeV.
- Gamma production in materials is proportional to concentrations of uranium, thorium and potassium.
- Coefficients of proportionality were taken from measurements of gamma production from PMT glasses with various levels of radioactivity.

The attenuation coefficients were checked by modeling the KamLAND detector, where single rates are known very well. This analytical model allows us to see the effects of the shield design interactively, such that coarse optimization can be done rapidly and adjusted later by detailed GEANT simulations. Radioactive contaminants used for this model are given in Table 21. They are typical values and not difficult to achieve with reasonable care. Figure 38 shows the activity per unit volume starting from the rock for both CHOOZ and Double Chooz. The largest difference comes from replacing the sand with a steel shield, which drops the activity rate considerably. Note that the PMTs have also been moved back from the target. In the end, the predicted activity per unit volume is much lower than CHOOZ, almost two orders of magnitude at 1 MeV.

### Activity of Materials

A survey of the literature has been done to get an idea of the radiopurity levels available in the materials used in Double Chooz. Representative values for each material are presented in Table 22 (Note: measured PMT activity is discussed in the photodetection section). These data do not represent the total survey sample, but are included to show what variations have been seen. Cobalt-60 is also a radioactive component of the stainless steels. The constraint for the Double Chooz Buffer vessel is about 15 mBq/kg.

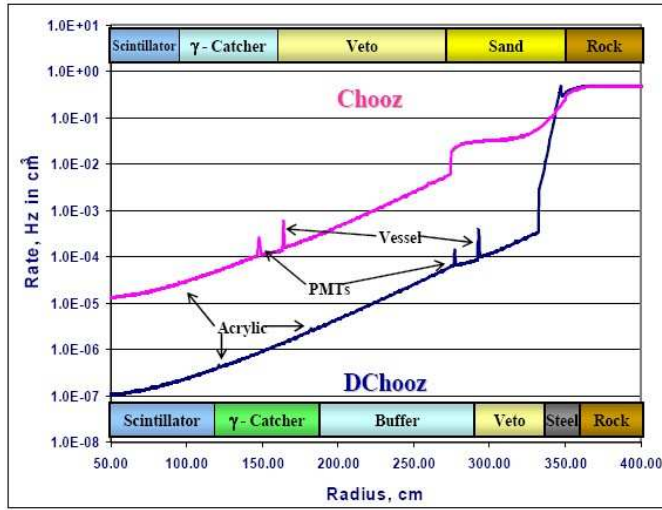


Figure 38: Comparison of the predicted singles rates in CHOOZ and Double Chooz. The figure illustrate a simple model where both CHOOZ and Double Chooz are considered to be spherical instead of Cylindrical. The single rate comes only from gamma, which flux is analytically computed according to radiopurity concentration of the different region and materials. The main differences between CHOOZ and Double Chooz arise with the addition of a non scintillating Buffer close to the PMTS, and the replacement of 70 cm of sand by 17 cm of steel to shield the detector from external gammas.

U(ppb)	Th(ppb)	K(ppm)	source
Steel			
0.7	0.7	1.7	KamLAND
0.3	0.7	0.85	KamLAND
5.0	14.	10.	SNO
Acrylic			
0.008	0.05	0.07	KamLAND
0.004	0.008		SNO
0.001	0.001	0.00012	Chooz
Chooz Rock			
14000.	5000.	2000.	Chooz

Table 22: Typical activities of various materials from a literature search.

component	High		Low	
	> 0.5 MeV	> 1.0 MeV	> 0.5 MeV	> 1.0 MeV
PMT	5.0	2.9	2.1	1.2
target tank	0.11	0.085	0.0034	0.0029
GC tank	0.17	0.12	0.0062	0.0037
buffer tank	1.8	0.93	0.67	0.25
veto and shield	1.7	1.0	0.11	0.063
Chooz rock	1.4	0.86	1.4	0.86
total	10.	5.9	4.3	2.4

Table 23: Expected rate (Hz) of single gammas above 0.5 and 1.0 MeV striking the scintillator. These results are based on a GEANT3 simulation using the material activities given above, with high and low indicating the activity value used for the simulation

### Check with a Detailed MC

GEANT3 and GEANT4 based simulations have been built for estimating the expected singles rate spectrum for the activities shown in Table 22. In addition, an event generator has been written that includes all the known gamma lines from 40-K, 208-Tl, and 214-Bi decay. These are the major radioactive species that could produce events above our threshold of around 0.7 MeV. Table 22 shows the activity expected from various detector components. The “high” and “low” designations refer to the highest and lowest radiopurities found in the literature, which gives an idea of the spread of possible values.

Thus we expect the background rate in Double Chooz at 1 MeV to be a factor of roughly twenty less than Chooz at 1.3 MeV. Assuming a neutron-like event rate of 90 per hour (based on the Chooz experience), an average value for the internal activity, and a 100  $\mu$ s coincidence window, this translates into a random coincidence rate of about one per day at Double Chooz Far.

### Radiopurity Monitoring

To ensure that the ambitious sensitivity goal of the Double Chooz experiment is attained, great care must be taken to keep the background trigger rate at or below the design level of a few Hz. This in turn requires that great care be taken in material selection, so that the intrinsic radioactivity of detector components does not produce too high a background rate. We will undertake a comprehensive radioactivity survey of the materials that will be used in the Double Chooz antineutrino detectors to ensure that all components will meet or exceed the required level of radiopurity. This survey will also prove useful to other types of highly sensitive experiments, including those searching for neutrino-less double beta decay and dark matter candidates. Activity measurements will be made at the Oroville Low Background Counting Facility. This facility, operated by Lawrence Berkeley National Lab, is located in the powerhouse of the Oroville Dam in Northern California, under 180 m of rock cover ( 600 m.w.e.). It has three Ge spectrometers: a 115% n-type, an 80% p-type, and a 30% p-type. Sensitivities of 50 parts-per trillion (PPT) for U and daughters, 200 PPT for Th and daughters, and 100 parts-per-billion for K are realized at the Oroville site. Others measurements are being done in the Heidelberg (MPIK) low background counting facility, as well as

in the very low background Gran Sasso Germanium detectors (scintillator and other liquid components, acrylics, . . .). The French underground laboratory of Modane is also providing access to its low background counting facility (Germanium detectors) for measurements of the inner materials of the detector, such as the acrylics and the stainless steel.

Sandia National Laboratories will manage this survey, collecting the results from the various groups building detector components, coordinating counting with LBNL, and analyzing and summarizing the results. All materials to be used in the Double Chooz will have to be validated in this way before being built into the detectors.

## 4 Scintillator, Fluid Handling and Purification

### 4.1 Detector liquids and fluid handling

In the Double Chooz detector design there are three separated volumes filled with liquids inside the stainless steel buffer tank. The inner volume is the  $\bar{\nu}_e$ -target and it will contain 10.3 m<sup>3</sup> liquid scintillator loaded with gadolinium (Gd-LS) at a concentration of approximately 1 g/ $\ell$ . The acrylic vessel holding the target volume is surrounded by the  $\gamma$ -catcher with a volume of 21.5 m<sup>3</sup>. This volume is filled with a Gd-free scintillator. Finally, there is a volume of about 100 m<sup>3</sup> outside the  $\gamma$ -catcher containing a non-scintillating buffer liquid. At the inner wall of this volume the PMTs will be mounted. The densities of the liquids should be similar in all of the three volumes in order to avoid strong buoyancy forces in the detector.

It is foreseen to do the purification and the mixing of the liquid scintillators off-site, both for the target region and as well as for the  $\gamma$ -catcher. The scintillators will then be shipped to the Chooz site in transport tanks. On-site the tanks will be hooked up to dedicated filling systems. All three volumes have to be filled simultaneously.

Material compatibility tests were made and will be made especially for the Gd-LS. All materials in contact with the Gd-LS in the detector or the liquid handling systems have to be checked thoroughly. To test the material compatibility with acrylic a mock up of the Double Chooz detectors was built (1/5 th scale). The inner volume of this mock up contains about 110  $\ell$  of Gd-LS (we did not tested the final scintillator recipe which was not yet available on the 100 liter scale). Smaller acrylic vessels with a capacity of approximately 30  $\ell$  are also available for long-term stability and material compatibility testing.

### 4.2 Target

Double Chooz will use a Gd-loaded liquid scintillator with 1 g/ $\ell$  Gd-loading, as already pointed out. The Gd-scintillator for both detectors should be produced together as “single batch” to assure identical proton per volume concentrations in both detectors, and to assure that if there are any aging effects, they are more likely to be the same. As scintillator solvent it is planned to use a PXE (phenyl-xylylethane)/dodecane mixture at a volume ratio of 20:80. The admixture of the dodecane reduces the light yield, but it improves the chemical compatibility with the acrylic and increases the number of free protons in the target. Besides technical requirements the solvent mixture was selected due to safety considerations. In particular, both components have high flash points (PXE: fp 145°C, dodecane: fp 74°C). The scintillation yield of the unloaded PXE based scintillator was measured as a function of dodecane concentration. A scintillation yield of 78% with respect to pure PXE is observed at a volume fraction of 80% dodecane. Pure phenyldodecane or pseudocumene based mixtures could be used as scintillator solvent as alternatives to the PXE/dodecane mixture.

Metal loading of liquid scintillators have been comprehensively studied at MPIK and LNGS/INR for several years. Research with gadolinium loaded scintillators in both institutes indicates that suitable scintillators can be produced. Two scintillator formulations have been investigated, one based on carboxylic acids and the other on Gd- $\beta$ -diketonates. Both systems show good performance and are viable candidate liquid scintillators for the  $\bar{\nu}_e$ -target.

## Beta-diketonate (BDK) Gd-LS:

The studies of the synthesis and properties of beta-diketonates of rare elements and their relevant chemistry, especially stability at high temperatures, is illustrated in References [70, 71]. First results of Gd-beta-diketonate loaded liquid scintillators have been reported in Reference [72]. Promising results were already achieved with the simplest beta-diketone molecule, acetylacetone (Hacac) that was also used to produce a highly In-loaded scintillator (5% wt. In) in the framework of the LENS (Low Energy Solar Neutrino Spectroscopy) R&D phase. With  $\text{Gd}(\text{acac})_3$  dissolved in PXE high light yields and reasonable attenuation lengths were achieved at a Gd-loading of 1 g/ $\ell$ . A Gd-loaded solution in pure PXE was produced and successfully tested for stability for more than 18 months.

However,  $\text{Gd}(\text{acac})_3$  does not dissolve at the required concentration in the preferred solvent for Double Chooz (PXE/dodecane at a ratio of 20/80) or in PC based solvents, therefore other beta-diketone molecules were tested. The best choice seems to be dipivaloylmethane (Hdpm). The  $\text{Gd}(\text{dpm})_3$  molecule is known to be more stable than the  $\text{Gd}(\text{acac})_3$  and can be purified by sublimation.

The observed light yield for the Gd-BDK system corresponds to approximately 80% of the unloaded scintillator mixture at a Gd-loading of 1 g/ $\ell$ . As primary and secondary fluor PPO (6 g/ $\ell$ ) and bis-MSB (approximately 20 mg/ $\ell$ ) were used in these tests. The achieved light yields are regarded to be sufficient for the requirements of the Double Chooz experiment. Improvements concerning the light yields appear to be possible by optimization of the fluor choice and concentration. Attenuation lengths of more than 10 m were measured for  $\text{Gd}(\text{dpm})_3$  solutions around 430 nm, the region of the largest scintillator emission, at the required Gd-concentration of 1 g/ $\ell$ . Long-term stability tests with  $\text{Gd}(\text{dpm})_3$  based scintillators gave promising results over several months. No significant degradation was observed at room temperature for the time period of the measurement of more than ten months.

About 500 g of  $\text{Gd}(\text{dpm})_3$  corresponding to more than 100 g of Gd were produced at MPIK in an optimized synthesis. This batch will be utilized to do long-term stability and material compatibility tests of the full scintillator mixture on the 100  $\ell$  scale.

## Carboxylate (CBX) Gd-LS:

The chemical preparation of Gd loaded carboxylic acid based scintillators (single acid, pH controlled) has been established and demonstrated to be sound [73, 74, 75, 76]. The Gd scintillator can be synthesized by adding a crystalline material or by a solvent extraction technique in a two phase system. Proper control of pH during the synthesis is crucial.

A variety of Gd-CBX scintillators have been produced, varying the Carbon number of the acid and using several solvent mixtures. The Gd-CBX systems have excellent optical properties. The light yields are above 80% compared to the unloaded scintillator version and attenuation lengths of about 10 m at 430 nm in the full scintillator mixture were achieved. Figure 39 shows the attenuation length of a Gd-CBX solution before the addition of fluors. The fluor absorption is not as critical as the absorbency of the other components since the light can be re-emitted at higher wavelengths and is therefore not necessarily lost. Along with the attenuation length the scintillator emission is plotted in the same figure. It is essentially the emission spectrum of the secondary wavelength shifter bis-MSB. The spectrum was measured in a triangular cell using a geometry that includes short distance self-absorption and reemission of photons.

Long-term stability tests at room temperature and at elevated temperatures of various CBX-

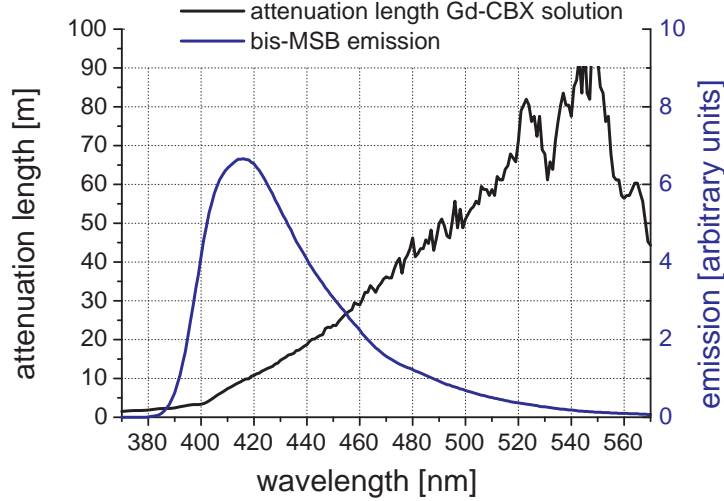


Figure 39: *The plot shows the wavelength dependence of the attenuation length of a Gd-carboxylate scintillator (1 g/l Gd) without wavelength shifters along with the emission spectrum of scintillator containing bis-MSB as secondary wavelength shifter.*

versions were performed for test periods of several months up to close to two years. Some degradation in the attenuation length was observed for the CBX-versions without any additives on time-scales of a few months and more. The changes were observed in the far UV moving into the optical regime. Several ingredients (stabilizers) are under investigation to prevent polymerization and oxidation in the scintillator (both can affect the attenuation length of the scintillator) and promising results were achieved using organophosphorous compounds. The choice of stabilizers will be optimized by additional long-term stability tests of concentrated CBX-solutions ( $> 10 \text{ g/l Gd}$ ) with different additives.

The final scintillator can be tested in a 1/5 th scale mock up of the Double Chooz detector. More than 100  $\ell$  of Gd-CBX-scintillator were already produced at MPIK and filled into the acrylic inner vessel of this detector mock up. Periodic tests of its optical properties will be performed. The general purpose of this mock up is to find technical solutions for the construction and integration of the detectors. In particular, the material compatibility of the scintillator with the acrylic as well as filling procedures of the detector are tested. Furthermore purification methods can be tested with this setup. Another Gd-CBX-scintillator version was produced by LNGS/INR people and is exposed to the same acrylic as in the mock up in a 30  $\ell$  vessel.

### 4.3 Gamma-Catcher

The 21.5  $\text{m}^3$  volume of the  $\gamma$ -catcher will also be filled with a liquid scintillator, but without Gd-loading. Its purpose is to detect gamma rays resulting from prompt positrons and gammas from delayed neutron capture from neutrino interactions in the target volume that escape. This scintillator is also enclosed in an acrylic vessel. Similar requirements as for the target liquid concerning material compatibility, density and optical properties have to be applied.

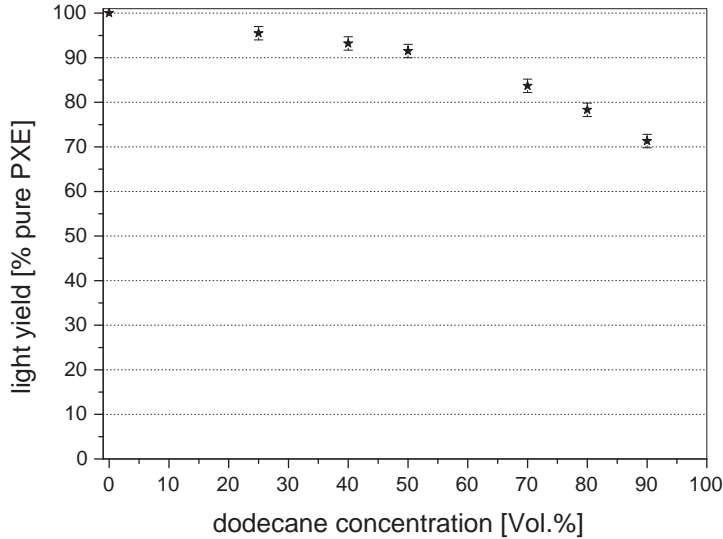


Figure 40: *Scintillation light yield of PXE/dodecane mixture with varying dodecane concentration. The PPO concentration is kept constant at 6 g/l.*

The  $\gamma$ -catcher scintillator has to match the density of the target scintillator which is about 0.80 within 1%. Since the Gd-loading does not affect the density of the liquid significantly the same PXE/dodecane ratio in the  $\gamma$ -catcher as in the target would fulfill the density requirements.

Furthermore, the light yield of the  $\gamma$ -catcher scintillator should be similar to the light yield of the Gd-scintillator. There is some quenching in the Gd-scintillator compared to the unloaded version and the light yield of the  $\gamma$ -catcher scintillator would therefore be 10 – 20% higher in the target. One option to adjust the light yield is to lower the aromatic fraction in the  $\gamma$ -catcher. The dependence of the light yield on the PXE-concentration is shown in Figure 40. On the other hand a change in the PXE/dodecane ratio implies a change in the density of the scintillator. This effect can be adjusted by replacing part of the dodecane by mineral oil having a higher density. The attenuation length in the  $\gamma$ -catcher for the wavelength region of interest is comparable or higher than in the target and the stability of the optical properties is not viewed as a problem, since this scintillator has no metal loading.

The  $\gamma$ -catcher volume of the mock up was filled with about 200  $\ell$  of liquid scintillator. In this test a composition was chosen to match the density and at the same time the light yield between the inner two volumes. The scintillator contains 10% PXE, 30% mineral oil and 60% dodecane. As in the target a PPO/bis-MSB combination was chosen to shift the light into the near UV and optical regions.

#### 4.4 Buffer

For the buffer volume each detector needs about 100 m<sup>3</sup> of non-scintillating liquid. This volume should shield the active volume from gamma rays emitted e.g. by the photomultipliers. Since there is a thin acrylic vessel between the  $\gamma$ -catcher and the buffer this liquid has to match the



density of the scintillators. Additional requirements are material compatibility with acrylic and the photomultipliers and high transparency in the wavelength region of the scintillator emission.

It is foreseen to use pure mineral oil in this region. The density of the mineral oil used in the mock up is slightly too high for the demands of the Double Chooz detector. Therefore optical pure mineral oil with lower density has to be found or the mineral oil has to be mixed with dodecane (density 0.749).

## 4.5 Fluid handling and purification

There will be a scintillator fluid system on-site at the reactor area and off-site at German institutes. All the mixing and purification of the liquids will be done off-site. On-site there will be the filling systems and it is foreseen to have enough storage area for all detector liquids. All three inner volumes and maybe the muon inner veto as well have to be filled simultaneously.

It is planned to purify and mix the target scintillator at MPIK Heidelberg. The liquid handling system for the target scintillator has to be made exclusively out of “Teflon” like material. A prototype system was already designed and built for the loading of the mock up. It can be used for the loading, unloading, filtering, mixing, storage and nitrogen purging of liquids. Additionally, a column for purification of organic liquids can be attached to the system. After the Gd-scintillator preparation off-site it will be transported in dedicated tanks to the Chooz site. The procedure for the  $\gamma$ -catcher will be similar. The volume of the  $\gamma$ -catcher fits into one typical ISO-container.

On-site there will be filling systems and storage tanks. The buffer liquid will be stored above ground in about four connected steel tanks per detector. It would be advantageous to have the ability to circulate and mix the target liquids in the detectors to assure that the optical and chemical properties are identical.

## 4.6 Material compatibility

All three inner volumes, target,  $\gamma$ -catcher and buffer are in contact with acrylic vessels, therefore the material compatibility of the respective liquids with the acrylic used in the experiment is crucial. The compatibility of several PXE/dodecane mixtures and of both Gd-scintillator versions with acrylic was tested at the company Roehm in Germany and in Saclay. These measurements confirmed the improving compatibility with increasing dodecane concentrations. The PXE/dodecane ratio of 20:80 by volume mentioned above seems to be the best compromise providing sufficient material compatibility and scintillator light yield. The PXE concentration in the target scintillator could be lowered to about 15% to improve the safety margin, since the overall loss of light would not only be a few percent (light output decreases, but transparency of oil is better than that of PXE). No significant difference concerning compatibility with acrylic was observed between the Gd-BDK-scintillator and the Gd-CBX-scintillator.

There are also other materials in contact with the scintillators during the measurement (calibration system), handling and purification. Steel surfaces should be avoided for the target scintillator, especially if the Gd-CBX-scintillator would be used. This system is expected to be surface reactive in contact with steel and the stability of the scintillator could be affected. In the production and synthesis of the 110  $\ell$  of Gd-CBX scintillator for the mock up only PFA, PTFE, PP, PE and glass was used. Only such materials should be used for the final Double Chooz systems as well.

## 4.7 Scintillator stability

During the first Chooz experiment, the Gd-loaded scintillator used in the  $\nu$ -target showed a fast and unexpected degradation of its transparency, which has been ascribed to the oxidation by nitrate ions[5]. In Double Chooz the long-term stability of the target scintillator is of fundamental importance, either to assure a sufficiently long running time (several years), and to avoid systematics due to a possible different evolution of the liquids in the two detectors.

The Heidelberg and Gran Sasso groups of the Double Chooz collaboration have been producing Gd-loaded scintillator since 2003. A large number of samples have undergone extensive monitoring of their chemical stability, in the laboratories, where these scintillators have been synthesized, and especially at Saclay.

Most of the first R&D samples have shown some worsening of their optical clarity within time-scales of several months. These failures have motivated a careful study of the underlying chemistry. In particular, the key role of several factors have been recognized: the presence of free water in the final scintillator, initial impurities in the base solvent (PXE), and the possible polymerizations of the Gd-complex molecules. A successful R&D on these items has resulted in the production of a second generation of Gd-loaded scintillators of remarkably improved optical properties and chemical stability.

During December 2005 the technological 1/5 Double Chooz mock-up has been filled with  $\sim 110$   $\ell$  of Gd-loaded scintillator (Gd concentration = 1 g/ $\ell$ ), and  $\sim 200$   $\ell$  of unloaded scintillator for the  $\gamma$ -catcher. Another  $\sim 30$   $\ell$  Gd-loaded scintillator sample is being tested in a special tank, made of the same acrylic selected for the mock-up. Furthermore, a third formulation is going to be tested by the same procedure. The optical monitoring of all these liquids will assess the long term stability of the Double Chooz scintillators under experimental conditions that are as close as possible to those of the full scale experiment. These tests are therefore intended as a final validation of the Double Chooz R&D on scintillators.

### 4.7.1 Methods

The long-term stability of the scintillators developed for Double Chooz has been investigated by means of spectro-photometric techniques. The transmission of a collimated light beam through 10 cm of material is routinely measured with a spectro-photometer. We are thus sensitive to any chemical evolution of the scintillator leading to an increase in the absorbency, i.e. to an optical degradation.

For any “fresh” scintillator sample, a 10 cm quartz cell is filled ( $V \sim 100$  ml) and the liquid is flushed with  $N_2$  for 15' in order to purge oxygen, which is a potential danger as regards the chemical stability of the scintillator. The cell is hermetically sealed through air-tight stoppers and stored in darkness at room temperature. The transmission  $T$  in the wavelength range  $300 \text{ nm} < \lambda < 800 \text{ nm}$  is routinely measured, approximately once a month. Since pure quartz shows very low absorption in the optical wavelengths of interest (the emission of the secondary fluor is centered around 400-500 nm), we usually reference our instrument to the transmission  $T$  of the beam in air, defined as  $T = 100\%$ .

The above spectro-photometric measurement can be used not only to monitor the relative changes of the transmission of a sample, but also to determine the absolute, wavelength-dependent attenuation length. For the latter case, the effect of the light losses due to reflections at the air-quartz-liquid and liquid-quartz-air interfaces must be corrected. This is done by self-referencing the

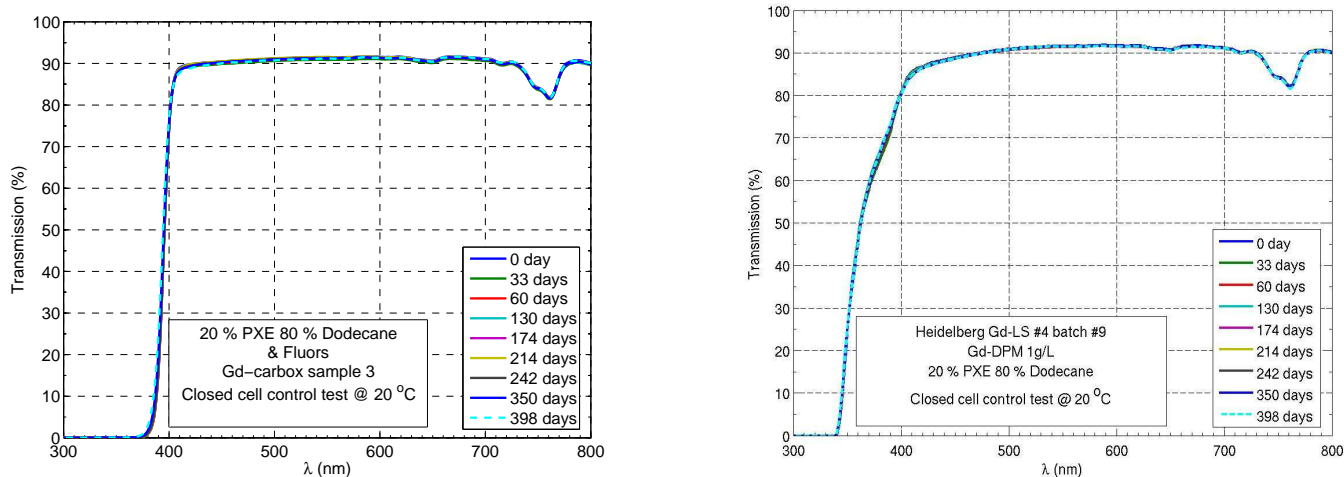


Figure 41: Transmission as a function of the wavelength for two R&D samples stored at room temperature. Left: Gd-dpm sample from Heidelberg. Right: Gd-cbx from Gran Sasso. For both the common base is 20% PXE + 80% dodecane. The sharp cut-off at  $\sim 400$  nm for the Gd-cbx system is due to the fluors (the Gd-dpm sample shown here has no fluors dissolved). Each curve corresponds to a scan at a different elapsed time with respect to the cell filling, from 0 to 242 days.

transmission spectra to the response around  $\lambda = 600$  nm. In this region the transmission is a very flat function of  $\lambda$  and it can be safely assumed that light absorption is negligible (i.e. the absorption length is infinite). To improve the accuracy of this absolute measurement, the tiny absorption from the quartz windows is also corrected, by zeroing the instrument with the response of the empty cell, instead of air.

The same experimental procedure described above is repeated with a twin sample stored at elevated temperature, typically  $40^\circ\text{C}$ . This is intended as an accelerated aging test, under the hypothesis that a change in the temperature influences just the dynamics of the chemical reactions. I.e. the chemical evolution at elevated temperature is the same as that at room temperature, only faster. Experimental and theoretical arguments exist in favor and disfavor of the above interpretation of the high-temperature tests (see Section 4.7.3).

Since the beginning of 2006 similar spectro-photometric tests are performed on the liquids filling the 1/5 mock-up. Samples are taken from the mock-up approximately every month. Their optical transmission is measured and compared to that of reference samples taken during the synthesis and the mock-up filling.

#### 4.7.2 Results

Figure 41 shows the optical survey of two R&D Gd-loaded scintillators synthesized in early 2005. Within the sensitivity of the instrument, no degradation has been observed for  $\sim 1$  year of data-taking. This can be compared to Figure 42, where two samples from the same batches have been tested at  $40^\circ\text{C}$ . Here a degradation is observed, particularly for the case of the Gd-cbx system. In the next section this effect will be discussed.

Regarding the survey of the mock-up liquids, to date only one sample has been taken from the tanks and analyzed, which happened one month after filling. The result, shown in Figure 43, shows

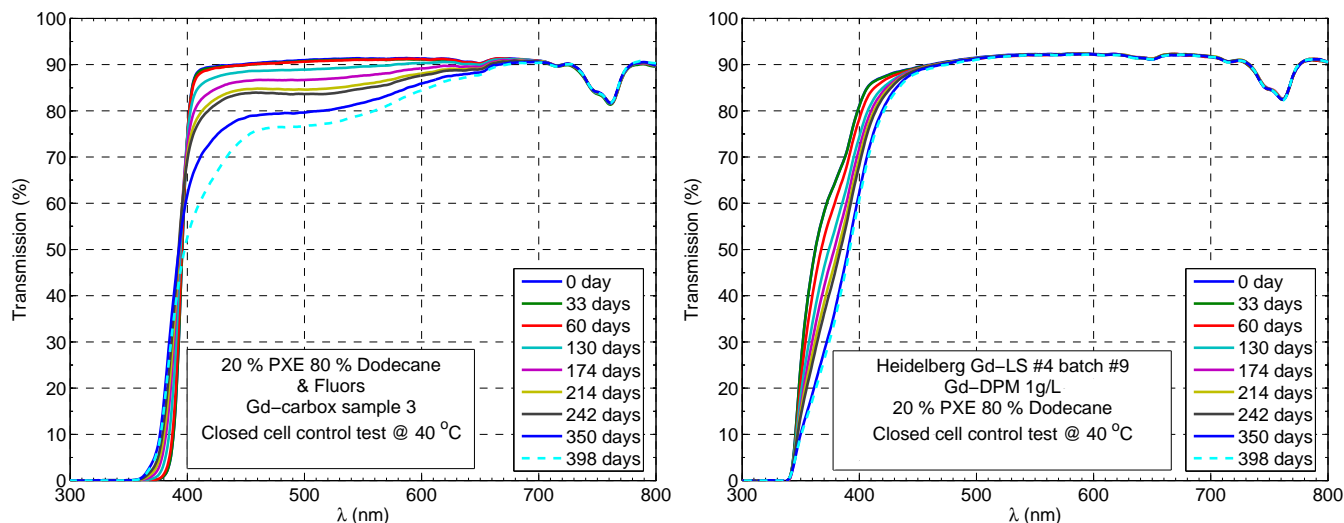


Figure 42: Transmission as a function of the wavelength for the same samples as Figure 41, stored at 40°C. Each curve corresponds to a scan at a different elapsed time with respect to the cell filling, from 0 to 242 days.

that the scintillator transparency is stable on this time scale

### 4.7.3 Discussion

Spectrophotometry provides a very powerful and precise tool to investigate the stability of our scintillators. The bin-to-bin error of each measurement due to the noise of the photo-detector is in all cases negligible, as it corresponds to a  $\gtrsim 100$  m equivalent attenuation length (this can be further improved by smoothing the curves, since one data-point is available per nm in wavelength). Moreover, the sample transmission scan over a large wavelength interval provides diagnostic and self-referencing capabilities. In fact, it is important to note that no optical degradation has ever been observed in the wavelength region  $\lambda \gtrsim 650$  nm. This gives a handle to correct the small fluctuations in the offset of each scan with respect to the others, which are believed to be due to surface effects and instrumental systematics. This offset-correction is of the order of a few tenths of percent, at most.

In the case of the first generation of R&D Gd-loaded scintillators, there has been a certain consistency between data at room- and elevated temperature. Whenever an instability appeared at 40°C, it showed up later with a slower dynamics at 20°C, as well.

On the other hand, it has been shown that the best formulations developed during 2005 have shown no degradation at all during  $\sim 1$  year survey time, while some worsening of the transmission has been observed at elevated temperature. It is not possible to correlate the results of the two tests by defining some “acceleration factor”. In general, the Gd-carboxylate scintillators have shown a worse performance at high temperature. These systems, however, are expected to be more fragile with respect to strong temperature variations, since synthesis is based on chemical equilibrium. The parameters of the synthesis are tuned to drive this equilibrium toward stability at room temperature, which does not necessarily imply stability at elevated temperature. In the case of the beta-diketonate system, instead, the degradation is believed to be due to the accelerated

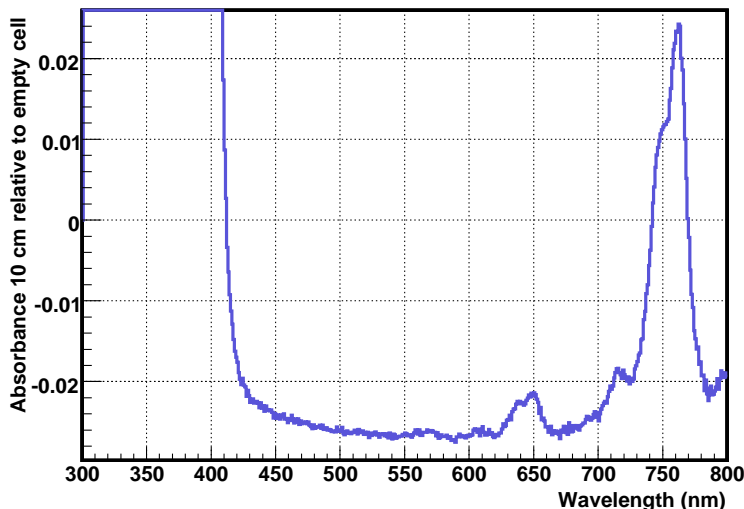


Figure 43: Absorbency spectrum for the same liquid (reference to the empty cell). Due to the uncorrected effect of Fresnel reflection at surfaces, only the differences with respect to the value at  $\lambda \sim 600$  nm are considered significant.

reactivity of impurities left from the synthesis.

#### 4.7.4 Simulation: Optical properties

In Double Chooz -more than in other neutrino detectors - optics is a crucial issue. The chemicals required to bring Gd in solution and stabilize the system have an influence on light generation and transport processes well beyond the typical cases of binary solvent-fluor systems. Furthermore, the chemical stability of the liquids are of major concern and all conceivable scenarios of aging of the liquids and drift of their optical properties must be carefully evaluated. Finally, due to the multi-shell structure of the inner detector, where each volume is filled with a different liquid and separated by acrylic, processes at the interfaces may have a non-negligible influence on the detector response. For these reasons, a considerable effort has been devoted to carefully modeling the detector optics.

#### Scintillators and other liquids

It has to be noted that the development of the Double Chooz scintillators has been (and -to some extent- still is) an R&D project and the best state-of-the-art formulations have been subject to change. Consequently, we have decided to build the optics using a micro-physical approach (see Reference [67] for a detailed description of the model). Most of the optical properties are derived by the actual liquid composition selected for the simulation (see previous section), and a database of input properties of the basic ingredients. This database includes the experimental, wavelength-dependent extinction coefficients, fluorescence spectra, fluorescence yields, etc. In this way, implementing new liquids is trivial and moreover the Monte Carlo can provide feed-back for the fine tuning of the scintillator formulation.

In DCGLG4sim the choice of fluor and WLS determines the emission and re-emission scintillation spectra (a-priori different, as opposed to GEANT4). Figure 44 shows some relevant examples. In a

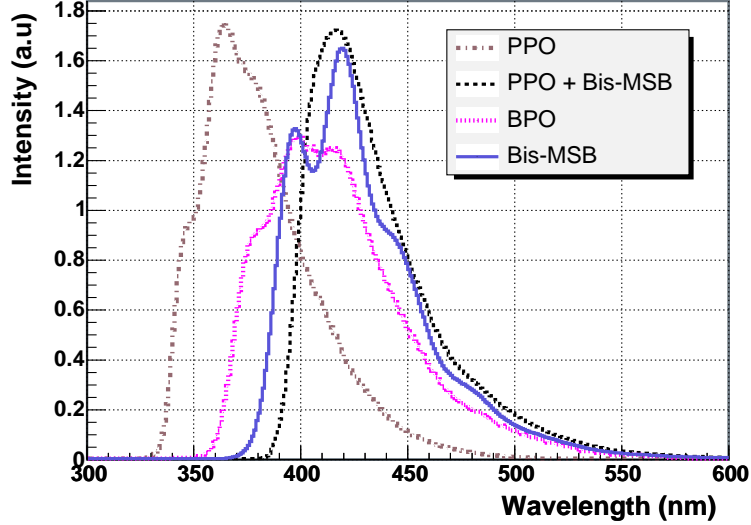


Figure 44: Emission spectra of several fluors. The primary emission spectrum typically used for the Double Chooz Monte Carlo is the curve “PPO + Bis-MSB”. Re-emission follows the bis-MSB curve (with the constraint  $\lambda_{\text{new}} > \lambda_{\text{old}}$ ). Data from MPIK-Heidelberg.

Table 24: Decay constants ( $\tau_i$ , in ns) and weights ( $q_i$ , fraction of light emitted with decay constant  $\tau_i$ ) of the time profile for photon emission after excitation with beta and alpha particles. Data from Borexino for a PXE/p-Tp(3.0 g/ℓ)/bis-MSB(20 mg/ℓ) mixture [77].

Excitation	$\tau_1$	$\tau_2$	$\tau_3$	$\tau_4$	$q_1$	$q_2$	$q_3$	$q_4$
beta	3.1	12.4	57.1	185.0	0.788	0.117	0.070	0.025
alpha	3.1	13.4	56.2	231.6	0.588	0.180	0.157	0.075

system with PPO and bis-MSB, the energy transfer from the primary to the secondary fluor is very efficient, since the emission spectrum of PPO matches very well the absorption band of bis-MSB. The resulting spectrum is essentially that of bis-MSB, peaked around 420 - 430 nm.

The light yield (LY) is assigned as a free constant material property, independently for each of the scintillating liquids. The LY of our scintillators depends on many factors: aromatic/oil ratio, fluor concentration, Gd-loading. Measurements have been performed in several laboratories of the collaboration, usually by comparing the response of the investigated sample to a known energy deposition with the response of a reference scintillator, whose absolute LY is known. Typical values for our Gd-loaded scintillators are LY of  $\sim 6000 - 7000$  photons/MeV. The formulation of the unloaded  $\gamma$ -catcher scintillator is tuned to reduce the LY and achieve a perfect match with the target scintillator. For the Inner Veto liquid, we consider a LY of  $\sim 5000$  photons/MeV.

An emission time is assigned to each emitted photon. This is chosen from a multi-exponential probability density function. So far, the scintillation time of our scintillators has not been measured; hence we are currently using the experimental response of pure PXE scintillators (see Figure 45). The decay constants are given in Table 24.

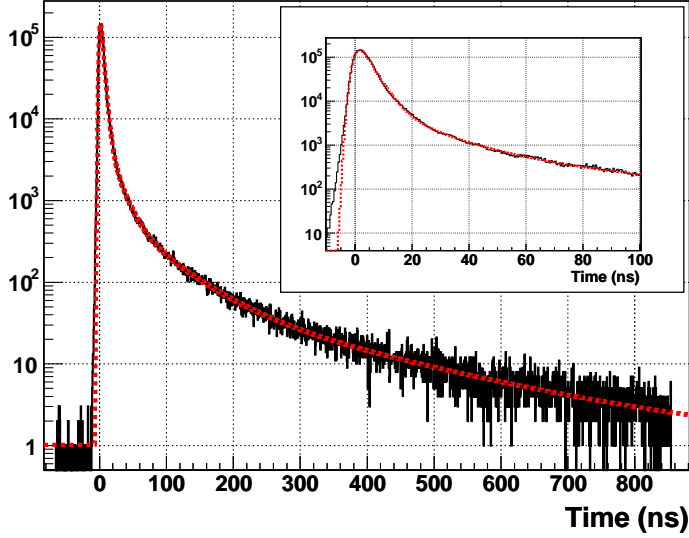


Figure 45: Experimental time profile for photon emission after excitation with beta-particles of the PXE-based scintillator loaded in the CTF of Borexino [77]. The red line is a 4-exponential fit including a convolution with the response function of the apparatus. The insert shows a magnification of the first 100 ns. Details of the measurement and analysis in [78].

Attenuation in the liquids is treated as the sum of three processes: absorption, wavelength-shift and scattering. Global attenuation lengths are calculated by adding the contribution of all molecular species present in the scintillator cocktail. Spectro-photometric measurements of the purified single components provide integral information about the sum of the three processes. By fluorimetric methods it is possible to disentangle wavelength-shift from the sum of absorption and scattering. As for the absorption/scattering relative weight, for the moment we assume that scattering from micro-particles is negligible (Rayleigh scattering is already included in GEANT4). The above assumption is conservative, since the possible contribution of the scattering to the interaction lengths is attributed to absorption. Figure 46 shows an example of attenuation lengths in a typical Gd-loaded scintillator formulation, as implemented in DCGLG4sim. The effective interaction length is given by the composition of all contributions, however it is important to know the relative weight of each one.

The re-emission probability is calculated for each wavelength by multiplying the probability that absorption was due to a fluorescent species (fluor and WLS) by their wavelength-dependent re-emission probability. The latter is assumed constant to its literature value up to a wavelength cut-off that is determined from fluorimetric measurements [67]. Figure 47 shows the calculation of the re-emission probability for the scintillator of Figure 46.

Figure 46 and 47 together demonstrate that for  $\lambda \lesssim 420$  nm, absorption is dominated by bis-MSB and largely results in a wavelength-shift. This is crucial, since the PPO emission falls in a wavelength region where absorption from non-fluorescing impurities is severe (compare Figure 44 and 46). In our scintillator, absorption is most important for  $\lambda \gtrsim 430$  nm, where bis-MSB is no longer an effective wavelength-shifter. In this range we anticipate an attenuation length of  $\sim 5 - 10$  m. This value can still be improved by further purification of the Gd-compound and PXE.

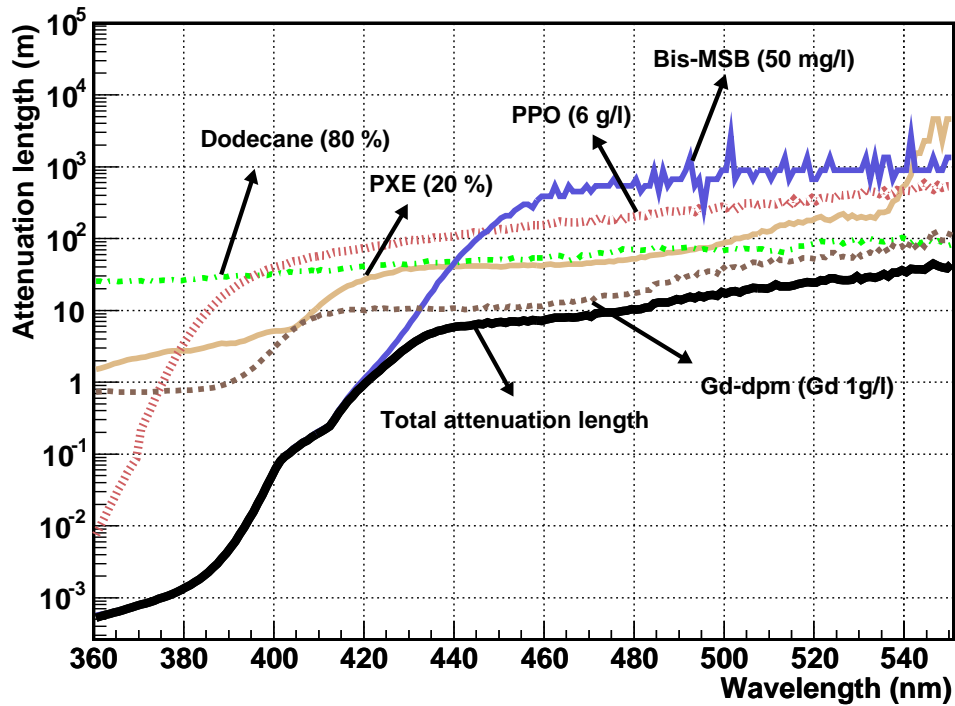


Figure 46: Attenuation lengths contributed from each component of a scintillator suitable for a  $\nu$  target for Double Chooz. All values are calculated for the given concentrations. Extinction coefficients from MPIK.

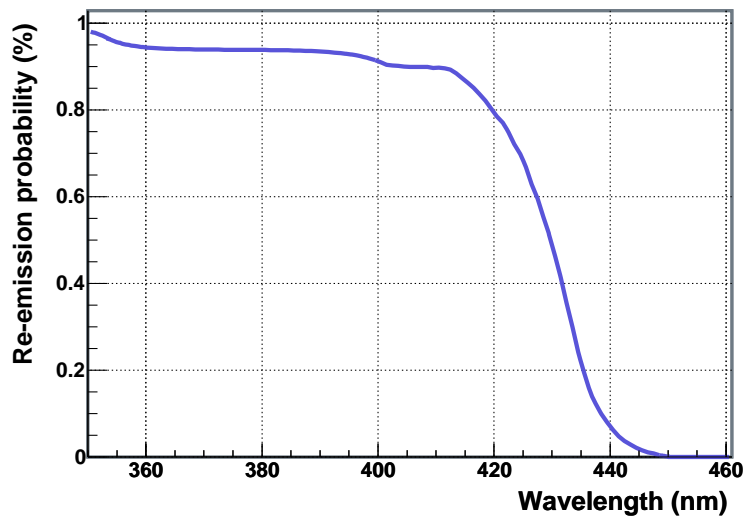


Figure 47: Re-emission probability calculated for the scintillator of Figure 46. The ordinates represent the probability that an absorption results in the emission of a new photon, with  $\lambda_{\text{new}} > \lambda_{\text{old}}$ .



## 5 Photodetection

### 5.1 Target and Gamma-Catcher

In this section we present the factors considered in the design of the Double Chooz target array of photomultipliers (PMTs). The requirement is to have sufficient coverage and PMT performance to allow the experiment to reach its sensitivity goals, while at the same time considering not only the cost of the array, but also the fact that PMTs are expected to be one of the major sources of uncorrelated internal background due to their relatively high level of radiological contaminants and their proximity to the target volume. This is an important point, as accidental correlations were roughly one-third of the background events recorded by CHOOZ[5]. In addition to standard concerns about PMT performance, Double Chooz also has a unique requirement that the detector response and hence the light collection be identical in two different detectors. This raises concerns about asymmetries in the PMT acceptance both due to inherent asymmetry in the dynode structure and due to magnetic fields, which might be different at the two detector sites. Significant progress has been made to measure this aspect of performance in addition to timing, gain, stability and dark noise. Since the Double Chooz experiment has a tight construction schedule without extensive R&D studies, we are choosing a conservative system design and use several technical solutions from the previous experiments where members of the Double Chooz collaboration were involved.

#### 5.1.1 Coverage

With respect to photodetection, the CHOOZ experiment[5] can be considered as a prototype for each of the two detectors in Double Chooz. Following the successful operation of CHOOZ with 15% photocathode coverage, we plan a similar photocathode coverage (13.5%) also using 8-inch photomultiplier tubes. With the given detector dimensions such coverage requires 534 8-inch photomultipliers per detector. The relatively large number of phototubes guarantees (as confirmed by simulations) that the loss of a few tubes per detector will still preserve the identity of each detector response at an acceptable level. We expect that this number of phototubes will give sufficient energy resolution to keep low-energy backgrounds from fluctuating above our threshold. Based on our best simulations, we expect the average light collection to be above 180 p.e./MeV at the center of the detector increasing by about five percent to the periphery of the target.

#### 5.1.2 Radiopurity Requirements

The goal for the detector trigger threshold is  $\sim 0.5\text{-}0.7$  MeV (with 90% efficiency at 0.8 MeV and  $\geq 99.97\%$  at 1.0 MeV) that will allow high-efficiency detection of antineutrino events independent of the systematics of energy-scale non-linearity and calibration. In the CHOOZ detector[5] the trigger threshold for prompt signal detection was chosen at 1.3 MeV. This resulted in a raw trigger rate of  $\sim 130$  Hz that after applying software cuts was reduced down to  $\sim 65$  Hz. Lowering thresholds in CHOOZ was limited by the DAQ system. In the Double Chooz detectors the single rate situation will be considerably improved by introducing passive 17-cm iron shielding around the detector (see Section 3.6). Also, a passive 1062 mm thick buffer layer of non-scintillating oil (+12-15 mm of acrylics) is being introduced between the scintillator and the wall on which photomultiplier tubes are mounted. Radioactivity of liquid scintillator and buffer oil will be controlled by the purification process during the liquid scintillator production and at detector filling time. The effect

source	K(ppm)	U(ppb)	Th(ppb)
ETL, glass, manufacturer	64	30	30
ETL, glass, Alabama	100	36	21
ETL, glass, MPIK	59	54	156
Hamamatsu, glass, Alabama	204	164	66
ETL, dynode, manufacturer	109	35	12

Table 25: Measurements of PMT radiopurity.

of radioimpurities is discussed in more detail in Section 2.3. In addition to the above, the careful selection and radioassay of construction materials will help to further reduce the single rates.

Since borosilicate glass of photomultipliers can contain radioimpurities ( $^{40}\text{K}$ ,  $^{232}\text{Th}$ ,  $^{238}\text{U}$ ) and the photomultipliers are positioned close to the scintillator volume, particular care was given to the selection of PMTs with low concentration of radioimpurities in the glass. Three leading PMT manufacturers (ETL, Hamamatsu, and Photonis/Burle) provided us with samples of low-radioactivity PMT glass. Radioassay of these samples (Photonis/Burle glass sample is currently being tested) was made at the low-counting facility at the University of Alabama and at MPI/Heidelberg. The results of these measurements are shown in Table 25. Radiopurity data for PMT glass from ETL and Hamamatsu companies are generally confirmed by our radioassay measurements, although there are some discrepancies between measurements performed by different groups. It is also possible to have tube to tube variations. We currently plan to test non-destructively several PMTs from ETL, Hamamatsu, and Photonis to verify and extend these results. The current measurements, when input into our U/Th/K/Co event generator and detector simulation, result in a background singles rate of less than 10 Hz at a threshold of 0.7 MeV. This rate would result in less than 2 events/day above 1 MeV in our far detector, which is acceptable. Thus the two manufacturers tested so far are capable of producing PMTs of sufficient radiopurity for our purposes. It is our intent, however, to include radiopurity in the PMT specifications, and to perform non-destructive counting on a random sample of delivered PMTs to ensure radiopurity quality and consistency. The low-counting facility at Alabama is large enough to be able to “whole body” count a PMT in this fashion. This facility will also be used to count a reference PMT, which will then be crushed and counted again for better accuracy. In this way a conversion factor from crushed to whole body counts can be obtained and used to ensure radiopurity quality during the manufacturing process. Capacitors and other components of the PMT base will be screened as well. The collaboration also has access to low background counting facilities in Heidelberg, Gran Sasso and Modane.

### 5.1.3 PMT Performance

Light produced in the liquid scintillator of the Far and Near targets of Double Chooz should be detected by two identical photomultiplier (PMT) systems. The number of phototubes (534 per detector) and their geometrical arrangements will be the same for both detectors. With the individual PMT threshold of 0.25 s.p.e. (single photo-electrons), one can expect the following global PMT system performance characteristics:

- light output and uniformity of detector response: minimum response of 180 spe/MeV in the center of the detector increasing by less than 10% (to 200 spe/MeV) at the periphery

of the target volume (5% is the predicted value). This dependence is correctable by the reconstruction of the spatial position of the event in the scintillator volume;

- expected accuracy of vertex reconstruction  $\sim 9 \text{ cm}/\sqrt{E(\text{MeV})}$  in x, y, z projections folded with particle energy deposition distribution;
- expected energy resolution  $\sim 7.5\%/\sqrt{E(\text{MeV})}$ ;
- PMT dark rate is expected to contribute  $\sim 1$  count per second at the energy threshold of 50 KeV. We plan the trigger threshold to be set at a level 0.7 MeV as determined by radiopurity considerations.

#### 5.1.4 Detailed Specifications

Below we discuss parameters of the PMT system that are being used in the design. These parameters either came from the baseline configuration and set of parameters, or were specified by the PMT manufacturers, or have been measured by us with the samples of phototubes provided by the manufacturers.

- 8-inch diameter PMT represents an optimal ratio of glass weight to photocathode area (active photocathode diameter 190 mm and mass of the phototube is  $\sim 1000$  g);
- the total number of PMTs is 534 per detector. On the cylindrical surface they are arranged as 12 rings of 30 PMTs in each. There are also 87 PMTs on each of the bottom and top caps. Figure 48 shows the positions of phototubes in the detector. The PMTs will be installed in the detector with their axis tilted to the center of the target. For non-tilted PMTs in the central plane the distance of the apex of PMT from the back supporting wall is 300 mm;
- from our experience in Chooz, KamLAND, and Super-Kamiokande we expect the possible losses of PMT in the detector to be at the level of less than 1%. The key to low PMT mortality rate is comprehensive testing program during PMT installation. Total number of PMTs should be large enough to keep the detector uniformity constant within  $\leq 1\%$  accuracy. For identical response of the two detectors inoperable tubes in one detector will require that the corresponding tube in the other detector be disabled in software and possibly removed from the trigger;
- the total number of PMTs to purchase is  $2 \times 550$ , which will include 3% spares;
- for the mechanical support of the PMTs we plan to use the light-weight mounting developed by the MiniBoone Collaboration. Figure 49 shows this support structure. During the installation PMTs will be mounted individually one-by-one on the walls and bottom/top lids of the stainless buffer vessel. Construction materials of the support structure (stainless steel and acrylic) have been radioassayed to be sure that they produce negligible contribution to the detector singles counting rate;
- positive supply voltage at the PMT anode provides the advantage of minimizing the dark current and the discharge rate, but introduces RC-coupling in the signal processing;
- a single cable will be used for supplying high voltage to PMT and for signal readout. This minimizes the ground loops noise, cross-talk, and cable cost;

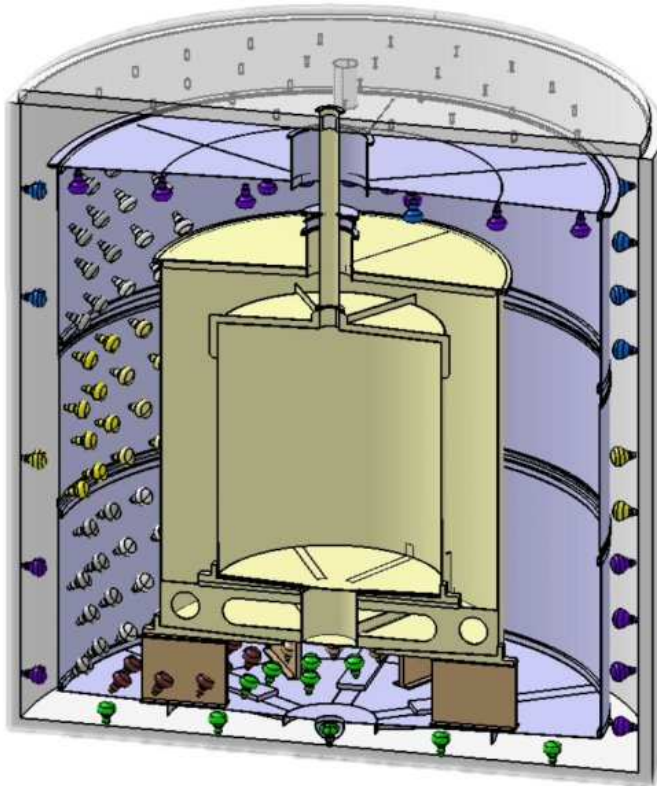


Figure 48: Target PMT layout in the Double Chooz detector.

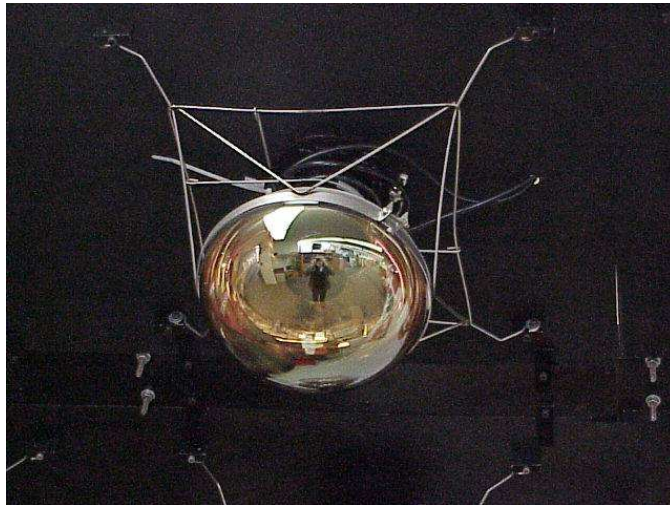


Figure 49: For support of 8-inch photomultiplier tubes in the Double Chooz detector we plan to use the mechanical design of the mini-Boone collaboration, but other solutions are also currently being investigated.

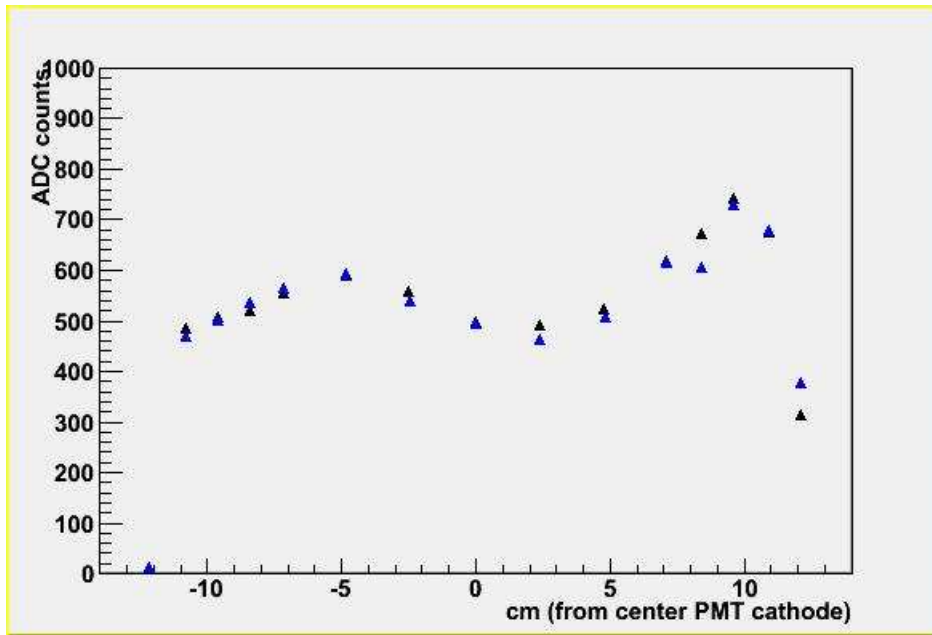


Figure 50: Example of photocathode non-uniformity for typical Hamamatsu R5912 photomultiplier tube.

- low-current PMT voltage dividers (0.1 mA at the nominal voltage) minimizes power dissipation in the detector;
- acrylic + epoxy potted and sealed bases will be constructed by PMT manufacturers;
- 20-m long oil-resistant RG-303C 50-ohm cable sealed in the PMT base with SHV connector at the outer end will be used. Such cables immersed in mineral oil are used in the KamLAND detector;
- the choice between stainless steel and black sheet between the PMTs is currently being discussed. This can be decided rather late in the construction schedule;
- PMT glass resistance to the buffer oil (dodecane) was tested for Hamamatsu and ETL tubes (with no effect for equivalent  $\geq 10$  years of operation).

Other PMT parameters important for detector operation (measured with PMT samples or provided by manufacturers):

- PMT operation gain is  $10^7$ ;
- PMT anode is 50-ohm back terminated for robust operation with large signals;
- quantum efficiency  $> 20\%$  at 400 nm. As an example Figure 50 shows measured non-uniformity of photocathode for Hamamatsu R5912 tube.
- single photoelectron resolution: s.p.e. peak-to-valley  $\geq 1.5$ . Figure 51 shows single photoelectron spectra for two measured samples of Hamamatsu and ETL phototubes with and without

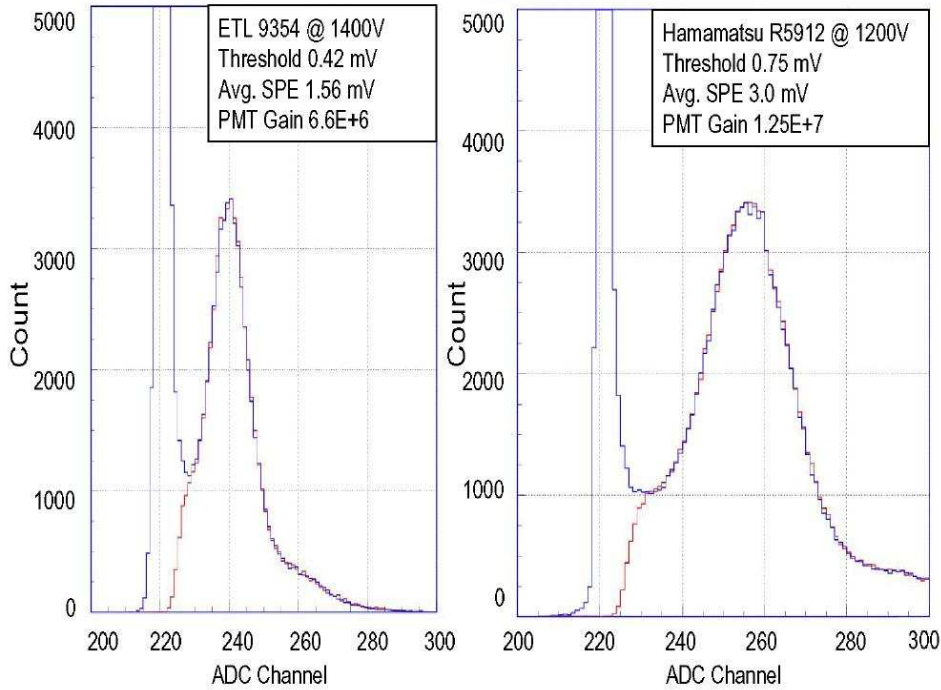


Figure 51: Untriggered (blue) and self-triggered (red) s.p.e. spectra of two tested photomultipliers: ETL 9354KB and Hamamatsu R5912 measured with low-efficiency LED.

discrimination threshold. They demonstrate that low thresholds  $\sim 0.25$  s.p.e. are practically possible to achieve;

- typical dark rate in air specified by manufacturers is 4,000 per second. Our measurements with 0.25 s.p.e. threshold can reproduce this rate; however, from our KamLAND experience, we know that the dark rate can be higher for tubes immersed in the mineral oil and looking at the large scintillator volume. The nature of this increase in KamLAND is not fully understood, however if we assume that the dark rate will not be scaling with the detector volume and the coverage but only with the PMT photocathode area we can conservatively estimate the average dark rate per phototube at the level of  $\sim 10,000\text{-}12,000\text{s}^{-1}$ ;
- s.p.e. after-pulses occurring within  $\sim 60$  ns after the main s.p.e. pulse are unfortunately present for all tested 8-inch photomultiplier tubes. They appear generally due to electron backscattering from the first dynode with the probability of a few percent. 8-inch PMT specifications allow after-pulses (within 60 ns after the main pulse) at the level of less than 3% and late pulses due to transport of residual ions (within 16  $\mu\text{s}$  after the main pulse) at the level of less than 10% per initial photoelectron.
- with tapered (B-type) voltage dividers, all tested phototubes show a linear response up to 80-100 mA of anode current (peak value), which satisfies the requirements of Double Chooz, where typical large muon signals will produce  $\sim 60$  mA peak value;
- the typical rise time for the s.p.e. signal (after 20-m of RG-303 cable) is  $\sim 4$  ns; FWHM  $\sim 7$  ns; and return-to-the-base time is  $\sim 30$  ns;

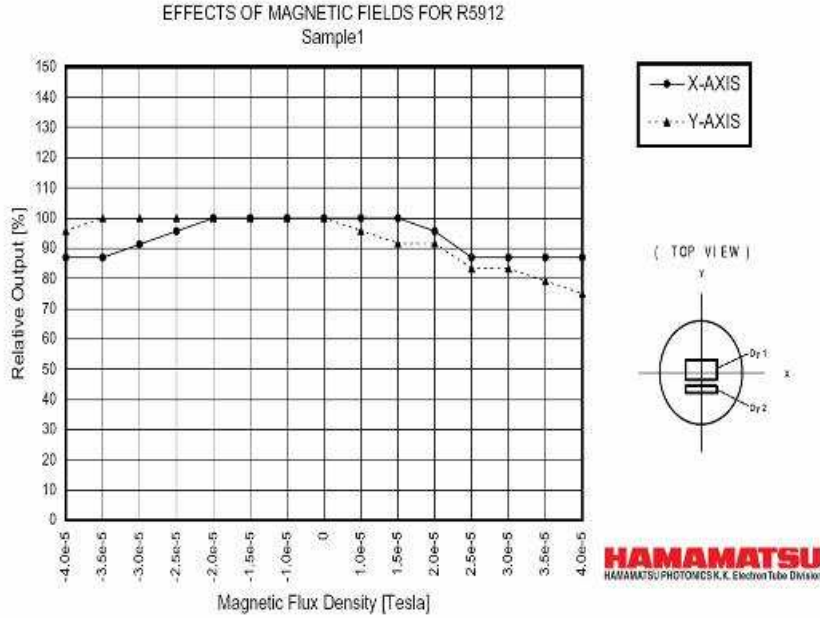


Figure 52: Effect of transversal magnetic field on the 8-inch PMT response. Measurements provided by Hamamatsu Corporation

- transition time spread  $\sim 2.5$  ns FWHM (specified by manufacturers);

### 5.1.5 Sensitivity to Magnetic Field

PMTs are sensitive to the magnetic field. As an example Figure 52 shows the typical effect of the magnetic field transversal to the PMT axis on one of the candidate PMTs (Hamamatsu R2512) [79]. It is expected that PMTs of other manufacturers will have similar sensitivity to the transversal magnetic field. The magnetic field as known from geomagnetic models [80] has the following components at the Chooz location: 0.43 Gauss Down, 0.20 Gauss North, 0.003 Gauss West. The unshielded magnetic field transversal to the PMT axis can create response difference for the tubes at different locations in the detector up to 30%. This difference in PMT response can potentially affect the identity of two Double Chooz detectors and thus should be eliminated or reduced. The presence of 17-cm iron shield around the detector, needed for the reduction of radioactivity counts by the scintillator, might result in additional non-uniform magnetic field inside the detector at the place where PMTs are installed. The issue of magnetic shielding is addressed in Section 5.1.5. The required residual transverse magnetic field should not exceed 0.05 Gauss at any PMT location in the detector.

### 5.1.6 PMT Purchase and Delivery

We have been in contact with three leading PMT manufacturers of 8-inch phototubes: Hamamatsu in Japan (R51912), Electron Tubes Limited in England (ETL 9354KB), and Photonis/Burle in France/US (XP1806). All three companies produce 8-inch photomultiplier tubes with low-radioactive borosilicate glass and with similar performance characteristics. All three companies

provided us with samples of their tubes for performance evaluation as well as with samples of low-radioactive glass for radioassay. Some initial results of tube measurements are shown in the previous subsections. We also asked manufacturers to integrate potted bases and oil-resistant cables in the construction of the deliverable product, so we could enlist their help in the R&D effort, save on construction time, and guarantee more robust operation of the tubes. Also, we plan to specify the type of the voltage divider optimized by us for Double Chooz operation which the manufacturer will build from high radiopurity components and seal in the PMT/base assembly. A final decision on the particular manufacturer product will be made after verifying the compliance with required level of radiopurity, detailed performance comparison, and *price*. All three manufacturers have agreed on the following production schedule: response to the bid specifications: within one month; preproduction time for the first 110 PMT batch delivery: 4 months; after that monthly production rate of 110 phototube. Thus, first 550 tubes needed for assembly of the Far detector will be produced and delivered in 8 months after signing the contract. It is important that the proposed rate is convenient to all manufacturers and does not saturate their production capability. We are negotiating with companies the possibility of separating the production into two groups of 550 pieces each with the gap in production of  $\sim 6$  months to reduce the high load on the funding profile.

### 5.1.7 Acceptance and Characterization Tests

We believe that the key to reliable and lasting operation of the large PMT array system is in comprehensive tests prior to installation and commissioning of the phototubes. We plan several levels of tests performed at different locations and times.

First we agreed with manufacturers that they will provide us with certificate of acceptance measurements made at the factory. It will typically include: cathode and anode luminous sensitivity, cathode blue sensitivity, anode dark current and dark counting rate, supply voltage at the gain  $10^7$ , peak-to-valley ratio for single photoelectrons, and transit time spread.

At the Chooz site we plan to rent a warehouse with area approx. 3,000 m<sup>2</sup> that will be converted to the clean room facility. There PMTs will be unpacked, tested, assembled, and stored. The rate of characterization and acceptance tests ( $\sim 5$  per day) should match the rate of PMT delivery (110 per month). These tests will include burning-in time of at least 24 hours for each phototube at the voltage providing gain of  $\sim 10^7$  followed by measurements of major performance parameters of each phototube. These parameters will include: single photoelectron peak vs high-voltage, dark rate vs high-voltage, photocathode quantum efficiency relative to the reference, s.p.e. spectrum at nominal gain  $10^7$  and peak-to-valley ratio, measurement of linearity at nominal gain  $10^7$ , measurement of transition time spread at nominal gain  $10^7$ , pedestal noise RMS, viewing the PMT signals with an oscilloscope.

The test station will be equipped with two sets of black boxes each for 6 PMT positions, with laser- and LED-based light sources, and with a VME or a CAMAC-based DAQ system, digital scope and a computer. 6 tubes simultaneously will be burn-in or tested at a time alternatively in two stations. All tests will be performed by a group of two people who besides performing the measurements will also maintain the database of all PMT measurements and installation parameters. These two people should stay at Chooz for extended period time to provide consistent and responsible test operation.

The purpose of the characterization/acceptance test will be to obtain a set of individual parameters for each tube: operating voltage for nominal gain, slope of gain vs high-voltage, s.p.e. spectrum, dark rate, transition time spread, and linearity which will be included in the data base to



characterize the detector performance. These data can later be used in the analysis and/or in the detector simulations. Furthermore, in a first stage of the experiment, we will need to group PMTs into groups with similar high-voltage parameters since four or eight tubes in a group will share the common power supply channel.

Selective acceptance radiopurity tests: 1-2 randomly selected tubes from each monthly delivery batch will be assayed for radiopurity (in non-destructive tests). If K, Th, or U content will exceed the specified level of contaminations, then other 10 randomly selected tubes from the same batch will be radioassayed. If more than 3 out of 10 PMTs will exceed the specified contamination level, the whole batch will be returned to the manufacturer.

### 5.1.8 Mechanical Assembly and Cleaning

The mechanical support system could be adopted from the Mini-BooNE design shown in Figure 49. It is light and can be made with radio-pure materials. The PMT circular grip can be firmly adjusted during the assembly of the support structure. It should provide a reliable hold of the phototube in all possible positions relative to the direction of the buoyant force. The assembly of PMTs and mechanical structures will be performed in a clean room next to the characterization/acceptance tests at the Chooz site not far from the detectors. Two trained technician will be involved. They will clean the PMT, the cable and all the mechanical parts with alcohol prior to and after the assembly, will tighten the PMT grip ring with a torque controlled tool and will seal the whole assembly in a hermetic plastic bag. Sealed assemblies will be stored and later transported to the detector site for installation. Sealing bags will be removed inside the clean area of the detector. Assembly production (of  $\sim 25$  PMTs per day) will go slightly ahead and in parallel with the PMT installation in the detector.

### 5.1.9 Installation in the Detector, testing and commissioning

According to the collaboration plans the installation of the PMTs in a detector will require coordinated work of a team of 12 people and should be performed within one month (installation of  $\sim 25$  PMTs per day). The work will include PMT transportation to the detector site and opening of the sealed bags. Before the installation each tube will undergo a short functionality test with HV in a special dark box. Tubes will be bolted to the angle rib and welded to the vessel wall. The position of the tube, its serial number, and cable label will be then entered in the computer database. Cables from several neighboring tubes will be arranged in bundles of 16 cables. These bundles will be routed to the cable exit tubes on the top of the detector rim through pre-installed Teflon conduit tubes. This cabling procedure has been successfully used in the KamLAND detector. The phototube installation will start from scaffoldings on the top of the cylindrical part of the detector and will proceed by patches down and around the cylinder. Photomultipliers on the bottom floor will be installed next with cable routed through pre-installed conduit tubes. PMTs on the upper lid of the detector will be mounted under the lifted lid. Bundles of PMT cables from the upper lids will be routed through the conduit tubes attached to the lid to the rim of the detector where the cable exit tubes are located. Cable bundles from top lid PMTs will loosely pass through the side exit tubes with significant slack. These cable bundles will be pulled out to their final extension when the lid will be closing.

## Functional test during installation

Newly installed PMTs will be tested daily one-by-one (during the evening shifts) for functionality and correct cable numbering to the position assignment. The final test with LEDs in the central position of the detector at the nominal PMT voltages will be accomplished upon the installation of all PMTs in the detector and before the installation of the central acrylic vessels. For this test all PMTs will be connected to the HV distribution system (HV-signal split boxes) and tested one-by-one with a dedicated DAQ station verifying the functionality of each channel and the correspondence between the HV channel number and the signal output. Daily functional tests during the installation will be performed by members of the installation crew.

## PMT System Commissioning

After the installation of the acrylic vessels, with the whole detector being closed and sealed, and before it is filled with scintillator and oil, a commissioning test will be performed. For this test the final HV-system and readout electronics need to be installed and connected. All tubes will be powered and held under nominal high-voltage for 2-3 days. Then, at several high-voltages close to the nominal HV corresponding to PMT gain  $10^7$  a discriminator threshold scan for every tube will be performed to establish the threshold corresponding to 0.25 spe. Together with that the s.p.e. spectra will be recorded and the dark rate for each PMT will be measured. The final choice of the high-voltage values will be made by equalizing the response of the PMTs in terms of single photoelectron response. After filling the detector with scintillator and oil the commissioning test described above will be repeated. The final goal of the commissioning test will be to provide the detector with the set of high-voltage values corresponding to equal response within  $\sim 1-2\%$  to single photoelectrons. Note, that relative quantum efficiencies (averaged over the whole photocathode area) of the tubes were to be measured during the earlier characterization tests. The commissioning of the PMT system will be performed by a group of 2-4 PMT group members together with other collaborators responsible for electronics and DAQ operation.

## PMT Documentation Database

The information from all results of PMT tests, history of each PMT performance, geometrical position in the detector, cable label, HV-channel, electronic channel etc. will be recorded and stored in the PMT database. Created as html data structure it should be accessible through the Internet and should allow extraction of formatted parameter tables that can be used in data analysis and for Monte Carlo simulations.

### 5.1.10 Optics of the PMTs

The optics of the PMTs in our Monte Carlo is managed by the program *GLG4sim*, through the class *GLG4simPMTOpticalModel*. This implements the full model of the thin absorbing photocathode with complex, wavelength dependent refractive index. The model and its parameters are given in [81]. It is based on experimental data on the optics of PMTs equipped with the same bialkali photocathode as the Double Chooz PMTs and leads to the prediction of the probability of photo-conversion, dissipation, reflection and transmission, for each crossing of the photocathode. These probabilities are dependent on the photon wavelength and impinging angle, and on the re-

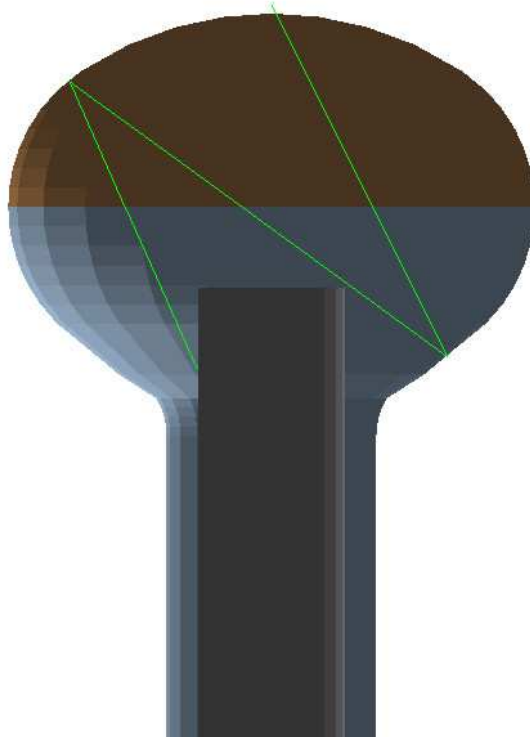


Figure 53: Photon tracking in GLG4sim. The optical model calculates the probability for detection, dissipation, reflection, and transmission at each interface.

refractive index of the medium where the PMT is immersed (e.g., mineral oil). Photons reflected or transmitted are further tracked, until they are either lost or detected (Figure 53).

### Other materials

The double acrylic vessel containing the scintillators of the target and  $\gamma$ -catcher is an optical interface between three regions, each filled with a different liquid. For the time being, we assume that the refractive indices of all liquids match perfectly. This is anticipated to be very close to the actual case, since the target and  $\gamma$ -catcher will have the same or a very similar PXE/dodecane ratio, and the mineral oil refractive index should also be in the same range as the PXE/dodecane mixture, since the density will be similar. Acrylics are expected to have a slightly higher index. For the moment we consider  $n \simeq 1.46$  and  $n \simeq 1.49$ , for liquids and acrylic respectively. This slight mismatch causes some Fresnel reflection at the liquid-acrylic interface, especially for grazing incidence. Acrylic is also a potential light absorber/scatterer. The attenuation lengths in acrylic have been measured in a 20 cm long sample of the same material chosen for the Double Chooz Mock up. Results are given in Figure 54. In the wavelength region of interest the photon mean free path is  $\gtrsim 3$  m. Another important optical interface is the buffer tank. Several scenarios are envisaged, and the Double Chooz Monte Carlo must include them all: blackened walls, raw stainless steel, Tivek coating, etc... The final decision will be a compromise optimizing light collection and spatial reconstruction. At the buffer tank an optical interface is implemented, which is based on the GLISUR model (from GEANT3). This means that the reflective properties are driven by two effective parameters: a reflection and 'polish' coefficients. The latter determines the amount of

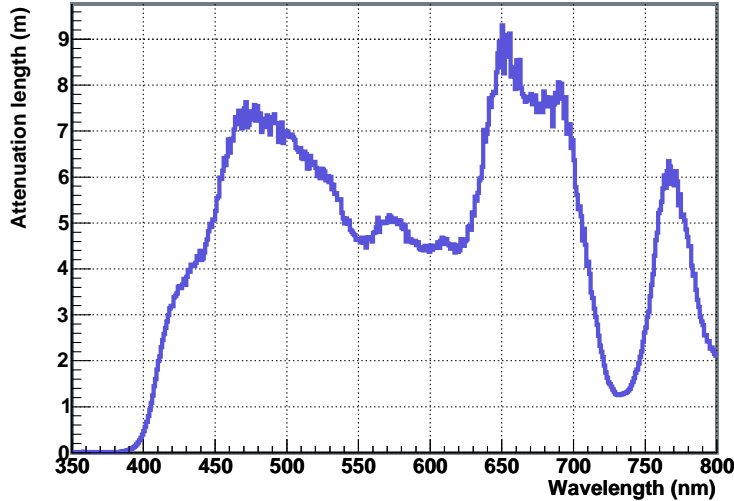


Figure 54: Attenuation length for light in the acrylic selected for the Double Chooz mock up. Data from CEA-Saclay.

isotropic diffusive reflection admixed to mirror reflection.

## 5.2 Inner Veto

Double Chooz will operate two detectors at a depth of 300 m.w.e. and 75-100 m.w.e., resp. Due to these shallow depths, the rate of cosmic muons that penetrate the shielding and enter the detectors is high, in particular for the near detector. In order to reach a signal-to-background ratio sufficient for the desired accuracy, backgrounds at both detector locations have to be well understood and controlled. The dedicated muon identification system that is described here will be used at both detectors to reject background events that are induced by cosmic muons. The muon system is an active detector based on liquid scintillator, surrounding the inner volumes of the experiment with  $4\pi$  coverage.

Backgrounds for the delayed coincidence events can be split into two main branches. In accidental uncorrelated background events, the neutrino signal is mimicked by two independent processes which happen at the same time. Correlated background events mimic the neutrino signal by a prompt and delayed energy deposition that is caused by the same initial particle. Cosmic muons are capable of producing such correlated background in different ways: They can produce fast neutrons via spallation in the surrounding rock, which in turn can cross the Veto and Buffer and deposit 1-8 MeV in the  $\gamma$ -catcher or target scintillator before being captured by Gadolinium; negatively charged muons can be captured in the detector, followed by neutron emission; also, muon spallation on  $^{12}\text{C}$  can produce  $^8\text{He}$ ,  $^9\text{Li}$  and  $^{11}\text{Li}$ . These isotopes decay on a timescale of 100 ms for  $^8\text{He}$  and  $^9\text{Li}$  and few ms for  $^{11}\text{Li}$  and can produce  $\beta n$  cascades. As the muon rate is of the order of 30 Hz (far) and 1000 Hz (near), it is not possible to veto these events without unacceptable dead times for both detectors. Therefore, a solid understanding of these processes and their rates is mandatory.

Although the veto identification system is not a hardware veto in the sense that it suppresses

any trigger on a hardware level, we will call it "Inner Veto" in this proposal. The part of the dataset taken with this system is used to suppress muon induced backgrounds during offline-analysis. Analysis, classification and finally rejection of events is possible on the basis of the data acquired by the veto photomultipliers. Moreover, it provides data for further research, e.g. in particle shower characteristics. To monitor stability and for timing calibration purposes, light flashers will be installed in various positions of the veto volume.

Compared to a water Cerenkov veto, the use of a scintillating liquid yields a factor of 30 more photoelectrons per typical muon event and grants the possibility of identifying incoming fast neutrons by their charged secondaries. The detection of light created by charged particles in the

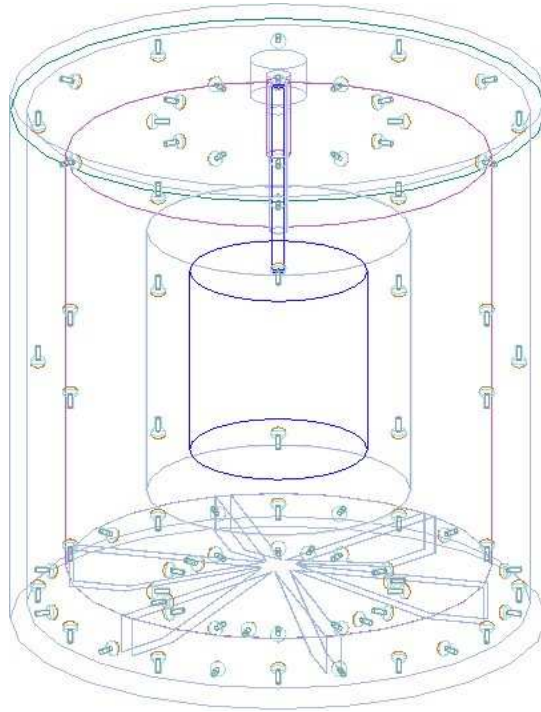


Figure 55: Detector with inner veto photomultipliers

scintillator is done with 8" low background photomultiplier tubes. The number and the arrangement of these PMTs was optimized using the Monte Carlo simulations that are described below. The standard layout that evolved from these simulations is an arrangement of 78 PMTs in five groups (Figure 55):

- a ring of 12 PMTs on top of the buffer vessel, pointing horizontally, alternating inward and outward,
- a ring of 12 PMTs attached to the side wall, 30 cm below the lid, pointing alternatively inward and down,
- a ring of 12 PMTs attached to the side wall, in the center, pointing alternatively up and down,
- a ring of 24 PMTs on the bottom of the veto, pointing alternatively inward and up,
- and a ring of 18 PMTs on the bottom of the veto, pointing alternatively inward and outward.

The support structure below the buffer vessel demands a higher number of PMTs below the vessel than above. The PMTs are of the type 9354KB of Electron Tubes Ltd. (or a comparable type of

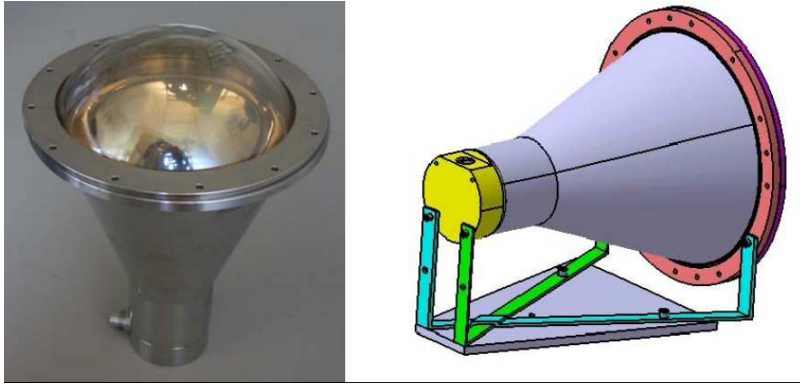


Figure 56: PMT encapsulation and mounting (Drawing P. Guillouët)

another manufacturer). The active diameter of the blue-green sensitive photocathode is 190 mm. The PMTs can be encapsulated in a stainless steel chassis (Figure 56), where the Borexino encapsulation design with PET pressure membrane can be used with small modifications. Encapsulating the PMTs has the advantage that no leaks in the vicinity of the connector and/or the voltage divider can occur and mechanical forces on the PM glass tube are minimized. In case of a broken tube, the risk of contamination of the veto liquid and impact on other tubes is reduced. An additional  $\mu$ -metal shielding inside the steel chassis suppresses the magnetic field of the Earth. An alternative PMT encapsulation design similar to the inner detector is under investigation.

With 78 PMTs of this type, the effective coverage amounts to 0.6% of the total surface area of the veto detector. To increase the light collection, almost all surfaces in the veto detector will be painted white or covered with a reflective coating (diffuse reflection). Compared to a stainless steel surface, this improves reflectivity by more than a factor of two. Where applicable,  $\text{TiO}_2$  based white paint will be spray-painted onto the steel surfaces after welding the pieces together. The side walls of the veto cylinder, the floor, the bottom side of the lid and parts of the vessel support can be treated in this way. Because of the limited space between buffer and veto vessel, it is not feasible for the buffer vessel which has to be welded on site. For this reason, highly reflective sheets of Tyvek (e.g. type 1073B or similar) will be attached to it after the three parts of the buffer are welded together. Tyvek was tested and used in Super-Kamiokande, Borexino and in the KamLAND experiment. Its diffuse reflectivity for visible light exceeds 90%. With an estimated optical attenuation length of several meters, multiple reflections are highly probable, increasing the light collection efficiency by roughly one order of magnitude. This is especially important for the detection of proton recoils.

Figure 59 illustrates the simulated light collection inside the veto region (for details on the simulations see below). The plot shows the average number of hit veto PMTs for a 5 MeV positron generated at random positions inside the veto. This energy corresponds to the projected energy threshold of the veto system. The lower light collection efficiency in the region below the buffer vessel is due to the support structure that creates shadow effects there.

### 5.3 Simulations

Extensive Monte Carlo simulations were performed to ensure the feasibility of the experiment and optimize the detector layout. In case of the muon veto, our simulations addressed general design questions (impact of changing the veto thickness on the detection capability, for instance) as well as more detailed questions like the position of single photomultipliers among the support structure on the bottom of the detector. Special attention was given to the performance of the veto in identifying and classifying muon and neutron events and the resulting background rates. Muon tracking possibilities were investigated as well. Preliminary results indicate that in many cases, at least a rough track reconstruction sufficient for classification purposes is possible. The parameters modified during the simulations were the dimensions of the veto vessel itself, the optical surface of the veto vessel, and the number and placement of the photomultipliers.

The Double Chooz Monte Carlo simulation is based on the Geant4.7.0p1 simulation framework provided by CERN[89], GLG4sim[90], which is a generic liquid scintillator neutrino experiment package for GEANT4, and a dedicated extension to this package called DCGLG4sim. In addition, the muon propagation tools MUSIC[27] and MUSUN[83] were used to obtain muon spectra for the detector sites, as they are shown in plots 11 and 13.

Choosing a sensible multiplier start distribution, local energy depositions of 5 MeV by positrons were uniformly distributed throughout the veto volume to test for locations where only few photomultipliers would register the scintillation light. By moving and adding photomultipliers, then performing the same simulation, and iterating the process, the multiplier distribution was optimized to give an homogeneous response regardless of the place of energy deposition. Figures 57, 58 and 59 show maps of the detector, where the color represents the average number of photomultipliers hit if an energy deposition in this part of the detector happens. In parallel, the effect of changing veto thickness and optical surfaces of the veto volume were investigated. As the total volume of the far detector is limited by the existing pit, there is some motivation for decreasing the veto thickness to increase the target size. It could be shown that reducing the veto thickness from 60 cm down to 50 cm does not significantly lower the muon identification power of the veto. Simulations indicate that due to the high reflectivity surfaces mentioned previously, six times as many photons are detected compared to stainless steel surfaces, as shown in Figure 60. Furthermore, the improved reflectivity makes it possible to achieve sufficient light collection with only one ring of side PMTs and facilitates the installation of the buffer vessel, which will be welded together inside the detector pit. With the usage of Winston cones, the side PMTs might even be unnecessary. Research and simulation work concerning this are in progress.

Using the information gathered with these simulations, the veto detector layout was defined. This allowed starting high statistics runs with either muons or neutrons as primary particles and analyzing their output regarding both the rejection power of the muon veto, as well as its classification capabilities.

To estimate the veto performance, two different definitions of “rejection power” are useful. We will call the term

$$R_\mu = \frac{\text{detected muons with energy deposition in the detector}}{\text{all muons with energy deposition in the detector}} \quad (14)$$

the muon rejection power, while

$$R_c = \frac{\text{correlated events due to muons recognized in muon veto}}{\text{all correlated events due to muons}} \quad (15)$$

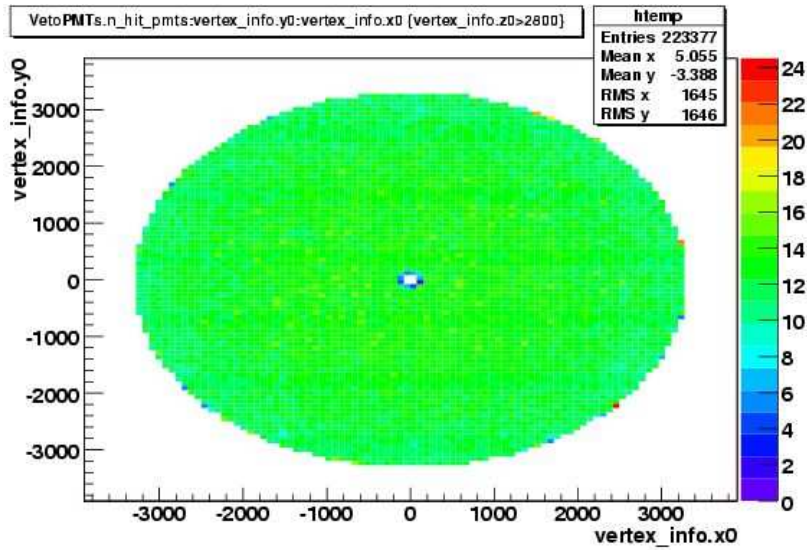


Figure 57: 5 MeV positrons started at a random point in the inner veto above the buffer vessel show a homogeneous detection multiplicity. The ring in the center corresponds to the neck.

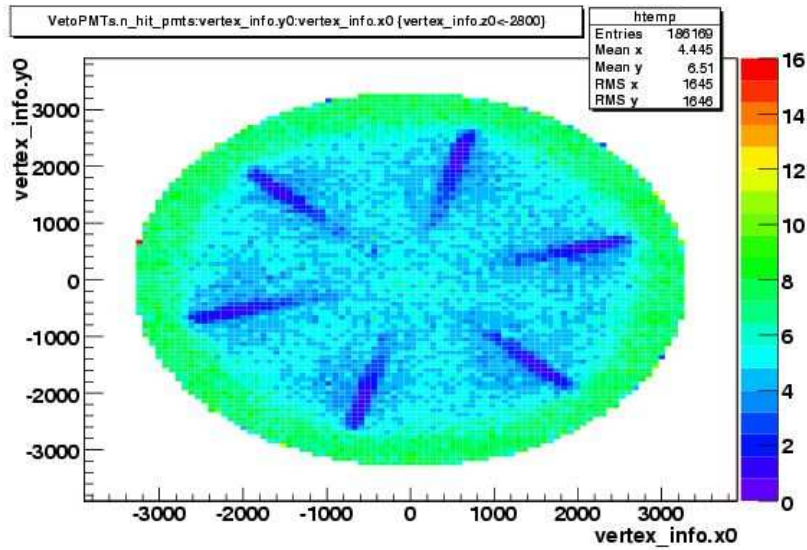


Figure 58: The support structure at the bottom of the veto strongly deteriorates photon propagation, leading to a position dependent multiplicity.



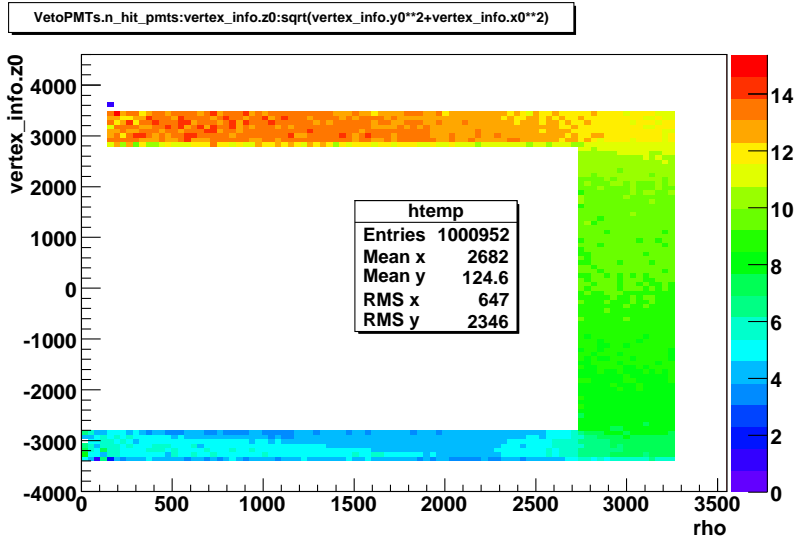


Figure 59: This side view shows the number of hit PMTs depending on the position of energy deposition. The effect of the support structure below the veto tank is visible.

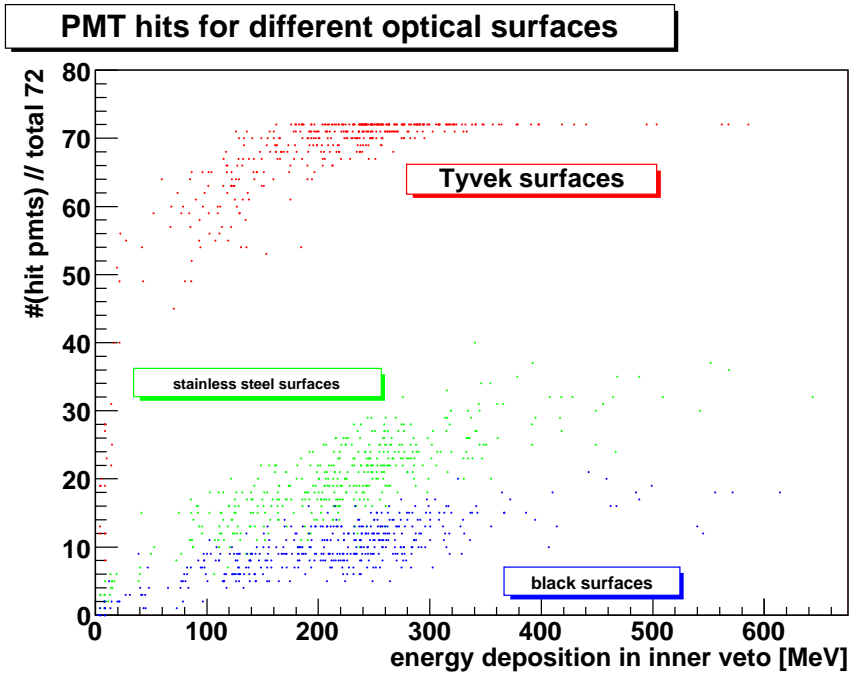


Figure 60: Comparison of different veto surfaces, using a previous PMT layout. The effect of high reflectivity surfaces is only weakly dependent on the details of the PMT distribution and equally valid for the updated 78 PMT geometry.

will be called the muon correlated event rejection power.

Both quantities require the definition of a “detected event ”in the inner veto. Several conditions can be imposed for such an event. One can demand a certain number of hit photomultipliers (i.e. a multiplicity threshold), in a typical time window of a few tens of ns. In addition, a threshold on the number of photoelectrons that are required for a valid photomultiplier hit is applied. Some of the muon events are seen only by few multipliers due to geometry reasons. Therefore, they have a low multiplicity, but possibly high individual PMT signals and can be identified by imposing a threshold for the sum of all collected signals. More sophisticated conditions divide the PMTs in different groups (e.g., rings, sectors, ...) and use the group signals in addition to individual and summed data to decide whether and which kind of a muon event has happened.

At the same time, there are additional practical considerations. Depending on the expected dark rate of the PMTs (about 4 kHz for the ETL tubes), a very low multiplicity condition may result in a high false trigger rate. High gain, which will be favorable for neutron detection, might result in fast saturation for muon events with long tracks in the veto.

In a simple scheme to get a multiplicity-optimized trigger condition, one just checks the scaling of the rejection power for variations of both multiplicity and required p.e. per PMT, and chooses conservative settings to compensate for simulation uncertainties. Figure 61 gives the number of identified muons as a function of multiplicity threshold and PMT threshold for a sample of 8646 muons.

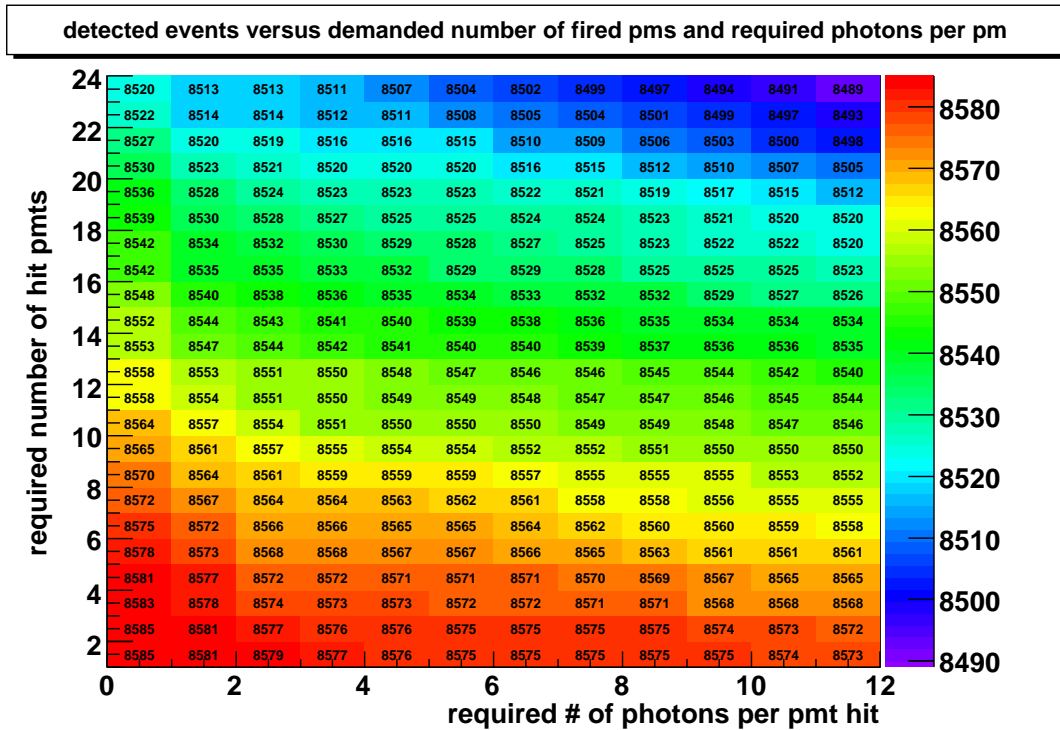


Figure 61: Muon identification probability plot for a geometry with 60 PMTs. In total, 10000 muons were simulated, 8640 of which generated an energy deposition in the veto or detector. A restriction to events with multiplicity of at least 15 and a PMT threshold corresponding to 5 p.e. would results in 98.8% muon rejection power without threshold on the energy deposition in the inner detector. The remaining 1.2% of events are due to very low energy deposition inside. Already a threshold of 10 keV increases this value to 99.5%.

To determine the muon correlated event rejection power  $R_c$ , we impose the following restrictions for a correlated event: there has to be an prompt visible energy deposition of 1-8 MeV in the target or  $\gamma$ -catcher, followed by a visible energy deposition of about 8 MeV up to  $200 \mu s$  later. In the current largest sample of muon events (about 100.000 events) with full scintillation, for all 30 events where these conditions are fulfilled, there is an identified muon in the veto, even when demanding more than 25 triggered PMTs and at least 15 p.e. per PMT. For reliable statistics, it is clear that a larger number of events has to be simulated. Currently, simulations are limited by calculation speed, as a single muon event with full scintillation processes takes about 30 seconds. To increase simulation speed, two main ideas are investigated. Simulation of secondary particles for events where the primary muon already deposits large amounts of energy in the veto can be skipped, spending full simulation time only on events where the identification might depend on secondary particle energy deposition. A huge speedup (on the order of factor 100) can be achieved if it is possible to omit scintillation simulation in favor of simple energy deposition simulation. This might be justified if we can generate a map of the veto volume which links energy deposition in a certain region to a PMT hit pattern.

To explore the feasibility of rejecting neutrons in particular, first simulations were done with a logarithmic energy distribution to check the veto response to neutrons of all energies with comparable statistics. The result is shown in Figure 62. As can be seen, high energy neutrons are generating large PMT signals and therefore have a high detection probability. Low energy neutrons, on the other hand, have only a slight probability of reaching the veto, as their range is limited (see Figure 63). Most dangerous are neutrons in the medium energy range, as they can reach the inner vessels without necessarily producing strong veto signals.

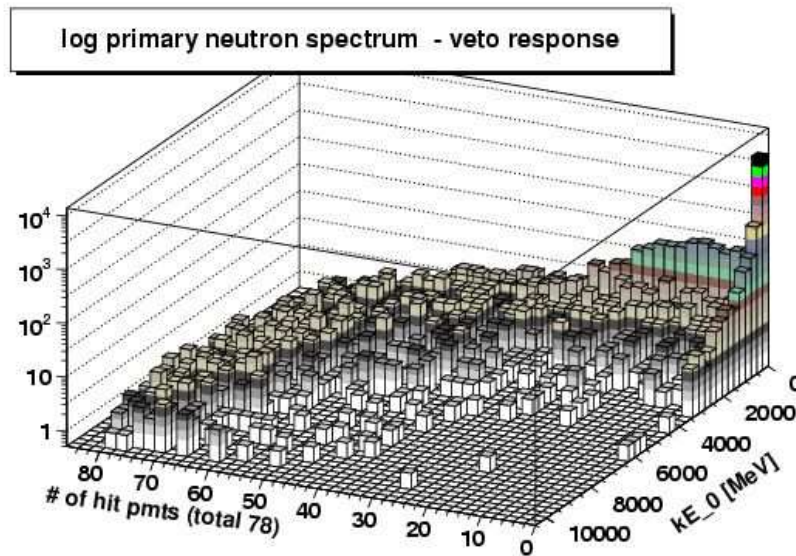


Figure 62: Neutrons with kinetic energies ( $kE_0$ ) exceeding 3 GeV create large amounts of charged secondaries, resulting in strong photon signals.

By using only the energy spectrum of the secondary neutrons and injecting them horizontally into the detector, it is possible to simulate a worst case scenario, where a neutron created right outside of the detector with no accompanying shower particles covers the minimum distance in the veto on its way to the inner vessels. The resulting rejection power can be regarded as a lower limit for the general case. Figure 64 shows the same plot for the neutron identification as Figure 61 for

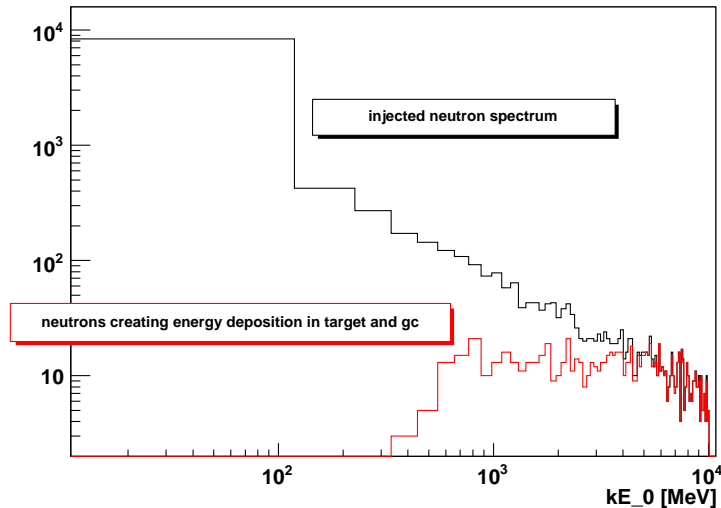


Figure 63: Low energy neutrons have a very low probability to reach the target or  $\gamma$ -catcher if they are created outside the veto.

muons. Comparison immediately shows neutron identification to be much more ambitious, due to the far lower amount of light generated. The neutron rejection power will therefore be significantly lower than the muon rejection power, as expected. Rejection power for candidates for neutron correlated events are shown in Figure 65. Performing only a minimum energy deposition cut for target and  $\gamma$ -catcher of 10 keV, one selects 272 neutrons out of 68000 injected. Of these, roughly one half does not show up in the veto at all. About 30-50 percent are detected in the muon veto, i.e. the thresholds conditions are fulfilled.

Another topic that was investigated with the simulation code was classification of events. Classification could be useful in two different situations. There will be an online classification scheme to decide how much information for a given event is to be saved. A second and more thorough classification can be achieved in the offline analysis of the data, where one has complete access to data registered both before and after the event under consideration. An important aspect of classification is track reconstruction. The scheme envisioned for track reconstruction starts with the first significant energy deposition identified with the photomultipliers. The velocity of muons is comparable to  $c$ , which gives us a time window in the ns range in which to expect signals from other multipliers, varying with their distance from the point of first detection. Crossing muons will produce such delayed signals and therefore allow classification. Events where no such delayed multiplier signal is found can either be stopped muon events or correspond to a muon track cutting through only a short section of the veto. By reconstructing the position of the first signal, some stopped muon events can be identified without doubt, for instance if the first signal indicates a position inside the inner top multiplier ring. A careful analysis of simulated events allows probability statements for the other cases. To incorporate some ordering structure for both simulation and experimental output, the following event classification scheme can be applied:

- Muons can cross the detector, either only through the veto or through inner vessels as well. These events will be called “veto crossing muon event” or “inner crossing muon event”, respectively.

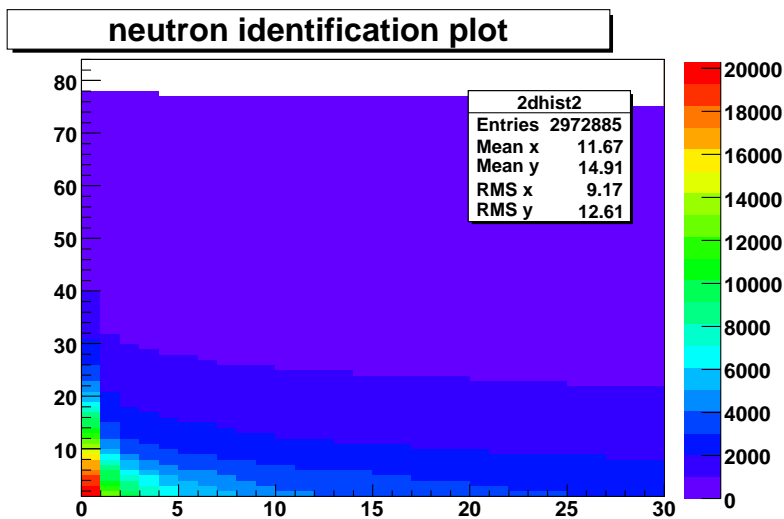


Figure 64: 22185 simulated neutrons out of 6800 lead to a energy deposition in detector and/or veto. For most neutron events, only one p.e. per PMT is registered. Imposing single p.e. threshold for the PMTs and a multiplicity threshold of 8, this results in a neutron rejection power of 71%.

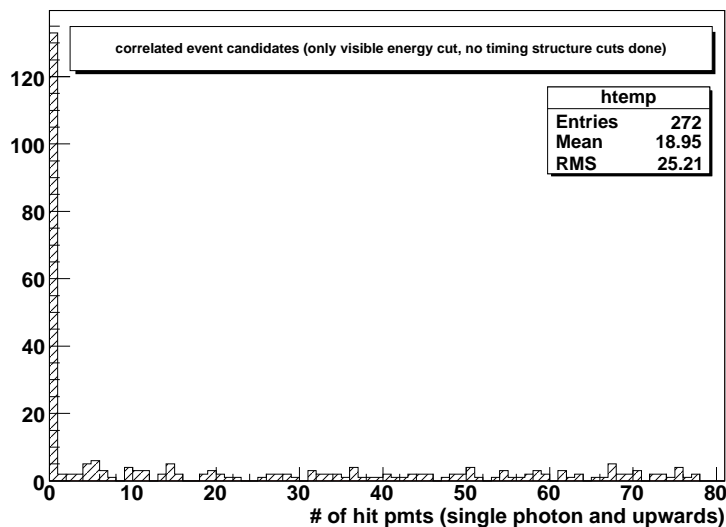


Figure 65: Starting from neutrons as primary particles, events with sufficient energy deposition for a correlated event in the target and/or  $\gamma$ -catcher are selected. About 30-50 percent of these are detected in the muon veto in this scenario.

- Muons that enter, but do not leave the detector (due to capture or decay) will generate “stopped muon events”. As muon capture is an important source of hard-to-veto background, the veto classification capability for this kind of event is of great importance.
- If a muon event is accompanied by a large amount of charged secondary particles, we will speak of a “showering muon event”.
- A showering muon missing the detector can lead to a “partially contained shower event”, where a sizable amount of secondaries are registered without the primary muon.
- Other event classes comprise “high energy photon events”,
- “internal decay events” resulting from alpha, beta or gamma emitters residing in the detector material,
- and “neutron events”, which are detected via recoil protons.

The simulations performed are currently analyzed in aspect to both to the rejection power for muon and neutron events, as well as its classification capabilities.

## 5.4 Magnetics

### 5.4.1 Sensitivity to Magnetic Fields

It is a well-known fact that large-area PMTs are subject to significant variation in collection efficiency due to magnetic fields on the order of the Earth’s field - i.e. a few 100 mG. For most applications this may not be important as such variations can be removed or reduced by calibrations. For detectors using very large PMTs such as Super-Kamiokande and KamLAND, compensating coils are used to reduce the field below 100 mG (the specification for Super-K). In the case of Double Chooz, the effects of magnetic fields are potentially more serious for two reasons:

- Since it is necessary to build two identical detectors, differences in the magnetic environment between the Near and Far detectors can lead to non-negligible systematic differences between them
- The necessity of reducing the singles rates from rock gammas to reduce accidental correlated events leads to including a relatively thick steel shield (17 cm or more) on the outside of the detector, roughly 65 cm from the first dynode of the PMTs. This mild steel could have a substantial permanent magnetic dipole moment. In addition, there could be significant differences in this moment between the Near and Far detector.

Several possible magnetic field mitigation schemes have been investigated:

- Replace 20-cm iron shield with 10-cm lead shield and use Helmholtz coils for Earth mag. field compensation. Replacement of the steel shield with lead after the construction is not practical. This option was investigated and found to be rather expensive;

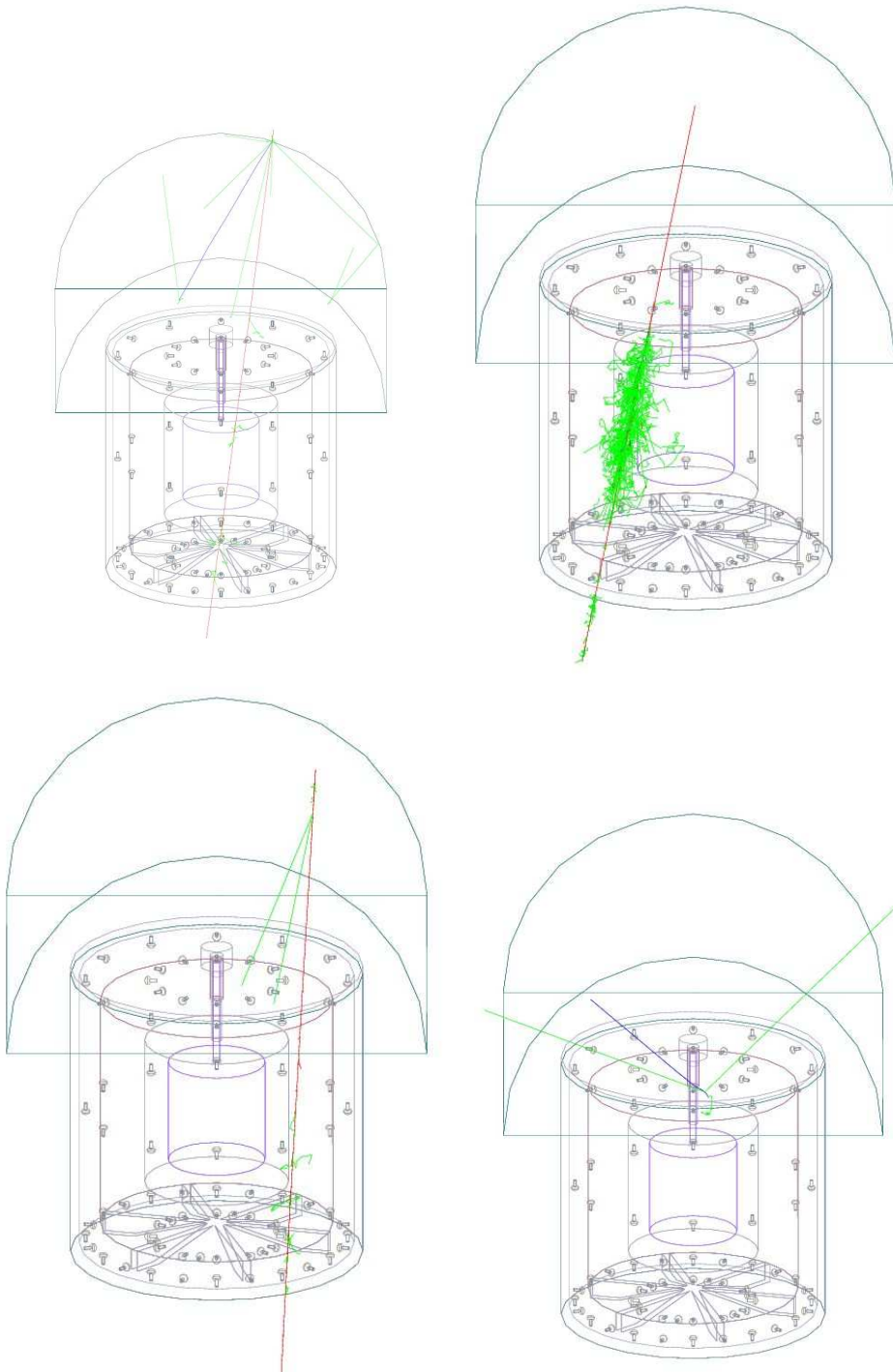


Table 26: Typical muon events (red:  $\mu^-$ , blue:  $\mu^+$ ): a through-going muon (upper left), a shower event next to the target (upper right), neutron creation near to the target (lower left) and a stopped muon (lower right).

- Global mu-metal shielding of PMTs. A mu-metal shield could be installed around the buffer vessel to reduce the magnetic fields inside the whole detector to acceptable levels. A shielding engineering company (Amuneal Manufacturing) was called in to make a preliminary design and costing for such a shield. This option, while feasible, turns out to be also quite expensive;
- Provide individual magnetic shielding for every PMT in the system. This shielding might be a simple mu-metal cylinder extending the length of PMT for about 10-15 cm above the PMT apex. Such shielding will restrict PMT angular acceptance and would have to be compensated for by installation of Winston cones. Construction of these hybrid cones and accompanying complicated PMT supports represents significant additional cost to PMT system.
- The effects of the steel shield could be reduced by measuring the overall dipole moment of individual pieces (which are in the shape of elongated rectangles) and assembling the shield in such a way that adjacent pieces have opposite directions. Particularly high-field pieces can be “de-permed” in a similar fashion to how Navy ships are demagnetized, a common practice for over 60 years. Compensating coils can then be installed on the outside of the detector to trim the resultant magnetic field down to acceptable, near-identical levels in the Near and Far detectors.

The last option listed above is now our baseline one, as it is the least expensive and has a relatively small impact on the construction schedule.

#### 5.4.2 Size of the Effect

The relative collection efficiency of a Hamamatsu R5912 8 inch PMT is shown in Figure 52 for a PMT with front face illumination from a point source on the central axis of the PMT (provided courtesy of Hamamatsu Photonics).<sup>5</sup> The x-axis shows the magnitude of the magnetic field applied along the x- and y-axis. Note that  $5 \times 10^{-5} T \sim 500 mG$  is about the magnitude of the earth’s field at the Chooz site. These data imply that if no action is taken then there would be a roughly 10% asymmetry introduced into the detector due to the Earth’s field alone.

More detailed measurements made on a Super-K Hamamatsu R5912 by our collaboration indicate that there can also be bias based on the position the photon strikes the PMT cathode, adding further complication. Using the same coordinate axis as in Figure 52, Figure 66 shows the variation in sensitivity across the front face of an R5912 which is sitting vertically in the Earth’s field and rotated 90 degrees about the vertical axis. These tests were done at LSU, where the Earth’s field is very similar to that expected at Chooz. Vertical/Horizontal is 426/242 mG for Baton Rouge and 439/200 mG for Chooz. Thus this figure corresponds to a transverse field of about  $2.4 \times 10^{-5} T$  across the face. The orientation of the x- and y-axis is the same as Figure 52. The right hand figure shows the same test done inside a mu-metal coated dark box, where the field is reduced to less than one-tenth of the ambient value. These figures confirm significant variation across the PMT face, especially near the edges where the path of the electron is very sensitive to the transverse field. They also show that reducing the field by a factor of ten essentially does away with this problem. In practice, the Super-Kamiokande collaboration found that a factor of five reduction was sufficient even for 20 inch PMTs for reliably being able to calibrate out any asymmetries. For Double Chooz we

---

<sup>5</sup>Although we use a Hamamatsu PMT to illustrate the point, the magnetic characteristics of all candidate PMTs is now under identical evaluation by laboratories inside the Double Chooz Collaboration. It is not expected that there will be significant differences between candidate tubes.



adopt this tested number as our design goal, which with our smaller PMTs is a conservative number.

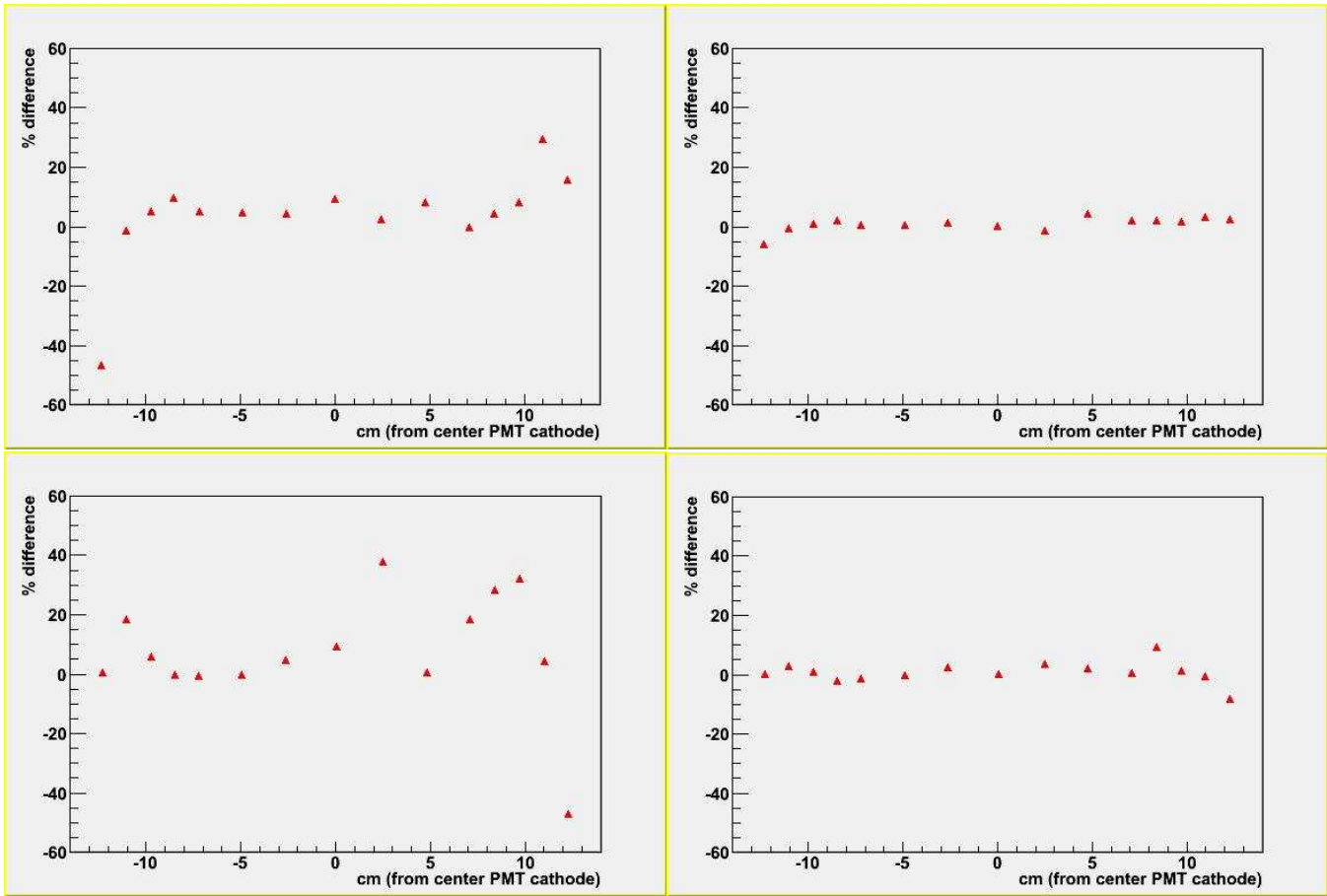


Figure 66: Percent variation in collection efficiency caused by the rotation through ninety degrees of an 8 inch PMT as a function of position across the face. Top (Bottom) is along the x-axis (y-axis). The right hand figure shows the same rotation inside a mu-metal shield. The x- and y-axes are defined as in the previous figure.

### 5.4.3 De-perming Experiments

We have determined the typical fields to be expected from mild steel of the type to be used for the Double Chooz gamma shield using a portable Hall probe and a 10x20x90 cm steel bar sample. For these measurements, the steel sample was elevated 1 meter above the floor on a wooden table near the center of a large open room. At 5 cm from the center of the sample the field is on the order of the Earth’s field, about 500 mG total. This falls to roughly 350 mG at 10 cm. At 50 cm the field due to sample is not detectable against the background field. Fitting the measured data to a single value of the magnetization ( $\vec{M}$ ) magnetic dipole moment density, fits the data poorly, so the actual situation is more complicated. There may be steel pieces in which fields are abnormally high, or in which the field is in an unusual direction. In this case, it may not be possible to use neighbors aligned oppositely to cancel the long-range field to the desired level and it will be necessary to de-magnetize (i.e. “deperm”) the steel piece on site. This is done by using a strong applied magnetic

field and driving the steel into saturation along one axis. The current is then reversed and the steel is polarized in the opposite direction, but with a field roughly 10% smaller. This alternating-current process continues with the applied field being smoothly brought to near zero, essentially walking the steel down the hysteresis curve to near magnetization.

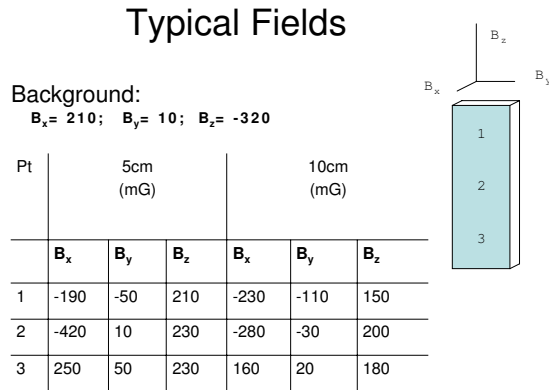


Figure 67: The fields measured near a sample piece of carbon steel using a Hall probe. Background from the Earth’s field is subtracted. Uncertainty is roughly  $\pm 50$  mG.

Experiments have been performed with small pieces of carbon steel in which the steel was successfully demagnetized to the level of the Earth’s field using an applied magnetic field of about  $10^4$  A/m. The process takes less than one hour. For large steel pieces, this implies that for a winding density of roughly 250 turns/m, that a current of approximately 40 amps will be required. This is possible with commercially-available power supplies and with standard high-current cables. We intend to next try this procedure on our 90 cm sample, which is roughly the thickness we plan to use for shielding pieces.

If successful, a deperming facility will be set up either at APC or the Chooz site. This facility will have a crane and solenoid capable of handling large shield pieces. It is envisioned that a few pieces per day could be depermed in this manner. Field measurements on individual pieces will be used to send pieces for deperming on an “as-needed” basis.

#### 5.4.4 Compensating Coils and Detectors

It is expected that the magnetic environment of the detector will be a relatively slow-varying field due to the sum of the Earth’s field and the residual field from the detector shield. In order to reduce this field to below 100 mG and to trim the fields in the Near and Far detector to as similar a value as possible compensating coils are planned for Double Chooz. Simulations show that currents of around 50 amps will be required with 5 coils in the vertical and 5 coils in the horizontal directions. Each coil (total 15) should be separately adjustable to minimize PMT transverse fields. It is planned to install a system of triaxial magnetometers inside the detector to allow for field trimming to make the Near and Far magnetic environments as similar as possible.

## 6 Trigger, Electronics, and DAQ

There are several major tasks that the Double Chooz electronics will undertake: processing signals from the detector and distributing them to acquisition systems; forming low-level triggers; and monitoring the stability and performance of the detector.

Each of these tasks are addressed in one or more electronics subsystems, to be implemented with a mix of commercial and custom electronics. The custom electronics is currently under development, and the status and plans for these parts of the Double Chooz electronics will be a major focus for this document. The subsystems will be discussed in the order in which signals pass from the detector to where they are digitized and stored.

### 6.1 High Voltage System

A research quality high voltage system will be specified and constructed for the near and far detectors of Double Chooz to provide clean, stable power for the PMTs and outer veto gas chambers. Optimally this system would have one HV channel controlling each PMT or gas chamber but to reduce the cost of the system, we plan to gang detector channels. A future upgrade could return to the single channel concept. The ganged configuration connects one HV channel to 8 PMTs or 20 gas chambers. It requires us to group PMTs based on their gain curve so that only a narrow range of HV values are required within a gang. To provide uniform detector response, fine adjustment of the HV to individual PMTs will be done with Zener diodes on the HV splitter boards. A single cable design for PMT connections will be used, so both HV and signal are carried on the same coaxial cable (RG-303).

#### 6.1.1 System Design

The HV system will be comprised of two parts, one for the near and one for the far detector. A single vendor will be chosen to provide the main high voltage components for the entire system. One type of mainframe (crate) and a minimum number of module types will be used throughout the system. Common software will be written to meet the controls, monitoring and safety requirements as described elsewhere in this document. To date, the three primary candidate-vendors are CAEN from Italy, Connecticut-based Universal Voltronics (UV) and ISEG from Germany. The baseline detector design calls for 93 and 84 channels of high voltage in the near and far detectors, respectively.

#### 6.1.2 Requirements and Specifications

The baseline PMT design requires +2.5 kVDC at 0.3 mA per tube. Ganging 8 such tubes results in a total current of 2.4 mA/HV channel. The outer veto gas chambers are planned to be +3 KVDC at 0.1 mA. Ganging 20 such chambers creates a load of 2 mA/ch. Ganging may need to be adjusted depending on vendor product capabilities.

- Ripple and noise – under full crate/module load these need to be below a level such that the effect on any signal is less than 1 mV peak-to-peak.
- Voltage set/monitor resolution - this will be at the level of 1 V or better.
- Maximum voltage – there must be a hardware provision that allows the setting of the maximum output voltage on a module or crate basis. This value shall be readback via software.

Software settable controls shall provide the ability to set software limits for the voltage settings.

- Current trip set/monitor resolution – it must be 1  $\mu$ A or better.
- Voltage Ramp up/down – it shall be in the range of approximately 10 to 500 Volts/sec, programmable.
- Operating range – it is approximately 0 C to 40 C, dry atmosphere.
- HV outputs shall be floating, such that the crate ground is independent of the return for the HV channels.
- AC power supply – it shall be approximately 220 VAC, 50 Hz.
- Polarity – both positive and negative polarity modules are required.
- Communications – complete control of the HV system must be able to be accomplished via a standard TCP/IP protocol based Ethernet connection. Provisions to control individual crates from either a front panel or a front panel connection must be provided.
- Electrical Connections – the HV connections must be through either standard SHV connectors or an HV certified multi-pin connector of proven reliability in this application.

### 6.1.3 Control and Monitoring Software

The software to run both detector sites will run on a single PC located at the far site, as it will be installed first. All HV crates will be controlled via an Ethernet connection. The type of software needed will depend somewhat on which manufacturer is chosen to supply the HV system. The basic specifications however are the same regardless of which vendor is chosen. The software will access and download to the crates a carefully controlled configuration file containing all channel voltages, trip current settings and limits. A crate polling routine will monitor and record voltages, currents and temperatures. Alarms will be sent out to the operators as needed should tolerances be exceeded. The slow controls system will also monitor temperatures, etc. but on a more global scale.

### 6.1.4 Uninterruptible Power Supply

A UPS will be used to prevent damage to the HV system components as well as the PMTs and gas chambers resulting from AC line fluctuations, brownouts or blackouts. A hold time of 5-15 minutes is planned, depending on estimated AC interruptions and UPS system cost. A double conversion will be used as only a true online, double-conversion UPS can provide pure, full-time sine wave AC output free of surges, voltage fluctuations and line noise. It actively converts raw input from AC to DC, then back to sine wave AC output with enhanced protection from harmonic distortion, fast electrical impulses and other hard-to-solve power problems not addressed by other UPS types.

### 6.1.5 Cabling

Cables from the HV modules to the HV splitter boards will be provided. The type and quantity of the cables will be determined after the vendor is selected as they may use different connector/cable types.

### 6.1.6 Evaluation Phase

This phase is to test and verify the manufacturers' specification claims by performing measurements on actual production HV modules and crates supplied by the vendors to the University of Tennessee. These units will be on loan to us and will be returned to the vendor at the conclusion of the testing. No direct cost is involved, other than shipping charges. Another aspect of this phase is to evaluate the software coding requirements for each vendor and to estimate the time and expertise required for the task. The deliverables from this phase of the development work will be HV and UPS requirements and specifications documents suitable for use in submitting RFQs.

## 6.2 Electronics

### 6.2.1 HV Splitter

For the inner detector, the PMT signals will first pass through High-Voltage (HV) Splitters. Double Chooz will use a single cable for each PMT, carrying both the HV and the PMT signals, for reasons of cost, for minimizing the dead-volume in the detector and the feed-through area as cables exit the detector, and to minimize the effects of ground loops between HV and signal cables. In all of this, it must be noted that the PMT signals are expected to be rather small ( $\sim 2$  mV), so noise must be kept well below the millivolt level. It is the primary job of the HV splitter to decouple the signals coming out of the PMTs from the HV supplies. In addition, the HV Splitters will terminate the PMT cable transmission line to minimize pulse reflections, distribute HV among several PMTs per HV channel to reduce the HV cost, and provide filtering of the HV to reduce noise that comes from the HV power supplies. Figure 68 shows a schematic for a simple four-channel prototype of the HV Splitter that has been fabricated, which has the basic features that are expected to be used in the final HV Splitter design. While it is unlikely that any of the Double Chooz PMTs will be operated above 2 kV, the specs from Hamamatsu indicate a maximum voltage around 2.4 kV. As a result, the HV Splitter is designed with components that are rated for a minimum of 2.5 kV, while most are rated at 3 kV. Figure 69 shows the simulated performance of the HV Splitter with a square-pulse input, with a back-terminated PMT and 100 ns of cable between the PMT and the HV Splitter. For this kind of 'RC' termination, required because of the need for HV decoupling, one can expect 3–5% signal reflections. Having termination at both the HV Splitter (where the terminating impedance is the output cable) and the PMT base reduces the reflections to well below 1%. An alternative termination scheme, similar to that used on the Borexino experiment [82], was examined and rejected because the presence of parasitic capacitance in inductors required the use of significantly smaller decoupling capacitors, with correspondingly more signal distortion. This prototype was designed to test the scheme of having one HV channel supply four PMTs; the final design will most likely have a HV channel supply between two and eight channels. This scheme depends on being able to group PMTs of similar nominal voltage, however the requirements are not particularly difficult to meet: with PMT nominal voltages ranging from 1.2 kV to 2 kV, on average one can find groups of 8 PMTs within a 10 V interval.

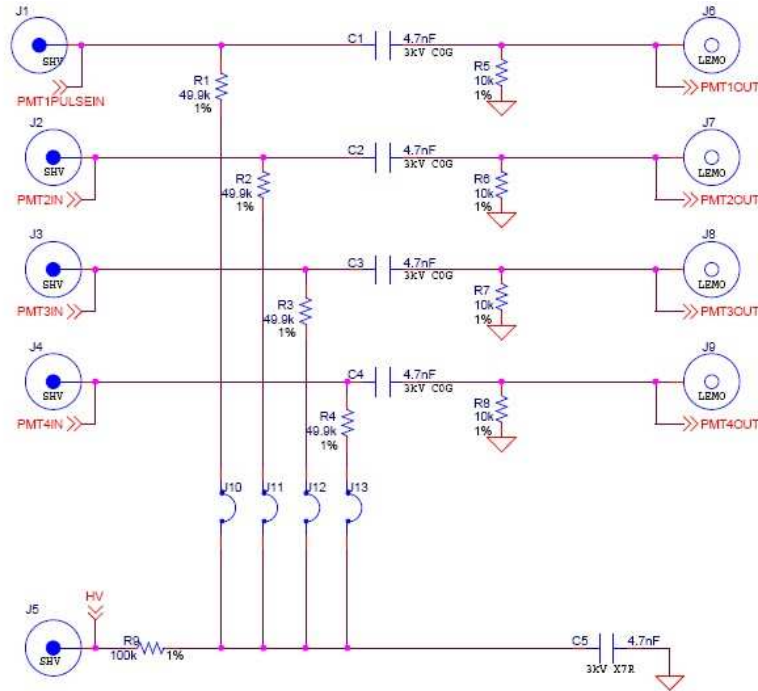


Figure 68: Schematic for a four-channel HV Splitter prototype. This schematic was used both for a prototype circuit board and to simulate the performance of the HV Splitter. The jumpers in the schematic can be replaced with Zener diodes to allow channel-to-channel variation in high voltage.

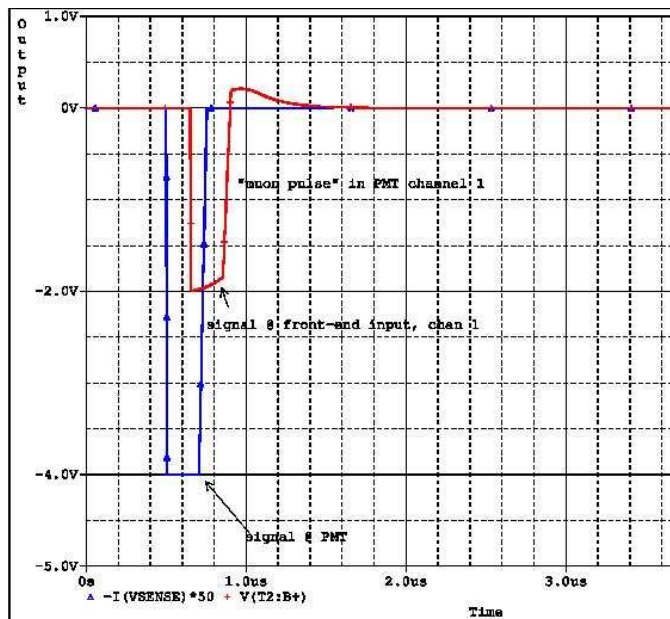


Figure 69: Simulated performance of HV Splitter with a square-pulse input. The use of a square-pulse emphasizes the differentiating effect of the HV blocking capacitance.



inductively-couple cross-talk between channels that is not apparent in the simulation. Tests will be conducted at every stage of the HV Splitter (and other downstream electronics) to measure, and if necessary mitigate, any cross-talk, but it must be noted that such cross-talk would be present regardless of the level of ganging of PMTs on the HV supplies.

### 6.2.2 Front-End Electronics

The Front-End subsystem receives PMT signals from the HV Splitter, performs amplification, pulse-shape and baseline corrections, and distributes the signals to downstream electronics (see Fig. 71). The input signals to the Front-End will be quite small (millivolt level), so the entire Front-End will be a pure-analog design to avoid any digital noise leaking into the signals.

- Amplification: total gain in the range of 10–15, so that single photoelectron signals are 20–30 mV amplitude.
- Calibration input: single analog input per Front-End module; the calibration pulse will be fed into all of the channel inputs.
- Channel disable: RF-relays used to disable input channels under computer control. This provides a more robust disable than ‘chip disable’ features on the amplifiers. The digital logic that controls the channel disable is completely quiescent during normal data-taking, and is a simple open-collector TTL bus driven from a single VME output register per detector.
- Pulse shaping: to restore pulse shape from cable attenuation and HV decoupling capacitor.
- Baseline restoration: we will avoid some of the baseline-shift problems caused by large (muon) signals and capacitive coupling, by using DC coupling wherever possible. The amplifiers needed for high-speed and low-noise performance, however, tend to have unacceptably large DC offsets. To avoid this, we are developing baseline restoration circuitry to remove the offsets. The first full-speed prototype, built and tested in September 2005, used active feedback of low-frequencies components in the signals (including DC) to remove the offsets and improve the rejection of line frequency pick-up. This prototype was completely successful at removing DC offsets, but was somewhat more complex than desirable, and required some minor modification to have acceptable performance for saturating pulses.

A new prototype is currently being produced for testing the front-end channel disable and summation functions. This new prototype will also test a different (‘feed-forward’) and simpler technique to cancel DC offsets. Results from SPICE simulation of the new circuit are very encouraging, but tests of the prototype will be needed before a final decision.

- Pulse summation: a simple analog sum of the input signals is produced, for use in trigger and diagnostic systems.
- Muon/Trigger channel: a separate attenuated path through the Front-End is provided for getting information about background muon events. This attenuation helps to avoid any electronic limitation of the muon signals, at the expense of low-amplitude signal information. We will have the option (by means of zero-ohm surface-mount jumpers on the Front-End board) of having individual muon outputs for each input, or of having only a summed muon output. Note that the circuitry for the muon channel is also used in the Level-1 Trigger implementation.



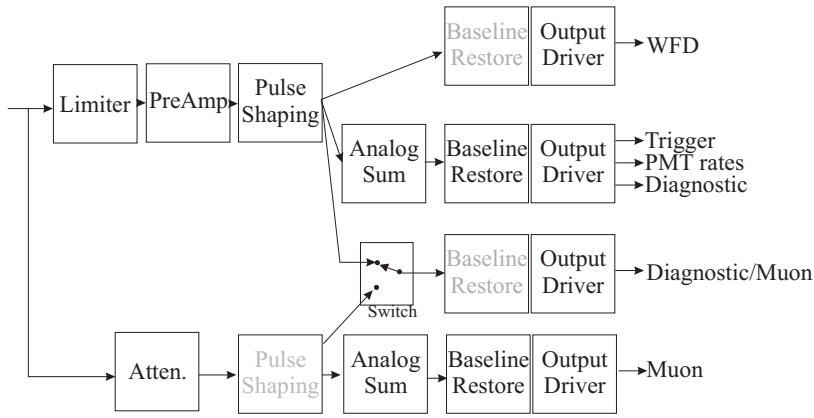


Figure 71: Block diagram of Double Chooz analog front-end functions. This design will also be used for performing analog summation for the L1 trigger. The ‘switch’ in the diagram will be implemented with a zero-ohm surface-mount jumper.

The implementation plan is to first test and optimize individual functions of the Front-End (summation, baseline restoration, etc.) using specific prototype circuit boards, then to produce a ‘few channel’ prototype that includes the full range of circuitry for a limited number of channels, before proceeding to a final design of the Front-End module.

### 6.2.3 Inner Veto Electronics

Since - in the current planning - the 78 veto PMTs are considered a part of the detector just as the inner PMTs, the general organization of electronics is very similar to that of the inner photodetection system. High voltage and signal are fed to/from the PMT with a single coax cable. The cables are running through the veto liquid up to the top and to a HV splitter box. The trigger condition relies on the number of hit PMTs, the analog sum and for more sophisticated trigger scenarios on the hit pattern. Inner Veto events can trigger the DAQ of the inner detector, and vice versa. The integration in the DAQ of the experiment will be done on two levels: one the hand using the trigger boards of the experiment on a hardware level, and also in the software that reads, processes and stores the FADC data for all channels .

### 6.2.4 Outer Veto Electronics

The electronics design is based on providing a digital output from the modules. A single discriminator threshold will be applied to each of the 24 chambers within a module. To provide this functionality, we foresee a single printed circuit board which will be placed on one end of each module. The board will connect to the threaded brass connections provided by the mechanical construction of each tube. A single high-voltage connection will supply all chambers in that module. The analog signal from each wire will be read-out and immediately put into a discriminator which operates in time-over-threshold mode with a 10MHz clock (i.e. digitized every 100 ns). This discriminated signal will be passed into an FPGA on the front-end card which will compile the output from all 24 chambers into a single 24-bit data word. When a trigger condition is satisfied, a 24-bit timestamp will be appended to each 24-bit encoded data word and it will be sent through a hot-link connection to the back-end VME system. We foresee the following three trigger conditions:

1) Simple Coincidence: Since any muon will have greater than a 99% chance of causing a signal in at least 2 out of 3 chambers within a single module, this will provide the most effective method for reducing the random singles rate while maintaining a very high efficiency of muon detection. In order to avoid missing events which may span a clock boundary, we propose to use a simple sliding window of two clock cycles which will be used to define a coincidence. 2) Long Pulse Trigger: A showering muon may have multiple particles interacting in a single chamber over a period of time up to  $1-2\mu\text{s}$ . For that reason, the data for a channel which is above threshold for contiguous clock-cycles will be stored. If the simple coincidence described above is satisfied at any time during the contiguous period, all digits for the contiguous period will be sent to the back-end system. 3) Diagnostic Trigger: For calibration or debugging purposes, a special trigger will be available. In this configuration, if any of the 24 channels are above threshold, the 24-bit data word will be triggered and sent to the back-end system. Since this will have a high rate, this is foreseen as a configurable trigger condition.

The back-end is expected to be based on a single VME 9U crate at each detector location. Communication between the front-end and back-end will be done serially with the use of fiber-optic cables, to reduce the possibility of ground loops. The VME modules will consist of independent data channels for each input channel. The data will have address and control codes appended and will be stored in the VME processor for collection by the main data acquisition system. A synchronized timing system will be provided that allows the correlation of events from the outer veto system with those recorded by the main detector to within 50 ns.

### 6.2.5 Toward the Level-1 Trigger

A detector of a geometry where an inner scintillator volume is surrounded by PMTs distributed uniformly on a surface, will have the property that the total amount of light collected by the PMTs is directly proportional to the energy deposition, in the absence of light attenuation. For Double Chooz the distribution of PMTs is not perfectly uniform, however it is close enough to uniformity to make total light a useful proxy for event energy. In addition, the small size of Double Chooz makes light attenuation only a small correction, negligible for the purposes of creating a trigger. As a result, a simple and natural *energy* trigger for Double Chooz is simply to sum up the phototube signals from the inner detector, and use a discriminator to set an energy level for the trigger. In practice, the summation of so many PMTs means that any common-mode noise (ground-loop noise, etc.) has to be very stringently suppressed, since it will be greatly amplified in the summation. This motivates much of the efforts in upstream electronics systems to avoid or ameliorate noise inputs. The trigger summation occurs in several stages; the first stage is in the Front-End modules, where all of the input signals handled by that module are summed and provided on a single output. Additional levels of summation are required. Details can be found in section 6.3.

## 6.3 Trigger and Timing

### 6.3.1 Concepts

The trigger and timing system has to provide a highly efficient trigger to the Double Chooz experiment for neutrino events as well as for several types of background events. The trigger has to be reliable, i.e. trigger failures must be rare and easily detectable, and the trigger efficiency must be measurable with sub-percent precision. The trigger system will also distribute a common clock signal to the experiment and provide a time stamp for all events.

A two-stage trigger system is foreseen. The level-1 trigger is based on the analogue signals from the detector which are discriminated and analyzed in FPGAs (Field-Programmable Gate Arrays). A positive Level-1 decision triggers the readout of the detector. The readout is followed by a level-2 software trigger. This section covers the level-1 trigger only.

There will be independent trigger systems for the far and near detector with independent clocks. The clocks will be synchronized between the two detectors through either a cable connecting the two triggers or through GPS systems. The frequency of the clocks in both detectors must be identical. Synchronization of the phases is not required.

The trigger will receive input from the PMTs of the inner target and the inner veto. The signals of 16 PMTs will be pre-summed in the electronics of the Front-End modules (see sect. 6.2). The trigger only receives the signal sums. Input from the outer veto and the calibration systems can also be processed (for example from the laser system sec. 7.2.3). It is possible, but not foreseen, to apply veto conditions on the trigger level. Instead an event in the veto detectors will be read out as well as a neutrino candidate following it. It is left to the offline analysis to reject cosmogenic events. The signals of the groups of PMTs are discriminated individually to provide an approximate multiplicity of the event. In parallel the total signal sums from the inner target and inner veto are derived and discriminated on several levels. The trigger will allow conditions on the total energy and multiplicity, or any combination of these, to be applied. Special care will be taken to avoid the amplification of baseline-shifts, common-mode noise and saturation through the summation.

To keep the trigger conditions flexible, FPGAs will be used to apply the trigger conditions to the discriminated signals. For redundancy, two independent trigger boards will be used for the inner target, each based on only half of the groups of PMTs. This guaranties that hardware failures do not result in the loss of events and can be easily detected. A third trigger board will handle the inner veto and additional trigger inputs. A careful simulation will determine the initial trigger conditions. They can be adapted once experience with the real detector is available. The following list gives initial ideas on some of the necessary trigger conditions:

- **Inner Target Neutrino Trigger A**

Approximately 0.5 MeV energy threshold on the total energy in the inner target and at least 2 groups of PMTs above noise (to exclude single sparking PMTs from triggering). The trigger is based on the first half of PMTs only (groups A).

- **Inner Target Neutrino Trigger B**

Same as above, but based on the second half of PMTs (groups B).

- **Low Energy Neutrino Trigger A + B**

This neutrino is the same as above, but with a lower energy threshold. It's rate will be too high and therefore only a prescaled selection of events will create a real trigger. The energy threshold and the prescale factor will be adjusted based on the detector noise. This trigger allows the threshold behavior of the main neutrino trigger to be studied.

- **Inner Target Muon Trigger A + B**

A muon will create a signal in the inner target that fires all groups of PMTs. The trigger will be based on multiplicity only.

- **Inner Target Muon Trigger A + B – PMT with low gains –**

Some PMT set with a low gain could be installed to better detect and tag showering muons.

- **Inner Veto Muon Trigger**

A trigger based on energy threshold and minimum multiplicity in the inner veto.

- **Inner Veto Low Energy**

A trigger on the inner veto with a lower threshold to study the trigger efficiencies. Scaled-down in rate as above.

- **Random Trigger**

A trigger with an adjustable frequency triggering the readout at fixed time intervals. The events will be uncorrelated with any physics process in the detector (therefore random) and will allow detector noise to be studied.

### 6.3.2 Trigger Outline

A schematic view of the trigger is shown in fig. 72. There will be three such units (trigger boards) for each detector. Two handling the inner target with half of the PMTs each and the third one handling veto and calibration. A global trigger word is combined from the three trigger boards on the master board and the trigger decision is formed as a logic 'OR' of all triggers.

Input signals from groups of PMTs are received and discriminated on two different, programmable thresholds. The energy sum is derived and discriminated on four levels. For the veto and calibration triggers the energy sum will be modified and input for logical signals will be provided. The output rate of the discriminators is available for monitoring. The status of the discriminators is stored in the input register and read out in case of an event. The trigger logic is fully programmable and may combine any input signals. Up to 8 different triggers can be created in each board. The output of the trigger logic is stored in the output register 0. A scaler for each trigger allows the reduction of its rate by accepting only every n.th trigger, where n is programmable. After down-scaling, the triggers are combined with a mask that allows individual triggers to be suppressed. The result is transmitted to the master board.

### 6.3.3 Clock and Timing

The trigger and timing system will provide a 62.5 MHz clock to the whole detector. For this purpose a free running oscillator will be placed on the master board to allow stand-alone running. A possibility of synchronizing the clock to an external reference is foreseen. With a cable connecting the far and the near detector the two clocks could be synchronized.

A separate timing module is under discussion that receives the clock and an absolute time from the GPS system. With such a timing module both detectors could be synchronized to GPS. It would also allow an absolute time stamp for each event, should this be necessary for physics.

The trigger will have the possibility to receive a busy signal from each subdetector should it not be ready for data taking.

## 6.4 Data Acquisition System

The Double Chooz Data Acquisition System aims to record neutrino interactions observed through the annihilation of a positron and the delayed capture of a neutron by a Gadolinium nucleus. In addition, many other events are also considered worth reading out, most of which are induced by cosmic rays. The event rate amounts will be around 600 Hz in the near detector.

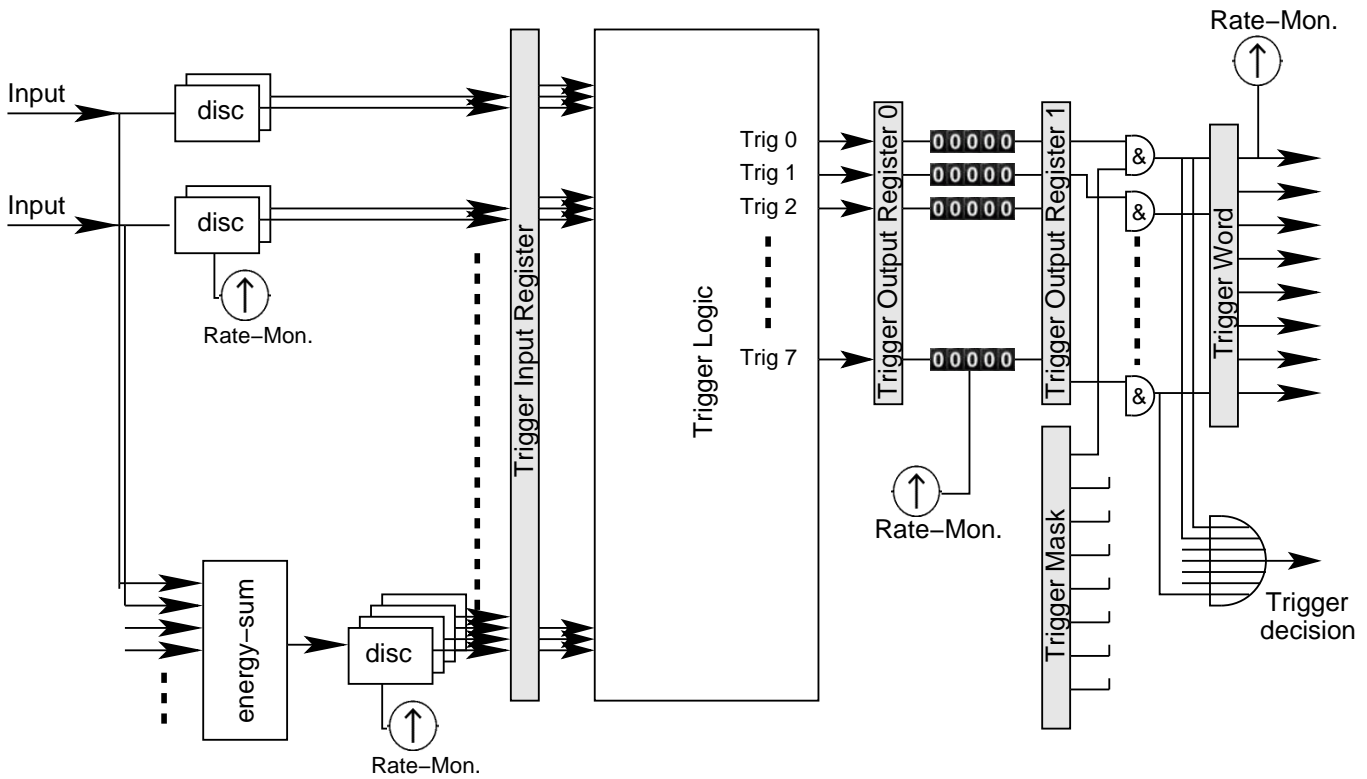


Figure 72: Schematic layout of the trigger. Input from the front-end electronics on the left, output to the data acquisition on the right. Shaded rectangles are registers that will be read out. The discriminators are labeled 'disc'.

The main principle of the designed system is to digitize and store on mass storage every event occurring in the detector which deposits more than 0.5 MeV in the inner cylinder (Target + Gamma Catcher) or 5 MeV in the Inner Veto. The digitization of the photomultipliers will be performed by Waveform Digitizers, with one channel per photomultiplier. This has been chosen in view of recording pulse shapes, for the absence of dead time and the simplicity of operation.

## 6.5 Main Features of The Waveform Digitizer module

The Waveform Digitizers are built from 8-bit Flash-ADCs operated at 500 MHz, static random access memory, and a smart memory controller, which allows uninterrupted digitization and read-out without dead time. The digitizer is currently under co-development at AstroParticle and Cosmology Laboratory (APC) and Costruzioni Apparecchiature Elettroniche Nucleari (CAEN). It will be commercially available as a NIM module with USB or optical fiber data link and as a VME64x module. Double Chooz will use the VME module which will house 4 channels in a 1-U-wide device. A NIM/USB prototype is currently under test. Important parts of the design have already been validated but the firmware is still under development. The transition from the NIM/USB model to the VME one will be straightforward, due to the modular design. The production of modules for Double Chooz will start at the end of 2006.

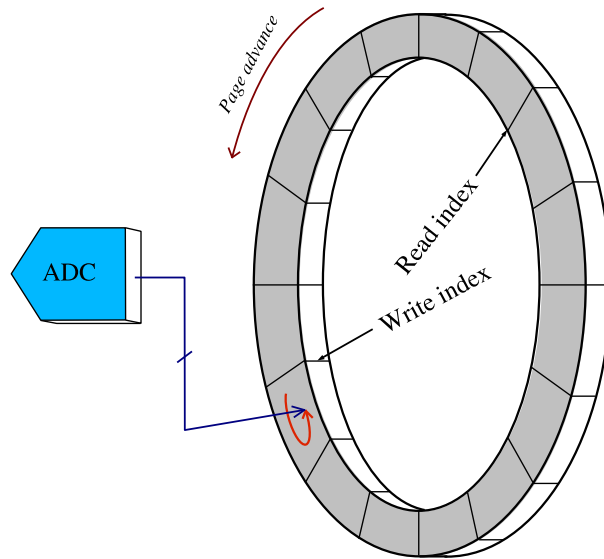


Figure 73: Operation of the Waveform Digitizer as a FIFO

### 6.5.1 Operation of the Waveform Digitizer

The four channels of the Waveform Digitizer module (WFD) are operated with one 62.5 MHz clock, which can be generated onboard or taken from a front-panel input. In Double Chooz, the WFDs will all use the same clock, delivered by the trigger system. In this way, all channels of all modules are synchronized. From the 62.5 MHz clock, a 500 MHz one is generated onboard by a Phased Lock Loop (PLL) to clock the flash-ADCs. Triggers are accepted at the 62.5 MHz clock rate. The onboard memory may be accessed through the VMEbus without disturbing the digitization, like with a dual-port memory. The memory controller manages the flash-ADC data in the following way, illustrated by Fig. 73:

- The ADC samples are continuously stored in a 1024 Bytes rotating buffer, thus keeping a history of the past 2048 ns. The memory is divided in 1024 such rotating buffers (or pages).
- On the first 62.5 MHz clock after detection of a trigger, the last ADC sample is written to the current rotating buffer; subsequent samples are written to the next buffer. The time difference between this trigger and the previous one is stored, along with the value of a 16-bit word read from the front panel. The time elapsed between triggers is later used to search for coincidences; the 16-bit word is used to read the event number and various flags generated by the trigger system. Rotating buffer, time difference and 16-bit word constitute an event for the waveform digitizer system.

The Waveform Digitizer's trigger logic and the computer in charge of the read-out keep synchronized by the mean of two registers:

- The Write Index indicates the buffer currently in use to store flash-ADC data. It is incremented at each trigger.

- The Read Index indicates the first buffer that cannot be re-used yet because it has not been read. This index is manipulated through the VMEbus. When the Write Index is just below the Read Index, the trigger is disabled, causing dead-time; therefore the absence of dead time depends on the ability of the VME master to smoothly read the incoming data.

This synchronization mechanism is exactly the one of a FIFO, where the elements are the events, with a capacity of 1023 events, but with the additional feature that the full content of the FIFO is exposed to the read-out system, not only the most ancient event.

### 6.5.2 VME layout of the Read-out

The Waveform Digitizer can handle a variety of VME access modes, ranging from D16/D32 random access to BLT64, 2eVME and 2eSST which allows data transfer rates from 160 to 320 MByte/s. The modules will be plugged into VME crates (7 for the PMTs of the inner cylinder), with 19 WFDs and a VME master in each crate. The VME masters will be interconnected by a 1 Gbit/s Ethernet private network to a computer in charge of event building. Each of them will perform the read-out of its own crate.

### 6.5.3 Second Level Trigger and Data Reduction

The principle of the Data Acquisition of Double Chooz is to record all single events, leaving to the offline analysis the task of deciding what to do with them. However the amount of data available in the Waveform Digitizers is too big to be easily managed offline.

For each event, a  $2 \mu\text{s}$  record is available. This is much more than the duration of an event, ( $< 200 \text{ ns}$ ). Considering a duration of 200 ns for each event and a trigger rate of  $600 \text{ s}^{-1}$ , the total data flow would be around 2.6 TB/d for only the pulse shapes of the target PMTs, which is still too big. Actually, in the near detector, most of the events will be cosmic muons crossing the Inner Veto and missing the Target. For these events, only the starting and ending times need to be recorded, while for neutrino candidates, the whole pulse shape could be recorded for all channels. For other events, various data reduction schemes can be considered if the events can be sorted online.

The second level trigger, implemented at the heart of the read-out software, addresses this goal, based on the following pieces of information:

- the trigger flags provided by the various discriminators,
- the time information recorded by the Waveform Digitizers.

Combinations of these informations lead to fast identification of coincident low energy events (neutrino candidates), low energy singles (gammas), and cosmic rays crossing the inner cylinder or not. No event will be rejected online; the second level trigger will only decide the size and format of the data. A possible data reduction strategy is detailed below.

### 6.5.4 A possible Data Reduction Strategy

A possible example of data reduction strategy is presented in table 27, where the following event categories have been considered:

- Coincidences: two energy depositions above the 0.5 MeV threshold in the target+ $\gamma$ -catcher volume of the detector, within a time window ( $\sim 200 \mu\text{s}$ ) chosen to be larger than the one applied for the offline identification of neutrino candidates. Besides neutrino interaction events, correlated backgrounds and accidental coincidences will be retained. The full available information on pulse shape will be stored for such events.
- Gammas: a single energy deposition above 0.5 MeV and below 50 MeV in the target+ $\gamma$ -catcher volume of the detector. The rate of such events will be about 10 Hz, dominated by gammas. Storing the full waveform information would lead to a huge data flow ( $\sim 70 \text{ GByte/d}$ ): one possibility is to record the pulse starting time for each PMT and the waveform for groups of PMTs. The full information could be stored for singles depositing an energy larger than 6 MeV, which include neutrons, occurring with a much lower rate ( $\sim 10^{-2} \text{ s}^{-1}$ ).
- Muons: a veto window will be applied in the offline analysis after each muon crossing the detector. For such events, it will be sufficient to record the global timing, together with the minimal information in the event header.
- Muons through target: muons interacting in the detector can give origin to radioactive ions which decay with rather long lifetimes ( $3\tau \sim 0.6 \text{ s}$ ) mimicking neutrino interactions. Whenever a coincidence occurs, all the muons crossing the target volume one second before will be recorded. The large deposited energy will cause all PMTs in the central region to be saturated and the only data which may be used is the starting and ending times of each pulse. This, combined with the timing and charge in Veto PMTs, can provide the necessary handle for a rough reconstruction of the muon direction and to distinguish muons stopping or showering inside the detectors from the ones crossing it. There is margin to store more details on the Veto PMTs, such as pulse rise time or charge in a given time window, or the charge and even full waveform for few dedicated PMTs with lower gain (non saturated) in the target region.

The final strategy will be defined after detailed simulation studies and on the basis of experience during the first year of data taking with the far detector alone, where the rate of singles and coincidences will be the same as in the near detector while the cosmic muon flux will be lower by about a factor of 10.

### 6.5.5 Dead time

The Waveform Digitizers behave like FIFOs; they do not incur any dead time as long as the read out system (VMEbus, processors, network, mass storage) can sustain the data rate. The designed system is able to sustain the data flow through the VMEbus and the Ethernet network; therefore the full read out process is free of dead time. Although the online data reduction aims mostly at making data easily manageable offline, as a side effects it keeps the data flow even farther below the capability of the system. In case, by some unforeseen effect, the digitizers would miss a trigger, this would be detected by the online program which would stop immediately the acquisition, to avoid corrupting the data already taken with a dead time uncertainty.

A general discussion of the dead time and the induced systematic uncertainty can be found on page 2.2.3.



Category	Identif. criteria	Rate ( $Hz$ )	Stored data	Data flow ( $GByte/d$ )
Coincidences	$2 \times E_T > 0.5$ in $< 200 \mu s$	0.1	Full	2
Singles	$0.5 < E_T < 50$ & $E_V < 5$	10	$t + Q$ for all PMTs + $WF$ per groups	5
- neutrons	$E_T > 6$	0.01	Full	
Muons	Inner Veto $\mu$ trigger	600	global time	1.5
Muons through target 1 s before coincidence	$E_T > 50$ (& Inner Veto $\mu$ trigger)	20	$t$ for all PMTs $Q$ for Veto PMTs	2.5

Table 27: A possible example of data selection on the basis of event sorting operated by the second-level trigger. The event categories are described in the text. Measured energy in the target volume and in the Veto are denoted by  $E_T$  and  $E_V$  respectively and are always expressed in MeV. The event rates are calculated for the Near Detector

## 6.6 Slow Monitoring

A slow monitoring and control system is required to control systematic effects that could impact the experiment, to allow automated scans of parameters such as thresholds and high voltages, and to provide alarms, warnings, and diagnostic information to the experiment operators. The quantities to be monitored and controlled include temperatures and voltages in electronics, experimental hall environmental conditions, line voltages, liquid levels and temperatures, gas system pressures, radon concentrations, photo-tube high voltages, and discriminator settings and rates. Most of these functions can be accomplished using “1-Wire<sup>®</sup>” devices from Dallas Semiconductor [84]. The high voltage and discriminator subsystems will have their own control and readback hardware. All slow monitoring and control systems will use the same database and history log software. A computer in each experimental hall will monitor the local 1-wire bus and a local radon monitor, acquire any data provided by other subsystems, record the data, and make the data available via the local internet connection.

### 6.6.1 Monitoring via 1-Wire interface

The “1-Wire<sup>®</sup>” line of semiconductors from Maxim IC / Dallas Semiconductor use a simple interface bus that supplies control, readback, and power to an arbitrary number of devices over a single twisted-pair connection [84], see Figure 74. A variety of sensor and control functions are available in traditional IC packages and stainless-steel-clad “iButton<sup>®</sup>s”, see Figure 75. Each device has a unique, factory-lasered and tested 64-bit registration number used to provide device identification on the bus and to assure device traceability. Some devices are available in individually calibrated NIST-traceable packages. The features of low cost, multidrop capability, unmistakable device ID, and versatility make this an attractive choice for implementing the slow instrumentation and control system. Implementation details and expected performance for several subsystems are given here.

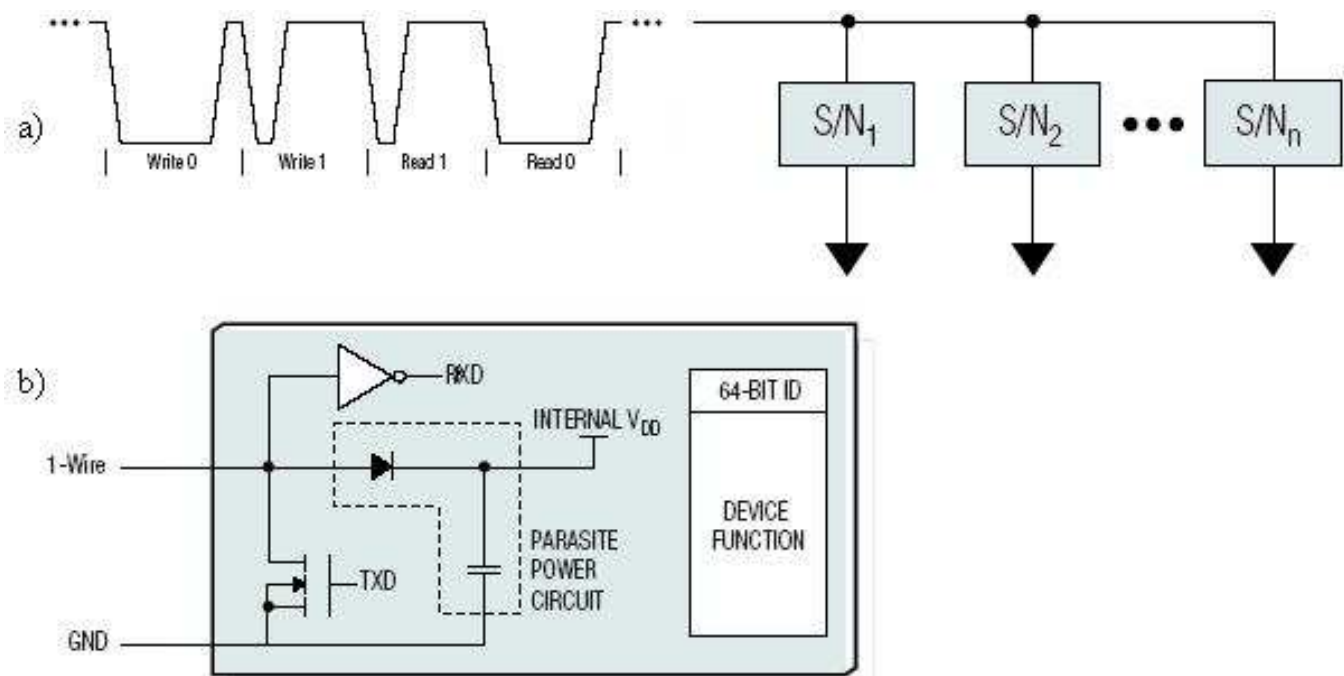


Figure 74: The 1-Wire<sup>®</sup> bus: (a) control, readback, and power provided to multiple devices over a “single” wire; (b) parasite power circuit captures power during high period of 1-Wire<sup>®</sup> waveform. (Adapted from figures by Maxim IC / Dallas Semiconductor.)

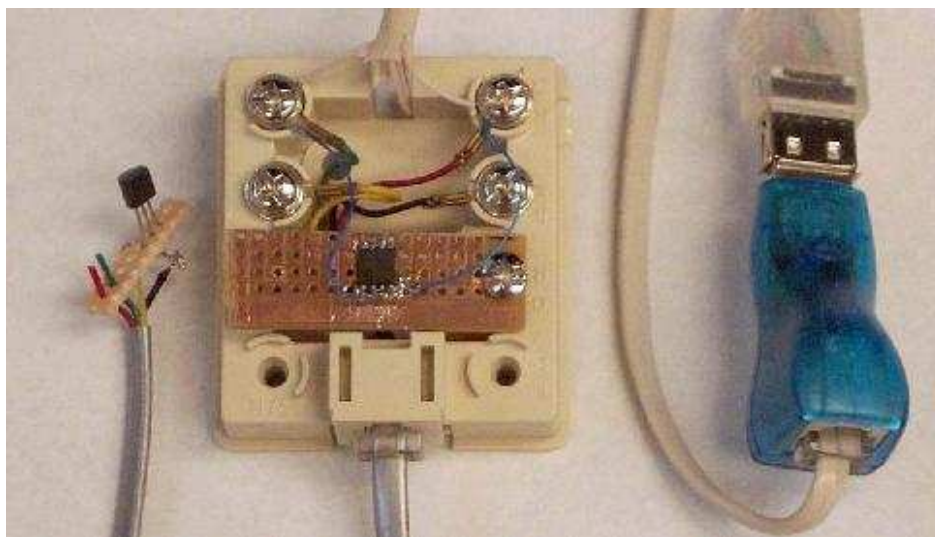


Figure 75: Examples of 1-Wire devices. From left to right: digital thermometer in TO-92 package; 4-channel ADC on prototype board, mounted in RJ-11 modular phone jack box; USB to 1-Wire interface.

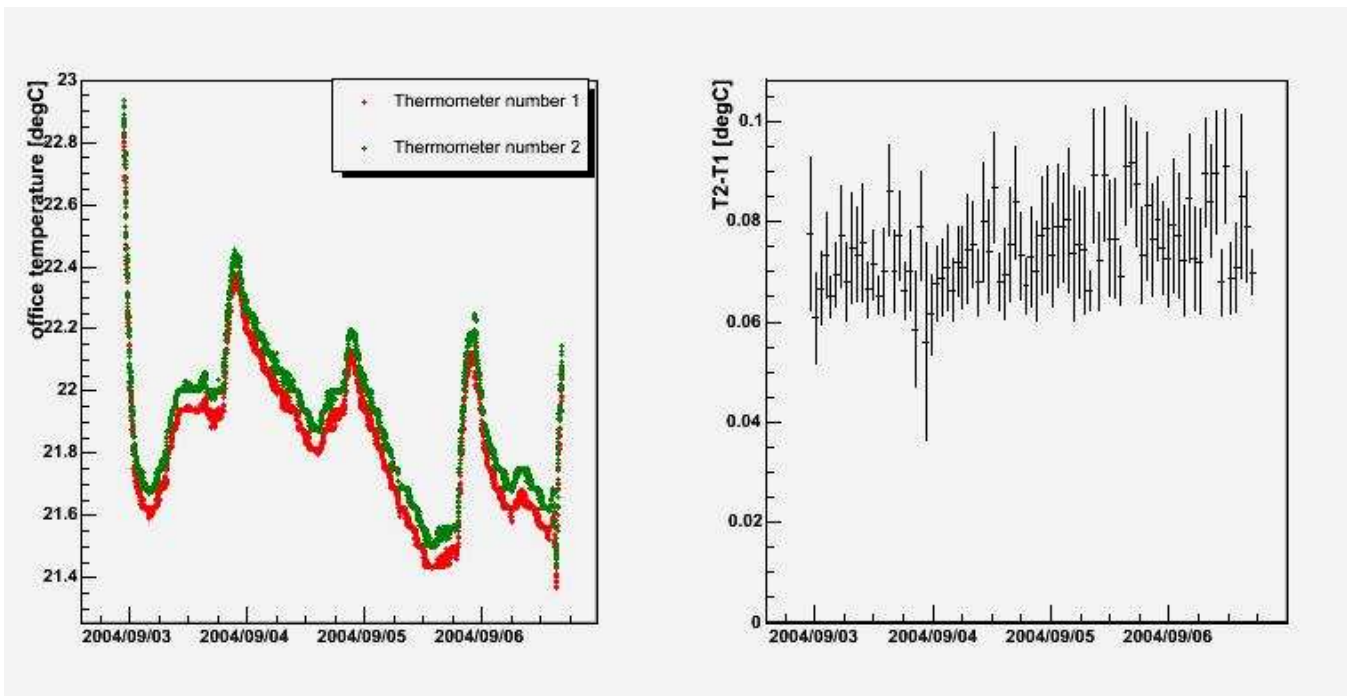


Figure 76: Data from three day test of several 1-Wire<sup>®</sup> samples: (a) temperature in an office at Kansas State University vs. time as read by two adjacent DS18S20 thermometer chips; (b) difference in reading of the two chips.

**Crate and card temperatures and voltages:**

Temperature and voltage monitoring can be included in any custom-built electronics at a component cost of only a few dollars per device using DS18S20 and DS2450 chips and low-cost modular connectors to connect to the 1-Wire<sup>®</sup> bus. Note in addition to the temperature and voltage functions, the unique ID on each chip provides automatic tracking of any card swaps. Trivial custom boards containing only these components can be used to monitor temperature and bus voltages on crates which otherwise contain no custom-built electronics.

In these chips, digitization of temperature and voltage is initiated by an explicit “convert” command from the bus master. Temperature conversion takes 900 ms, and digitization of the four 12-bit channels of the DS2450 takes less than 4 ms total. During conversion, the bus master may communicate with other devices if the chips have an external source of power; if a chip is powered parasitically from the bus, then the master must maintain the bus level high throughout the conversion. Testing of samples provided by Maxim IC / Dallas Semiconductor confirm that multiple devices can maintain their internal state while all are powered parasitically from the same bus. Figure 76 shows data from a three day period during which two DS18S20 thermometers were sampled once a second by a program written in Java. The two thermometer chips were mounted in direct contact with each other, and recorded the same temperature to within a small fraction of a degree. In this test, the thermometers were located about two meters from the bus master, and another 1-Wire<sup>®</sup> device was connected on the same bus about three meters further downstream. No failures or interruptions occurred during this period.

## **Experimental hall environment:**

The DS1923 “Hygrochron” iButton<sup>®</sup> looks ideal for monitoring temperature and humidity. In addition to the humidity and temperature functions, this device features on-board battery backup and automatic logging to internal memory independent of external control. Power or computer failures will not interrupt the temperature and humidity record. This iButton<sup>®</sup> is designed for tracking sensitive products during shipment or other handling. Each DS1923 is individually calibrated and NIST traceable. Another iButton<sup>®</sup>, the DS1922, provides similar functionality without the humidity function.

Monitoring of barometric pressure and other environmental factors is easily achieved using the DS2450 ADC and one or more external transducers. (Note: A complete 1-Wire<sup>®</sup> weather station is even available [85].) Another interesting “environmental” condition to monitor is ambient light level in the experimental area: many systematic effects in past and present neutrino experiments have been attributed, correctly or incorrectly, to electrical or optical noise introduced by lighting, and a simple phototransistor addresses the issue handily. The phototransistor technique also can be used to monitor status LEDs on devices which lack electrical status outputs. AC line voltage is also easily monitored using a 1-Wire<sup>®</sup> ADC and a trivial circuit.

## **Liquid levels and temperatures, and gas pressures:**

Transducers should be provided for monitoring important aspects of the detector such as scintillator and buffer oil levels, temperatures, and pressures in any gas systems used. Transducers should produce voltages in the 0 to 5 V range for maximum compatibility with the DS2450 ADC. The further specification, purchase, and installation of such transducers are the responsibility of the respective subsystems.

## **Simple controls:**

The DS2890 is a 1-Wire<sup>®</sup> digitally controlled potentiometer. It can be used to provide slow control for simple servos, power supplies, or other devices controllable by an external analog signal. At present, there is no definite plan to use this capability, although the discriminator levels could possibly be controlled in this way. Support for slow control as well as monitoring should be provided in the software for maximum flexibility.

### **6.6.2 Radon monitoring**

Professional continuous radon monitors have become readily available and relatively inexpensive. An example is Sun Nuclear’s Model 1027 [86]. Each experimental hall will have at least one radon monitor read out by the slow control PC. The data will be stored and made available via the same interface used for all slow monitor data.

### **6.6.3 Interface to other subsystems**

Some hardware subsystems may have important slow monitor that cannot be made available on the 1-Wire<sup>®</sup> interface or the serial ports of the slow monitor computers. Examples may include the clean room particle counters, the high voltage power supplies, and the discriminator circuitry in the trigger system. In such a case, either the hardware itself or a computer which monitors

and controls it should make the data available via network TCP connection. “Virtual” monitor data, such as capture time, event rates, or other quantities determined by online analysis, could also be recorded by this mechanism. The software on the master slow monitor computers will poll these external servers and make all slow monitor data available in a common framework. This is preferable to each subsystem providing a separate data interface. In the common framework, systematic correlations may be studied among any variables. Support for control functions and synchronization with externally controlled devices should be provided in the software to allow for scans of controlled parameters such as high voltages and threshold levels. The common framework will allow dependent variables observed in one subsystem, *e.g.*, discriminator rates, to be easily correlated with parameters monitored or controlled by some other subsystem, *e.g.*, high voltage.

# 7 Calibration

## 7.1 Calibration Goals

The two main tasks for which calibration is critical are the estimate of the inverse beta decay detection efficiency and the determination of the energy scales for positrons, gammas, and neutrons. Over time, the relative detection efficiency between the near and far detectors should be known with an uncertainty less than 0.5% including all deadtime effects. With regard to energy scales, the tolerable uncertainty depends on the level and nature of backgrounds. We have adopted 1% as the maximum uncertainty on the absolute energy scales for gammas and positrons because it is realistically achievable; the corresponding relative uncertainties between the near and far detectors should then be much less than 1% since the same energy-scale determination methods will be used for both detectors.

For the neutron energy scale, a less stringent requirement suffices: the uncertainty in the estimate of the visible neutron kinetic energy should be limited to 20%. This relaxed requirement reflects the large signal-to-background ratio expected for each detector as well as the mild energy dependence of the fast-neutron background across the reactor-neutrino energy range. Our approach in specifying a system to achieve these goals builds on our extensive experience in calibrating the Palo Verde, CHOOZ, Super-Kamiokande, KamLAND, and MiniBooNE detectors.

The uncertainty budget for the relative detection efficiency is taken to be (a) 0.2% from the energy cut (“6 MeV cut”) applied to select neutron candidates, (b) 0.1% from the cut on the neutron capture time, (c) 0.25% from deadtime, and (d) <0.2% from the requirement (if used) of spatial correlation between the prompt and delayed subevents.

The uncertainty in the absolute energy scale receives contributions from the uncertainties in extrapolating the energy response of the scintillator from gammas to positrons and uncertainties in the corrections associated with event position. These uncertainties combined must be controlled to 1% or better.

In developing the design of the calibration program described below, it has been assumed that the contributions to the absolute positron energy-scale uncertainty are controlled to (a) 0.7% from energy response extrapolation and (b) 0.7% from position corrections.

It is practically unavoidable that calibrations probe the detectors under different conditions than do the signals and backgrounds of interest. It is likely not feasible to build and deploy inverse beta decay sources, and even the detector responses to positrons and neutrons separately cannot be directly measured. For example, the typical energies of neutrons produced in inverse beta decay induced by reactor neutrinos are tens of keV, whereas the energies of neutrons produced by available calibration sources lie above 1 MeV. Moreover, the calibration process introduces structures into the detector that are not present during normal data taking. It is therefore necessary to use detector simulation to estimate the detector response to inverse beta decay and relevant backgrounds; the role of calibration is then to provide the information needed for tuning and checking the simulation to the required accuracy. Included in this process is correcting the calibration data for the effect of structures introduced into the detectors for calibration.

In addition to providing measurements of detector response that will control its uncertainties within the levels stated above, the calibration program must provide information that can be used to check assumptions about other aspects of detector performance and to carry out analyses using different sets of selection criteria or alternate methods of background subtraction. Specifically, the scope of calibration will also include the following:

Table 28: Gamma sources to be used in calibrating Double Chooz

	Source	$E_\gamma$ (MeV)	Half-life
1	$^{203}\text{Hg}$	0.289	46.6 d
2	$^{137}\text{Cs}$	0.667	30.1 y
3	$^{68}\text{Ge}$	0.511 + 0.511	271 d
4	$^{60}\text{Co}$	1.333 + 1.173	5.27 y
5	$n$ capture on H	2.223	
6	$n$ capture on C	4.94	

1. A check that the trigger is fully efficient for inverse beta decay events.
2. Calibration of the efficiency of a spatial correlation cut to within 0.2%.
3. Measurement of the detector response to neutrons, for modeling the background due to fast neutrons.

## 7.2 Calibration Sources and Deployment

We will employ three types of calibration sources: gamma sources, neutron sources, and light flashers.

### 7.2.1 Gamma Sources

Gamma sources will be used for the following purposes:

1. Precisely measure the response of scintillator (target and  $\gamma$ -catcher) to gammas from well below inverse beta decay threshold to at least  $\approx 5$  MeV. Spanning this range and beyond will also facilitate understanding the roles of quenching and Cerenkov radiation, uncertainties in which propagate through to the uncertainties in the positron energy scale derived from the gamma energy scale.
2. Measure light transport properties (absorption, re-emission, speed of light) of the liquids in the target,  $\gamma$ -catcher, and buffer.
3. Measure PMT  $t_0$ 's.
4. Check relative efficiency of far and near detectors with respect to trigger, data acquisition, event reconstruction, and event selection.
5. Global monitoring of detector stability.

The set of gamma sources to be used is enumerated in Table 28.

The sources will be encapsulated and stored so that the same physical sources can be deployed in all volumes in both detectors. Gamma sources 2–4 could be encapsulated in a single package. The activities of at least one of the sources  $^{68}\text{Ge}$ ,  $^{60}\text{Co}$ , or  $^{137}\text{Cs}$  will be accurately known (1–2%) to check absolute efficiencies. The activity of each isotope (and the total activity of any combined

sources) should be well above the expected background trigger rate but low enough to avoid large detector deadtimes. Over the course of the experiment, new sources may need to be prepared for the isotopes with half-lives much shorter than a year. For the convenience of global monitoring and other calibration tasks that may be carried out more frequently, sources may also be provided for use in only one detector or sub-volumes within a detector. There will be significant continuum background due to  $n$  capture on Gd underlying the 4.94 MeV line and hence it is likely to be visible only for long source deployments. The feasibility of deploying other high-energy gamma sources is being explored.

Detector simulations have been carried out to estimate how the detector response to gammas will vary with position. The results are typified by what is shown in Figure 77 for samples of 1 MeV gammas generated along the  $x$ -axis. The strongest variations occur near the target- $\gamma$ -catcher boundary and across the  $\gamma$ -catcher. To avoid unacceptable uncertainties in energy reconstruction, the deployment system will have the capability to position gamma sources near the target- $\gamma$ -catcher boundary and at points within the  $\gamma$ -catcher. Furthermore, to ensure that the uncertainty in the energy reconstruction due to position uncertainty is less than 0.7%, the systematic uncertainty in source position must be less than 1.5 cm. The particular choice of deployment positions in the  $\gamma$ -catcher will be further discussed in connection with calibrations with neutron sources.

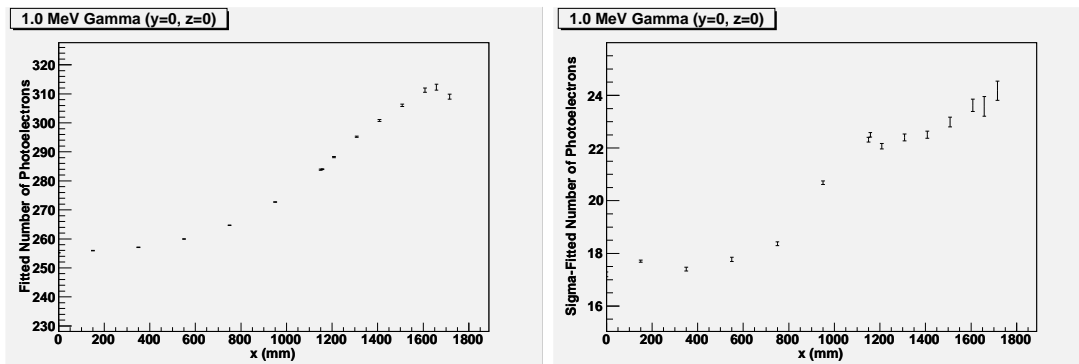


Figure 77: Center of Gaussian fitted to peak in photoelectron distribution versus Center (left) and sigma (right) of Gaussian fits to peak in photoelectron distribution versus distance along the  $x$ -axis for 1 MeV gammas.

### 7.2.2 Neutron Sources

Neutron sources will be used for the following purposes:

1. Measure the relative neutron detection efficiency between the two detectors.
2. Measure the absolute neutron detection efficiency at selected points in each detector. Such a measurement is required to help check the accuracy of the neutron simulation and for analysis of data for which there is only one detector, most notably the far detector data taken before the near detector is turned on.
3. Measure the energy response of the target and  $\gamma$ -catcher to neutrons, to enable accurate simulation of the prompt energy spectrum of fast neutron events.



#### 4. Gauge the relative deadtime of the two detectors to a source of correlated events.

As with the gamma sources, the neutron sources will be encapsulated and stored so that the same sources can be deployed in both detectors. To measure the absolute efficiency, deployment of a source instrumented with a dedicated device to tag neutron emission, such as the one used in the CHOOZ experiment, is planned. Using the detector itself to tag neutron emission, by registering the prompt energy deposited by accompanying gammas, is under study. Am-Be, for example) will overlap In order to measure the energy response of the detector to neutrons, the energy distribution of the neutrons emitted by each source must be well known and corrections must be made for the energy deposited by any gammas accompanying the neutron emission.

Detector simulation has been carried out at the photoelectron multiplicity and timing level to understand where neutron sources should be deployed and the degree of corrections that would have to be applied to the efficiencies measured with Cf-252 or Am-Be sources to obtain the efficiency for neutrons produced by inverse beta decay. Monoenergetic neutrons were generated uniformly throughout the target, uniformly throughout the  $\gamma$ -catcher, or at specific points. Several energies were simulated: 0.01 MeV as a characteristic energy for reactor neutrino events, 2 MeV as the approximate energy for Cf-252 neutrons, and 4 MeV, which is close to the mean energy for Am-Be neutrons. For each event, photoelectrons were classified as prompt or delayed, depending on whether they were registered less or more than 200 ns from the start of the event. The mean time of the delayed photoelectrons was used as the capture time. Neutron selection cuts were defined based on the total number of photoelectrons detected and the neutron capture time.

The following points can be drawn from the simulations performed to date:

- The neutron detection efficiency varies significantly throughout the target, hence the calibration system should have the capability to deploy neutron sources throughout the target volume. Figure 78 shows the neutron detection efficiency as a function of distance to the target- $\gamma$ -catcher boundary for neutrons generated uniformly in the target.
- Efficiency loss due to neutrons produced in the target escaping into the  $\gamma$ -catcher is termed “spill-out” while efficiency gain due to neutrons produced in the  $\gamma$ -catcher being captured on Gd in the target is termed “spill-in”. For neutron sources such as Am-Be and Cf-252, spill-in and spill-out are separately large effects ( $\approx 5\%$ ) but appear largely to cancel, as would be expected. However, since (a) the neutron detection efficiency is to be estimated with an uncertainty of a fraction of a percent and (b) the range of distance over which spill-in and spill-out occur is much greater ( $\approx 20$  cm) for Am-Be and Cf-252 sources than it is ( $\approx 5$  cm) for neutrons from inverse beta decay, deployment of neutron sources is planned both within the  $\gamma$ -catcher and in the target near the target- $\gamma$ -catcher boundary, so as to measure this effect at representative points and help tune/check the MC simulation of neutron transport and capture.
- The neutron detection efficiency depends on the energy distribution of the neutrons. The differences in neutron detection efficiency between neutron sources and inverse beta decay are large enough that corrections must be applied in order to satisfy the requirements on uncertainty in detection efficiency. Multiple sources (Cf-252 and Am-Be), with different neutron energy spectra, will be deployed so as to measure and reduce this uncertainty. The possibility is also being explored of deploying a low-energy neutron source, in order to reduce the uncertainty in transferring efficiency measurements made at higher neutron energies to the energy range of neutrons produced by reactor neutrinos.

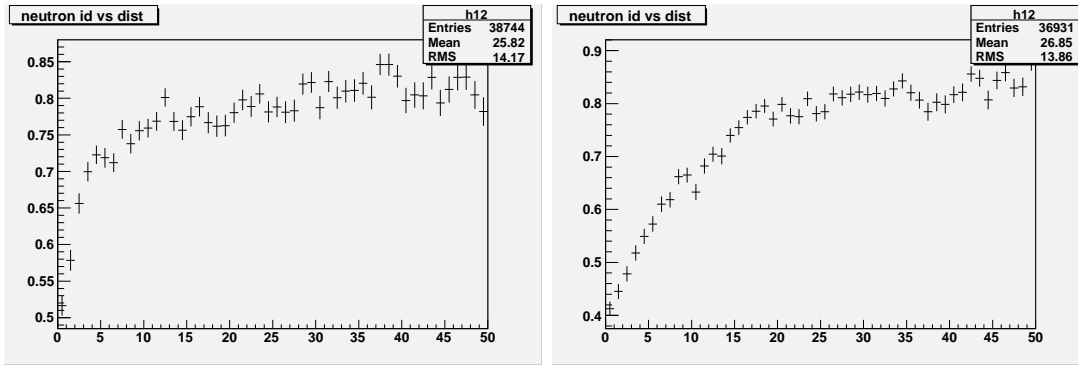


Figure 78: Neutron detection efficiency versus distance (in cm) between neutron creation point and target- $\gamma$ -catcher boundary for neutrons generated in the target: (left) 0.01 MeV neutrons; (right) 4 MeV.

Detector simulation was also used to estimate the relative uncertainty in energy scale between the near and far detectors that could be tolerated while maintaining an uncertainty of 0.2% in neutron detection efficiency due to the “6 MeV” cut. The energy-scale uncertainty so obtained is 100 keV.

### 7.2.3 Light Flashers

Fast lasers of several wavelengths will also be used to calibrate the detector. The main purpose is for vertex reconstruction, which depends critically on light transport and PMT timing. In principle, vertex reconstruction could be calibrated with gamma sources alone, but laser calibrations have the advantages of (a) providing signals of precisely known timing and amplitudes and (b) probing the response of the detector to specific wavelengths. Moreover, the laser systems can be designed to provide a wide range of well-known intensities, so that laser calibrations can be used to help interpolate the detector response between gamma calibrations and extrapolate it beyond the range of signal strength covered by gamma calibrations. The capability of lasers to provide very strong signals is useful in understanding the response of the detector to cosmic events, many of which excite the detector in a regime where the PMT response is expected to be significantly nonlinear. We have adopted the following as requirements for the laser calibration system:

- The laser light output must either be highly isotropic (preferred) or its anisotropy must be precisely known: this greatly simplifies the use of laser calibration data for light transport and energy calibration studies.
- The width of the laser pulse must be small compared to the scintillator decay times so that the distribution of photon arrival times at the PMTs does not depend strongly on the details of the laser pulse timing. Furthermore, the timing of the leading edge of the laser pulse (before attenuation filtering) must be known with a precision better than 1 ns so that studies of PMT timing can be carried out using as a timing reference a trigger pulse derived from the leading edge of the laser pulse.
- At least two widely separated wavelengths must be provided: one that excites the scintillator to produce pulses with the same spectral and timing characteristics as those due to charged

particles, and the other whose absorption length in scintillator is very long so that calibrations of PMT timing can be carried out with minimum complications due to re-emission and scattering.

- The dynamic range of the laser system must extend from much less than one photoelectron per PMT on average to several hundred photoelectrons per PMT.
- Fiber assemblies and diffusers must be selected so as to ensure that light is injected at precisely known points and the self-shadowing of the system is either negligible or adequately known.

Because of (a) the overlapping capabilities of calibrations with light flashers and those with radioactive sources and (b) the expectation that measurements of intrinsic PMT gain and timing characteristics will not depend significantly on the position of the source, deployment of the light flasher sources only on a vertical line through the target is sufficient. For the sake of simplicity, the symmetry axis of the detector is preferred, but deployment along another vertical line would also be suitable.

## 7.3 Calibration Deployment

### 7.3.1 Introduction

The purpose of the calibration deployment system is to deploy calibration sources into the target and  $\gamma$ -catcher regions. The calibration sources, the motivation for using them, and basic deployment requirements have been described above. The deployment systems utilized by the near and far detectors will be identical.

The deployment system must be designed to accommodate gamma sources, terminated fibers illuminated by external lasers, and neutron sources (untagged and tagged). The characteristic dimensions of these source will range from a few mm to a few cm, and their masses from a few tens to a few hundreds of grams. The calibration system must be capable of positioning sources at representative points in the target and  $\gamma$ -catcher with an uncertainty less than 1.5 cm.

The materials and geometry of the deployment system must be chosen to minimize uncertainties in the corrections for shadowing and absorption. Detector simulation studies have been carried out to set the maximum dimensions that can be used and still meet the energy-calibration uncertainty requirements. Each material used in the calibration system must be compatible with all elements of the detector environment to which it is exposed. Furthermore, measures must be taken to protect the detector from radio-contamination by the calibration systems. The process of deploying the calibration system must not affect detector performance. The setup of the calibration deployment system should not be awkward or time-consuming, hence calibrations that are carried out frequently will be largely automated.

We next describe the deployment system in three parts: deployment methods, detector interface, and control systems.

### 7.3.2 Deployment Methods

The methods of source deployment for the target region will differ from that for the  $\gamma$ -catcher region because of the different geometries and different calibration requirements; therefore, they are discussed separately.

## Target

Because we intend to use the entire volume of the target, the calibration sources must be deployable throughout the target region. This will be accomplished using an articulated arm shown schematically in Figure 79. The articulated arm is comprised of a telescoping vertical shaft, supported from the calibration interface above the detector, with a fixed-length arm pivoting at the lower end. By adjusting the length and azimuthal angle of the telescoping shaft and the angular position of the arm, a source attached to the end of the arm can be deployed at any position within a cylindrical volume. During calibration, an operator will attach a calibration source to the source holder, deploy the source into the target at the desired positions, and then retract the source to the detector interface. A cable and winch system (“fish-line”) will also be installed for frequent deployment of sources along the target  $z$ -axis.

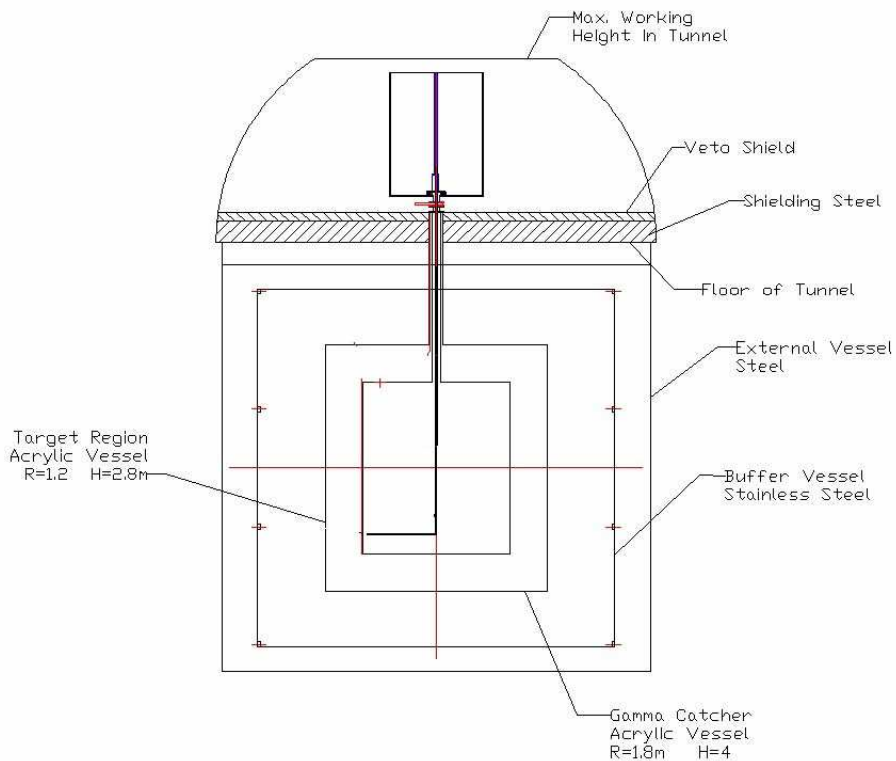


Figure 79: Schematic of the articulated arm system for deploying calibration source throughout the target region.

Those components of the deployment system that come into direct contact with the scintillator will be checked for material compatibility. samples for changes in Components that will not come into direct contact with the scintillator but that will be exposed to its vapors must also be tested.

## $\gamma$ -catcher

The  $\gamma$ -catcher requires its own calibration because its light yield and properties of light and neutron transport will likely differ from those of the target. These differences can be measured using gamma and untagged neutron sources.

A guide tube system will be used to deploy calibration sources in the  $\gamma$ -catcher. The tubes must be small in diameter in order to avoid shadowing of scintillator light and to minimize dead material and absorption. The tubes will run into the  $\gamma$ -catcher from a manifold in the detector interface. Figure 80 shows a path that a guide tube, designed to have two accessible ends, could take in order to allow sources to be positioned at representative points within the  $\gamma$ -catcher. The calibration sources will be attached to a wire and pushed through the tube. The position of the source can be determined from the length of wire inserted into the tube and an accurate survey of the guide-tube geometry.

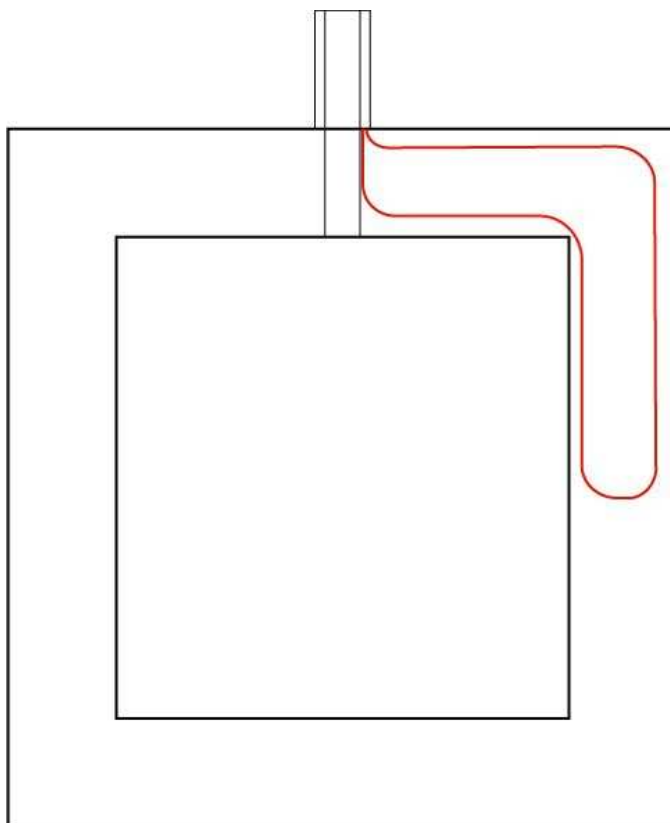


Figure 80: A possible guide-tube path for deployment of sources in the  $\gamma$ -catcher

The number of guide tube(s) to be deployed in the  $\gamma$ -catcher is being studied. The connection of the wire to the sources must be such that the same sources can be deployed in the  $\gamma$ -catcher as in the target. As with the deployment system for the target, all components will have to be checked for material compatibility before final selection and carefully cleaned before installation into the experiment.

### 7.3.3 Detector Interface

The detector interface is the region that has access to the target and  $\gamma$ -catcher and that can be accessed from the outside to introduce and remove calibration sources. To prevent contamination of the detector, the detector interface will incorporate a glovebox for source manipulation and an airlock through which sources can be inserted and removed. The volume of the glovebox must be

large enough that sources can be easily manipulated and the deployment system can be assembled and disassembled safely and easily as needed. The glovebox must be connected to an  $N_2$  gas system and purged so that it has the same atmosphere each time it is opened to the detector. avoid introducing backgrounds. The glovebox will be equipped with radon and oxygen monitors for flagging leaks and monitoring the progress of purging. While the detector interface is open to the detector, it must also be light tight, which may mean that the operator must view the interior of the glovebox using infrared illumination and cameras. Feedthroughs for laser fibers and control and power cables must be hermetic. To bring sources into the detector interface, a transfer box is needed: sources are placed into this box through an external door, then the transfer box is purged, after which the operator opens an internal door and brings the source inside the detector interface.

### 7.3.4 Control Systems

All control and sensor channels for the deployment systems must be interfaced to a computer system for purposes of automation and monitoring. Although it should be possible to monitor the state of the deployment system remotely, for safety and convenience, the computer system controlling and monitoring the deployment system should be installed near the detector interface. Interlocks, both hardware and software, must be implemented to ensure that the detector is not opened to light, that the door between the detector interface and the detector is not closed while sources are being deployed, etc. Full exercise of the control program and interlock system will be part of the testing of the deployment systems.

## 7.4 Calibration and Monitoring Plan

During the commissioning of each detector, it is assumed that a light flasher will be deployed at the center of the detector for debugging and for adjusting PMT gains. Once commissioning is complete and detector operation has stabilized, a full calibration program of the detector will be carried out using gamma, neutron, and light flasher sources deployed at representative points in the target and  $\gamma$ -catcher.

After the first full calibration, the process of monitoring begins. The purpose of the monitoring process is to provide the data needed to accurately interpolate detector performance between full calibrations and to help determine when the detector performance has changed to the degree that a full calibration is needed to maintain the required accuracy. On a regular basis (initially at least once per week), a gamma source and a neutron source will be deployed both in the target (along the  $z$ -axis using the “fish-line” system) and in the  $\gamma$ -catcher. Once both detectors are operational, monitoring will be carried out on the same schedule for both detectors, with at least one gamma source and one neutron source deployed in both detectors. In addition to monitoring with sources, analyses looking at natural backgrounds should be developed to provide information on detector stability on a day-by-day basis. The frequency of monitoring with sources can be adjusted once the collaboration has experience with the actual stability of the detectors and the irreducible impact of the monitoring process itself on detector stability.

Full calibrations are to be carried out (a) when the detector performance has changed to the degree that monitoring data alone, combined with the previous full calibration, no longer suffices to meet the calibration goals of the detector, (b) after a major change to the detector, or (c) when the maximum interval between full calibrations as set by the collaboration has been reached. To

the greatest extent practicable, full calibrations of the near and far detectors will follow the same schedule.

## 8 Simulation and Software

It is not unusual that the design and engineering of a new experiment is heavily aided by computer simulations. Rightfully speaking, a large portion of the Double Chooz proposal is assisted by simulation studies in such a way that simulated results are fully integrated into all of the essential parts of the entire document. The role of the simulation studies is best appreciated in their proper context so that there is no need to reiterate simulation results already explained elsewhere in the proposal. However there are interesting facts related to simulation and software that are not already mentioned in other parts of the proposal and are most suited in a chapter dedicated for a panoramic view of the architecture and philosophy of software development in Double Chooz. This chapter outlines the basic concepts of the software tools used in detector R&D and data analysis for the Double Chooz experiment.

### 8.1 Software and Simulation Goals

The main goals of simulation studies can be divided into two major categories: (1) R&D including engineering and detector designs, and (2) data analysis and physics discoveries. The first category constitutes the main emphasis of the studies during the proposal writing phase of the project while the second category typically continues until the end of the project.

#### Simulation Requirements

One of the key purposes of simulations is to optimize the detector design. The optimization is done with respect to background sensitivity, detector resolution and cost. The simulation is expected to faithfully model the gamma ray and nuclear properties of the detector, particle transport, backgrounds and shielding studies. It must correctly represent the optical properties of the scintillator, acrylic, photo-tubes and detector walls. Possible distortion from electronic effects must be included.

#### Software Acceptance Tests

Reliability and stability are the goals of Double Chooz software. A lot of efforts are invested in cross-checking the simulation results with existing experimental data as well as the detection of programming bugs such as inability to compile, runtime crashes and memory leaks. Nominal stability tests and detailed comparisons with observations are made to insure that the physics model accurately represents the Double Chooz environment.

#### Comparison with Prior Measurements

There are existing experimental results on scintillation light yield, attenuation, emission spectra, absorption spectra and surface optical properties that are compared with the simulation. Nuclear and electromagnetic properties such as photon attenuation length, neutron absorption gammas and capture time are also checked against the known properties of the materials. For example, the simulated angular distributions of the muon background at the far site using MUSIC has been checked with the experimental results of a 1994 cosmic ray measurement on location and are shown to be in good agreement [87].



## Comparison with CHOOZ Data

We are fortunate that a middle baseline neutrino experiment CHOOZ has already been carried out at the far detector site using similar technology [5]. Data from the first CHOOZ experiment for both reactor on and reactor off running are available for Double Chooz. This has helped in tuning the neutron response and in modeling the background.

## Quality Control

All software packages are subject to rigid quality criteria for reliability, accuracy and practicality. Double Chooz software packages are designed to help the collaborators to be productive in physics research. Documentation is actively maintained which includes operating instructions, summaries of test runs and descriptions of the algorithms employed.

The Double Chooz software packages are centralized in the CVS repository at Lyon (code named CC-IN2P3). This repository is easily accessed via the internet for all members of this international collaboration. It permits version control so that certified codes can be used in production, while new codes are being developed. If problems are encountered during quality testing, the prior version of the code can be retrieved from the archive. Documentation on the accessibility of Double Chooz software packages is also an important part of the quality control program.

## 8.2 Software Tools

Double Chooz programming tools are built on a collection of scientific software packages such as GEANT, FLUKA, MCNP, MUSIC and ROOT. There are enough overlaps in functionality among these software packages that they provide a means for the necessary cross checks for the physics goals, engineering and design of the experiment. For example, a recent study has shown that GEANT4 produces fewer muon-induced spallation neutrons than FLUKA above 100 GeV by almost a factor of 2 in some materials [88]. In a high precision experiment such as a reactor  $\theta_{13}$  measurement, variation in simulated results by a factor of 2 from various software packages tends to make a difference. For this reason, efforts are made in the collaboration to maintain some level of redundancy and repetition as cross checks to ensure the reliability of the engineering design of the detectors.

### GEANT 4

The primary tool for modeling detector response for Double Chooz is GEANT4 [89] and more particularly an extension of it called GLG4sim [90] which is a general purpose detector simulation package derived from a special purpose counterpart called KLG4sim used by the KamLAND collaboration. The full acronym of the Double Chooz version of GLG4sim is DCGLG4sim which is usually referred to as DCG4sim or simply DCsim for short. DCsim simulates all the relevant physics processes that occur in a liquid scintillator detector. Generation of primary events is accomplished by using either external event generators or codes already built into GEANT4, GLG4sim, or DCsim. Electronics is simulated by a separate software package called esim [91] which has no inherent dependence on GEANT4, GLG4sim or DCsim.

With a few exceptions, standard GEANT4 toolkits are used to implement essentially all physical processes involving the passage of particles with energies above a few keV through the materials in the detector. A combination of standard GEANT4 plus GLG4sim extensions are used to simulate optical photon physics, from optical photon production to photoelectron emission at the surface

of the photocathode. Double Chooz collaborators from Saclay have made critical contributions to this code [92]. Neutron thermalization in **GEANT4** is implemented in the module **NeutronHP** using version 3.7 of the **GEANT4** neutron data libraries and supplementary data files supplied by the author of **NeutronHP**. Neutron capture on all isotopes except Gd is handled by **NeutronHP**, while capture on Gd is calculated using a code written by Double Chooz collaborators from Subatech [93]. Fast neutron production can be simulated using **GEANT4** modules for lepton-hadron processes or external packages (*e.g.* **FLUKA** [94]) with the products fed to **DCsim** as externally generated primary events.

### **GEANT 3**

A **GEANT3**-based simulation package has been written mainly for the modeling the detector response and the calculation of internal and external radioactive backgrounds. This simulation includes all the known materials and their geometrical characteristics, including a database of multiple measurements of the U, Th, K, and Co concentrations of typical materials. Some examples of the typical materials are steel, acrylic, PMT glass, and PMT dynode structures. Shield design against external gammas and the assessment of the effect of PMT radioactivity are aided by this simulation.

The package contains a U, Th, K, Co event generator that has incorporated all of the known beta transitions and gamma lines of these decays. The generator includes the appropriate multiple gamma-gamma correlations and branching ratios for each of the decays. The high speed performance of the package makes it possible to simulate several billion nuclear decays and to track the daughter particles to assist the design of the detector.

### **MCNP**

**MCNP** [95] (Monte Carlo N-Particle code) is developed and owned by Los Alamos National Lab. It is used to study nuclear processes, in particular thermal neutron transport and capture in the studies of non-invasive calibration of the gamma-catcher. This calibration method uses neutron activation of sources within the gamma-catcher. **MCNP** is used to study neutron diffusion.

### **FLUKA**

Low energy neutrons in **FLUKA** are simulated by a multi-group strategy. Below the energy threshold (typically  $E_n < 19.6$  MeV), neutron energy is divided into multiple (typically 72) groups. The transition probability from one group to the next during neutron transport is computed through the down-scattering matrix. Above the energy threshold, continuous cross sections are used. The usage of **FLUKA**[94] at Double Chooz is mostly limited to the estimation of the muon-induced neutron rate at the near detector site. Studies [96] show that **FLUKA** reproduces observations of underground neutrons very accurately so that it is an indispensable tool to model fast neutrons. The muon flux is defined at the surface [97] and **FLUKA** is used to propagate muons and neutrons to the new laboratory depth through standard rock. The studies performed with **FLUKA** are used particularly to optimize designs for the near laboratory and the outer veto system.

### **MUSIC**

**MUSIC** (Muon Simulation Code) [27] is a **FORTTRAN** subroutine that calculates muon energy loss and angular deviation in a material. The default cross section files that come with the **MUSIC** package are calculated for standard rock only. In the present application, the material used in the simulation

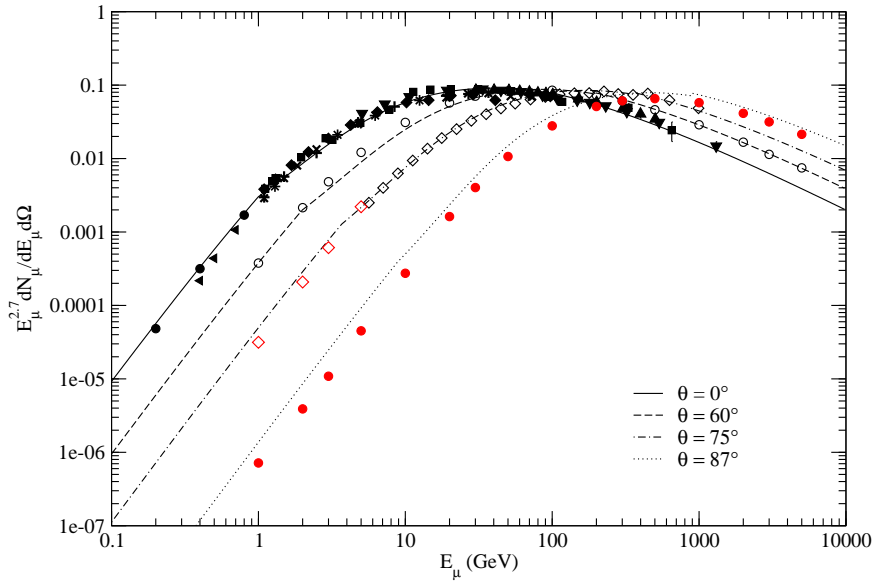


Figure 81: Fits of the modified Gaisser parameterization to experimental data in the low energy regime between  $\theta = 0$  and  $\theta = 87^\circ$ . The experimental data are taken from References [98]–[99].

is defined by the real Ardennes Mountain rock profile that has a mean density, atomic number, atomic mass and radiation length of  $\langle Z \rangle = 11.8$ ,  $\langle A \rangle = 24.1$ ,  $\rho = 2.81 \text{ g/cm}^3$  and  $\lambda = 23.3 \text{ g/cm}^2$  respectively. The approximate chemical composition of the Ardennes rock is 58%  $\text{SiO}_2$ , 19%  $\text{Al}_2\text{O}_3$ , 17%  $\text{FeO}$ , 4%  $\text{MgO}$  and 2%  $\text{K}_2\text{O}$  in elemental percentages. The above information of the rock composition is used in the calculation of the cross section files used with MUSIC for this specific case. MUSIC is well tested and its results are shown to agree with experimental data [87]. The advantage of MUSIC is its modularity that gives it the flexibility to be easily integrated into more complicated simulations involving non-standard geometry that are not defined in other simulation packages such as FLUKA and GEANT. This is particularly useful when simulating underground muon overburden with a non-flat topographic mountain profile. Since there is sufficient information specific to the Ardennes Hill that is built into the present MUSIC simulation, the package is sometimes referred to as DCMUSIC (MUSIC for Double Chooz) by the collaborators.

The standard Gaisser parameterization for surface muons is not accurate in the low energy regime. Typical  $\theta_{13}$  reactor experiments place the near detector close to the reactors and subsequently close to ground surface so that an accurate parameterization of low energy surface muons is needed in this situation. In the case of Double Chooz, the far detector is sufficiently close to the steep shallow hill side that a good description of the low energy surface muons is also needed. For these reasons, the low energy part of the Gaisser parameterization is modified. The fits of the modified parameterization to experimental data are illustrated in Fig. 81.

DCMUSIC computes average observables such as average final muon energy, flux and rate as well as various distributions. The integrated muon intensity and average energy are defined as

$$J_\mu = \int_\Omega d\Omega \int_0^\infty dE_{\mu 0} P(E_{\mu 0}, X, \theta^*, \phi) \frac{dN_{\mu 0}(E_{\mu 0}, \cos \theta^*)}{dE_{\mu 0} d\Omega},$$

$$\langle E_\mu \rangle = \frac{1}{J_\mu} \int_S d\Omega \int_0^\infty dE_{\mu 0} \frac{dN_{\mu 0}(E_{\mu 0}, \cos \theta^*)}{dE_{\mu 0} d\Omega} \int_0^\infty dE_\mu E_\mu P(E_\mu, E_{\mu 0}, X, \theta^*, \phi),$$

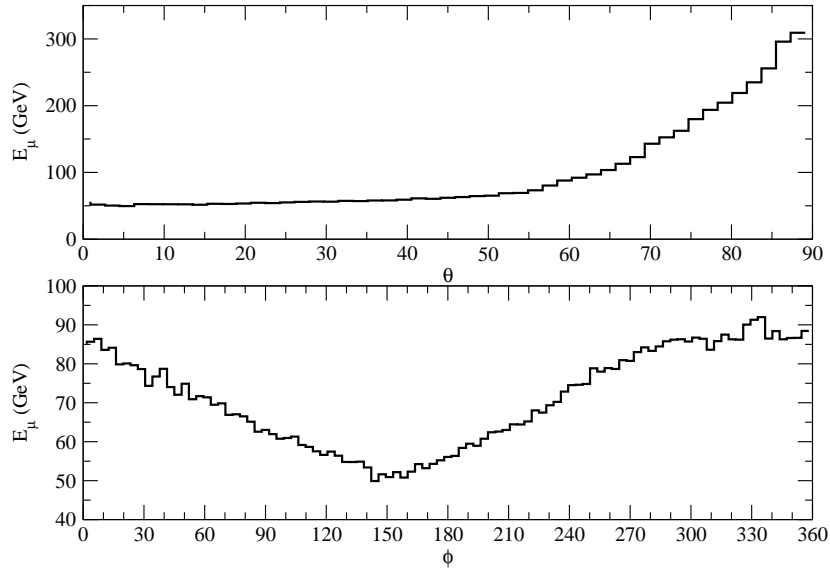


Figure 82: Average muon energy  $E_\mu$  versus  $\theta$  and  $\phi$  at the Double Chooz far site. The total number of simulated events is  $5 \times 10^6$ .

where  $dN_{\mu 0}(E_{\mu 0}, \cos \theta^*)/dE_{\mu 0} d\Omega$  is the modified Gaisser parameterization. The probability function  $P(E_{\mu 0}, X, \theta^*, \phi)$  defines the survival probability of a muon with initial energy  $E_{\mu 0}$  traversing a slant depth  $X$  from the zenith angle  $\theta^*$  and the azimuthal angle  $\phi$ . In order to simulate the integrals accurately, the solid angle covering the mountain profile from the perspective of the detector must be sampled uniformly. In fact initial muon energy  $E_{\mu 0}$ , cosine of the zenith angle  $\cos \theta$  and the azimuthal angle  $\phi$  are generated uniformly in the present algorithm. Muons with uniformly generated energies and zenith angles are propagated through the Ardennes rock along slant depths that are specified by uniformly generated values of  $\theta$  and  $\phi$ . At the end, all the surviving muons are multiplied by the corresponding values of the modified Gaisser function as weights, added up, divided by the total number of throws and then multiplied by the proper range of integration. The result is a very accurate and efficient method of computing average muon energy and integrated intensity. Furthermore, the simulated muon data can be easily binned to produce all kind of distributions. An example is the average muon energy per angle as shown in Fig. 82. The muon rate in a detector can be calculated as

$$R_\mu = \int d\mathbf{A} \cdot \hat{r} \int_\Omega d\Omega \int_0^\infty dE_{\mu 0} P(E_{\mu 0}, X, \theta^*, \phi) \frac{dN_{\mu 0}(E_{\mu 0}, \cos \theta^*)}{dE_{\mu 0} d\Omega},$$

where  $d\mathbf{A}$  is a differential area element along the the detector wall and  $\hat{r}$  is a unit vector along the muon line of sight. The simulated results of muon flux, average energy and rate at the far site are  $J_\mu = 6.23 \times 10^{-5} \text{ cm}^2 \text{ s}^{-1}$ ,  $E_\mu = 60.2 \text{ GeV}$  and  $R_\mu = 45.4 \text{ Hz}$  respectively. It is sometimes assumed that final muons inside an underground lab are mostly vertical. On the contrary, it is found from the DCMUSIC simulation that a substantial fraction of the muons reach the far lab from the shallow hill side at an angle around  $45^\circ$ . This information is useful not just for Double Chooz but the optimization of inner veto designs of future underground detectors.

Uniform generation is a very accurate and efficient method to compute average observables but not the most straightforward way to generate muon events as inputs for FLUKA and GEANT.

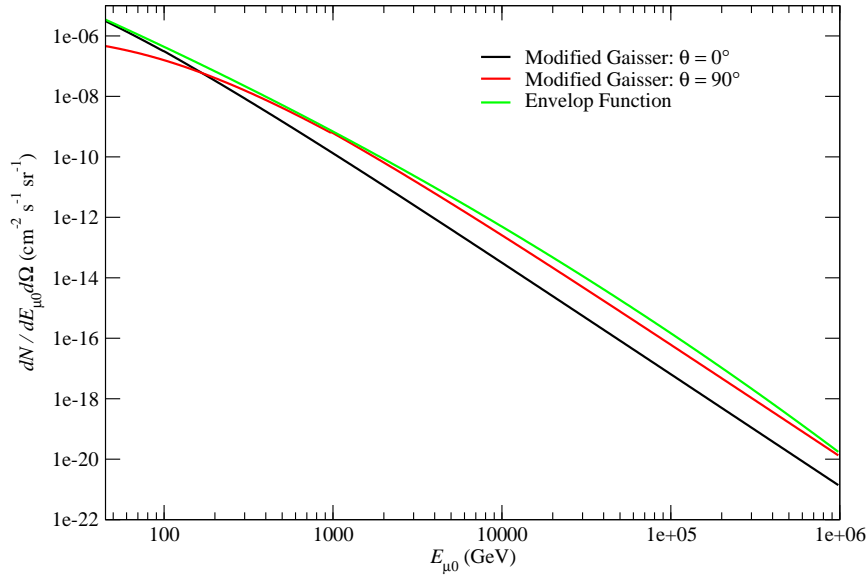


Figure 83: A ketch of the envelop function  $f(E_{\mu 0})$  in relation to the modified Gaisser function at  $\theta = 0^\circ, 90^\circ$  for  $45 \leq E_{\mu 0} \leq 10^6$  GeV.

To this end, generation according to the surface muon distribution is still the preferred method. The traditional approach of generation according to a distribution is to randomly simulate a value between the maximum and the minimum of the distribution and then try to invert the distribution by trial-and-error. This technique usually fails in the case of a sharply peaked distribution because inversion by trial-and-error tends toward an infinite loop because randomly generated trial solutions tend to miss the sharp peak. Fortunately a trick is found to envelop the sharply peaked distribution with a function that defines a narrower range of values to try during the inversion process. The envelop function is

$$f(E) = 4 \times 10^{16} \exp(-42E^{0.05})$$

Fig. 83 illustrates the quality of the functional envelop. The result is a very efficient inversion algorithm despite the sharpness of the modified Gaisser distribution. At the Double Chooz far site, the minimum rock slant depth is about 93 m so that initial muons of energy less 45 GeV are not expected to survive so that the simulation can begin at that energy.

The strength of DCMUSIC is concentrated on the simulations of muon overburden underneath complicated mountain profiles because they cannot be easily constructed by standard software packages. In this sense, DCMUSIC is useful mostly in the case of the far detector. The near detector on the other hand is located underneath a flat overburden so that either FLUKA or GEANT can easily define a simple topographic geometry. Other details on muon background simulations can be found in section 2.3.2.

### 8.2.1 Event Generators

Members of the Double Chooz collaboration have developed a fairly complete neutrino event generator. The code includes the source neutrino distribution of two extended reactor cores with built-in time variation due to fuel evolution. Neutrinos are propagated point to point from their creation

in the reactor to their interaction in the near or far detector. Oscillation effects are included in the propagation. Interactions can occur in any portion of the detector, including the target.

### 8.2.2 Nuclear Transport Properties

The nuclear properties of the simulated detector materials have been checked against measured and tabulated values. For photon and neutron transport, the attenuation lengths and inelastic properties are consistent with observation. Efforts have been made to simulate the multiple photon cascades from neutron capture on Gadolinium. This process is either not modeled or is poorly implemented in many standard simulation packages, such as **GEANT**. The simulation has been carefully tuned to give a neutron capture cascade consistent with that observed with the first CHOOZ experiment.

### 8.3 Vertex and Energy Reconstruction

The event reconstruction developed for Double Chooz is based on a maximum likelihood algorithm that makes use of all information available in any given event. An event is fully characterized by the four-vertex  $(x, y, z, t)$  in the coordinate system of the detector, direction  $(\phi, \theta)$ , and energy  $(E)$ . Thus, for any given event defined by the set of parameters  $\vec{\alpha}$ ,

$$\vec{\alpha} = (x, y, z, t, \phi, \theta, E),$$

the likelihood for measuring a set of PMT charges  $(q_i)$  and times  $(t_i)$  in the Double Chooz detector is the product over the individual charge and time likelihoods at the PMTs:

$$\mathcal{L}_{event} = \prod_{i=1}^{N_{PMTs}} \mathcal{L}_q(q_i; \vec{\alpha}) \mathcal{L}_t(t_i; \vec{\alpha}).$$

Reversing the meaning of the likelihood function,  $\mathcal{L}_{event}$  is the likelihood that the event is characterized by the set  $\vec{\alpha}$  given the set of measured charges  $(q_i)$  and times  $(t_i)$ . Maximizing the event likelihood  $\mathcal{L}_{event}$  (or equivalently minimizing  $-\ln \mathcal{L}_{event}$ ) with respect to  $\vec{\alpha}$  determines the optimal set of event parameters.

Given the scintillator concentration in the target volume of Double Chooz, one can safely assume that events emit effectively only isotropic scintillation light of strength  $\Phi$  (photons per steradian), which is proportional to the event energy  $E$ . The average number of photoelectrons (PEs),  $\mu_i$ , expected at a PMT of quantum efficiency  $\varepsilon_i$ , at a distance  $r_i$  from the event vertex, and subtending a solid angle  $\Omega_i$  is given by

$$\mu_i = \varepsilon_i \Omega_i \Phi \exp(-r_i/\lambda).$$

For distances  $r_i$  much larger than the PMT radius  $R$ ,  $r_i \gg R$ , the solid angle is defined by

$$\Omega_i = \frac{\pi R^2}{r_i^2} f(\cos \eta_i),$$

where  $f(\cos \eta)$  is the angular response function of the PMT, i.e., the PMT efficiency as a function of the angle of incidence of the light with respect to its normal,  $\eta_i$ . Although the scintillation attenuation length  $\lambda$  and the individual quantum efficiencies of the PMTs are wave-length dependent, only average, effective values are used in this approach – which provide a very good description

of the light model. All reconstruction parameters (attenuation lengths, solid angles and quantum efficiencies) are determined self-consistently from control data samples.

The charge likelihood  $\mathcal{L}_q(q; \vec{\alpha})$  for any given PMT is directly obtained from the (normalized) probability of measuring a charge  $q$  for a predicted value  $\mu$ ,  $\mathcal{P}(q; \mu)$ , since  $\mu$  itself depends on the set of event parameters  $\vec{\alpha}$ . The negative charge log-likelihood look-up tables can be obtained in two different ways:

- (a) Assuming that the probability of measuring  $n$  PEs at a given PMT at which one predicts a charge  $\mu$  in the presence of the light source is governed by Poisson statistics,

$$P(n; \mu) = \frac{1}{n!} e^{-\mu} \mu^n,$$

the probability of measuring a charge  $q$  for the predicted value  $\mu$  is given by

$$\mathcal{P}(q; \mu) = \sum_{n=0}^{\infty} P(q; n) P(n; \mu),$$

where the  $P(q; n)$  functions are the charge response functions of the PMTs, *i.e.* the probability of measuring a charge  $q$  given a number of PEs  $n$ . The single PE response function,  $P(q; 1)$ , can be obtained directly from low intensity laser calibration runs, while the higher ones ( $n > 1$ ) can be obtained from  $P(q; 1)$  by multiple random sampling.

- (b) Alternatively, the entire two-dimensional  $\mathcal{P}(q; \mu)$  distribution can be obtained from laser calibration runs which cover a wide range of light intensities. This method is independent on the underlying photon statistics at the PMTs, and can be also cross-checked with similar measurements derived from other data sets.

The time likelihood for any *hit* PMT is a function of both the corrected time,  $t_{corr}^{(i)}$ , defined as:

$$t_{corr}^{(i)} = t_i - t - \frac{r_i}{c_n},$$

(where  $t_i$  is the measured time at the PMT,  $t$  is the event time,  $r_i$  is the distance from the event vertex to the PMT, and  $c_n$  is the speed of light in the medium), and the predicted charge at that particular PMT,  $\mu_i$ . Several such distributions are illustrated in Figure 84 for  $\mu = 0$ ,  $\mu = 2$ , and  $\mu = 4$  PE. In essence they are obtained through folding a sum of exponential decays (typical for scintillation light) with a Gaussian representing the PMT jitter, taken to be  $\sigma_t = 1.2$  ns throughout these simulations.

The position reconstruction performance of this algorithm is shown in Figure 85 for 1-MeV electrons generated uniformly throughout the target volume of Double Chooz. The accuracy is about 8.8 cm in each direction, corresponding to a spatial position resolution of 15.3 cm, without any systematic pulls in any direction.

The energy reconstruction can be obtained by two different methods: either through the total visible charge with corrections as a function of  $\rho = \sqrt{x^2 + y^2}$  and  $z$ ,

$$E = Q f(\rho, z),$$

given the cylindrical geometry of the detector, or directly through the fitted flux  $\Phi$ , after a simple rescaling,

$$E = c_E \Phi.$$

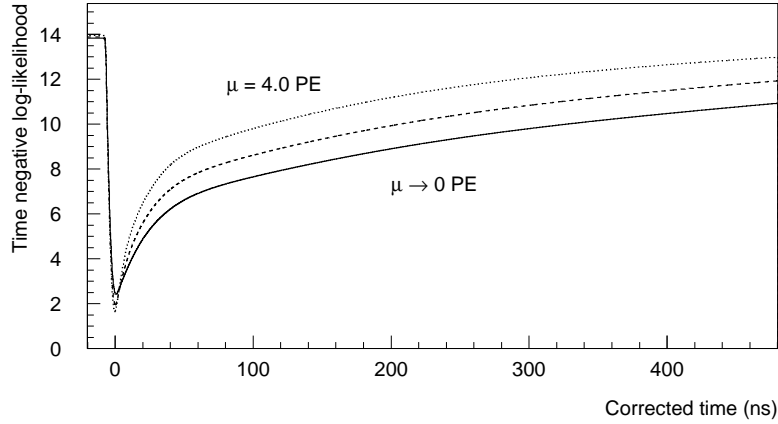


Figure 84: Negative time log-likelihood functions for  $\mu = 0, 2,$  and  $4$  PE.

The proportionality constant  $c_E$  can be obtained from known radioactive calibration sources. The variation of the reconstructed event energy as obtained from the total visible charge is shown in Figure 86, as obtained from the same sample of 1-MeV electrons. The same figure also illustrates the fact that the reconstructed energy as obtained directly from the flux is essentially independent on the event position in the detector. The energy resolution obtained through this method is 7.4%.

The reconstruction performance has also been investigated in the case in which the detector walls are painted white (instead of black), in order to enhance the reflections. In turn, these would increase the overall light level in the detector, leading to a better energy resolution and a more uniform charge response. For a reflectivity coefficient of 0.4, the average total visible charge increased by about 38% in the presence of raw stainless steel walls, *i.e.*, the energy resolution is expected to improve by a factor of approximately  $\sqrt{1.38} = 1.17$ . At the same time one expects the position resolution to be slightly degraded, as a direct consequence of the broadening of the timing distributions by additional reflections. With the new set of time log-likelihood functions, we find that the position reconstruction has an overall spatial position resolution of 15.3 cm, which happens to be identical to the performance of the detector with non-reflective walls. The negative effect introduced by the broadening of the timing distributions is counter-balanced by the increase in the number of hit PMTs. The energy reconstruction obtained from the fitted flux yields a resolution of 6.4%, in good agreement with the expected improvement calculated from the total amount of light. The optical model in this case is slightly different than that in the case of no reflections, with a different effective attenuation length and a solid angle  $\Omega$  that scales differently than  $1/r^2$ .

## 8.4 Calibration

### 8.4.1 Light Sources

The primary purpose of the laser calibration system is to quantify and monitor pertinent properties of each individual PMT, such as PMT gain, relative quantum efficiency, pulse-height versus photoelectron linearity, and timing. Other functions of the system include the measurement and monitoring of the effective attenuation length of the scintillator over the lifetime of the experiment, the determination of the charge and time likelihood functions as needed by the reconstruction algorithms, as well as *in-situ* measurements of the position reconstruction accuracy.



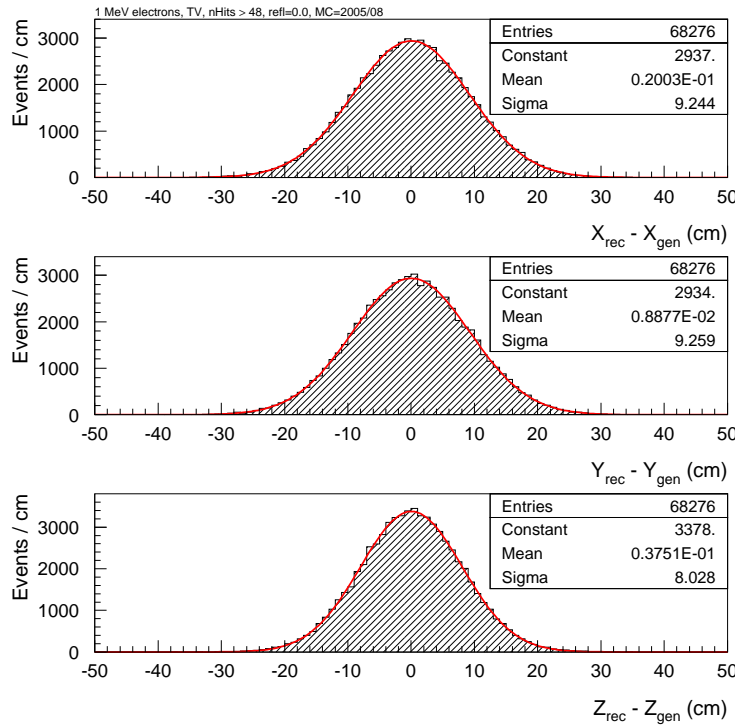


Figure 85: Position reconstruction accuracy for 1 MeV electrons generated uniformly throughout the target volume.

Single PE response, relative quantum efficiencies, and gain calibrations can be obtained from low intensity, low frequency background runs using the central laser light source. Special calibration runs with high intensity light levels via the central light source determine uniquely the time offsets of the PMTs. Time slewing corrections are determined from laser calibration runs covering all intensities and all light sources. These data sets will also be of essence in determining the charge and time likelihood functions.

## 8.5 Resources

The offline computing environment of Double Chooz is defined by a number of constraints: smooth transition between the two stages of the experiment (far detector only first and then both the far and near detectors together), issues of the data flow, on-site storage and analysis capabilities, networking and the data transport, off-site long term storage capabilities and data analysis.

### 8.5.1 On site resources

#### (a) Initial stage: Far detector only

During this first stage, site huts will be installed at the exit of the tunnel equipped with a user room for the computing and storage equipments. Databases supported by reliable mass storage devices (RAID drives) guarantee a few weeks of raw data buffering for calibration data. A cluster of workstations are used for offline processes on-site analysis of the calibration runs, and first level raw data analysis if needed.

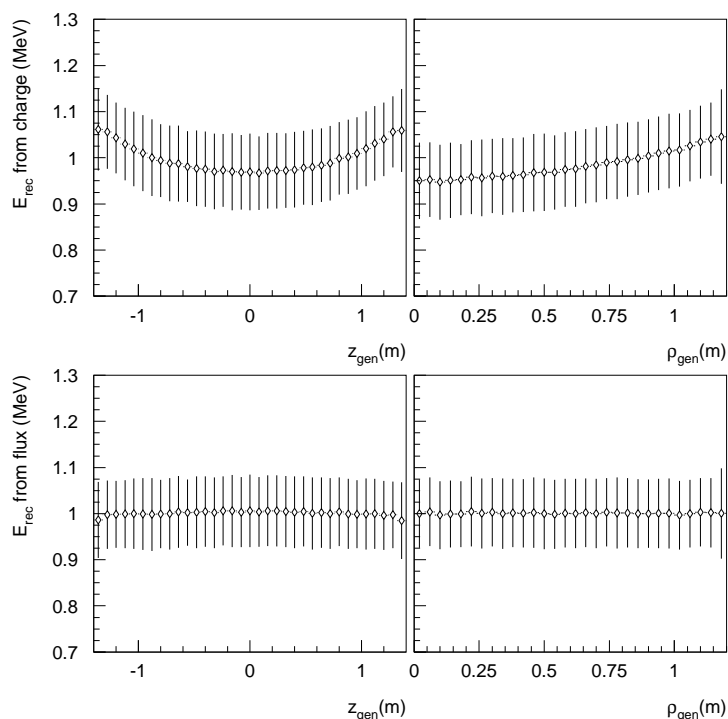


Figure 86: Reconstructed energy versus generated  $z$  and  $\rho$  (radial distance) as obtained from the total visible charge (top) and fitted flux (bottom) – both without any position corrections.

Internet connections will be configured via a regional network to the nearest university, the French national IN2P3 network PHYNET and the French university network RENATER. Raw data will be transferred to the IN2P3 Computing Center using file transfer protocols such as bbFTP and gridFTP optimized for the transfer of large data files over the internet.

A special connection utilizing the Chooz village internet infrastructure will be provided to Chateau de L'Aviette for the remote control and monitoring of the detector, on site alarms, and all things necessary to shift workers.

(b) Final stage: far and near detector

When both detectors will be ready to run at the same time, the user room will be moved closer to the near detector site, together with the workstations and storage facilities. A high bandwidth fiber optic or wireless link will connect the far site and the new user room.

The rate of data flow projected in the final configuration is of the order of 15-25 GB/d (see the DAQ summary paragraph). Like the initial stage of the experiment, a few weeks of raw data storage capacity and databases are planned on site for calibration runs. This operation conserves the RAID drives (a few TBs) used during the first stage of the experiment.

The local network to Chateau de L'Aviette and the internet connection in the new user room will stay the same.

### 8.5.2 Off-site resources

The IN2P3 Computing Center (CC-IN2P3) in Lyon (France) will be used as a data repository (raw data and processed data) for off-line analysis, as it is already used for the CVS code repository.

Based on the data flow rate foreseen in the final configuration, the total amount of raw data accumulated during the life time of the experiment should be of the order of few tens of TB taking into account an usual value of duty cycle of the order of 70%. CC-IN2P3 is equipped with the HPSS (High Performance Storage System) designed to cope with the increasing storage capacity demand coming from several experiments, and will easily handle the full set of Double Chooz data over its life time. HPSS gives its users a transparent and fast access to data as though if they were on disk. A bookkeeping database for the data files is probably needed. Some simulation data files larger than 100 MB can also be stored in HPSS.

User accounts will be granted to all Double Chooz Collaboration members who want to use the computing facility consisting of more than 1300 processors running under UNIX (mainly Scientific Linux and SL3). CC-IN2P3 will provide general assistance to Double Chooz users, including the use of site-licensed softwares, technical support and 24-hour operators.

### 8.5.3 RoSS

RoSS (Read-Out System Simulation) is a package that relies on MC data generated with `DCsim` to simulate the response of the readout system of the Double Chooz detectors. It holds all the knowledge about the readout system elements (simplistically regarded as a set of gains and threshold with time-windows) so that we can characterize their effect to the physics responses to be measured by Double Chooz to high accuracy.

`DCsim` simulates all the relevant scintillator-light interactions between the point of creation in the liquid scintillator and the point of detection on the PMT photocathode. It outputs the PEs (photo-electrons) from each PMT to calculate the energy deposition in the detector. RoSS takes each PE simulated by `DCsim` as an input, whose only information is the time of creation on the photocathode. All effects associated to the quantum efficiency of the photocathode are calculated by `DCsim`, while all processes converting each PE into a sampled digitized electrical signal are simulated by RoSS. In order to accomplish these functionalities, RoSS includes responses in the DAQ system (PMT and electronics), time and charge modulations (bandwidth, linearity and fluctuations) in the entire analogue-to-digital conversion process. Response correlations both in time (PMT after-pulsing) and across channels (crosstalk) are integrated into the simulation by default, along with the trigger logic and electronics (discriminators) behaviors. As part of the trigger, Double Chooz relies on level-2 software-online-trigger to perform some event-type classification necessary to cope with the expected DAQ rates.

Conceptually, the design philosophy of RoSS relies on as little simulation of "micro-physics" (behind the readout system response) as possible. Instead, it utilizes empirical responses curves obtained from measurements in dedicated test-benches. This approach has, at least, two major advantages: (1) The simplification of the implementation since empirical response PDFs (probability distribution functions) integrate inclusively over all effects that matter, and (2) this approach avoids the introduction of readout element models that are difficult to test or tune (if feasible at all) and do not necessarily improve the accuracy of the overall performance of the simulation for the scope of Double Chooz while enlarges the number of unnecessary degrees of freedom of the simulation. This approach is expected to model the necessary complexity adequately in the final MC versus

DATA comparisons. Therefore, a possible oversimplification of the simulation can be tackled when motivation is found data-driven. The only one external dependence of RoSS beyond DOGS is ROOT.

#### 8.5.4 DOGS

DOGS (Double Chooz Offline Group Software) refers to the whole offline software of Double Chooz. It relies on ROOT for I/O functionalities. It contains dedicated packages devoted to specialized tasks necessary for the offline data analysis. However, the main feature of DOGS is a common interface (or framework) by which all packages can interact and/or exchange information and data easily. The built-in functionalities carry out data processing operations such as energy deposition, position reconstruction, event-type recognition, energy reconstruction (upon calibration), sub-detectors monitoring and so on. Currently most of these packages beyond the common interface are still under construction.

The common interface for data exchange is incorporated into the "Event" package. Its function is to wrap data within a group of smart data-capsules which are designed for the flexibility of the data structure necessary to reuse the same data containers (and depending software) throughout the full lifetime of data along the offline analysis. As a critical feature for the remaining DOGS software design, once the Event structure is defined, all packages know how to exchange information/data independently of the type of data treated. Simulated and experimental data can be held within the data-capsules transparently so that the analysis software cannot distinguish between simulated and experimental data. The data-capsules are "smart" in that they have the capability to save and retrieve their contents from the storage area. This flexibility allows the selection of the data to be used at each analysis such that the user can configure the run with as little I/O overhead as possible.

## 9 Non proliferation activities

Within the Double Chooz collaboration and at the request of the International Atomic Energy Agency (IAEA), studies are being conducted to evaluate the interest of using antineutrino detection to remotely monitor nuclear power station. Indeed, the existence of an antineutrino signal sensitive to the power and to the isotopic composition of a reactor core, as proposed by Mikaelian et al. [100] and as demonstrated by the Bugey [101] and Rovno experiments [102], could provide a means to address certain safeguards applications. If this method proves to be useful, the IAEA may decide that any new nuclear power plants should include an antineutrino monitor.

The high penetration power of antineutrinos and the detection capability might provide a means to make remote, non-intrusive measurements of plutonium content in reactors [103]. The antineutrino flux and energy spectrum depend upon the thermal power and on the fissile isotopic composition of the reactor fuel. Based on predicted and observed  $\beta$  spectra, the number of antineutrinos per fission from  $^{239}\text{Pu}$  is known to be less than the number from  $^{235}\text{U}$ , and the energy released larger by 5%. Hence an hypothetical reactor able to use only  $^{235}\text{U}$  would induce in a detector an antineutrino signal 60% higher than the same reactor producing the same amount of energy but burning only  $^{239}\text{Pu}$  (see table). This may offer a means to monitor changes in the relative amounts of  $^{235}\text{U}$  and  $^{239}\text{Pu}$  in the core. If made in conjunction with accurate independent measurements of the thermal power (with the reactor temperature and the flow rate of cooling water), antineutrino measurements might provide an estimate of the isotopic composition of the core, in particular its plutonium inventories. The shape of the antineutrino spectrum can provide additional information about core fissile isotopic composition.

Because the antineutrino signal from the reactor decreases as the square of the distance from the reactor to the detector a precise “remote” measurement is really only practical at distances of a few tens of meters if one is constrained to “small” detectors of the order of few cubic meter in size. Without any extra experimental effort, the near detector of the Double Chooz experiment will provide the most important dataset of anti neutrino detected ( $5 \times 10^5$  events per year). The antineutrinos energy spectrum recorded at a given time will be correlated to the fuel composition and to the thermal power provided by EDF; it is expected that individual components due to each fissile element ( $^{235}\text{U}$ ,  $^{239}\text{Pu}$ ) could be extracted with some modest precision and serve as a benchmark for this techniques. To fulfill the goal of non-proliferation additional lab tests and

	$^{235}\text{U}$	$^{239}\text{Pu}$
Released Energy per Fission	201.7 MeV	210.0 MeV
Mean Energy of $\nu$	2.94 MeV	2.84 MeV
$\nu$ per fission $>1.8$ MeV	1.92	1.45
Reactor neutrino cross section	$\sim 3.2 \cdot 10^{-43} \text{ cm}^2$	$\sim 2.76 \cdot 10^{-43} \text{ cm}^2$

Table 29: Main features of fissions elements chains producing electron antineutrinos.

theoretical calculations should also be performed to more precisely estimate the underlying neutrino spectra of plutonium and uranium fission products, especially at high energies. Contributions of decays to excited states of daughter nuclei are mandatory to reconstruct the shape of each spectrum. As concluded by P. Huber and Th. Schwetz [24] a reduction of the present errors on the anti-neutrino fluxes of about a factor of three is necessary to achieve this goal.

## 9.1 Experimental effort

The precise measurement of  $\beta$ -decay spectra from fission products produced by the irradiation of a fissile target can be performed at the high flux reactor at Institut Laue Langevin in Grenoble (ILL). The reactor produces the highest neutron flux in the world. The fission rate of a fissile material target placed close to the reactor core is about  $10^{12}$  per second. It is possible to choose different fissile elements as target in order to maximize the yield of the nucleus of interest. Using the LOHENGRIN recoil mass spectrometer [104], measurement of individual  $\beta$ -spectra from short lived fission products are possible; in the same irradiation channel, measurements of integral  $\beta$ -spectrum with the Mini-INCA detectors [105], could be envisaged to study the evolution with time of the antineutrino energy spectrum of a nuclear power plant.

### 9.1.1 Experiments with Lohengrin

The LOHENGRIN recoil mass spectrometer offers the possibility to measure  $\beta$ -decays of individual fission products or at least of isobar fission products. This is done by selecting, within the A/q ratio, the fission products released by the fissile target located 23 m upstream. The fissile target ( $^{235}\text{U}$ ,  $^{239}\text{Pu}$ ,  $^{241}\text{Pu}$ , ) is placed into a neutron flux of  $6 \times 10^{14} \text{ ncm}^{-2}\text{s}^{-1}$ , 50 cm from the fuel element. Recoil fission products are selected with a bipolar magnetic field followed by an electrostatic condenser. Before the focal plane of the spectrometer, a focusing magnet has been added in the last few years to reduce the dispersion of particles and to increase the count rate by a factor 7. At the focal plane, the detection of the fragments is done in an ionization chamber. At the end of the ionization chamber, the fragments could be implanted on a moving tape, and the measurement of subsequent  $\beta$  and  $\gamma$ -rays are recorded by a  $\beta$ -spectrometer and Ge-clover detectors, respectively. Coincidences between these two quantities could also be made to reconstruct the decay scheme of the observed fission products or to select one fission product. Fragments with half-lives down to  $2 \mu\text{s}$  can be measured, so that nuclei with large  $Q_\beta$  (above 4 MeV) can be measured. The LOHENGRIN experimental objectives are to complete existing  $\beta$ -spectra of individual fission products [106] with new measurements (for the main contributors to the detected  $\beta$ -spectra) and to provide integral  $\beta$ -energy spectra for mass-selected fission products coming from different fissile isotopes ( $^{235}\text{U}$ ,  $^{239}\text{Pu}$ ,  $^{241}\text{Pu}$ ). This ambitious experimental program is motivated by the fact - noted by C. Bemporad [107] - that unknown decays contribute as much as 25% of the antineutrinos at energies  $> 4$  MeV. Folding the antineutrino energy spectrum over the detection cross-section for inverse beta decay enhances the contribution of the high energy antineutrinos to the total detected flux by a factor of about 10 for  $E_\nu > 6$  MeV. Although integral spectra measured by Schreckenbach et al. [108] are rather precise, better than 2% up to 8 MeV, there is a disagreement with experimental integral spectra made by Tengblad et al. [106], with important errors: 5% at 4 MeV, 11% at 5 MeV and 20% at 8 MeV quoted. The focus of these experiments will be on neutron rich nuclei with yields very different in  $^{239}\text{Pu}$  and  $^{235}\text{U}$  fission. In the list:  $^{86}\text{Ge}$ ,  $^{90-92}\text{Se}$ ,  $^{94}\text{Br}$ ,  $^{96-98}\text{Kr}$ ,  $^{100}\text{Rb}$ ,  $^{100-102}\text{Sr}$ ,  $^{108-112}\text{Mo}$ ,  $^{106-113}\text{Tc}$ ,  $^{113-115}\text{Ru}$  ... contribute to the high energy part of the spectrum and have never been measured.

### Irradiation tests

A test-experiment has been performed during two weeks of the summer of 2005. The isobaric chains A=90 and A=94 were studied. Indeed some isotopes of these selected masses possess a high  $Q_\beta$  energy, and contribute significantly to the high energy part of the antineutrino spectra following  $^{235}\text{U}$  and  $^{239}\text{Pu}$  fissions, ( $^{99}\text{Br}$ :  $Q_\beta = 10.3$  MeV,  $^{90}\text{Rb}$ :  $Q_\beta = 6.6$  MeV,  $^{94}\text{Br}$ :  $Q_\beta = 13.3$  MeV,  $^{94}\text{Kr}$ :

$Q_\beta = 7.7$  MeV,  $^{94}\text{Rb}$ :  $Q_\beta = 10.3$  MeV). Moreover they exhibit different fission yields after  $^{235}\text{U}$  and  $^{239}\text{Pu}$  fission [110]. The half-lives (from a few tens of ms to years) and yields (from  $10^{-4}$  to a few per 100 fissions) of these nuclei are diverse. The well-known nuclei, such as  $^{90}\text{Br}$ , will serve as a test of the experimental set-up, while the beta decay of more exotic nuclei such as  $^{94}\text{Kr}$  and  $^{94}\text{Br}$  will constitute a test case for how far one can reach in the very neutron rich region with this experimental device. The fission fragments arising from a 6 mg  $^{235}\text{U}$  target placed in the thermal neutron flux reactor (a few  $10^{14}$   $\text{ncm}^{-2}\text{s}^{-1}$ ) were selected through the LOHENGRIN spectrometer. The  $\beta$ -spectrometer was a thick cooled Si(Li) detector allowing a  $\beta$  detection up to 15 MeV. The recorded data (see Figure 87) will also validate the simulation described in the following section, in particular the evolution over time of the isobaric chains beta decay spectra. Indeed, thanks to the chopper we could vary the implantation durations on the tape, selecting longer or shorter lived nuclei, and adjusting the velocity to enhance some nuclei with respect to the others, depending on their half-life. Moreover the fission rate of the  $^{235}\text{U}$  target diminishes quite rapidly, and the target was changed during the experiment, so that the simulation of the burn up of the target will be tested. Because of the huge background due to the other nuclear charges within the same mass line, an accurate measurement of individual beta spectra is not possible with such a set-up. An identification of the atomic number of the fission products coming out from LOHENGRIN is required. Coincidence measurements between  $\beta$  and  $\gamma$  could be used with an increased solid angle

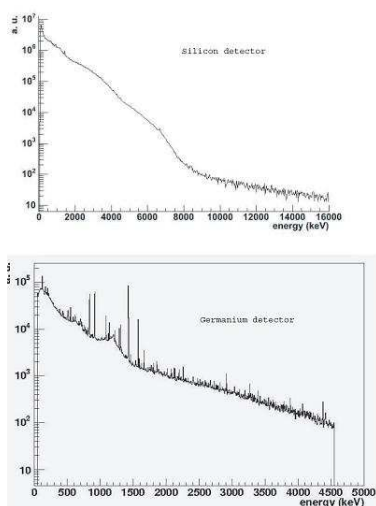


Figure 87: Beta energy spectrum (a) recorded with the silicon detector corresponding to beta decay of fission products with mass  $A=94$ . The fission products arising from the LOHENGRIN spectrometer were implanted on a mylar tape of adjustable velocity in front of the silicon detector. The highest velocity was selected in order to enhance shorter-lived nuclei such as  $^{94}\text{Kr}$  and  $^{94}\text{Br}$ . The gamma energy spectrum (b) obtained with the germanium detector corresponding to the same runs is displayed also.

but the identification of the decaying nucleus is not possible when the decay occurs toward the ground state. The best solution would be to identify the atomic number of the fission products through their trajectory in an ionization chamber, and to be able to detect the trajectory of the emitted electron. The spatial correlation would allow us to determine from which fission product the electron comes. The track of the electron could be measured with a wire chamber, in which the electron would lose only a very small part of its energy and the rest of its energy would be measured

in a silicon detector. These improvements of the experimental set-up are under study. Experiments on other facilities (ISOLDE, GANIL...) could be also performed, depending on the nuclei to study.

### **Integral $\beta$ spectra measurements**

In complement to individual studies on LOHENGRIN, more integral studies can be envisaged using the so called “Mini-INCA chamber” at ILL [105] by adding a  $\beta$ -spectrometer (to be developed). The existing  $\alpha$ - and  $\gamma$ -spectroscopy station is connected to the LOHENGRIN channel and offers the possibility to perform irradiations in a quasi thermal neutron flux up to 20 times the nominal value in a PWR. Moreover, the irradiation can be repeated as many time as needed. It offers then the unique possibility to characterize the evolution of the  $\beta$  spectrum as a function of the irradiation time and the irradiation cooling. The expected modification of the  $\beta$  spectrum as a function of the irradiation time is connected to the transmutation induced by neutron capture of the fissile and fission fragment elements. It is thus related to the “natural” evolution of the spent-fuel in the reactor. The modification of the  $\beta$  spectrum as a function of the cooling time is connected to the decaying chain of the fission products and is then a mean to select the emitted fragments by their lifetime. This information is important because long-lived fission fragments accumulate in the core and after a few days mainly contribute to the low energy part of the antineutrino-spectra. Due to the mechanical transfer of the sample from the irradiation location to the measurement station an irreducible delay time of 30 min is imposed leading to the loss of short-lived fragments.

### **Prospect to study fission of $^{238}\text{U}$**

The integral beta decay spectrum arising from  $^{238}\text{U}$  fission has never been measured. All information relies on theoretical computations [111]. Some experiments could be envisaged using few MeV neutron sources in Europe (Van de Graaf in Geel, SING in PSI, ALVARES or SAMES accelerators at Valduc ...). Here the total absence of experimental data on the  $\beta$  emitted in the fission of  $^{238}\text{U}$  changes the context of this measurement compared to the other isotopes. Indeed any integral measurements performed could be used to constraint the present theoretical estimations of the antineutrino flux produced in the fission of  $^{238}\text{U}$ . In any case it seems rather difficult to fulfill the goal of a determination of the isotopic content from antineutrino measurements as long as this important part of the energy spectrum is so poorly known.

## **9.2 Simulations**

### **9.2.1 Simulations of diversion scenarios**

The IAEA recommends the study of specific safeguards scenarios. Among its concerns are the confirmation of the absence of unrecorded production of fissile material in declared reactors and the monitoring of the burn-up of a reactor core. The time required to manufacture an actual weapon estimated by the IAEA (conversion time), for plutonium in partially irradiated or spent fuel, lies between 1 and 3 months. The significant quantity of Pu to be sought is 8 kg, to be compared with the 3 tons of  $^{235}\text{U}$  contained in a Pressurized Water Reactor (PWR) of power 900 MW<sub>e</sub> enriched to 3%. The small magnitude of the desired signal requires a careful feasibility study.

The proliferation scenarios of interest involve different kinds of nuclear power plants such as light water or heavy water reactors (PWR, BWR, CANDU...), it has to include isotope production



reactors of a few tens of MW<sub>th</sub>, and future reactors (e.g., PBMRs, Gen IV reactors, accelerator-driven sub-critical assemblies for transmutation, molten salt reactors). To perform these studies, core simulations with dedicated Monte Carlo codes should be provided, coupled to the simulation of the evolution of the antineutrino flux and spectrum over time.

We started a simulation work using the widely used particle transport code MCNPX [112], coupled with an evolution code solving the Bateman equations for the fission products within a package called MURE (MCNP Utility for Reactor Evolution) [113]. This package offers a set of tools, interfaced with MCNP or MCNPX, that allows us to define easily the geometry of a reactor core. In the evolution part, it has access to the 3834 nuclei possibly considered, the set of nuclear data: nuclear masses from “The 2003 Atomic Mass Evaluation” data (National Nuclear Data Center, BNL), the NNDC nuclear wallet card and the nuclear decay data from the JEF3T library. The nuclear reaction data used are taken from the usual nuclear databases [114]. MURE is perfectly adapted to simulate the evolution with time of the composition of the fuel, taking into account the physics of a reactor core, especially the simulations of neutrons. We are adapting the evolution code in order to be able to simulate the antineutrino spectrum and flux, using simple Fermi decay as starting point. The constitution of a database of more specific beta decay for each fission product will be necessary in order to improve the accuracy of the computed antineutrino spectra.

The extended MURE simulation will allow to perform sensitivity studies by varying the Pu content of the core in the relevant scenarios for the IAEA. By varying the reactor power, the possibility to use antineutrinos for power monitoring can be evaluated.

The implementation of the simulation is under way. Antineutrinos from reactors arise from the beta decay of several hundreds of fission products. Each decay occurs generally toward several excited states of the daughter nucleus, and the antineutrino energy spectra are the sum of hundreds of individual beta spectra. It is then necessary to know the decay scheme of these nuclei (branching ratios and available energies toward different final states, shape of the spectrum related to the transition type, allowed -Fermi or Gamow-Teller or forbidden). Moreover the decay schemes of the most unstable isotopes are not well determined and sometimes unknown. Preliminary results show that nuclei with half-lives lower than 1 s emit about 70% (50%) of the <sup>235</sup>U(<sup>239</sup>Pu) antineutrino spectrum above 6 MeV. The high energy part of the spectrum is the energy region where Pu and U spectra differ mostly (see Figure 87). The influence of the beta decay of these nuclei on the antineutrino spectrum might be dominant too in scenarios where rapid changes of the core composition are performed, e.g. in CANDU reactors refueled on line.

The appropriate starting point for this scenario is a representative PWR, like the Chooz reactors. For this reactor type, simulations of the evolution of the antineutrino flux and spectrum over time will be provided and compared to the accurate measurement provided by the near detector. This should provide the precision on the fuel composition of an antineutrino detector like Double Chooz and of independent thermal power measurements. An interesting point to study is at the time of the partial refueling of the core, thanks to the fact that reactor like Chooz (N4-type) does not use MOX fuel. In any case the measurement performed by the Double Chooz experiment with its near detector will constitute the most precise determination of the antineutrino emitted by a PWR. In addition the detailed follow-up of the evolution of the fuel burn-up, controlled by the use of fission chambers, will constitute an excellent experimental basis for the above feasibility studies of potential monitoring and for bench-marking fuel management codes.

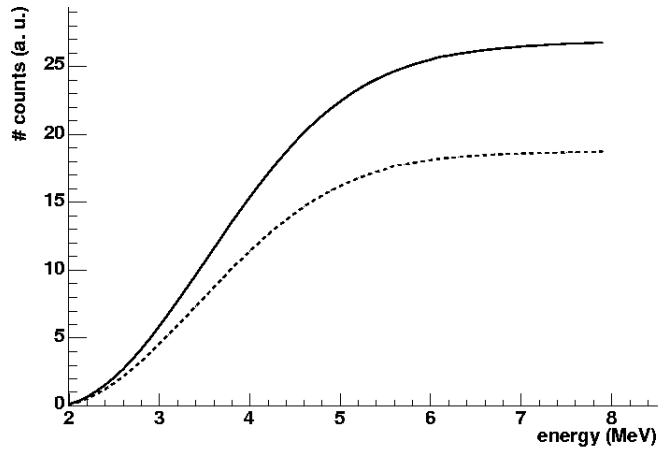


Figure 88: Cumulative number of antineutrinos folded over the detection cross-section, as a function of antineutrino energy for  $^{235}\text{U}$  (plain line) and for  $^{239}\text{Pu}$  (dashed line), computed with the MURE program.

### 9.3 Experimental effort in the U.S.

The experimental program for development of nonproliferation detectors in the United States is led by Lawrence Livermore National Laboratory and Sandia National Laboratories. The LLNL/SNL work has consisted of installing and operating a prototype detector at the 3.46  $\text{GW}_{th}$  San Onofre Nuclear Generating Station (SONGS) in Southern California. The detector, now operating at SONGS at a distance of 25 meters from the core, and with an overburden of about 20 m.w.e., is shown in Figure 89. It has a one cubic meter active liquid scintillator volume and an approximate 2.5 meter  $\times$  3 meter footprint including shielding. It consists of a muon veto system for rejecting cosmic ray backgrounds, a water/polyethylene shield to reject neutron and gamma backgrounds, and a central doped liquid scintillator detector which registers antineutrino interactions. As seen in Figures 90 and 91, the data clearly demonstrates: detection of a high rate of reactor antineutrinos with good signal to background; that the rate is consistent with what the theory of antineutrino interactions predicts; and that changes in reactor power can quickly (within a few hours) be detected by tracking the antineutrino rate. The plot of daily rate versus time (Figure 90) also shows a two sigma deviation of the antineutrino rate from a constant value over a six month period, with the linear reduction in total rate consistent with a prediction that includes a fuel burnup estimate. Current effort is focused on confirming the indications of fuel burnup seen in this data.

### 9.4 Toward a prototype

If we want to propose to the IAEA a neutrino detector able to help in monitoring future nuclear power plants, the next step in this effort has to merge the two present approaches: the Double Chooz approach with a good energy measurement, a good signal to noise ratio, but expensive; and the SONGS approach with a robust, simple, automatic, cheap, but with poor antineutrino detection efficiency (about 10%), a modest signal to background ratio (3 to 1), and poor energy resolution. We thus are considering a new prototype with a size small enough to be installed very close to the reactor core (30 meters or so), but using a technique able to clearly detect neutrinos. Such a prototype will be considered as a demonstrator to be shown to the IAEA and at the same time

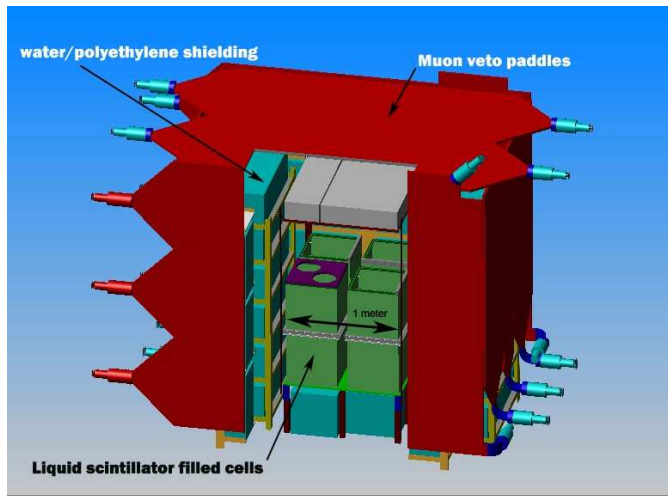


Figure 89: A cutaway view of the LLNL/SNL antineutrino detector deployed at the San Onofre Nuclear Generating Station.

it is already usable tool to measure the thermal power. As an intermediate goal, we can foresee measurements with this prototype at ILL with its core of roughly pure  $^{235}\text{U}$ . It would allow the recording of a very pure neutrino signal from  $^{235}\text{U}$  fission only followed by the evolution due to burn-up. Such a clean experiment would help to calibrate the neutrino signal versus the thermal power, and will also give some confidence for the simulation effort.

#### 9.4.1 Complementary studies

At this stage it would be important to evaluate alternative techniques of antineutrino detection ( $^3\text{He}$  counters,  $^6\text{Li}$  liquid scintillators). Indeed some stability requirements (temperature, humidity...) could favor one particular technique over another one. For a realistic device we cannot expect that the coverage against external muons will be as important as in the case of Double Chooz, hence the impact of backgrounds to the antineutrino signal has to be evaluated carefully.

## 9.5 Conclusions

A realistic diversion (about 10 kg of Pu) has an effect on the antineutrino signal which is very small. The present precision on the antineutrino spectrum emitted in fissions is not enough to allow a determination of the isotopic content in the core sensitive to such diversion. On the other hand, the thermal power measurement is a less difficult job. Neutrinos will sample the whole core, without attenuation, and thus would bring valuable information on the power with totally different systematics than present methods. Even if its measurement is not persuasive by itself, the operator cannot hide any stops or change of power, and in most cases, such a record made with an external and independent device, virtually impossible to fake, will act as a strong deterrent. In spite of the uncertainty mentioned previously, we see that the most energetic part of the spectrum offers the best possibility to disentangle fission from  $^{235}\text{U}$  and  $^{239}\text{Pu}$ . The comparison between the cumulative numbers of antineutrinos as a function of antineutrino energy detected at low vs. high energy is an efficient observable to distinguish pure  $^{235}\text{U}$  and  $^{239}\text{Pu}$ . The IAEA also seeks the possibility of monitoring large spent-fuel elements. For this application, the likelihood is that antineutrino

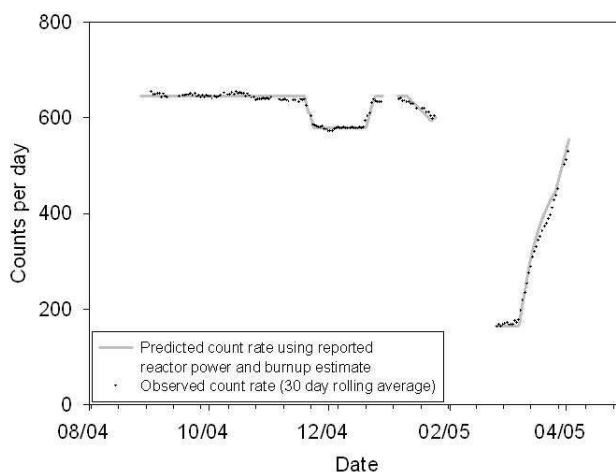


Figure 90: Demonstration of reactor power tracking in SONGS. A 30 day rolling average of observed antineutrino candidate events plotted with an estimate of the expected observation calculated from publicly reported reactor power data and a simple linear approximation of fuel burnup. Data in February-March 2005 with a daily count rate below 200 candidates per day corresponds to a period of zero reactor power, and is thus a measure of the antineutrino mimicking background. The net antineutrino detection rate at full reactor power is thus about 400 antineutrinos per day.

detectors could only make measurements on large quantities of beta-emitters, e.g., several cores' worth of spent fuel. In the time of the experiment the discharge of parts of the core will happen and the Double Chooz experiment will quantify the sensitivity of such monitoring. More generally the techniques developed for the detection of antineutrinos could be applied for the monitoring of nuclear activities at the level of a country. For example a KamLAND type detector deeply submerged off the coast of the country, would offer the sensitivity to detect a new underground reactor located at several hundreds of kilometers. In that respect, progress in detecting media (Gd doped liquid scintillators) would be of great help.

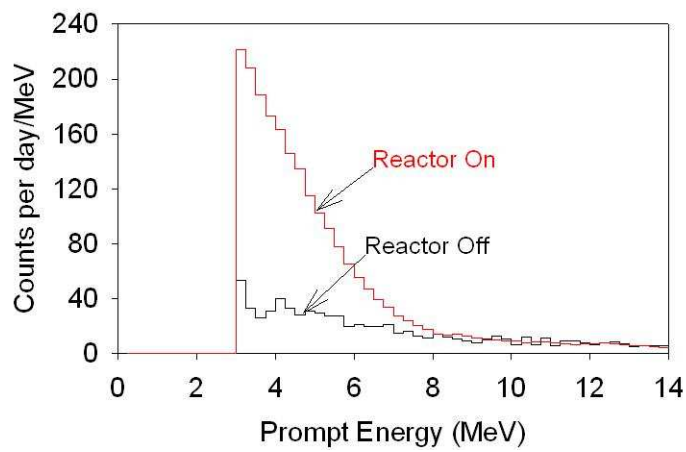


Figure 91: Comparison of the measured energy spectra in SONGS with the monitored reactor on and off. The different shapes of the two spectra conform to expectations and confirm that reactor antineutrinos are being detected. These measure the energy spectrum of the first event in an antineutrino-like event pair. The reactor on and off spectra are expected to be equivalent above about 9 MeV as is seen.

## References

- [1] Yu. Kozlov, L. Mikaelyan, V. Sinev "Two Detector Reactor Neutrino Oscillation Experiment Kr2Det at Krasnoyarsk. Status Report", *Phys.Atom.Nucl.* 66 (2003) 469-471; *Yad.Fiz.* 66 (2003) 497-499.
- [2] H. Minakata, H. Sugiyama, O. Yasuda, K. Inoue, F. Suekane "Reactor Measurement of  $\theta_{13}$  and Its Complementarity to Long-Baseline Experiments", *Journal-ref: Phys.Rev. D68* (2003) 033017; *Erratum-ibid. D70* (2004) 059901.
- [3] P. Huber, M. Lindner, T. Schwetz, and W. Winter, "Reactor neutrino experiments compared to superbeams," *Nucl. Phys.*, **B** 665, 487 (2003).
- [4] Électricité de France. [www.edf.fr](http://www.edf.fr).
- [5] Apollonio, et al., *Eur. Phys. J. C27* (331-374), 2003.
- [6] The White Paper, "A New Nuclear Reactor Neutrino Experiment to Measure  $\theta_{13}$ ," is available at <http://www.hep.anl.gov/minos/reactor13/white.html>, also hep-ex/0402041.
- [7] J.C. Anjos et al., "Angra Neutrino Project" hep-ex/0511059.
- [8] Y. Wang, *Int.J.Mod.Phys. A20* (2005) 5244-5253.
- [9] F. Ardellier et al., "Letter of Intent for Double-CHOOZ: a Search for the Mixing Angle  $\theta_{13}$ ." hep-ex/0405032.
- [10] S. Berridge et al., "Proposal for U.S. participation in Double-CHOOZ: A New  $\theta_{13}$  Experiment at the Chooz Reactor," hep-ex/0410081. hep-ex/0409028.
- [11] M. Kuze et al., "The KASKA project - a Japanese medium-baseline reactor-neutrino oscillation experiment to measure the mixing angle  $\theta_{13}$ ." hep-ex/0502002.
- [12] For a discussion of RENO, see the next reference.
- [13] M. Goodman, "Low Energy Neutrinos", presented to the ICFA workshop in Daegu South Korea, 28 Sep 2005, <http://www.hep.anl.gov/mcg/goodmankorea.ppt>.
- [14] Th. Lasserre and H. Sobel, *Comptes Rendus Physique* 6 (2005) 749-757 (nucl-ex/0601013).
- [15] Astroparticle Physics European Coordination (ApPec) <http://appec.in2p3.fr/>.
- [16] Freedman and Kayser, *The Neutrino Matrix*, DNP/DPF/DAP/DPB Joint Study on the Future of Neutrino Physics, physics/0411216.
- [17] Report on Reactor and Accelerator-based Neutrino Oscillation Experiments from the Neutrino Scientific Assessment Group (NuSAG). <http://www.science.doe.gov/hep/NuSAG2ndRptFeb2006.pdf>.
- [18] Summary Letter (from Chair) from the HEPAP Meeting on March 3-4, 2006, Washington, DC. <http://www.science.doe.gov/hep/HEPAPSummaryLtrMarch2006.pdf>.

- [19] Centre d'Ingénierie, Déconstruction et Environnement Nuclaire of E.D.F.  
<http://fo.gnie.free.fr/unites.ingenierie/CIDEN.htm>.
- [20] <http://www.edf.fr/35070i/Accueilfr/InfosNucleaire/Planrapproche/Lessitesfrançais/Chooz.html>.
- [21] Mahn and Shaevitz, “Comparisons and Combinations of Reactor and Long-Baseline Neutrino Oscillation Measurements,”
- [22] H. Minakata, H. Sugiyama, O. Yasuda, K. Inoue, and F. Suekane, “Reactor measurement of  $\theta_{13}$  and its complementarity to long-baseline experiments,” *Phys. Rev D* **68**, 033017 (2003).
- [23] This proposal.
- [24] Huber, P. and Schwetz, T., *Phys. Rev. D* **70** (053011), 2004.
- [25] Bemporad, C. and Gratta, G. and Vogel, P., *Rev. Mod. Phys.* **74** (297), 2002.
- [26] Declais, Y. et al., *Nucl. Phys. B* **434** (1995) 503-534.
- [27] P. Antonioli et al., *Astropart. Phys.* **7**, 4 (1997), 357-368.
- [28] A. Baldini et al., *Geology at the CHOOZ site*, 1995 (unpublished).
- [29] A. Tang, a talk given at the MAND-sim Workshop in Kansas State University, Manhattan, KS (June 2005). See <http://neutrino.phys.ksu.edu/MAND-sim/MAND-sim%20talks> for a file labelled *DayaBay\_ksutalk.pdf*.  
 A. Tang et al., *Muon simulations for Super-Kamiokande, KamLAND and Chooz*, paper in preparation.
- [30] Schwetz, Thomas and Winter, Walter, “Testing mass-varying neutrinos with reactor experiments”, *Phys. Lett. B* **633**, 2006, 557-562, hep-ph/0511177.
- [31] Particle Data Group book, *Phys. Lett. B* **592** (2004).
- [32] “Future Neutrino Detectors and their Impact on Particle- and Astrophysics” Christian Grieb, Dissertation, Technische Universität München, (2004).
- [33] G. Mention, PhD. Thesis, APC-Collège de France, Paris (2005),  
[http://doublechooz.in2p3.fr/Scientific/Publications/Theses/these\\_gmention.php](http://doublechooz.in2p3.fr/Scientific/Publications/Theses/these_gmention.php).
- [34] Declais, Y. et al., *Nucl. Phys. B* **434** (503-534), 1995.
- [35] Diwan, M. et al., NuMI-L-714, 2001.
- [36] Valle, J. W. F., hep-ph/0509262, 2005.
- [37] See the MINOS experiment result recently reported at  
[http://www.fnal.gov/pub/presspass/press\\_releases/minos\\_3-30-06.html](http://www.fnal.gov/pub/presspass/press_releases/minos_3-30-06.html).
- [38] M. Shiozawa (Super-Kamiokande Collaboration), *Nuclear Physics B (Proc. Suppl.)* **118** (2003).
- [39] S. Fukuda *et al.* (Super-Kamiokande Collaboration).

- [40] P. Huber, M. Lindner, and W. Winter, *Comput. Phys. Commun.* **167**, 195 (2005), <http://www.ph.tum.de/~globes>, [hep-ph/0407333](#).
- [41] Hung, P. Q., "Sterile neutrino and accelerating universe", 2000, [hep-ph/0010126](#).
- [42] P. Huber, J. Kopp, M. Lindner, M. Rolinec, and W. Winter (2006), [hep-ph/0601266](#).
- [43] M. G. Albrow *et al.* (2005), [hep-ex/0509019](#).
- [44] S. Antusch *et al.* (2006), d. Harris, S. Brice, and W. Winter (editors), to appear.
- [45] A. Cervera, F. Dydak, and J. Gomez Cadenas, *Nucl. Instrum. Meth.* **A451**, 123 (2000).
- [46] P. Huber, M. Lindner, M. Rolinec, and W. Winter (2005), [hep-ph/0506237](#).
- [47] P. Huber, M. Lindner, and W. Winter, *Nucl. Phys.* **B645**, 3 (2002), [hep-ph/0204352](#).
- [48] P. Huber, M. Lindner, and W. Winter, *Nucl. Phys.* **B654**, 3 (2003), [hep-ph/0211300](#).
- [49] J. Burguet-Castell, D. Casper, J. J. Gomez-Cadenas, P. Hernandez, and F. Sanchez, *Nucl. Phys.* **B695**, 217 (2004), [hep-ph/0312068](#).
- [50] C. Aalseth *et al.* (2004), [hep-ph/0412300](#).
- [51] H. V. Klapdor-Kleingrothaus, H. Pas, and A. Y. Smirnov, *Phys. Rev.* **D63**, 073005 (2001), [hep-ph/0003219](#).
- [52] S. M. Bilenky, S. Pascoli, and S. T. Petcov, *Phys. Rev.* **D64**, 053010 (2001), [hep-ph/0102265](#).
- [53] F. Feruglio, A. Strumia, and F. Vissani, *Nucl. Phys.* **B637**, 345 (2002), [hep-ph/0201291](#).
- [54] S. Pascoli, S. T. Petcov, and T. Schwetz (2005), [hep-ph/0505226](#).
- [55] S. Choubey and W. Rodejohann (2005), [hep-ph/0506102](#).
- [56] A. de Gouvea and J. Jenkins (2005), [hep-ph/0507021](#).
- [57] M. Lindner, A. Merle, and W. Rodejohann (2005), [hep-ph/0512143](#).
- [58] Gu, Peihong and Wang, Xiulian and Zhang, Xinmin, "Dark energy and neutrino mass limits from baryogenesis, *Phys. Rev.* D68, 2003, 087301, [hep-ph/0307148](#).
- [59] "Hung, Pham Quang and Pas, Heinrich, "Cosmo MSW effect for mass varying neutrinos", *Mod. Phys. Lett. A20*, 2005, 1209-1216, [astro-ph/0311131](#).
- [60] Fardon, Rob and Nelson, Ann E. and Weiner, Neal, "Dark energy from mass varying neutrinos", *JCAP* 0410, 2004, 005, [astro-ph/0309800](#).
- [61] "Kaplan, David B. and Nelson, Ann E. and Weiner, Neal, "Neutrino oscillations as a probe of dark energy", *Phys. Rev. Lett.* 93, 2004, 091801, [hep-ph/0401099](#)".
- [62] Peccei, R. D., "Neutrino models of dark energy", *Phys. Rev.* D71, 2005, 023527, [hep-ph/0411137](#).



- [63] J.-E. Campagne (2005), [hep-ex/0511013](#).
- [64] M. Mezzetto (2005), [hep-ex/0511005](#).
- [65] Y. Itow *et al.*, Nucl. Phys. Proc. Suppl. **111**, 146 (2001), [hep-ex/0106019](#).
- [66] J. Burguet-Castell, D. Casper, E. Couce, J. J. Gomez-Cadenas, and P. Hernandez (2005), [hep-ph/0503021](#).
- [67] D. Motta, C. Buck, F.X. Hartmann, Th. Lasserre, S. Schnert, U. Schwan, “Prototype scintillator cell for an In-based solar neutrino detector”, *Nucl. Instr. Meth. A*, **547** (2005), 368-388.
- [68] <http://www.roehm.com/>.
- [69] <http://www.cecalc.ula.ve/documentacion/tutoriales/castem/castem3.html>.
- [70] F.X. Hartmann and R.A. Naumann, Nucl.Inst. and methods in Physics Research A 313 (1992) 237.
- [71] F.X. Hartmann and R.A. Naumann, Phys.Rev. C (Rapid Comm.) 31 (1985) 1594-1596.
- [72] C. Buck, F.X. Hartmann, D. Motta, S.Schönert, U. Schwan, “Metal beta-diketone scintillators”, Presentation at the Workshop on Future Low Energy Neutrino Experiments, TU Munich, Munich, 9–11 October (2003).
- [73] C. Cattadori et al, “Formulation of an indium loaded scintillator based on indium extraction in trimethyl-benzene by means of C<sub>3</sub>–C<sub>5</sub> carboxylic acids, in presence of neutral organophosphorous compounds”, submitted to Radiation Physics and Chemistry (2004).
- [74] C. Cattadori et al, “A novel formulation for high light yield high transparency indium loaded liquid scintillator”, submitted to Radiation Physics and Chemistry (2004).
- [75] N.A. Danilov, Yu.S. Krylov, C. Cattadori, Radiochemistry, 45 (2) (2003) 128-133.
- [76] F.X. Hartmann, “Low Level Scintillators and Gadolinium”, Presentation at the Workshop on Future Low Energy Neutrino Experiments, TU Munich, Munich, 9–11 October (2003).
- [77] Borexino Collaboration, “Phenylxylylethane (PXE): a high-density, high-flashpoint organic liquid scintillator for applications in low-energy particle and astrophysics experiments”, submitted to *Nucl. Instr. Meth. A*, 2004.
- [78] D. Motta, “Feasibility analysis and prototype measurements of a novel approach for the real-time spectroscopy of low energy solar neutrinos”, dissertation, University of Heidelberg, 2004.
- [79] we are grateful to Hamamatsu Corporation for providing results of their measurements with R5912 phototube.
- [80] <http://www.ngdc/noaa.gov/seg/geomag/jsp/struts/calcPointIGRF>.
- [81] D. Motta and S. Schnert, “Optical properties of bialkali photocathodes”, *Nucl. Instr. Meth. A*, **539** (2005), 217 - 235

- [82] T. Lagomarsino and G. Testera, NIM A430 435 (1999).
- [83] Energy calibration of large underwater detectors using stopping muons, Kudryavtsev et al., Phys. Lett. B, 494 (2000) 175-180.
- [84] <http://www.maxim-ic.com/1-Wire.cfm>.
- [85] <http://www.ibutton.com/weather/>.
- [86] <http://www.sunnuclear.com/products/radon/radon.asp>.
- [87] A. Tang, G. Horton-Smith, V. A. Kudryavtsev and A. Tonazzo, hep-ph/0604078.
- [88] H. M. Araújo, V. A. Kudryavtsev, N. J. C. Spooner and T. J. Sumner, Nuclear Inst. and Methods in Phys. Research A **545** (June 2005), 398-411.
- [89] S. Agostinelli, *et al.*, NIM A 506 (2003), 250-303; see also Geant4 home page at <http://geant4.cern.ch/geant4/>.
- [90] GLG4sim home page: <http://neutrino.phys.ksu.edu/~GLG4sim/>.
- [91] The ESIM simulator is described at <http://www.cs.umbc.edu/~squire/esim.shtml>.
- [92] D. Motta, “Monte Carlo for Double Chooz”, presented at the MeV Antineutrino and Neutrino Detector simulation workshop (MAND-sim 2005), June 14, 2005, slides 10-32. (Workshop home page at <http://neutrino.phys.ksu.edu/MAND-sim/>.)
- [93] *Ibid*, slides 34-41.
- [94] “FLUKA: a multi-particle transport code”, A. Fassò, A. Ferrari, J. Ranft, and P.R. Sala, CERN-2005-10 (2005), INFN/TC\_05/11, SLAC-R-773
- [95] MCNP is described at <http://mcnp-green.lanl.gov/index.html>.
- [96] Y.-F. Wang *et al.*, Phys. Rev. **D64**, 013012 (2001).
- [97] D. Reyna hep-ph/0604145 (submitted to Astroparticle Physics, April 2006).
- [98] T. K. Gaisser and T. Stanev, “Cosmic Rays,” Review of Particle Physics, edited by L. Alvarez-Gaumé *et al.*, Physics Letters, **B592**, 228 (2004).
- [99] P. J. Hayman and A. W. Wolfendale, Proc. Phys. Soc. **80** (1962), 710.
- [100] Mikaelian L.A. Neutrino laboratory in the atomic plant, Proc. Int. Conference Neutrino-77, v. 2, p. 383-387.
- [101] Y. Declais et al., Nucl. Phys. B434, 503 (1995).
- [102] Klimov et al., Atomic Energy, v.76-2, 123, (1994).
- [103] A. Bernstein, Y. Wang, G. Gratta, and T. West, J. Appl. Phys. 91, 4672 (2002).
- [104] ILL Instrument Review, 2004/2005.

- [105] F. Marie, A. Letourneau et al., Nucl. Instr and Meth A556 (2006) 547.
- [106] O. Tengblad et al., Nuclear Physics A 503 (1989) 136-160.
- [107] Bemporad et al., Rev. of Mod. Phys., Vol. 74, (2002).
- [108] K. Schreckenbach, G. Colvin, W. Gelletly, F.v. Feilitzch, Phys. Lett. B160 (1985) 325.
- [109] Mutti et al., ILL proposal 3-01-477. "Characterization of the antineutrino spectra emitted from a nuclear reactor."
- [110] T.R. England and B.F. Rider, ENDF-349, LA-UR-94-3106.
- [111] P. Vogel and J. Engel, Phys. Rev. D39, 3378 (1989).
- [112] Monte Carlo N-Particle eXtended, LA-UR-05-2675, J.S.Hendricks et al.
- [113] MURE: MCNP Utility for Reactor Evolution -Description of the methods, first applications and results. Mal'plan O., Nuttin A., Laulan O., David S., Michel-Sendis F. et al. In Proceedings of the ENC 2005 (CD-Rom) (2005) 1-7.
- [114] ENDF/B-VI.8, JENDL-3.3, JEFF-3.1, evaluated nuclear reaction datafiles from the NNDC (<http://www3.nndc.bnl.gov/index.jsp>).